

Final Report

EVALUATION OF ASPHALT PAVEMENT INTERFACE CONDITIONS FOR ENHANCED
BOND PERFORMANCE

UF Project No.: 118906 Contract No.: BDV31-977-37

Submitted to:

The Florida Department of Transportation
Research Center, MS 30
605 Suwannee Street
Tallahassee, FL, 32399-0450



Dr. Reynaldo Roque, P.E.
David Hernando
Bongsuk Park
Dr. Jian Zou
Jeremy A. M. Waisome

Department of Civil and Coastal Engineering
College of Engineering
365 Weil Hall, P.O. Box 116580
Gainesville, FL, 32611-6580
Tel: (352) 392-9537 Extension 1458
Fax: (352) 392-3394

May 2017

DISCLAIMER

The opinions, findings, and conclusions expressed in this publication are those of the authors and not necessarily those of the State of Florida Department of Transportation.

Prepared in cooperation with the State of Florida Department of Transportation.

SI* (MODERN METRIC) CONVERSION FACTORS

APPROXIMATE CONVERSIONS TO SI UNITS

SYMBOL	WHEN YOU KNOW	MULTIPLY BY	TO FIND	SYMBOL
LENGTH				
in	inches	25.4	millimeters	mm
ft	feet	0.305	meters	m
yd	yards	0.914	meters	m
mi	miles	1.61	kilometers	km
AREA				
in ²	square inches	645.2	square millimeters	mm ²
ft ²	square feet	0.093	square meters	m ²
yd ²	square yard	0.836	square meters	m ²
ac	acres	0.405	hectares	ha
mi ²	square miles	2.59	square kilometers	km ²
VOLUME				
fl oz	fluid ounces	29.57	milliliters	mL
gal	gallons	3.785	liters	L
ft ³	cubic feet	0.028	cubic meters	m ³
yd ³	cubic yards	0.765	cubic meters	m ³
NOTE: volumes greater than 1000 L shall be shown in m ³				
MASS				
oz	ounces	28.35	grams	g
lb	pounds	0.454	kilograms	kg
T	short tons (2000 lb)	0.907	megagrams (or "metric ton")	Mg (or "t")
TEMPERATURE (exact degrees)				
°F	Fahrenheit	5 (F-32)/9 or (F-32)/1.8	Celsius	°C
ILLUMINATION				
fc	foot-candles	10.76	lux	lx
fl	foot-Lamberts	3.426	candela/m ²	cd/m ²
FORCE and PRESSURE or STRESS				
lbf	poundforce	4.45	newtons	N
lbf/in ²	poundforce per square inch	6.89	kilopascals	kPa

APPROXIMATE CONVERSIONS FROM SI UNITS

SYMBOL	WHEN YOU KNOW	MULTIPLY BY	TO FIND	SYMBOL
LENGTH				
mm	millimeters	0.039	inches	in
m	meters	3.28	feet	ft
m	meters	1.09	yards	yd
km	kilometers	0.621	miles	mi
AREA				
mm ²	square millimeters	0.0016	square inches	in ²
m ²	square meters	10.764	square feet	ft ²
m ²	square meters	1.195	square yards	yd ²
ha	hectares	2.47	acres	ac
km ²	square kilometers	0.386	square miles	mi ²
VOLUME				
mL	milliliters	0.034	fluid ounces	fl oz
L	liters	0.264	gallons	gal
m ³	cubic meters	35.314	cubic feet	ft ³
m ³	cubic meters	1.307	cubic yards	yd ³
MASS				
g	grams	0.035	ounces	oz
kg	kilograms	2.202	pounds	lb
Mg (or "t")	megagrams (or "metric ton")	1.103	short tons (2000 lb)	T
TEMPERATURE (exact degrees)				
°C	Celsius	1.8C+32	Fahrenheit	°F
ILLUMINATION				
lx	lux	0.0929	foot-candles	fc
cd/m ²	candela/m ²	0.2919	foot-Lamberts	fl
FORCE and PRESSURE or STRESS				
N	newtons	0.225	poundforce	lbf
kPa	kilopascals	0.145	poundforce per square inch	lbf/in ²

*SI is the symbol for the International System of Units. Appropriate rounding should be made to comply with Section 4 of ASTM E380.

(Revised March 2003)

TECHNICAL REPORT DOCUMENTATION PAGE

1. Report No.	2. Government Accession No.	3. Recipient's Catalog No.	
4. Title and Subtitle Evaluation of Asphalt Pavement Interface Conditions for Enhanced Bond Performance		5. Report Date May 2017	
		6. Performing Organization Code	
7. Author(s) Reynaldo Roque, David Hernando, Bongsuk Park, Jian Zou, and Jeremy A. M. Waisome		8. Performing Organization Report No. 118906	
9. Performing Organization Name and Address University of Florida Department of Civil and Coastal Engineering 365 Weil Hall, PO Box 116580 Gainesville, FL 32611-6580		10. Work Unit No. (TRAIS)	
		11. Contract or Grant No. BDV31-977-37	
12. Sponsoring Agency Name and Address Florida Department of Transportation Research Center, MS 30 605 Suwannee Street Tallahassee, FL, 32399-0450		13. Type of Report and Period Covered Final 02/28/15-05/28/17	
		14. Sponsoring Agency Code	
15. Supplementary Notes			
16. Abstract <p>This project describes a comprehensive modeling effort aimed at examining the potential impact of interface debonding on near-surface longitudinal cracking in the wheelpath of asphalt pavements. A critical zone defined by high shear stress coupled with low confinement was found at a depth of about 2 in and extending to 2 in from the edge of the tire, regardless of asphalt layer thickness. These critical stress states can promote a debonded strip below the wheelpath if an interface is located at an approximate depth of 2 in. The introduction of a debonded strip along the interface caused a stress redistribution that intensified shear stress ahead of the tip of the debonded zone and tensile stress immediately behind the tip (tension at this location exceeded that under the tire). A finite element parametric study based on maximum tension and maximum Von Mises stress (associated with the strain energy of distortion) identified three potential mechanisms of near-surface longitudinal cracking in an asphalt pavement with localized interface debonding: (1) bending caused by repeated traffic can initiate a crack below the edge of the debonded strip that reflects to the surface due to traffic wander and thermal cycles, especially given near-surface differential aging; (2) traffic wander can initiate a vertical crack above the edge of the debonded strip and promote upward propagation; and (3) internal tension due to partially restrained dilation can result in a crack that propagates upward through the more aged and less fracture-tolerant mixture near the surface. Future work should focus on achieving a better understanding of the mechanism of interface breakdown to prevent debonding in the first place. Identification of bonding agents more resistant to interface bond breakdown can help prevent and, in turn, mitigate the occurrence of near-surface longitudinal cracking.</p>			
17. Key Words Debonding, interface, crack, von Mises stress, friction		18. Distribution Statement No restrictions	
19. Security Classif. (of this report) Unclassified	20. Security Classif. (of this page) Unclassified	21. No of Pages 161	22. Price

Form DOT F 1700.7 (8-72)

ACKNOWLEDGEMENTS

The authors would like to acknowledge and thank the Florida Department of Transportation (FDOT) for providing technical and financial support for this project. Special thanks go to the project manager, Greg Sholar, and panel members for their contributions throughout the course of this work. Their efforts are sincerely appreciated.

EXECUTIVE SUMMARY

Field observations indicate a potential link between interface debonding and near-surface longitudinal cracking in the wheelpath of asphalt pavements. However, it is unclear whether near-surface cracking starts first and promotes debonding of the interface, interface bond breakdown leads to near-surface cracking, or both. This project describes a comprehensive modeling effort aimed at examining the potential impact of interface debonding on near-surface longitudinal cracking. The research approach consisted in determining the potential location and extent of interface debonding in order to introduce a debonded area in a pavement section and study the effect of interface debonding on stress redistribution and potential crack development.

The first step was to investigate the level of sophistication required for modeling purposes. Finite element analyses of a pavement structure under varying modeling conditions and loading modes showed that the use of an equivalent elastic analysis with a static load was suitable for the study of critical stress states potentially conducive to interface debonding. Then, a multilayer linear elastic parametric study on fully bonded asphalt pavement sections was conducted to identify areas of high shear stress in combination with low confinement where interface debonding could develop. A critical zone defined by stress states of high shear (>25 psi) coupled with low confinement was found for a broad range of depths (between 1 and 3 in) with a maximum at about 2 in and extending to 2 in from the edge of the tire regardless of asphalt concrete (AC) thickness. Structures with a high AC-to-base stiffness ratio or a stiffness gradient in AC layer resulting from field oxidative aging were more critical. Localized interface debonding can potentially occur as a result of the repetition of these critical stress states when an interface between asphalt layers is present at an approximate depth of 2 in. More importantly, the existence of a critical stress-state zone around the edge of a tire can promote a debonded strip along the wheelpath as truck traffic travels the highway. Debonding extent will depend upon dominant tire configuration (single or dual), tire width, and traffic wander. The width of the debonded strip can range from 12 in for conventional tires with no wander to 42 in in the case of new-generation wide-base tires and a traffic wander standard deviation of 10 in.

Finite element analysis of pavement structures showed that the introduction of a debonded strip along the interface caused a stress redistribution that intensified shear stress ahead of the tip of

the debonded zone and tensile stress immediately behind the tip. Tension at this location exceeded that under the tire, indicating that near-surface longitudinal cracking is more likely at the wheelpath edges, which is consistent with field observations. A parametric study of maximum tensile stress showed that pavement sections with high AC-to-base stiffness ratio or a gradient in stiffness (field oxidative aging effect) were more susceptible to crack development. Also, crack initiation appeared to be more likely as debonding extent increased. Moreover, introduction of frictional resistance along the debonded strip reduced the likelihood of bottom-up cracking below the center of the tire while the potential remained for cracking to initiate below the tip of the debonded zone. However, traffic wander was found to promote crack development above the tip of the debonded strip.

A parallel parametric study of Von Mises stress, which is associated with the strain energy of distortion, revealed that the entire area surrounding the tip of the debonded strip was subjected to large distortion that can lead to internal tension and failure. High AC-to-base stiffness ratio and a gradient in AC stiffness caused by oxidative aging increased the susceptibility to failure. Frictional resistance along the debonded strip did not significantly reduce stress intensification at the tip. Furthermore, while the maximum tension criterion showed that the likelihood of crack development increased as debonding extent increased, the study of Von Mises stress indicated the existence of a critical debonding extent at which initiation of a crack was more likely. Regarding crack development, initiation of a crack above the tip of the debonded strip, followed by upward propagation, seemed dominant, given the presence of an asphalt layer above the interface subjected to higher levels of aging with diminished tolerance to fracture.

This study concluded that the presence of critical stress states can potentially lead to a debonded strip along an interface located about 2 inches below the wheelpath. Investigation of the stress redistribution resulting from the introduction of a debonded strip found three potential mechanisms for development of near-surface longitudinal cracking in asphalt pavements: (1) bending caused by repeated traffic loads applied at the center of the wheelpath can initiate a crack below the edge of the debonded strip that reflects to the surface due to traffic wander and thermal cycles, especially given near-surface differential aging in the asphalt mixture; (2) traffic wander can initiate a vertical crack above the edge of the debonded strip and promote further

upward propagation; and (3) internal tension due to partially restrained dilation in areas of large distortion around the edge of the debonded strip can induce failure. Since the asphalt layer above the interface is subjected to higher levels of aging, its tolerance to fracture is diminished, thereby making upward crack propagation more likely.

Since the presence of a debonded strip along the interface was found to promote the development of near-surface longitudinal cracking, future efforts towards mitigating cracking should focus on preventing debonding in the first place. Identification of bonding agents and interface surface characteristics more resistant to interface bond breakdown can help prevent and, in turn, mitigate the occurrence of near-surface longitudinal cracking in asphalt pavements.

TABLE OF CONTENTS

DISCLAIMER	ii
SI* (MODERN METRIC) CONVERSION FACTORS	iii
TECHNICAL REPORT DOCUMENTATION PAGE	iv
ACKNOWLEDGEMENTS	v
EXECUTIVE SUMMARY	vi
LIST OF TABLES	xii
LIST OF FIGURES	xiii
CHAPTER 1 INTRODUCTION.....	1
1.1 Problem Statement.....	1
1.2 Scope.....	5
1.3 Objectives	6
CHAPTER 2 LITERATURE REVIEW	7
2.1 Factors affecting interface performance	7
2.2 Interface modeling efforts.....	11
2.3 Concluding remarks.....	22
CHAPTER 3 INVESTIGATION OF SOPHISTICATION LEVEL REQUIRED FOR MODELING PURPOSES	26
3.1 Finite element models for identifying critical locations	26
3.1.1 Pavement structure and layer properties.....	26
3.1.2 Determination of relaxation moduli for viscoelastic analysis	29
3.1.3 Axisymmetric finite element models.....	32
3.1.4 Three-dimensional finite element models	35
3.2 Results.....	36

3.2.1 Axisymmetric (elastic) analysis under a static load	36
3.2.2 Axisymmetric (viscoelastic vs. elastic) analysis under a stationary half-sine load	40
3.2.3 Three-dimensional (viscoelastic vs. elastic) analysis under a moving load	45
3.2.3.1 Transverse cross-section	48
3.2.3.2 Longitudinal cross-section	54
3.2.3.3 Preliminary analysis of critical stress states.....	61
3.3 Concluding remarks.....	63
CHAPTER 4 POTENTIAL LOCATION AND EXTENT OF DEBONDING	65
4.1 Effect of pavement structure.....	65
4.2 Effect of interface conditions.....	69
4.3 Effect of tire size and traffic wander	72
4.4 Summary.....	75
CHAPTER 5 IMPACT OF LOCALIZED DEBONDING ON STRESS DISTRIBUTION AND CRACK DEVELOPMENT.....	76
5.1 Introduction.....	76
5.2 Model development	77
5.2.1 General description.....	77
5.2.2 Analysis of mesh quality	79
5.2.3 Final model	80
5.2.4 Bending stress ratio (BSR)	81
5.3 Overall stress distribution	82
5.4 Investigation based on tensile stress	87
5.4.1 Parametric study	87
5.4.1.1 Bending stress ratio.....	87
5.4.1.2 Effect of stiffness ratio.....	87
5.4.1.3 Effect of interface friction.....	89
5.4.1.4 Effect of debonding extent.....	96
5.4.1.5 Effect of traffic wander.....	98
5.4.2 Potential failure mechanisms.....	99
5.4.2.1 Crack initiated below tip of debonded strip.....	102
5.4.2.2 Crack initiated above tip of debonded strip	104

5.5 Investigation based on energy of distortion.....	106
5.5.1 Distortion concept	106
5.5.2 Parametric study	109
5.5.2.1 Effect of stiffness ratio.....	109
5.5.2.2 Effect of interface friction.....	111
5.5.2.3 Effect of debonding extent.....	111
5.5.2.4 Effect of traffic wander.....	115
5.5.3 Potential failure mechanisms.....	115
CHAPTER 6 FINDINGS AND CONCLUSIONS.....	118
6.1 Summary of findings	118
6.2 Conclusions.....	119
CHAPTER 7 RECOMMENDATIONS	121
LIST OF REFERENCES	122
APPENDIX A STRAIN RESPONSES OF THREE-DIMENSIONAL FINITE ELEMENT ANALYSIS	128
APPENDIX B VERIFICATION OF BENDING STRESS RATIO (BSR)	137

LIST OF TABLES

Table 2-1 Interface characteristics used by Ozer et al. (2012) based on shear test results.	20
Table 2-2 Effect of various factors on interface bond strength.	23
Table 2-3 Summary of previous interface modeling efforts reported in the literature.	24
Table 3-1 Unbound layer properties for the selected pavement structure	27
Table 3-2 Prony series parameters for viscoelastic AC layer selected in this chapter	28
Table 3-3 Equivalent elastic moduli for AC layer at 20°C.....	29
Table 3-4 Total time and step time for one pass of the moving load.....	36
Table 4-1 Approximate contact width of different radial tires (Myers et al., 1999; Wang and Roque, 2011; Greene et al., 2009).	74
Table 5-1 Layer thickness and material properties of pavement structure.	78
Table 5-2 Bending stress ratio (BSR) values for pavement sections under evaluation	87

LIST OF FIGURES

Figure 1-1 Potential distresses associated with poor interface conditions.....	2
Figure 1-2 Presence of cracks confined to the top asphalt layers in combination with interface debonding (Willis and Timm, 2007).....	3
Figure 1-3 Cores exhibiting debonding in combination with near-surface longitudinal cracking (I-10, Duval County). Note: reference measurement in inches.	5
Figure 2-1 Possible interface conditions encountered during the construction process in the field (Muench and Moomaw, 2008).....	10
Figure 2-2 Schematic of relative displacement (Δu) between two bonded surfaces.	11
Figure 2-3 Constitutive interface model proposed by Romanoschi and Metcalf (2001a).....	15
Figure 2-4 Yield and potential failure curves for hyperbolic Mohr-Coulomb frictional interface constitutive model (Ozer et al., 2012).....	19
Figure 2-5 Traction-separation law for cohesive elements used to represent the interface between concrete and carbon fiber-reinforced polymer sheet (Smitha et al., 2014).....	21
Figure 3-1 Pavement structure for investigating modeling level of sophistication	27
Figure 3-2 Dynamic modulus master curve fitted using a sigmoidal function at 20°C.....	28
Figure 3-3 Prony series functions: a. Storage and loss moduli; b. Relaxation modulus.....	33
Figure 3-4 Axisymmetric finite element model.....	34
Figure 3-5 Stationary half-sine loading curve: a. Slow traffic; b. Fast traffic	34
Figure 3-6 Three-dimensional FE model: a. Geometry and mesh; b. Moving load	36
Figure 3-7 Stress contours for FE axisymmetric elastic analysis (static load) and low-speed AC modulus: a. Shear stress (psi); b. Horizontal stress (psi); c. Vertical stress (psi)	37
Figure 3-8 Selected locations in the axisymmetric plane for further evaluation	38
Figure 3-9 Comparison between axisymmetric FEA and BISAR results: a-b. Shear stress and strain at AC mid-depth; c-d. Vertical stress and strain at AC mid-depth; e-f. Horizontal stress and strain at AC bottom.	39
Figure 3-10 Axisymmetric shear stress/strain evaluation: a-b. Shear stress/strain at L1 (slow traffic); c-d. Shear stress/strain at L1 (fast traffic); e-f. Shear stress/strain distribution along AC mid-depth at peak loading time (slow/fast traffic).	41

Figure 3-11 Axisymmetric vertical stress/strain evaluation: a-b. Vertical stress/strain at L1 (slow traffic); c-d. Vertical stress/strain at L1 (fast traffic); e-f. Vertical stress/strain distribution along AC mid-depth at peak loading time (slow/fast traffic). 42

Figure 3-12 Time history of horizontal responses at L2: (a) horizontal stress (slow traffic); (b) horizontal strain (slow traffic); (c) horizontal stress (fast traffic); (d) horizontal strain (fast traffic); And, global distribution along the bottom of AC layer at the time of peak loading: (e) horizontal stress; (f) horizontal strain 43

Figure 3-13 Representation of the rectangular loading area in BISAR 46

Figure 3-14 Validation results of 3D FE model along transverse and longitudinal cross-sections. a-b. Shear stress at AC mid-depth; c-d. Vertical stress at AC mid-depth; e-f. Horizontal stress at AC bottom. 47

Figure 3-15 Locations selected for evaluation of 3D FE models: a. Transverse cross-section; b. Longitudinal cross-section. 49

Figure 3-16 3D shear stress (transverse) evaluation for moving and stationary half-sine load: a-b. Shear stress at L1 (slow traffic); c-d. Shear stress at L1 (fast traffic); e. Shear stress along AC mid-depth when moving load reached path center (slow/fast traffic); f. Shear stress along AC mid-depth at peak loading time (slow/fast traffic). 50

Figure 3-17 3D vertical stress (transverse) evaluation for moving and stationary half-sine load: a-b. Vertical stress at L1 (slow traffic); c-d. Vertical stress at L1 (fast traffic); e. Vertical stress along AC mid-depth when moving load reached path center (slow/fast traffic); f. Vertical stress along AC mid-depth at peak loading time (slow/fast traffic). 52

Figure 3-18 3D horizontal stress (transverse) evaluation for moving and stationary half-sine load: a-b. Horizontal stress at L2 (slow traffic); c-d. Horizontal stress at L2 (fast traffic); e. Horizontal stress along AC bottom when moving load reached path center (slow/fast traffic); f. Horizontal stress along AC bottom at peak loading time (slow/fast traffic). 53

Figure 3-19 3D horizontal stress (longitudinal) evaluation for moving and stationary half-sine load: a-b. Horizontal stress at L2 (slow traffic); c-d. Horizontal stress at L2 (fast traffic); e. Horizontal stress along AC bottom when moving load reached path center (slow/fast); f. Horizontal stress along AC bottom at peak loading time (slow/fast).. 55

Figure 3-20 3D shear stress (longitudinal) evaluation for moving load: a. L3 (slow traffic); b. L4 (slow traffic); c. L3 (fast traffic); d. L4 (fast traffic); e. Shear stress along AC mid-depth when moving load reached path center (slow/fast traffic).	56
Figure 3-21 3D shear stress (longitudinal) evaluation for a stationary half-sine load: a. L3 (slow traffic); b. L4 (slow traffic); c. L3 (fast traffic); d. L4 (fast traffic); e. Shear stress along AC mid-depth at peak loading time (slow/fast traffic).	58
Figure 3-22 3D vertical stress (longitudinal) evaluation for a moving load: a. L3 (slow traffic); b. L4 (slow traffic); c. L3 (fast traffic); d. L4 (fast traffic); e. Vertical stress along AC mid-depth when moving load reached path center (slow/fast traffic).	59
Figure 3-23 3D vertical stress (longitudinal) evaluation for a stationary half-sine load: a. L3 (slow traffic); b. L4 (slow traffic); c. L3 (fast traffic); d. L4 (fast traffic); e. Vertical stress along AC mid-depth at peak loading time (slow/fast traffic).	60
Figure 3-24 Stress contours at AC mid-depth for low moving speed (plan view): a. Plan view of depicted area; b. Maximum shear stress (viscoelastic); c. Maximum shear stress (equivalent elastic); d. Vertical compressive stress (viscoelastic); e. Vertical compressive stress (equivalent elastic).	62
Figure 4-1 Pavement sections selected for evaluation of structural characteristics (layer thickness shown in brackets).	66
Figure 4-2 Shear stress distribution of pavement structures with a 4-in AC layer.	67
Figure 4-3 Shear stress distribution of pavement structures with an 8-in AC layer.	68
Figure 4-4 Interface model for evaluation of smeared bonding conditions proposed by Uzan (1976).	70
Figure 4-5 Horizontal shear stress and average vertical stress at a depth of 2 in for different interface reaction modulus (K) values (4-in AC layer pavement structure, stiffness ratio=32).	71
Figure 4-6 Horizontal normal stress under the center of the tire through the depth of the AC layer for different interface reaction modulus (K) values (4-in AC layer pavement structure, stiffness ratio=32).	72
Figure 4-7 Schematic representation of development of a debonded strip along the lane wheelpath.	73

Figure 4-8 Potential extent of localized debonding strip along the wheelpath considering traffic wander and tire width.....	74
Figure 5-1 Geometry of a pavement with localized interface debonding along the wheelpath. ..	76
Figure 5-2 Presence of a debonded zone along the AC interface (2D plane-strain model).....	78
Figure 5-3 Convergence analysis of different stresses for evaluation of mesh quality. Note: positive normal stress denotes tension.	79
Figure 5-4 2D plane-strain FE model (half model due to symmetry).....	80
Figure 5-5 Close-up view of the mesh around the tip of the debonded zone (singularity).....	81
Figure 5-6 Vertical compressive stress distribution (psi) for different bonding conditions.	82
Figure 5-7 Horizontal shear stress distribution (psi) for different bonding conditions.	83
Figure 5-8 Horizontal shear stress along AC interface (psi) for different bonding conditions. ...	84
Figure 5-9 Maximum tensile stress distribution (psi) for different bonding conditions.....	85
Figure 5-10 Horizontal normal stress below AC interface (psi) for different bonding conditions.	86
Figure 5-11 Direction of principal tensile stress around the tip of the debonded zone.	86
Figure 5-12 Maximum tensile stress distribution (psi) throughout the AC layer of a 4-in AC pavement section with varying stiffness ratio (SR).	88
Figure 5-13 Horizontal tensile stress below 2-in deep interface for a 4-in AC pavement section with varying stiffness ratio (SR).	89
Figure 5-14 Relationship between critical shear stress and normal pressure for a frictional interface according to Coulomb frictional model.	90
Figure 5-15 Horizontal shear stress distribution (psi) throughout the AC layer of a 4-in AC section with SR=32 for different interface friction coefficients.	91
Figure 5-16 Maximum tensile stress distribution (psi) throughout the AC layer of a 4-in AC section with SR=32 for different interface friction coefficients.	92
Figure 5-17 Horizontal shear stress distribution (psi) throughout the AC layer of a 4-in AC section with SR=5 for different interface friction coefficients.	93
Figure 5-18 Maximum tensile stress distribution (psi) throughout the AC layer of a 4-in AC section with SR=5 for different interface friction coefficients.	94
Figure 5-19 Horizontal tensile stress below 2-in deep interface (psi) for a 4-in AC pavement section with varying friction coefficients.....	95

Figure 5-20 Finite element models for evaluation of extent of debonded zone (half model due to symmetry).	97
Figure 5-21 Horizontal tensile stress below 2-in deep interface for a 4-in AC pavement section with SR=32 and varying debonding extent.....	98
Figure 5-22 2D plane-strain FE model for evaluation of traffic wander effects (entire wheelpath).	99
Figure 5-23 Maximum tensile stress distribution (psi) throughout the AC layer of a 4-in AC section with SR=32 for different tire load locations.	100
Figure 5-24 Maximum tensile stress distribution (psi) throughout the AC layer of a 4-in AC section with SR=5 for different tire load locations.	101
Figure 5-25 2D plane-strain FE model with a 0.2-in crack below tip of debonded strip (half model due to symmetry).	102
Figure 5-26 Maximum tensile stress distribution of a 4-in AC pavement structure with a 0.2-in crack below tip of debonded strip and varying stiffness ratio (SR).....	103
Figure 5-27 Propagation of a crack initiated below tip of debonded strip: a. Prediction from FE model (downward propagation); b. Field observation (crack through the entire AC layer).	104
Figure 5-28 Propagation of a crack initiated below tip of debonded strip: a. Interpretation of FE results (reflective cracking); b. Field observation (crack above the interface).....	104
Figure 5-29 2D plane-strain FE model with a 0.2-in crack above tip of debonded strip (entire wheelpath).....	105
Figure 5-30 Detail of FE model with a 0.2-in crack above tip of debonded strip (left tip shown).	105
Figure 5-31 Maximum tensile stress distribution of a 4-in AC pavement structure with a 0.2-in crack above tip of debonded strip and varying stiffness ratio (SR).....	106
Figure 5-32 Effect of loading in a granular material. a. Initially dense array of particles; b. Increase in volume (dilation) before failure (Lambe and Whitman, 1969).	107
Figure 5-33 Effect of loading in an asphalt mixture. a. Initially dense array of particles; b. Increase in volume (dilation) before failure; c. Internal tension induced in the binder.	108

Figure 5-34 Von Mises stress distribution (psi) throughout the AC layer of a 4-in AC pavement section with varying stiffness ratio (SR).....	110
Figure 5-35 Von Mises stress distribution (psi) throughout the AC layer of a 4-in AC section with SR=32 for different interface friction coefficients.....	112
Figure 5-36 Von Mises stress distribution (psi) throughout the AC layer of a 4-in AC section with SR=5 for different interface friction coefficients.....	113
Figure 5-37 Von Mises stress distribution (psi) around the tip of the debonded strip of a 4-in AC section with SR=32 and varying debonding extent.	114
Figure 5-38 Von Mises stress distribution (psi) throughout the AC layer of a 4-in AC section with SR=32 for different tire load locations (d=distance from the center of the wheelpath to the load center).	116
Figure 5-39 Von Mises stress distribution (psi) throughout the AC layer of a 4-in AC section with a 0.2-in crack above the interface (load centered in wheelpath).....	117
Figure 5-40 Von Mises stress distribution (psi) throughout the AC layer of a 4-in AC section with a 0.2-in crack above the interface (load aligned with tip of debonded strip)...	117
Figure A-1 Validation results of 3D FE model along transverse and longitudinal cross-sections. a-b. Shear strain at AC mid-depth; c-d. Vertical strain at AC mid-depth; e-f. Horizontal strain at AC bottom.....	128
Figure A-2 3D shear strain (transverse) evaluation for moving and stationary half-sine load: a-b. Shear strain at L1 (slow traffic); c-d. Shear strain at L1 (fast traffic); e. Shear strain along AC mid-depth when moving load reached path center (slow/fast traffic); f. Shear strain along AC mid-depth at peak loading time (slow/fast traffic).	129
Figure A-3 3D vertical strain (transverse) evaluation for moving and stationary half-sine load: a-b. Vertical strain at L1 (slow traffic); c-d. Vertical strain at L1 (fast traffic); e. Vertical strain along AC mid-depth when moving load reached path center (slow/fast traffic); f. Vertical strain along AC mid-depth at peak loading time (slow/fast traffic).	130
Figure A-4 3D horizontal strain (transverse) evaluation for moving and stationary half-sine load: a-b. Horizontal strain at L2 (slow traffic); c-d. Horizontal strain at L2 (fast traffic); e. Horizontal strain along AC bottom when moving load reached path center (slow/fast	

traffic); f. Horizontal strain along AC bottom at peak loading time (slow/fast traffic).	131
Figure A-5 3D horizontal strain (longitudinal) evaluation for moving and stationary half-sine load: a-b. Horizontal strain at L2 (slow traffic); c-d. Horizontal strain at L2 (fast traffic); e. Horizontal strain along AC bottom when moving load reached path center (slow/fast); f. Horizontal strain along AC bottom at peak loading time (slow/fast).	132
Figure A-6 3D shear strain (longitudinal) evaluation for moving load: a. L3 (slow traffic); b. L4 (slow traffic); c. L3 (fast traffic); d. L4 (fast traffic); e. Shear strain along AC mid-depth when moving load reached path center (slow/fast traffic).	133
Figure A-7 3D shear strain (longitudinal) evaluation for a stationary half-sine load: a. L3 (slow traffic); b. L4 (slow traffic); c. L3 (fast traffic); d. L4 (fast traffic); e. Shear strain along AC mid-depth at peak loading time (slow/fast traffic).	134
Figure A-9 3D vertical strain (longitudinal) evaluation for a stationary half-sine load: a. L3 (slow traffic); b. L4 (slow traffic); c. L3 (fast traffic); d. L4 (fast traffic); e. Vertical strain along AC mid-depth at peak loading time (slow/fast traffic).	136
Figure B-1 Stress distribution along AC interface and AC bottom for a fully bonded pavement. Note: positive normal stress denotes tension.	138
Figure B-2 Ratio between stresses from an axisymmetric model and a 2D plane-strain model.	139
Figure B-3 Stress distribution immediately below AC interface and along AC bottom for a pavement with localized debonding. Note: positive normal stress denotes tension.	140
Figure B-4 Ratio between stresses from an axisymmetric model and a 2D plane-strain model.	141

CHAPTER 1

INTRODUCTION

1.1 Problem Statement

Asphalt pavements are multilayer structures composed of bonded asphalt layers on top of a base course. Bonding reduces bending stress induced by traffic loads by making the pavement act as a monolithic structure. In order to enhance bonding, a tack coat (i.e., a thin application of asphalt in the form of an emulsion or a pure binder) is typically applied at the interface between asphalt layers. Nevertheless, according to a worldwide survey conducted by Mohammad et al. (2012), some highway agencies still do not require tack coat.

An extensive number of cases of interface debonding or bond failure in many countries has been summarized by Sutanto (2009). In general terms, poor bonding conditions of asphalt layers can potentially lead to three major distresses: slippage, delamination of the surface layer and cracking (Figure 1-1).

Slippage is associated with relatively thin surface layers (typically less than or equal to 1.5 in) and areas of high horizontal shear stress, mostly braking zones. It is characterized by crescent or half-moon shaped cracks generally having two ends pointed in the direction of traffic. Extensive research has been conducted to evaluate slippage potential, mainly in the form of shear strength tests, for different interface bonding conditions.

Delamination involves complete separation of the surface course from the layer underneath. It can result from severe slippage deterioration and disintegration of the asphalt mixture for causes not related to the interface, such as moisture damage (trapped water that separates the asphalt binder from the aggregate in a mixture) and oil spills.

As far as cracking is concerned, most research has focused on the effect of debonding on the tensile stress/strain distribution in the asphalt layer and the potential acceleration of bottom-up cracking, i.e., cracking starting at the bottom of the asphalt layer.



a. Slippage



b. Delamination of surface layer



c. Longitudinal cracking in the wheelpath in I-75 (Hamilton County)

Figure 1-1 Potential distresses associated with poor interface conditions.

More attention has been brought to debonding after studies conducted by Willis and Timm (2007) at the National Center for Asphalt Technology (NCAT) test track showed a potential link between interface debonding and near-surface cracking (as opposed to traditional bottom-up cracking). Near-surface cracking is perceived to be one of the most common forms of deterioration in asphalt pavements (COST-Transport, 1997, 1999). As a reference, approximately 2,000 lane miles are resurfaced annually in the State of Florida, mostly due to a deficient crack rating, with surface cracking being a major part of the percentage of cracks.

Figure 1-2 shows a trench from section N8 constructed as part of the 2003 research cycle at the NCAT test track. As can be seen, this section exhibited cracking confined to the top asphalt layers (i.e., near-surface cracking) in combination with interface debonding. According to the results of an analytical study and a physical investigation of trenches and cores taken from the damaged section, Willis and Timm (2007) concluded that the loss of bond was likely the cause of cracking and they recommended further research efforts on the interface bond breakdown mechanism under repeated shear loading.

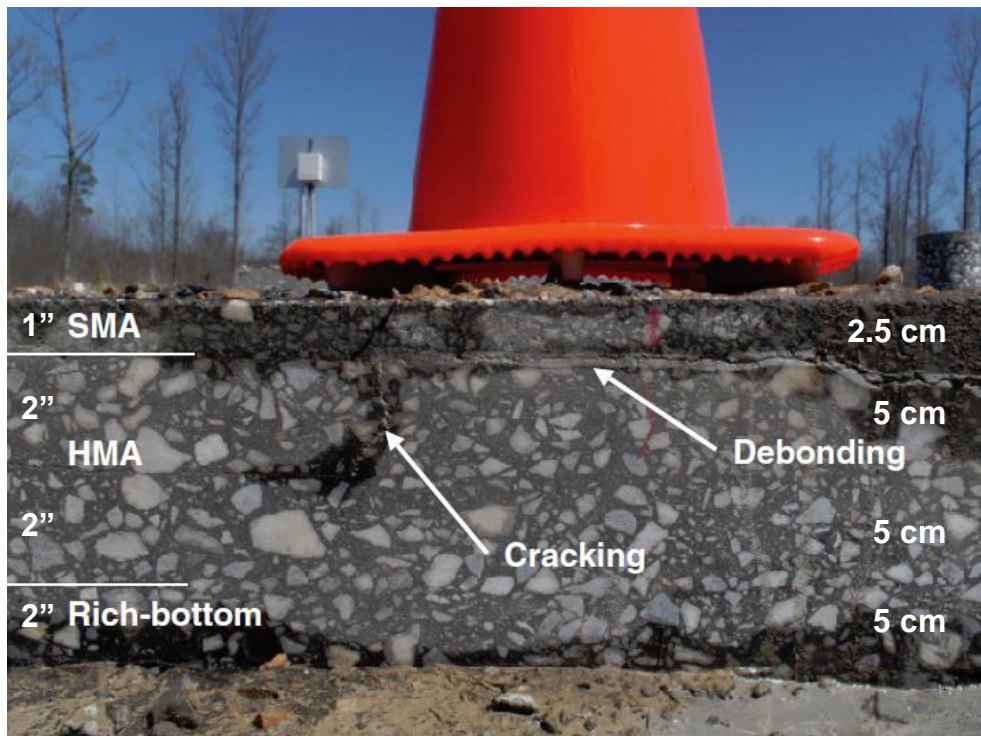


Figure 1-2 Presence of cracks confined to the top asphalt layers in combination with interface debonding (Willis and Timm, 2007).

Studies conducted by the Washington State Department of Transportation (WSDOT) showed one third of cores exhibiting top-down cracking debonded at the interface between the existing pavement and the subsequent overlay during extraction (Tashman et al., 2008). Furthermore, observations by Muench and Moomaw (2008) on SR 28 (East Wenatchee) indicated a link between cracking in the wheelpath and interface debonding. Extracted cores tended to show debonding of the overlay only in cracked areas of the wheelpath. They suggested bonding was adequate during construction; otherwise, debonding would have been found in non-cracked cores outside the wheelpath. Although this explanation seems reasonable, the authors want to point out that tack tracking during construction could also explain debonding in the wheelpath. Similar observation was made on SR 2 (Tumwater Canyon) by Muench and Moomaw (2008): “cores reportedly taken near debonded cores exhibited no debonding or distress.” In addition, the average depth to the first debonded interface was found to be 1.8 in, which closely corresponded to the typical WSDOT overlay thickness. Another important finding was that overlay service life in Eastern Washington, where all projects showing debonding were located, ranged from 8 to 12 years, whereas surfaces in Western Washington tended to last about 14 to 18 years. This observation appeared to indicate interface debonding contributed to faster pavement deterioration. Although the link between cracking and debonding seemed evident, it was unclear whether infiltration of water through cracks and areas of low mixture density (due to thermal segregation and mixture segregation) caused debonding or interface bond breakdown led to near-surface cracking.

Likewise, investigation performed by the University of Florida on section trenches found existence of near-surface longitudinal cracking in combination with interface debonding. Unfortunately, those trenches are no longer available and the authors could not include any graphic proof in the current project. However, debonding concurrent with longitudinal surface cracking in the wheelpath was found on some cores extracted as part of a Superpave monitoring project (Roque et al., 2011), as shown in Figure 1-3.

Field observations indicate a clear link between interface debonding and near-surface longitudinal cracking in the wheelpath. In fact, Muench and Moomaw (2008) stated that “Evidence of de-bonding and its extent may already exist in pavement management system

records. However, debonding is not routinely measured and it may not manifest itself in a consistent manner and therefore would be difficult if not impossible to identify consistently.” Although the link is evident, the question remains as to whether near-surface cracking starts first and promotes debonding of the interface, interface bond breakdown leads to near-surface cracking, or both. Therefore, further research is needed to identify potential mechanisms connecting debonding and near-surface longitudinal cracking.



Figure 1-3 Cores exhibiting debonding in combination with near-surface longitudinal cracking (I-10, Duval County). Note: reference measurement in inches.

1.2 Scope

Some clarification on the differences between potential distress mechanisms associated with deficient interface bonding conditions is warranted. First, slippage is associated with single events where high contact stresses from braking reach bond strength, whereas cracking is thought to be related to progressive interface bond breakdown under repeated traffic loads (multiple events). Second, slippage is restricted to the very top of the pavement; it results from failure of the uppermost interface located directly beneath the surface layer. Conversely,

interface bond breakdown may occur at an interface deeper in the pavement structure. Finally, slippage is a local distress that may appear in braking zones, while interface bond breakdown could occur anywhere and, according to Muench and Moomaw (2008), could potentially be much more prevalent on highways and represent a greater concern. The focus of this project was to enhance our understanding of debonding resulting from interface bond breakdown and to determine whether its occurrence can lead to development of near-surface longitudinal cracking.

1.3 Objectives

The main objective of this research was to evaluate the potential impact of interface debonding on near-surface longitudinal cracking. Detailed objectives are:

- Determine the location of critical stress states where onset of interface debonding is possible.
- Evaluate the effect of debonding on stress redistribution and its potential contribution to near-surface longitudinal cracking.

CHAPTER 2

LITERATURE REVIEW

2.1 Factors affecting interface performance

The state of practice on tack coat materials, application rates and application methods was assessed by Mohammad et al. (2012) through a vast literature review and a worldwide survey. The most frequently used tack coat materials were found to be slow-setting emulsions, either anionic or cationic, followed at a great distance by rapid-setting emulsions. The use of a slow-setting emulsion may be counterintuitive since this type of emulsion takes a longer time to set and is considered the preferable choice for prime coats. However, slow-setting emulsions can be diluted, which has the advantage of better flow and more uniform spray application (Asphalt Institute 2001, 2008; Mohammad et al., 2012). With respect to application rates, residual binder application typically varies from 0.09 to 0.36 l/m² (0.02 to 0.08 gal/yd²) depending on surface condition (new, old, milled, etc.).

As far as factors affecting the response of an interface are concerned, the following list compiles observations reported in the literature by different authors (Uzan et al., 1978; Romanoschi and Metcalf, 2001a; Mohammad et al., 2002; Raab and Partl, 2004; Canestrari and Santagata, 2005; Tashman et al., 2008; Mohammad et al., 2012):

- Interface shear strength decreases with increasing temperature. Asphalt is highly susceptible to temperature, showing a reduction in strength as temperature rises.
- Interface shear strength increases with increasing normal pressure (i.e., confinement). Asphalt materials follow a Mohr-Coulomb failure law and, as such, shear resistance increases with the level of confinement.
- The effect of binder residue can be inferred from results by Mohammad et al. (2012) on three different emulsions: cationic rapid-setting (CRS-1), anionic slow-setting with a hard binder (SS-1h), and non-tracking anionic slow setting with hard binder and modification (NTSS-1hM). Interface shear strength increased with viscosity (both rotational and absolute viscosity) and hardness (measured from penetration test) of binder residue.
- The effect of application rate on shear strength is still controversial. Uzan et al. (1978) found an optimal application rate at which shear strength peaked (optimal application rate

was temperature dependent). Sholar et al. (2004) observed a minor effect of application rate on shear strength within the range 0.09 to 0.36 l/m² (0.02 to 0.08 gal/yd²). West et al. (2005) measured higher shear strength for lower application rates in the case of fine-graded mixtures, whereas almost no effect was found with coarse-graded mixtures. Tashman et al. (2008) indicated that absence of tack coat on specimens cored from test sections did not significantly affect the bond strength on milled surfaces, whereas it severely decreased it for non-milled surfaces. Mohammad et al. (2012) measured the highest bond strength at the maximum application rate used for their experiment with several tack coats (0.70 l/m² or 0.155 gal/yd²). Other studies obtained higher strength values on specimens with no tack coat.

- Similarly, the effect of emulsion curing time on bond strength is unclear.
- Muench and Moomaw (2008) reported that dilution of asphalt emulsions can help achieve a more uniform application and could potentially reduce tack tracking. However, they also indicated dilution can cause issues such as excessively low residual application rate, premature emulsion break (due to thermal shock if cold water is added), and extended curing time.
- Presence of water and dirt on existing surface generally resulted in lower shear strength.
- As for surface roughness, Sholar et al. (2004), West et al. (2005), Tashman et al. (2008) and Mohammad et al. (2012) obtained higher shear strength on specimens with a milled surface. Conversely, Raab and Partl (2004) reported higher shear strength on specimens with smooth surface conditions (cut surface) as compared to those with rough surfaces (sandblasted surface). Their explanation for that effect was that smooth surfaces presented higher contact area than rough surfaces, where contact might have occurred through a limited number of points. In other words, the better interlocking effect of a rough surface could have been shadowed by a lower contact area.
- The gradation of the layers surrounding the interface affects shear strength. Coarse-graded layers typically provide higher strength values because of better interlocking (Sholar et al., 2004).
- An increase in normal pressure has been reported to decrease dilation during testing (Canestrari and Santagata, 2005).

- Muench and Moomaw (2008) questioned whether laboratory prepared specimens may adequately reproduce bonding conditions in the field. This observation was made after a literature review showed that laboratory specimens with no tack coat yielded substantial shear resistance, but in many instances, field specimens could not even be tested.

Of note, Uzan et al. (1978) stated that interface strength is governed mostly by three components: adhesion, which is represented by the tensile properties of the slip plane; interlocking, which is provided by the penetration of aggregates from one layer to another; and friction, defined by the roughness of the two faces. As temperature increases, roughness becomes the most relevant component on interface strength. The adhesion component is dominant at low normal pressure level. As normal pressure increases, the relative effect of interlocking increases and tends to dominate the response of the interface. As application rate increases, the tack coat fills surface voids and increases the adhesion component. However, excessive tack increases the film thickness of the interface and decreases the interlocking component.

It is noteworthy that most results reported in the literature are based on strength tests performed under monotonic load. Only a few studies (Romanoschi and Metcalf, 2001a; Diakhaté et al., 2011; Kruntcheva et al., 2006) have performed repeated loading tests on interfaces. Under monotonic loading conditions, stiffer materials are expected to yield higher strength and, thus, potentially better performance. However, this is not necessarily true when it comes to a progressive distress mechanism like interface bond breakdown. For this reason, the UF Materials Research Group is currently developing a testing procedure aimed at investigating the mechanism of interface bond breakdown under repeated load. This research is expected to provide insights as to whether monotonic loading (e.g., a strength test) is suitable to characterize interface bond breakdown.

In addition to the factors discussed above, the actual surface condition in the field during the construction process, which can greatly differ from that in a laboratory, is a key variable to interface performance that only a few studies have addressed. Figure 2-1 summarizes various interface conditions often encountered in the field.



a. Good coverage on SR 101 (milled surface)



b. Clogged nozzles on SR 500



c. Streaky coverage on SR 5



d. Spotty coverage on SR 500



e. Tack tracking on SR 2/97



f. Thin debonded layer after milling on SR 97A

Figure 2-1 Possible interface conditions encountered during the construction process in the field (Muench and Moomaw, 2008).

One of the most common problems encountered in the field is a non-uniform tack coat application due to clogged nozzles in the spray bar of the distributor truck (Figure 2-1b). Clogged nozzles result in streaky (Figure 2-1c) or spotty coverage (Figure 2-1d), which in turn cause areas of poor or no bond between asphalt layers. In addition, construction vehicles, namely haul trucks, drive on the tack coat and pick it up with their rubber tires, which is known as ‘tack tracking’ (Figure 2-1e). Tack tracking is most likely in the wheelpath, which happens to be the area where surface cracking is typically observed. Finally, thin debonded layers can remain in the pavement surface after milling in a rehabilitation process (Figure 2-1f). Muench and Moomaw (2008) speculate that thin debonded layers may be broken up by compaction of the asphalt overlay (particularly when vibratory compaction is used), which can promote debonding as well as areas of low density where water can get trapped and promote moisture damage.

2.2 Interface modeling efforts

One of the first documented studies on the effect of interface conditions on pavement response was performed by Uzan (1976). He derived a linear model to simulate the behavior of partially rough interfaces based on Goodman’s constitutive law. He assumed the interface to be a layer of finite thickness h on which a shear stress τ is applied (Figure 2-2).

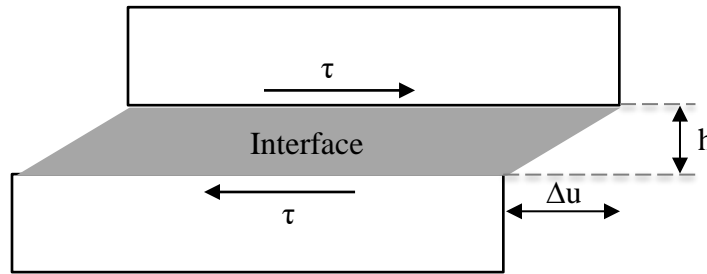


Figure 2-2 Schematic of relative displacement (Δu) between two bonded surfaces.

The relation between shear stress τ and shear strain γ for an elastic material is as follows:

$$\tau = G \cdot \gamma \quad (2.1)$$

where G is the shear modulus of the interface material. For small displacements, shear strain is defined as:

$$\gamma = \frac{\Delta u}{h} \quad (2.2)$$

in which Δu denotes the relative horizontal displacement between the two sides of the interface, and h is the thickness of the interface. Substituting Eq. 2.2 into Eq. 2.1 gives:

$$\tau = G \cdot \frac{\Delta u}{h} = K \cdot \Delta u \quad (2.3)$$

where K is defined as the reaction modulus of the interface.

This model was employed to perform a sensitivity analysis on the effect of various interface conditions, as represented by different K values, on the responses of a four-layer pavement structure (two asphalt layers, base and subgrade). Only the interface between the two asphalt layers was modeled using Eq. 2.3; the other two interfaces were assumed fully bonded. The interface between the asphalt layers was located at a depth equal to half the radius of the load, which for a typical load radius of 5 to 6 in results in a depth of 2.5 to 3 in. Three different elastic moduli were considered for the upper asphalt layer. For the purpose of the analysis, K was assumed to be an intrinsic interface property, independent of interface thickness, normal load and relative displacement rate, which seemed to be appropriate in the context of linear elastic layered systems. Uzan (1976) found that most of the change in the radial stress (and strain) at the bottom of the upper asphalt layer occurred when K varied between 1 and 100 N/mm³ (100-10,000 kgf/cm³). When K was less than 1 N/mm³ or greater than 100 N/mm³, the results were within 10% of those for slip and full bond conditions, respectively (Uzan, 1976).

Field experiences discussed by Uzan et al. (1978) suggested that the state of adhesion in real conditions is an intermediate one between full adhesion and zero adhesion, depending on material properties and construction quality. In other words, there is some inherent compliance associated with the interface. In fact, Uzan et al. (1978) recommended a K value of 10 N/mm³ to model an interface in the upper part of an asphalt pavement subjected to a tire pressure of 75-100 psi at normal highway speed and 25 °C.

In the multilayer linear elastic program BISAR (Bitumen Stress Analysis in Roads) developed by Shell, the interface between any two pavement layers is represented by an infinitely thin layer characterized by a shear spring compliance parameter AK. AK describes the relative horizontal displacement induced by shear stress at the interface:

$$AK = \frac{\text{Relative horizontal displacement}}{\text{Interface shear stress}} = \frac{\Delta u}{\tau} \quad (2.4)$$

Note that shear spring compliance AK is the inverse of the shear reaction modulus K. The relationship described in Eq. 2.4 is treated mathematically through the slip parameter α ($0 \leq \alpha \leq 1$), defined as:

$$\alpha = \frac{AK}{AK + \frac{1 + \nu}{E} \cdot a} \quad (2.5)$$

where E (Pa) and ν are the elastic modulus and the Poisson's ratio of the layer above the interface, respectively; AK is the shear spring compliance (m^3/N); and a is the radius of the load (m). The slip parameter α varies from 0 (full bond) to 1 (full slip).

Slip can also be defined in BISAR through the reduced shear spring compliance ALK (m):

$$ALK = \frac{\alpha}{1 - \alpha} \cdot a \quad (2.6)$$

The relation between AK and ALK is given by the following equation:

$$AK = ALK \cdot \frac{1 + \nu}{E} = \frac{\alpha}{1 - \alpha} \cdot \frac{1 + \nu}{E} \cdot a = \frac{\Delta u}{\tau} \quad (2.7)$$

Note that, for a given interface compliance value, α depends on the radius of the applied load. Thus, α is not a pure material property and it should not be considered as a ‘classic’ friction coefficient.

Maina et al. (2007) utilized a similar concept to that implemented in BISAR in order to model interface slip of flexible pavements on airports. They defined the relationship between relative horizontal displacement and shear stress as follows:

$$\frac{\Delta u}{\tau} = \frac{\alpha}{1 - \alpha} \cdot \beta \quad (2.8)$$

in which α is a slip parameter and β is a parameter that allows consideration of different shear compliance models:

$$\beta_1 = a^* \cdot \left(\frac{1 + \nu_i}{E_i} + \frac{1 + \nu_{i+1}}{E_{i+1}} \right) \quad (2.9a)$$

$$\beta_2 = 2a^* \cdot \left(\frac{1 + \nu_i}{E_i} \right) \quad (2.9b)$$

$$\beta_3 = 2a^* \cdot \sqrt{\left(\frac{1 + \nu_i}{E_i} \right) \cdot \left(\frac{1 + \nu_{i+1}}{E_{i+1}} \right)} \quad (2.9c)$$

where a^* was selected as the maximum radius among the various surface loads; and E_i , E_{i+1} and ν_i , ν_{i+1} are the elastic modulus and Poisson’s ratio of the i^{th} and $(i+1)^{\text{th}}$ layers, respectively.

Maina et al. (2007) used the three models described by Eq. 2.9 to examine critical responses as well as strain energy of distortion (SED) per unit volume (considered as failure criterion) of a typical airport flexible pavement subjected to vertical and horizontal loads. According to calculations carried out by the authors, K values used by Maina et al. (2007) may have ranged from 0.18 N/mm^3 ($\alpha=0.9$) to 6.5 N/mm^3 ($\alpha=0.2$), apart from the full bond case ($\alpha=0$). SED was found to be maximum at the surface of the pavement structure, regardless of the slip level α . As α increased, SED at the bottom of the top layer (where interface slip was introduced) increased. These results were observed for the three slip models, although the effects became more evident

for model 3 (Eq. 2.9c). Note that this study did not predict failure of the interface, but rather evaluated the potential effect of interface compliance (as represented by a varying slip level) on deterioration of the asphalt layer. Based on SED results, the study concluded that slip of the interface between the surface and the binder layer (2 in deep in this case) could potentially lead to deterioration from both the top and the bottom of the surface layer.

Romanoschi and Metcalf (2001a) derived a two-stage constitutive model (Figure 2-3) to characterize the interface between two asphalt layers from direct shear test results. Laboratory testing included three temperatures (15, 25 and 35 °C), four normal load levels (20, 40, 60 and 80 psi) and two different interface conditions (tack coat and no tack coat). In the first stage, called stick condition, the relative displacement of the two layers is proportional to shear stress until the shear strength of the interface (τ_{max}) is reached (failure criterion). The relationship between shear stress and relative displacement is given by the interface reaction modulus K . Relative displacement is elastic and recoverable in this first stage. In the second stage (post-failure), a simple frictional model defined by a coefficient of friction μ is used to represent the mechanical behavior of the interface (friction condition). The friction coefficient relates normal stress (i.e., confinement) to shear stress.

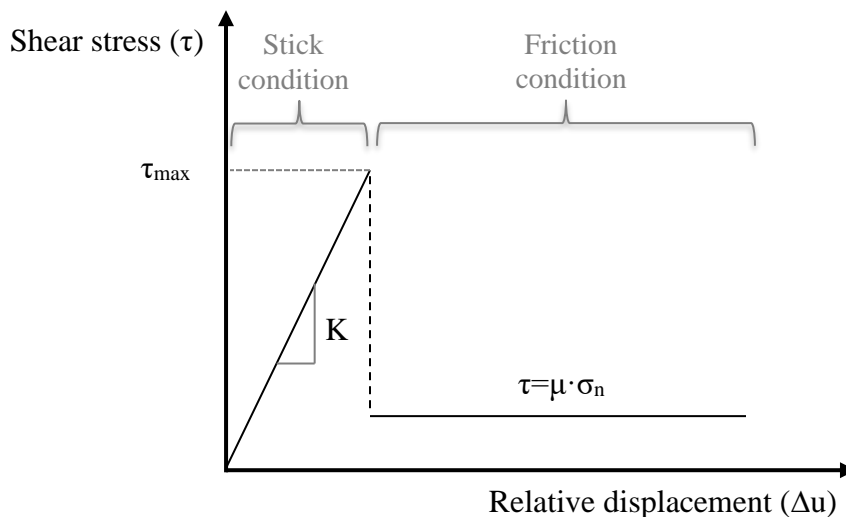


Figure 2-3 Constitutive interface model proposed by Romanoschi and Metcalf (2001a).

Interface reaction modulus values measured by Romanoschi and Metcalf (2001a) varied from 0.2 to 1.2 N/mm³. As for the coefficient of friction of the post-failure response, normal stress and temperature had almost no influence on testing results for the no tack coat case and an average value of 0.75 was obtained. For the tack coat case, average values of 0.65, 0.70 and 0.93 were found for the coefficient of friction at 15, 25 and 35 °C, respectively. Again, normal stress had no effect on μ .

Results from laboratory testing were employed by Romanoschi and Metcalf (2001b) to conduct a modeling study for evaluation of the effect of interface conditions on the life of flexible and semi-rigid pavements. For the interface between the surface course and the binder course, the following conditions were modeled by the contact interaction feature available in the finite element (FE) software ABAQUS:

- Full bond condition: each node of a slave surface was tied to the nearest node on a master surface.
- Interface with tack coat: the relative displacement at the interface was proportional to shear stress. In this case, shear strength and interface reaction modulus were defined as independent of normal stress; values of 1.415 MPa (205 psi) and 0.885 N/mm³ were selected for τ_{max} and K, respectively, based on direct shear test results at 25 °C.
- Interface without tack coat: the relative displacement at the interface was also proportional to shear stress. However, τ_{max} and K were defined as normal stress dependent:

$$\tau_{max}[kPa] = 842.5 + 7.66 \cdot \sigma[kPa] \quad (2.10)$$

$$K[N/mm^3] = 0.361 + 0.2307 \cdot \sigma[MPa] \quad (2.11)$$

- Friction condition: the resistance to movement was proportional to the normal stress at the interface (Coulomb's friction law). This condition was used to represent post-failure behavior, characterized by a friction coefficient $\mu=0.7$.

Maximum horizontal strain was used to estimate pavement life in terms of fatigue cracking. For both pavement types (flexible and semi-rigid), the full bonding condition exhibited the highest number of cycles to failure. For most cases, the interface with a tack coat yielded a lower number of cycles than the interface without tack coat. However, Romanoschi and Metcalf pointed out

that for different loading magnitude and temperature, the results might be different because of the normal stress dependency of interfaces without tack coat and the effect of temperature on interface response (for both with and without tack coat). Regarding critical depth, the maximum tensile strain was found at the bottom of the binder asphalt course for the full bond condition and at the bottom of the surface course for the other three conditions. In other words, the introduction of an interface model to account for some level of compliance at the interface between the surface and binder layer moved the maximum tensile strain location to the bottom of the surface course. Despite having an interface model with a failure criterion and a post-failure component, the study focused on tensile strain and, unfortunately for the purposes of the current project, no assessment was made as to whether failure may have occurred at any point across the interface plane.

Mohammad et al. (2012) employed the constitutive model developed by Romanoschi and Metcalf (Figure 2-3) to predict interface shear stress of six different pavement structures. Results from shear strength tests on four different tack coats at three residual application rates (0.14, 0.28 and 0.70 l/m²; or 0.031, 0.062 and 0.155 gal/yd²) were used to determine the interface reaction modulus K. The following observations can be made from their results: (1) shear stress was directly proportional to the level of bending; thus, sections with thicker asphalt layer exhibited lower shear stress; (2) predicted interface shear stress exceeded shear strength in only two out of 72 combinations; and (3) interface shear stress was barely sensitive to tack coat type and application rate. It should be pointed out K values obtained from testing were below 0.3 N/mm³ for all cases. According to the sensitivity analysis performed by Uzan (1976), K values below 1 N/mm³ yield similar results to those provided by a slip condition. Therefore, low interface shear stress is expected for low interface reaction modulus. The authors believe that low K values may have been the result of the low displacement rate used for testing (0.1 in/min). Although a low displacement rate may be relevant in the context of slippage, it may not be so useful for the problem of interface bond breakdown under repeated loads.

Kruntcheva et al. (2006) employed a 0.4-in thick linear elastic layer of variable stiffness to characterize the interface in a 3D FE model of a shear box test. For an interface stiffness of 100 MPa (14,500 psi), which was intended to represent a weak interface, interface shear stress

significantly decreased as compared to the full bonded case. This result was expected since stiffness is known to attract stress. It should be pointed out that modeling conditions were not realistic because that interface thickness (0.4 in) would correspond to a residual tack coat application rate of 10 l/m² (2.2 gal/yd²), which is about 10 times greater than rates normally considered as very high. In addition to modeling, cyclic shear tests followed by strength tests were performed on laboratory specimens with multiple interface conditions (no tack, normal tack coat application rate, excess tack coat rate and dirty interface) and surfacing materials (stone mastic asphalt and porous asphalt). Testing results showed that interface response was more affected by the type of materials in contact than by application rate and interface conditions. A dry and clean interface with no tack coat yielded similar results to an interface with a ‘standard’ tack coat application rate. Although there is value in the research conducted, application of the conclusions to the problem at hand is questionable.

Ozer et al. (2008) implemented a fracture-based elastoplastic constitutive relationship into a hyperbolic Mohr-Coulomb frictional model to define the behavior of tack-coated interfaces. This model is able to capture the entire range of interface behavior, from the initial elastic response when the interface is fully bonded to the post-peak response when the interface is fully debonded. In addition, the model allows consideration of surface roughness and normal stress dependency of the interface. The hyperbolic yield (failure) function (F) is defined by Equations 2.12 and 2.13 and is illustrated in Figure 2-4.

$$F = \tau_{eq}^2 - (c - \sigma_{nn} \cdot \tan \Phi)^2 + (c - s \cdot \tan \Phi) \quad (2.12)$$

$$\tau_{eq} = \sqrt{\tau_{ns}^2 + \tau_{nt}^2} \quad (2.13)$$

where τ_{eq} is the equivalent tangential traction on the interface plane, which is a function of the two components τ_{ns} and τ_{nt} ; σ_{nn} is the normal traction; s is the tensile strength; c is the cohesion, and Φ is the friction angle. The strength parameters c and Φ can be measured from shear tests, while s can be obtained from a pullout test. If pullout data is not readily available, s could be assumed equal to cohesion. Shear test results are also used to characterize the initial elastic response of the interface, which is defined by the modulus of interface reaction K .

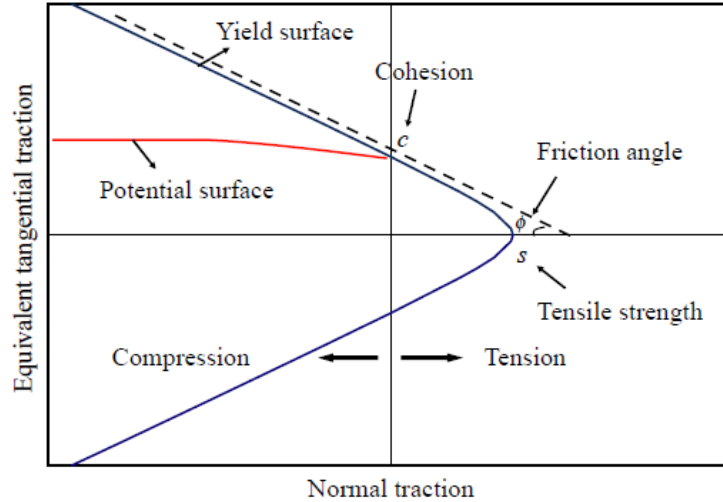


Figure 2-4 Yield and potential failure curves for hyperbolic Mohr-Coulomb frictional interface constitutive model (Ozer et al., 2012).

Interface damage resulting from repeated loads is formulated by means of fracture-based softening rules. In other words, the strength parameters that define the hyperbolic yield surface (i.e., s , c and Φ) are reduced by way of an exponential decay function that depends on the ratio of the plastic work done at the interface to the fracture energy in mode I (tension) and mode II (shear). Furthermore, the model can simulate interface response under various loading conditions, such as shear, tension, shear with compression and shear with tension.

Another additional feature of this model is the ability to predict volumetric expansion (dilation) associated with shear by means of a non-associated flow rule introduced in the plasticity framework of the model. After interface shear stress reaches a maximum value, it drops to a relatively small constant value with further shear deformation. During this drop in shear stress (governed by the softening rules discussed in the previous paragraph), the volumetric deformation of the interface increases until it reaches a critical value at which no further dilation occurs (Ozer et al., 2008).

Ozer et al. (2012) employed direct shear test results on specimens composed of a 2.2-in thick asphalt layer overlay on a smooth concrete surface to build a 3D FE model. A rapid curing

cutback asphalt (RC-70) at three application rates (0.09, 0.23 and 0.41 l/m²; or 0.02, 0.05 and 0.09 gal/yd²) was used to tack the asphalt overlay to the concrete surface. The FE model considered the viscoelastic characteristics of asphalt mixture, moving traffic loading and six different interface conditions (Table 2-1). Interface reaction modulus in the two tangential directions (K_{ns} and K_{nt}) and shear strength values were selected based on shear test results. Additional assumptions included a friction angle of 35°, tensile strength values equal to cohesion, and strain energy release rates values for modes I, II and III equal to 2 kJ/m².

Table 2-1 Interface characteristics used by Ozer et al. (2012) based on shear test results.

Parameter	Unit	Case					
		I	II	III	IV	V	VI
K_{nn}	N/mm ³	15,000	15,000	15,000	15,000	N/A	N/A
K_{ns}	N/mm ³	0.01	0.1	1	100	Full bond	Full slip
K_{nt}	N/mm ³	0.01	0.1	1	100	Full bond	Full slip
Φ	°	35					
c	MPa	0.05 and 0.2					
s	MPa	0.05 and 0.2					
G_I, G_{II}, G_{III}	kJ/m ²	2, 2, 2					

Notes:

-Interface for cases I through IV was modeled using the hyperbolic Mohr-Coulomb frictional constitutive model developed by Ozer et al. (2008).

-Cases I and II are the parameter sets representing experimental test results. Cases III-VI were used to perform a numerical sensitivity analysis.

The 3D FE model was used by Ozer et al. (2012) to evaluate the effect of interface conditions on fatigue cracking by examining the transverse strain at the bottom of the asphalt layer. The transverse strain distribution under single wide-base and dual tire configurations with K values lower than 0.1 N/mm³ agreed with the no-bond condition. Likewise, a K value of 100 N/mm³ yielded similar response to the full bonded scenario. Furthermore, they also investigated the potential for instability rutting based on the octahedral shear stress distribution through the depth of the asphalt layer. The maximum octahedral shear stress was found at approximately 0.5 in below the surface of the pavement due to the combined effect of bending and lateral stresses at

the tire-pavement contact, regardless of interface reaction modulus. However, the magnitude of the maximum octahedral stress did increase as K decreased. Again, K values below 0.1 N/mm^3 yielded almost identical results to the no-bond condition, whereas K values above 100 N/mm^3 matched the full-bond condition. Note that the sensitivity results obtained by Ozer et al. (2012) agreed with the findings reported by Uzan (1976). Unfortunately, no assessment of failure at the interface was reported.

It is noteworthy to briefly describe the work conducted by Smitha et al. (2014), despite involving concrete instead of asphalt mixture. They conducted a non-linear FE analysis of a concrete column wrapped by a carbon fiber-reinforced polymer (CFRP) sheet under uniaxial compression. Cohesive elements were introduced to model the response of the interface created by an epoxy resin employed to bond the CFRP sheet to concrete. Since the discretization level in the cohesive layer was finer than that in the surrounding layers, the top and bottom surface of the cohesive layer were tied using a tie constraint available in ABAQUS. Cohesive elements were defined by a traction-separation law in the normal and the two local shear directions (Figure 2-5).

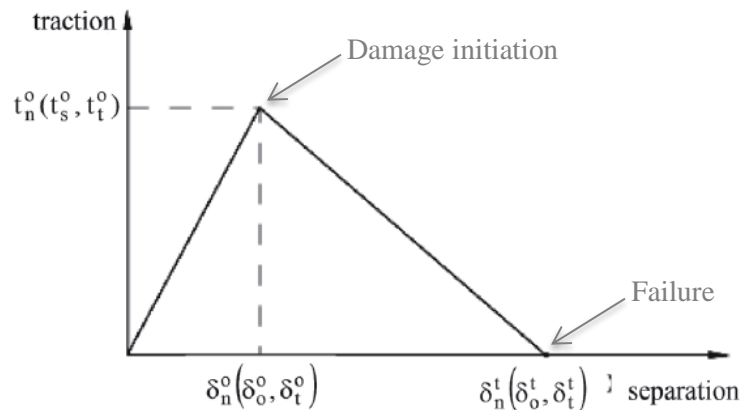


Figure 2-5 Traction-separation law for cohesive elements used to represent the interface between concrete and carbon fiber-reinforced polymer sheet (Smitha et al., 2014).

The relative motion of the bottom and top parts of the cohesive element measured along the thickness direction represented the opening or closing of the interface, whereas the relative motion in the transverse direction represented the shear behavior. An energy approach was introduced to define failure (i.e., delamination) of the cohesive elements, which accounted for

the work done by the tractions and their relative displacements in the normal and two shear directions. Once the cohesive elements were fully delaminated, the response in the normal direction was characterized by a hard contact, whereas the tangential behavior was defined by a friction coefficient of 0.2 (similar to the post-failure response introduced by Romanoschi and Metcalf (2001a)). The stress-strain response obtained from FEM agreed fairly well with actual testing results and showed significant improvement with respect to analytical models available in the literature. These results indicated that cohesive elements can potentially be an effective tool for simulation of the damage process leading to interface failure. However, the focus of this research project is the potential link between debonding and near-surface longitudinal cracking, rather than the debonding failure mechanism itself. Thus, introduction of cohesive elements is not considered a need at the moment.

2.3 Concluding remarks

In summary, factors such as tack coat type, residual application rate, surface cleanliness, surface roughness, gradation of surrounding layers, temperature and normal pressure appear to affect interface performance (findings are summarized in Table 2-2). In addition to these factors typically evaluated in the laboratory, field studies suggest that insufficient compaction of the asphalt layers due to thermal segregation and mixture segregation can facilitate entrance of water, which can promote interface bond breakdown. Furthermore, even when tack coat material meets specification requirements and adequate mixture compaction is achieved, a poor bond between asphalt layers may sporadically occur as a result of tack tracking, clogged nozzles, light tack application, presence of dirt or even overly-diluted tack coat.

With respect to interface modeling, efforts have focused on the study of the potential effects of interface conditions on the global stress and strain distribution in the pavement structure and, thus, the potential contribution to pavement distress. Most attempts to characterize the response of the interface are based on results from strength tests conducted under monotonic loading conditions (usually at a constant rate of deformation). While monotonic loading may be representative of a braking event conducive to slippage, it is still debatable whether monotonic loading is relevant for the study of progressive bond breakdown under repeated traffic loads of an interface located deeper in the pavement structure.

Table 2-2 Effect of various factors on interface bond strength.

Factor	Effect on bond strength
Temperature	As temperature increases, shear strength decreases
Normal pressure	As normal pressure increases, shear strength increases
Binder residue viscosity	As viscosity of binder residue increases, shear strength increases
Binder residue hardness	As hardness of binder residue increases, shear strength increases
Application rate	Controversial
Emulsion curing time	Unclear
Dilution	Unclear
Surface cleanliness	A clean surface provides higher shear strength
Surface roughness	Surface roughness increases shear strength
Surrounding layers	Coarser gradations provide higher interface shear strength than finer gradations

A summary of interface modeling efforts reported in the literature, including model parameters, failure criteria and post-failure response is presented in Table 2-3. Most studies have employed a reaction modulus to represent the compliance associated with an interface between two asphalt layers. Romanoschi and Metcalf (2001a) introduced a failure criterion (shear strength) and a frictional post-failure response. Ozer et al. (2008) proposed a different approach based on two major modifications. First, their failure criterion follows a Mohr-Coulomb law; in other words, shear strength is not constant but rather depends on normal stress (confinement). Second, strength parameters are reduced as load progresses; this is, their model accounts for damage accumulation as part of the failure process. It is unclear to the authors whether this model incorporates a post-failure response in the form of a residual strength or a frictional component. Finally, Smitha et al. (2014) proposed a model based on cohesive elements that includes damage initiation following a quadratic stress interaction function and definition of failure according to a fracture energy criterion. After failure, normal behavior of the two surfaces is defined by a hard contact whereas tangential behavior is frictional.

Table 2-3 Summary of previous interface modeling efforts reported in the literature.

Model	Parameters	Failure criteria	Post-failure response
Uzan (1976) and Uzan et al. (1978)			
BISAR	K	No	No
Maina et al. (2007)			
Romanoschi and Metcalf (2001a, 2001b)	K, τ_{max} , μ	$\tau = \tau_{max}$	Frictional
Mohammad et al. (2012)			
Kruntcheva et al. (2006)	h, E, ν	No	No
Ozer et al. (2008)	K, c, Φ , s,	Hyperbolic yield	Unclear
Ozer et al. (2012)	G_I , G_{II} , G_{III}	surface	
		Quadratic nominal	Hard contact
	h, E, G, K,	stress criterion	(normal direction)
Smitha et al. (2014)	t^0 , δ^0 , δ^t , G_I ,	(damage initiation)	Frictional
	G_{II} , G_{III} , μ	Fracture energy	(tangential
		(failure)	direction)

Two final remarks should be made for the purposes of this project. First, although some studies introduced an interface failure criterion when modeling a pavement structure, most of them either reported that the failure criterion was not met or no comment was made in this regard. Only Mohammad et al. (2012) stated that failure criterion ($\tau = \tau_{max}$) was reached in two out of 72 pavement structure combinations. So far, modeling efforts have not identified the potential location and extent of interface debonding. Fortunately, field efforts have suggested that the wheelpath area at an approximate depth of 1 to 2 in appeared to be the most likely location for interface debonding to occur. Second, prior modeling efforts have evaluated maximum tensile stress/strain under the load through smeared bonding conditions. This approach assumes the same properties and same response (either fully bonded, fully debonded or with some degree of compliance) across the entire interface. However, field evidence indicates debonding is a local phenomenon, which starts at a critical location and gradually progresses through a portion of the interface. Therefore, the use of smeared bonding conditions may not be representative for analysis of the link between localized interface debonding and near-surface cracking. The authors are of the opinion that modeling efforts should introduce localized debonding at critical

locations to better evaluate stress redistribution resulting from interface failure and ultimately identify a potential mechanism connecting localized debonding and near-surface longitudinal cracking.

CHAPTER 3

INVESTIGATION OF SOPHISTICATION LEVEL REQUIRED FOR MODELING PURPOSES

This chapter investigated the level of sophistication required to conduct a modeling study on the potential impact of localized interface debonding on near-surface longitudinal cracking. Effects of the viscoelastic behavior of asphalt materials on pavement response with an emphasis on interface debonding when subjected to a wheel load moving at varying speeds were evaluated. The chapter focused on finite element models developed for identifying the critical location and extent of debonding by comparing results of viscoelastic (VE) and equivalent elastic (EE) finite element analyses. Furthermore, it provided recommendations for the subsequent chapters.

3.1 Finite element models for identifying critical locations

3.1.1 Pavement structure and layer properties

A flexible pavement structure employed in a prior FDOT full-scale field study (Chun et al., 2015) was selected for use in this chapter. The pavement section includes a 3-in AC layer, a 10-in limerock base, and a 12-in granular subbase on top of the subgrade. As shown in Figure 3-1, bedrock was placed 100 in below the subbase layer to consider real conditions typically encountered in Florida. It is important to note that the 3-in thin AC layer was purposely selected in an effort to identify critical locations for interface debonding. According to a recently completed modeling study, a pavement structure with a thinner AC layer was found to be more vulnerable to asphalt layer interface debonding than other structures (Cho et al., 2016).

The unbound layers (i.e., base, subbase and subgrade) were assumed to be linear elastic in the finite element model. Table 3-1 presents elastic moduli of the unbound materials determined from back-calculation using falling weight deflectometer (FWD) testing results. The AC layer, whose response depends on loading frequency/time and temperature, was assumed to be linear viscoelastic. The viscoelastic response was characterized from dynamic modulus tests conducted with an asphalt mixture performance tester (AMPT) at four loading frequencies (0.01, 0.1, 1 and

10 Hz) and three temperatures (4, 20 and 40°C). Figure 3-2 presents a dynamic modulus master curve in the form of a sigmoidal fitting function constructed using the test results in the frequency domain. An intermediate temperature of 20°C was selected as reference temperature.

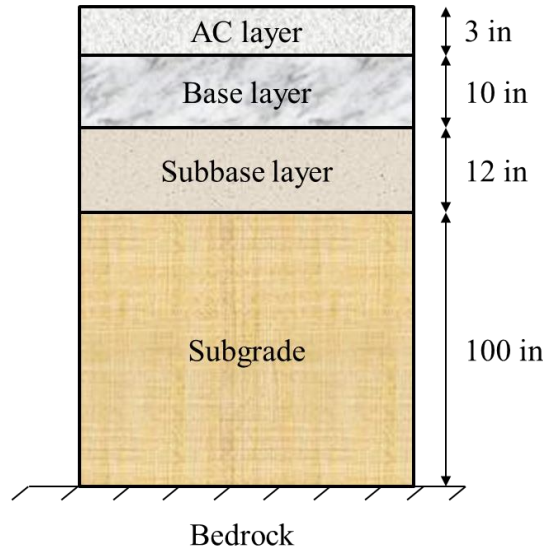


Figure 3-1 Pavement structure for investigating modeling level of sophistication

Table 3-1 Unbound layer properties for the selected pavement structure

Layer	Modulus of elasticity (ksi)	Poisson's ratio
Base	27.5	0.4
Subbase	18.6	0.4
Subgrade	12.8	0.4

Based on linear viscoelasticity theory, relaxation modulus in the time domain $E(t)$ and complex modulus in the frequency domain $E^*(\omega)$ are interchangeable. Hence, relaxation modulus in the form of Prony series was calculated from complex modulus through interconversion. A Prony series with eight relaxation components spread over eight decades was used for modeling purposes in this chapter. Table 3-2 provides the Prony series parameters at 20°C, where g , k and e are dimensionless shear, bulk and elastic relaxation moduli, and τ denotes relaxation time. The instantaneous elastic modulus E_0 was determined to be 2,700 ksi. Assuming a constant Poisson's ratio of 0.35 typically used for AC materials, the instantaneous shear and bulk moduli were 1,000

ksi and 3,000 ksi, respectively. More details on the calculation of these parameters are included in the next section.

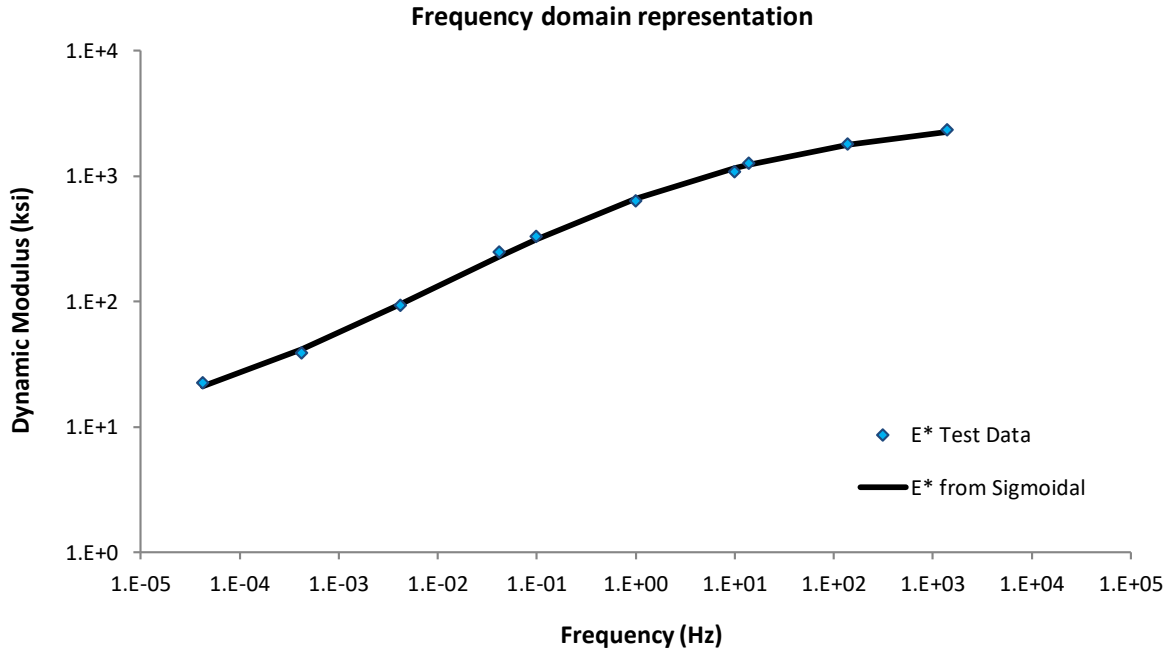


Figure 3-2 Dynamic modulus master curve fitted using a sigmoidal function at 20°C

Table 3-2 Prony series parameters for viscoelastic AC layer selected in this chapter

$$E(t) = E_0 \left(1 - \sum_{i=1}^8 e_i (1 - \exp(-t/\tau_i)) \right)$$

No.	g	k	e	τ (s)
1	0.2514	0.2514	0.2514	1.0E-04
2	0.2042	0.2042	0.2042	1.0E-03
3	0.2091	0.2091	0.2091	1.0E-02
4	0.1589	0.1589	0.1589	1.0E-01
5	0.1005	0.1005	0.1005	1.0E+00
6	0.0508	0.0508	0.0508	1.0E+01
7	0.0112	0.0112	0.0112	1.0E+02
8	0.0068	0.0068	0.0068	1.0E+03

In addition, equivalent elastic moduli for the AC material were determined using the dynamic modulus master curve. According to Huang (2004), the load experienced at a given point due to a moving vehicle can be assumed to follow to a sinusoidal or haversine function. For a vehicle traveling at 40 mph, the duration of the load is 0.1s, which corresponds to a loading frequency of 10 Hz (sinusoidal function). Two vehicle speeds were considered in this study, including a low speed of 7.5 mph (a typical HVS speed) and a high speed of 60 mph (a typical highway speed). The loading frequencies corresponding to these two speeds were estimated as 1.875 and 15 Hz, respectively. Based on the dynamic modulus master curve shown in Figure 3-2, the corresponding equivalent elastic moduli were 784 and 1258 ksi, respectively (Table 3-3).

Table 3-3 Equivalent elastic moduli for AC layer at 20°C

Speed (mph)	Loading frequency (Hz)	Equivalent elastic modulus (ksi)
7.5	1.875	784.1
60	15	1258.4

3.1.2 Determination of relaxation moduli for viscoelastic analysis

Many finite element programs including ABAQUS require shear $G(t)$ and bulk $K(t)$ moduli (or their normalized form with respect to the instantaneous values) as inputs for viscoelastic materials. These moduli can be obtained from the relaxation modulus $E(t)$, which is expressed in the form of a Prony series as shown below:

$$E(t) = E_0 \left(1 - \sum_{i=1}^N e_i (1 - \exp(-t/\tau_i)) \right) \quad (3.1)$$

$$G(t) = \frac{E(t)}{2(1 + \nu)} \quad (3.2)$$

$$K(t) = \frac{E(t)}{3(1 - 2\nu)} \quad (3.3)$$

where E_0 = instantaneous modulus, e_i = dimensionless relaxation moduli, τ_i = relaxation times, N = number of terms in the Prony series, ν = Poisson's ratio. For practical implementations, the viscoelastic material is typically assumed to respond the same way in volumetric and shear relaxation, which results in a constant Poisson's ratio.

In this study, the dynamic modulus test (Bonaquist, 2008) in accordance with AASHTO TP 79 was selected as the mechanical rheology test to determine the relaxation modulus (after interconversion of the complex modulus). Three temperatures (4, 20 and 40°C) and four frequencies (0.01, 0.1, 1 and 10 Hz) were used to determine the complex modulus E^* . Complex modulus can be expressed in terms of dynamic modulus $|E^*|$ and phase angle δ or storage modulus E_s and loss modulus E_l , as shown in Eq. 3.4 (i is the imaginary unit).

$$E^* = |E^*|(\cos(\delta) + i \cdot \sin(\delta)) = E_s + i \cdot E_l \quad (3.4)$$

There are two main steps involved in the determination of the relaxation modulus:

1. Determination of shift factors as part of the dynamic modulus master curve.
2. Determination of Prony series parameters.

In Step 1, dynamic modulus data at different temperatures were shifted to a preselected reference temperature (20°C in this case) and a master curve was determined by minimizing the least-square error between the measurements and the following sigmoidal fitting function:

$$\log|E^*| = \log(\text{Min}) + \frac{\log(\text{Max}) - \log(\text{Min})}{1 + \exp(\beta + \gamma \cdot \log(\omega_r))} \quad (3.5)$$

in which Max = limiting maximum modulus in ksi, Min = limiting minimum modulus in ksi (treated as a fitting parameter), β and γ = fitting parameters, and ω_r = reduced frequency in Hz. The limiting maximum modulus Max was estimated from mixture volumetric properties using the Hirsch model:

$$\text{Max} = P_c \cdot A + \frac{1 - P_c}{B} \quad (3.6a)$$

$$P_c = \frac{(20 + 435000(VFA)/VMA)^{0.58}}{650 + (435000(VFA)/VMA)^{0.58}} \quad (3.6b)$$

$$A = 4200000 \left(1 - \frac{VMA}{100}\right) + 435000 \left(\frac{VFA \cdot VMA}{10000}\right) \quad (3.6c)$$

$$B = \frac{1 - VMA/100}{4200000} + \frac{VMA}{435000(VFA)} \quad (3.6d)$$

where VMA = voids in mineral aggregate in %, and VFA = voids filled with asphalt in %.

The reduced frequency ω_r was computed using the Arrhenius equation:

$$\log(\omega_r) = \log(\omega) + \log(a(T)) \quad (3.7)$$

in which ω = loading frequency in Hz at any test temperature T, and $a(T)$ = shift factor at temperature T, which is defined as follows:

$$\log(a(T)) = \frac{\Delta E_a}{19.14714} \left(\frac{1}{T} - \frac{1}{T_r} \right) \quad (3.8)$$

where T_r = reference temperature in °K, and ΔE_a = activation energy treated as a fitting parameter.

In total, four fitting parameters (β , γ , Min and ΔE_a) were obtained during the optimization process, which resulted in the master curve presented in Figure 3-2 and three shift factors ($\log(a(T))$ was equal to 2.146 for 4°C, 0 for 20°C, and -2.374 for 40°C). These factors were used to shift measured storage and loss moduli to the reference temperature.

In Step 2, Prony series parameters were determined by minimizing least square errors between the measurements and the Prony series functions described below. Using Fourier transforms, the relaxation modulus in time domain (Eq. 3.1) could be converted into complex modulus (expressed as storage and loss moduli) in frequency domain as follows:

$$E_s(\omega_r) = E_0 \left(1 - \sum_{i=1}^N e_i \right) + E_0 \sum_{i=1}^N \frac{e_i^2 \tau_i^2 \omega_r^2}{1 + \tau_i^2 \omega_r^2} \quad (3.9a)$$

$$E_l(\omega_r) = E_0 \sum_{i=1}^N \frac{e_i \tau_i \omega_r}{1 + \tau_i^2 \omega_r^2} \quad (3.9b)$$

where E_0 = instantaneous modulus (treated as a fitting parameter), e_i = dimensionless relaxation moduli (fitting parameters), τ_i = relaxation times (with one decade interval, e.g., 10^{-6} , 10^{-5} ... 10^3 sec), ω_r = reduced frequency, N = number of terms in the Prony series.

A total of nine fitting parameters were obtained through the optimization process, including the instantaneous modulus E_0 (2700 ksi) and eight dimensionless relaxation moduli e_i (Table 3-2). As shown in Figure 3-3a, the Prony series functions matched very well the measured data in the frequency domain including both storage and loss moduli. Once the fitting parameters were determined, relaxation modulus in time domain was also obtained (Figure 3-3b).

3.1.3 Axisymmetric finite element models

Axisymmetric finite element models, in conjunction with more complex 3D models, were developed to identify critical locations of AC layer interface debonding and to determine whether elastic analyses with equivalent properties can be used to reach the same level of accuracy as viscoelastic analyses.

Due to its computational efficiency, axisymmetric finite element models are commonly used to predict responses of a multilayer pavement system subjected to a circular load uniformly applied on the pavement surface. Figure 3-4 depicts the axisymmetric model used to simulate the pavement section. The lateral size of the model, element type and mesh density were selected based on results of a sensitivity analysis. As can be seen, a fine mesh with small size elements was defined close to the loading area, while a coarser mesh was used farther at a farther distance. Eight-node quadratic elements with reduced integration (CAX8R) were used for the body of the system whereas infinite elements (CINAX5R) were used as a lateral boundary to simulate the far-field region. A roller boundary condition was applied along axis of symmetry, and a fixed boundary condition was used at the bottom of the subgrade to simulate bedrock support.

A circular load with a 5-in radius and a uniform pressure was used. The magnitude of the pressure varied with time from 0 to 100 psi following a half-sine waveform to simulate one pass of a moving load. This type of load was called stationary since it was applied at a fixed location.

Figure 3-5 plots the stationary half-sine load for a low vehicle speed (7.5 mph) and a high vehicle speed (60 mph). A lower speed clearly resulted in a longer duration of the waveform.

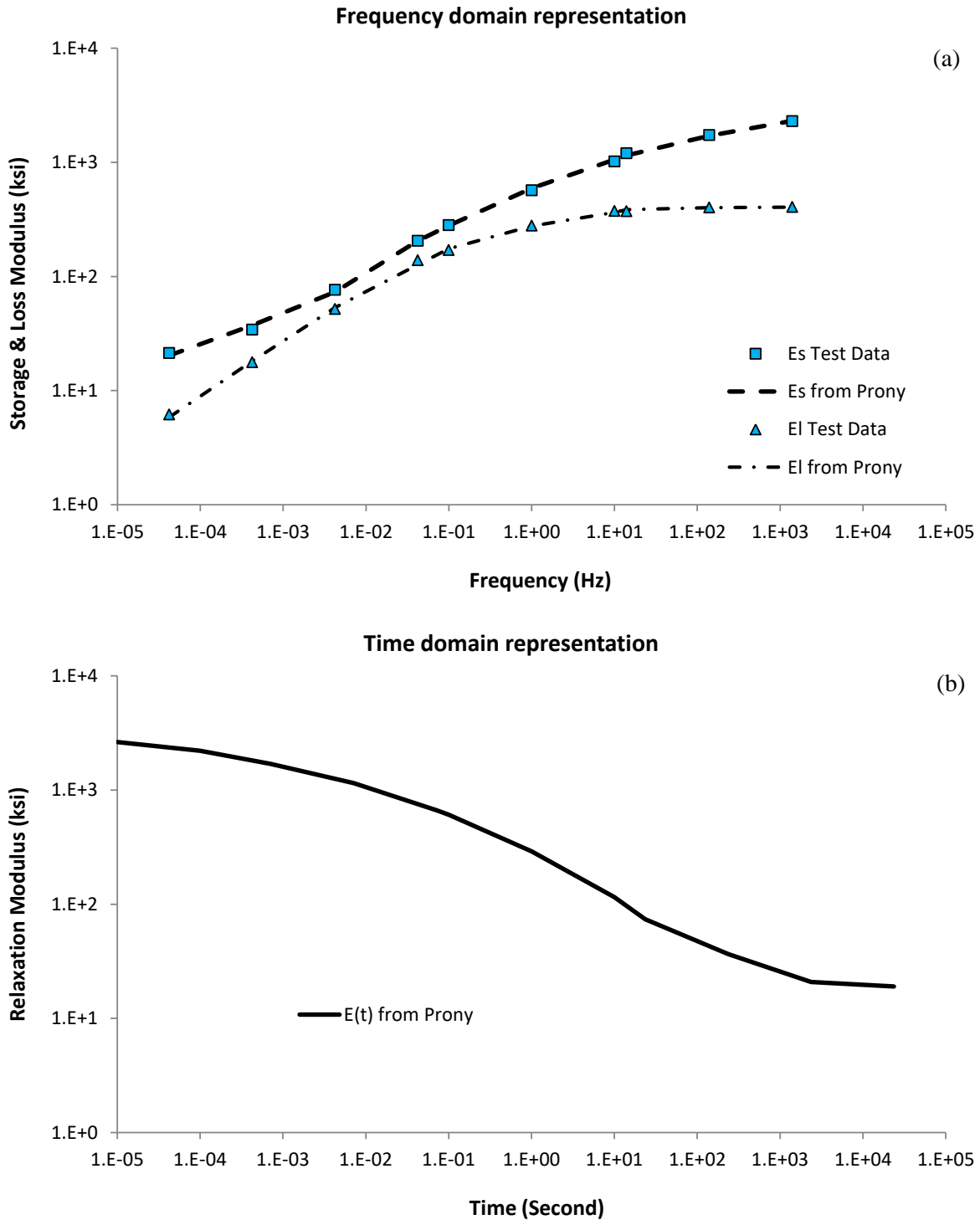


Figure 3-3 Prony series functions: a. Storage and loss moduli; b. Relaxation modulus

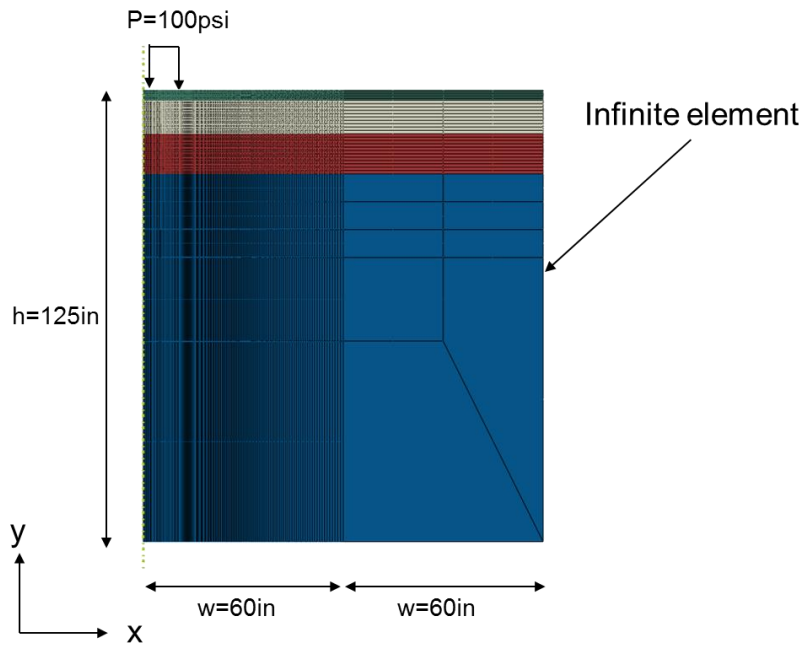


Figure 3-4 Axisymmetric finite element model

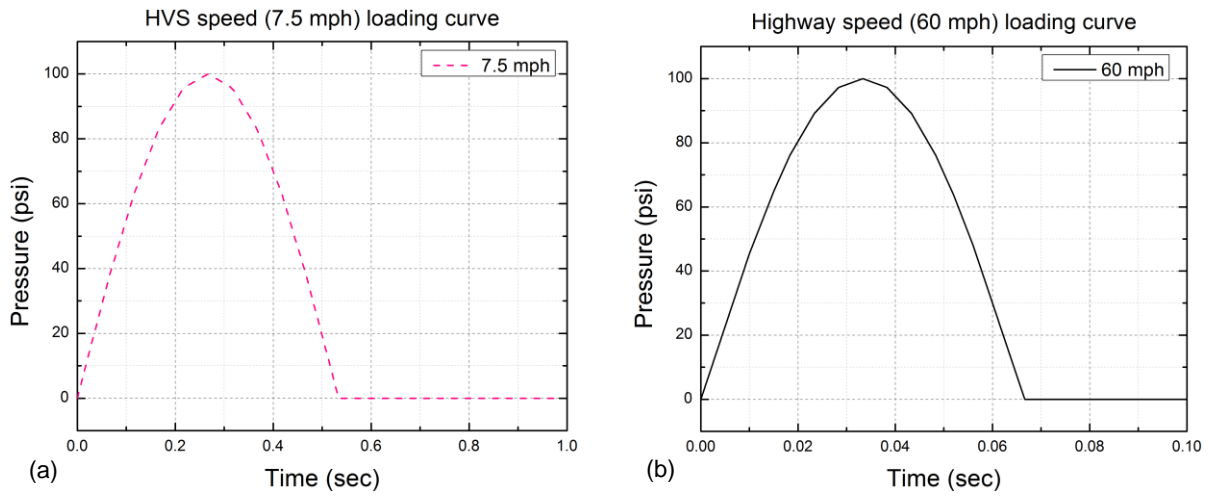


Figure 3-5 Stationary half-sine loading curve: a. Slow traffic; b. Fast traffic

3.1.4 Three-dimensional finite element models

Although known to be computationally efficient, axisymmetric models cannot realistically simulate responses of a layered system subjected to a moving wheel load. Furthermore, the shape of the load in the axisymmetric condition must be circular, while footprints of real tires are approximately rectangular (Roque et al., 2007). More importantly, the movement of a load in the axisymmetric condition can only be simulated by means of a stationary waveform (i.e., at a fixed location). Thus, three dimensional (3D) finite element models were developed to overcome the above-mentioned limitations of axisymmetric models.

Figure 3-6 presents the 3D model that simulates the selected pavement section, where traffic direction was defined along the Z-axis. Due to the symmetry of the model with respect to the Y-Z plane, one-half of the pavement section subjected to one half of the vertical load was considered. Twenty-node quadratic brick elements (C3D20) were used for the body of the system whereas infinite elements (CIN3D12R) were used as the front, back and lateral boundaries to simulate the far-field region. A roller boundary condition was applied along the plane of symmetry and a fixed boundary condition was used at the bottom of the subgrade to simulate bedrock support. It is important to note that even though linear brick elements have been used in 3D FE analyses to reduce computation time (Kim et al., 2008; Wang, 2011), they were found not able to provide accurate prediction of vertical stress based on the results of a sensitivity study. Therefore, quadratic (higher order) brick elements were considered necessary for this study.

Figure 3-6b shows the rectangular load (with a pressure of 100 psi) and moving path of the load (with a length of 60 inch) in the model. Based on the size of the elements along the moving path in the X-Z plane (1 in by 1 in), the load was devised to move 1 in per step. In total, 53 steps were required to complete a load pass. Given the total length of the moving path, the total time for one complete pass as well as the step time can be determined for any vehicle speed. Table 3-4 summarizes the total time and step time corresponding to the two selected vehicle speeds (7.5 and 60 mph). It is important to point out the stepwise moving distance of 1 in (i.e., one element size) was found to provide the most accurate results through a sensitivity analysis.

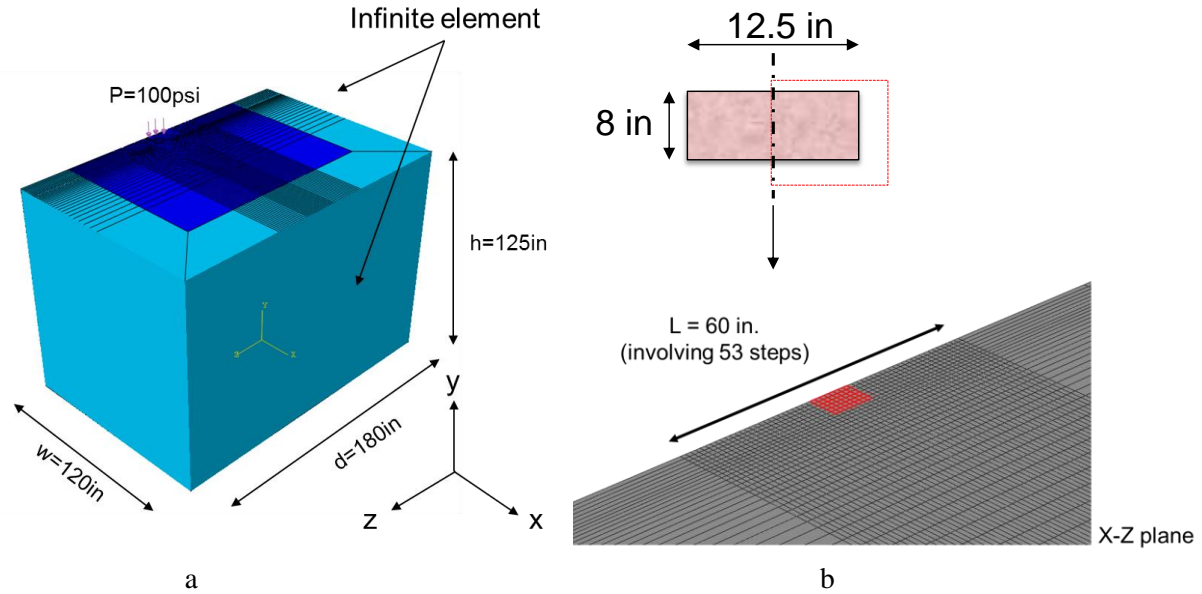


Figure 3-6 Three-dimensional FE model: a. Geometry and mesh; b. Moving load

Table 3-4 Total time and step time for one pass of the moving load

Speed (mph)	Total time for one pass (s)	Step time (s)
7.5	0.4545	0.00857
60	0.0568	0.00107

3.2 Results

3.2.1 Axisymmetric (elastic) analysis under a static load

Axisymmetric elastic analyses of the pavement section shown in Figure 3-1 were conducted using equivalent elastic modulus for the AC layer. Two AC moduli at an intermediate temperature of 20°C were considered (Table 3-3): one represents the AC modulus at a typical HVS speed of 7.5 mph (i.e., the low vehicle speed case), and the other corresponds to the AC modulus at a typical highway speed of 60 mph (i.e., the high-speed case). A uniform pressure of 100 psi with a radius of 5 in was applied on the pavement surface to simulate the peak loading condition during one pass of the wheel load.

Figure 3-7 presents the stress contours obtained for the low speed case. As can be seen, high shear stress in the range of 70-80 psi was confined in a small area (high-shear zone) with a radius of 0.5 in and centered approximately at the mid-depth of the AC layer below the edge of the tire (Figure 3-7a). Due to bending, the horizontal stress was high in compression right below the load and high in tension at the bottom of AC layer, with the neutral axis being approximately through the high-shear zone (Figure 3-7b). The compressive vertical stress was maximum immediately below the load and reduced gradually with depth. The high-shear zone appeared to sit in the area with the highest gradient in vertical stresses (Figure 3-7c). For example, the vertical stress dropped quickly from about 50 psi located at 0.5 in to the left of the center of the high-shear zone to about 20 psi at 0.5 in to the right of the center. A similar stress distribution was observed for the high-speed case.

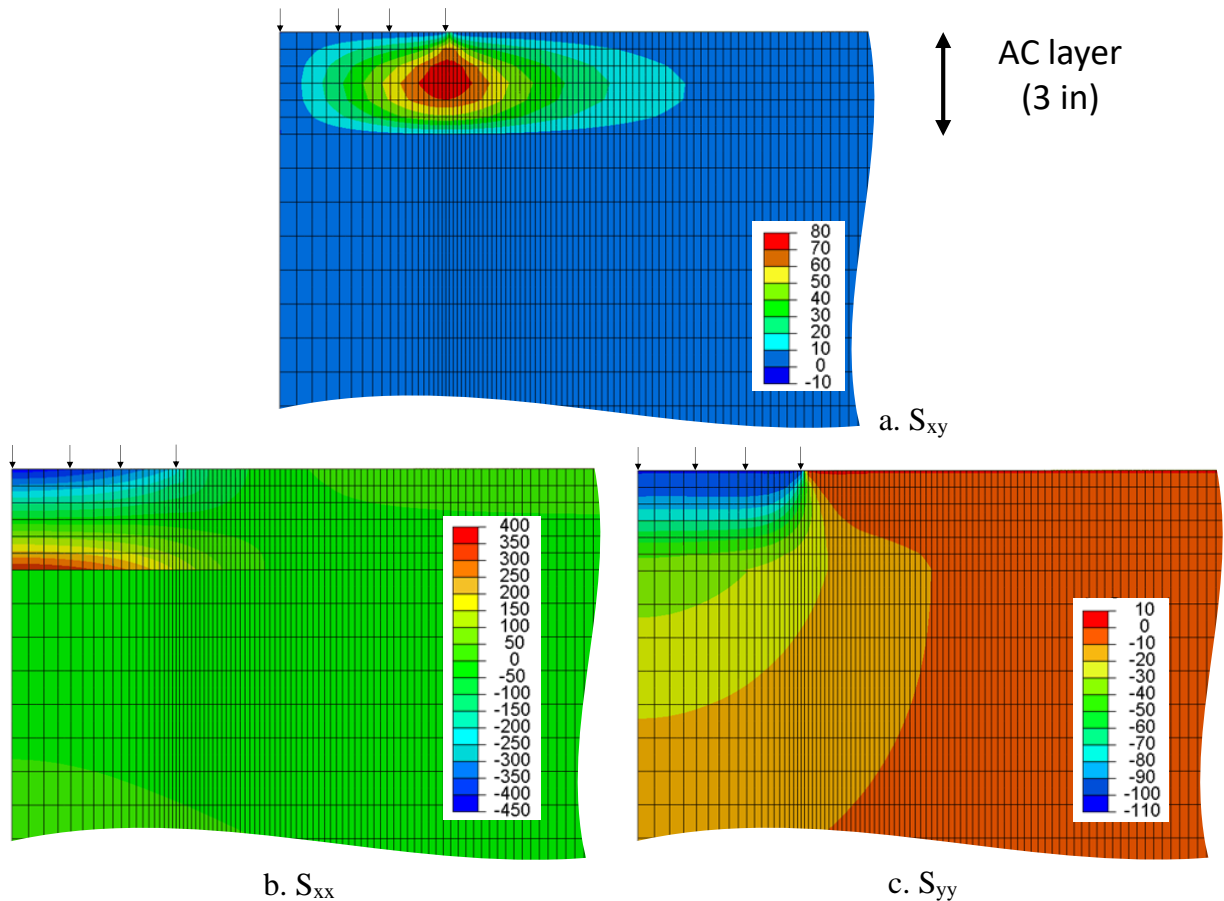


Figure 3-7 Stress contours for FE axisymmetric elastic analysis (static load) and low-speed AC modulus: a. Shear stress (psi); b. Horizontal stress (psi); c. Vertical stress (psi)

It appeared that the area where high shear stress (70-80 psi) coupled with low confinement (20-30 psi) could be the potential location of debonding if an asphalt layer interface was constructed right through this area. Therefore, the center of the high-shear zone (i.e., location L1 in Figure 3-8) and the line through the mid-depth of AC layer were selected for further evaluation of stress and strain distributions. In addition, the location of maximum horizontal tensile stress (i.e., location L2 in Figure 3-8) and the line through the bottom of AC layer were included to provide information supplemental to the findings at the aforementioned locations.

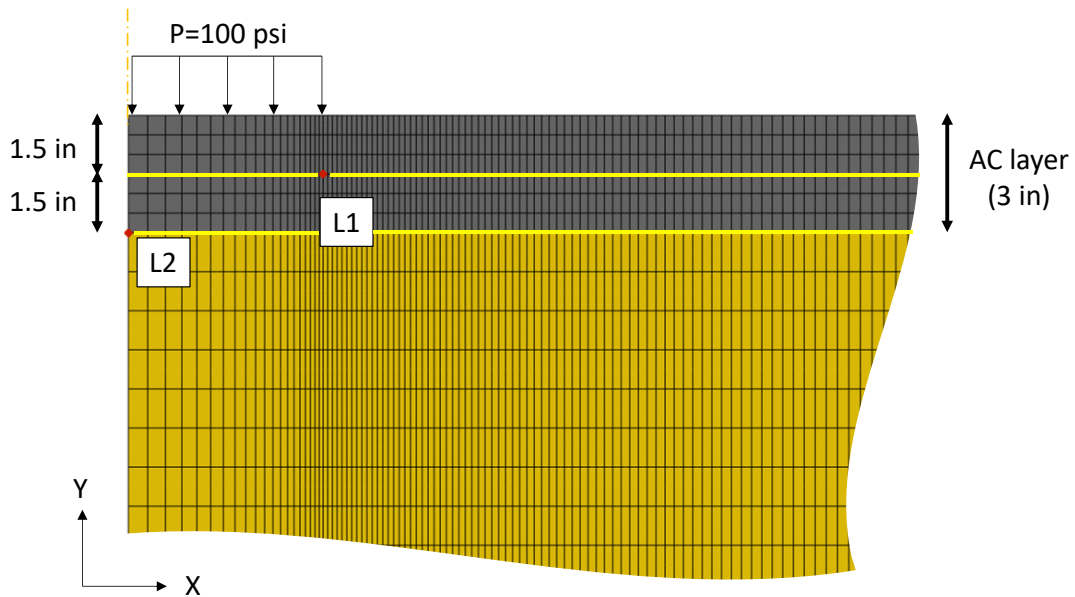


Figure 3-8 Selected locations in the axisymmetric plane for further evaluation

Figure 3-9 shows the stress and strain distribution along the mid-depth of AC layer (Fig. 3-9a-d) as well as along the bottom of AC layer (Fig. 3-9e-f) predicted by finite element analysis (FEA) using continuous lines. Also, the results of the multilayer linear elastic program BISAR (based on analytical solutions) were included in the figure using symbols. As can be seen, FEA results including all three stress and strain components (i.e., shear, horizontal and vertical components) agreed well with BISAR results for both low-speed (7.5 mph) and high-speed (60 mph) cases, which demonstrated the accuracy of the finite element model developed in this part of the study.

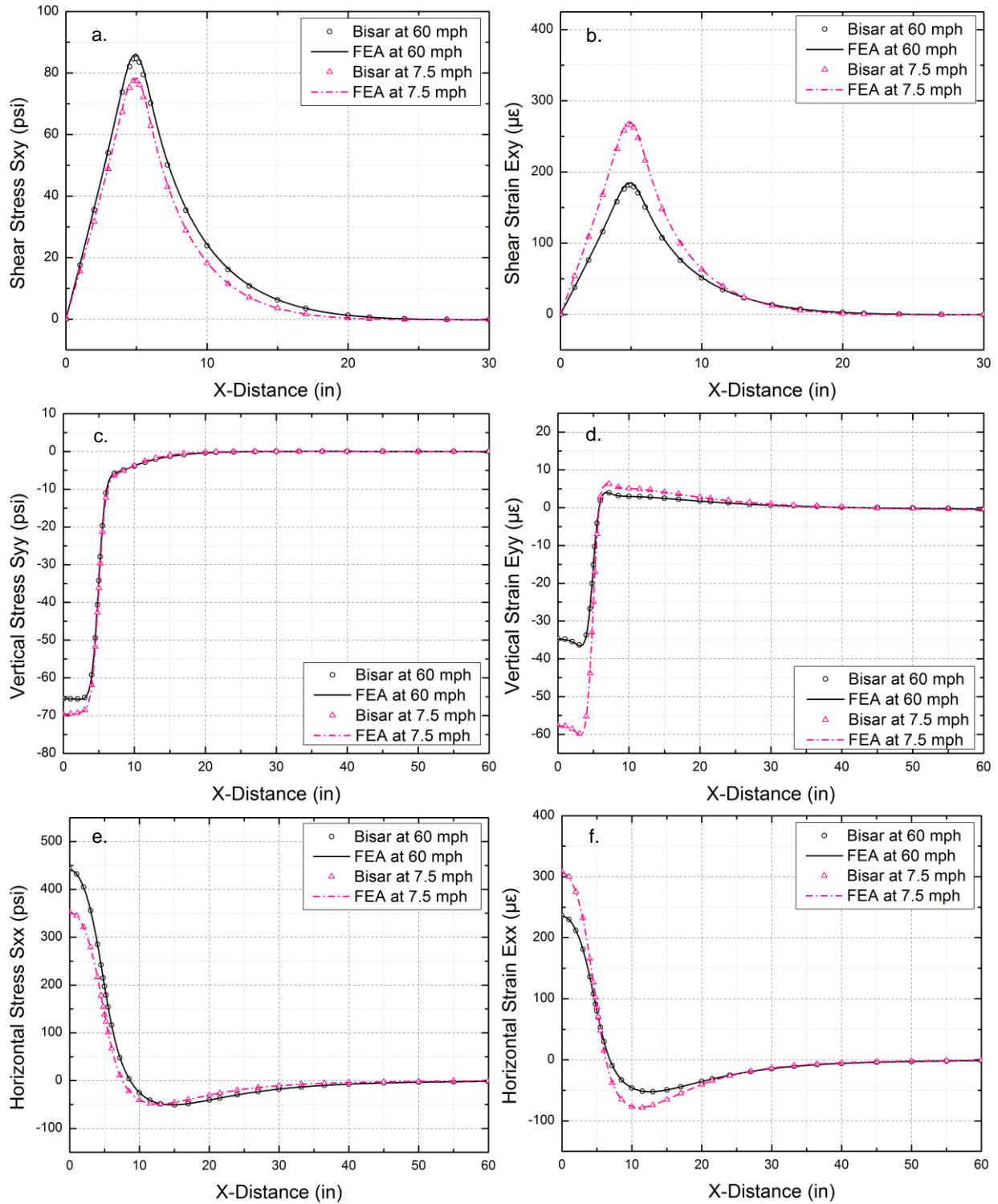


Figure 3-9 Comparison between axisymmetric FEA and BISAR results: a-b. Shear stress and strain at AC mid-depth; c-d. Vertical stress and strain at AC mid-depth; e-f. Horizontal stress and strain at AC bottom.

A further examination of vehicle speed in terms of AC effective modulus showed that a higher speed (i.e., a stiffer response from the AC layer) led to higher shear stress and lower shear strain along the mid-depth of AC layer and higher horizontal tensile stress and lower horizontal tensile strain at the bottom of AC layer. Regardless of magnitude, the location of peak values stayed the same. Furthermore, a stiffer AC layer yielded lower vertical compressive stress and strain at the mid-depth of AC layer (Fig. 3-9c-d) due to a better redistribution of the load. Load gradually transfers downward through the pavement layers in the shape of a trapezoid. The slope of the trapezoid is related to the stiffness of AC layer. A stiffer AC material resulted in a larger slope, i.e., stress spread over a larger area, which led to lower vertical compressive stresses.

3.2.2 Axisymmetric (viscoelastic vs. elastic) analysis under a stationary half-sine load

The viscoelastic response (i.e., linear viscoelasticity) of the AC layer under a stationary half-sine load was evaluated in this section. The relaxation modulus master curve (Table 3-2) determined from dynamic modulus test results was employed to characterize the AC layer. For simplicity and computational efficiency, the pavement structure was represented using the axisymmetric finite element model shown in Figure 3-4. A stationary half-sine pressure load was uniformly applied on the pavement surface at two loading frequencies (1.875 and 15 Hz) to simulate one pass of a slow vehicle and a fast vehicle, respectively (Figure 3-5). In addition, results obtained with AC equivalent elastic moduli (Table 3-3) were included for comparison with viscoelastic responses. Detailed results at selected locations illustrated in Figure 3-8 are shown in Figures 3-10 through 3-12. Viscoelastic responses are plotted using solid lines, whereas responses from equivalent elastic analysis are shown in dash-dot lines.

Figure 3-10 presents shear stress/strain time history at L1 for slow (Fig. 3-10a-b) and fast speed (Fig. 3-10c-d) as well as shear stress/strain distribution along the AC mid-depth at peak loading time (Fig. 3-10e-f). As shown in Fig. 3-10a and 3-10c, shear stress during loading and unloading were different. The AC viscoelastic response caused stress reversal (change in stress sign) during unloading. Note that viscoelastic predictions were almost identical to the elastic ones during the loading period and became slightly smaller than the elastic ones throughout the unloading period. An increase in vehicle speed led to higher AC stiffness and shorter loading time, which resulted in increased shear stresses and reduced difference between the viscoelastic and elastic solutions.

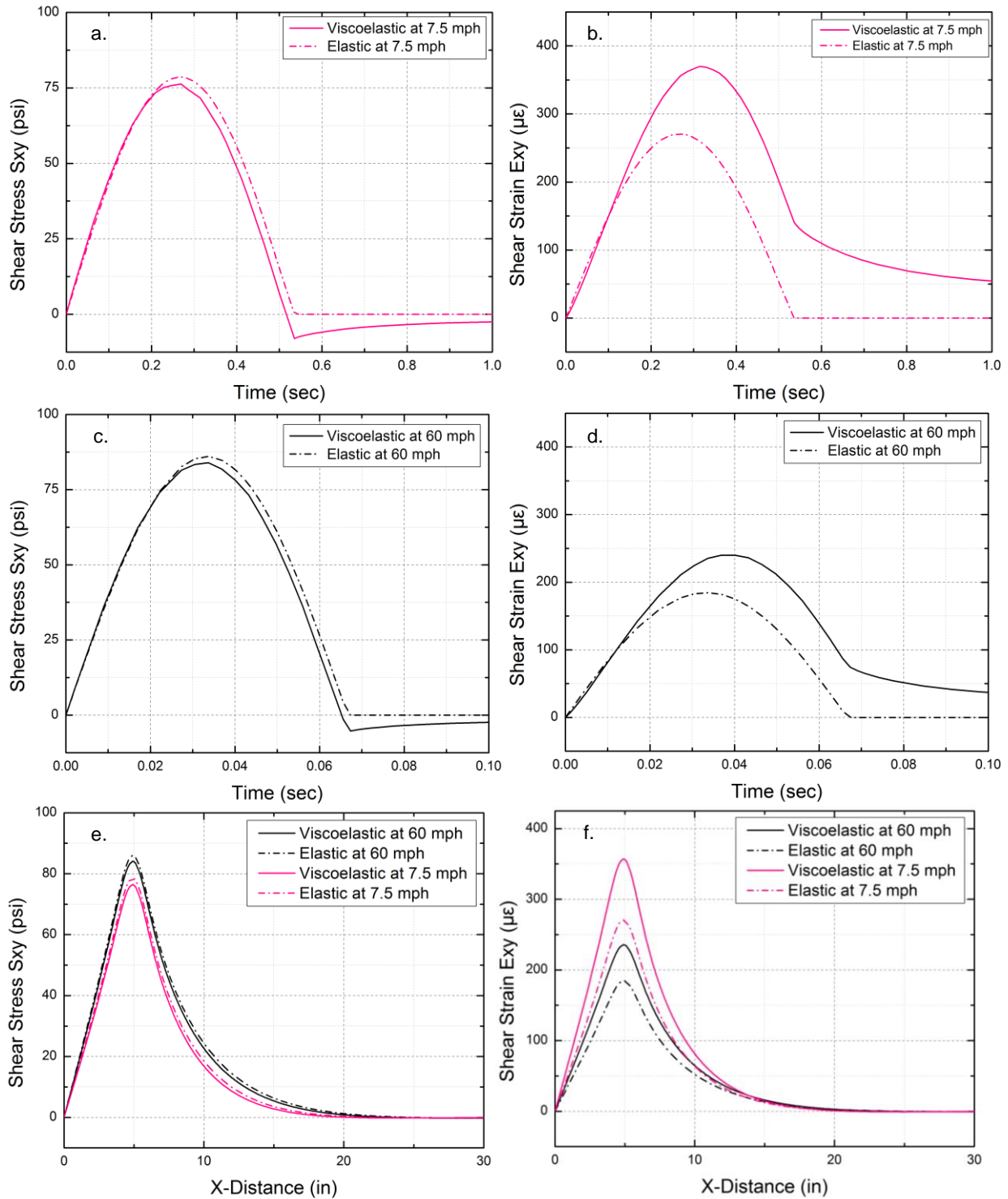


Figure 3-10 Axisymmetric shear stress/strain evaluation: a-b. Shear stress/strain at L1 (slow traffic); c-d. Shear stress/strain at L1 (fast traffic); e-f. Shear stress/strain distribution along AC mid-depth at peak loading time (slow/fast traffic).

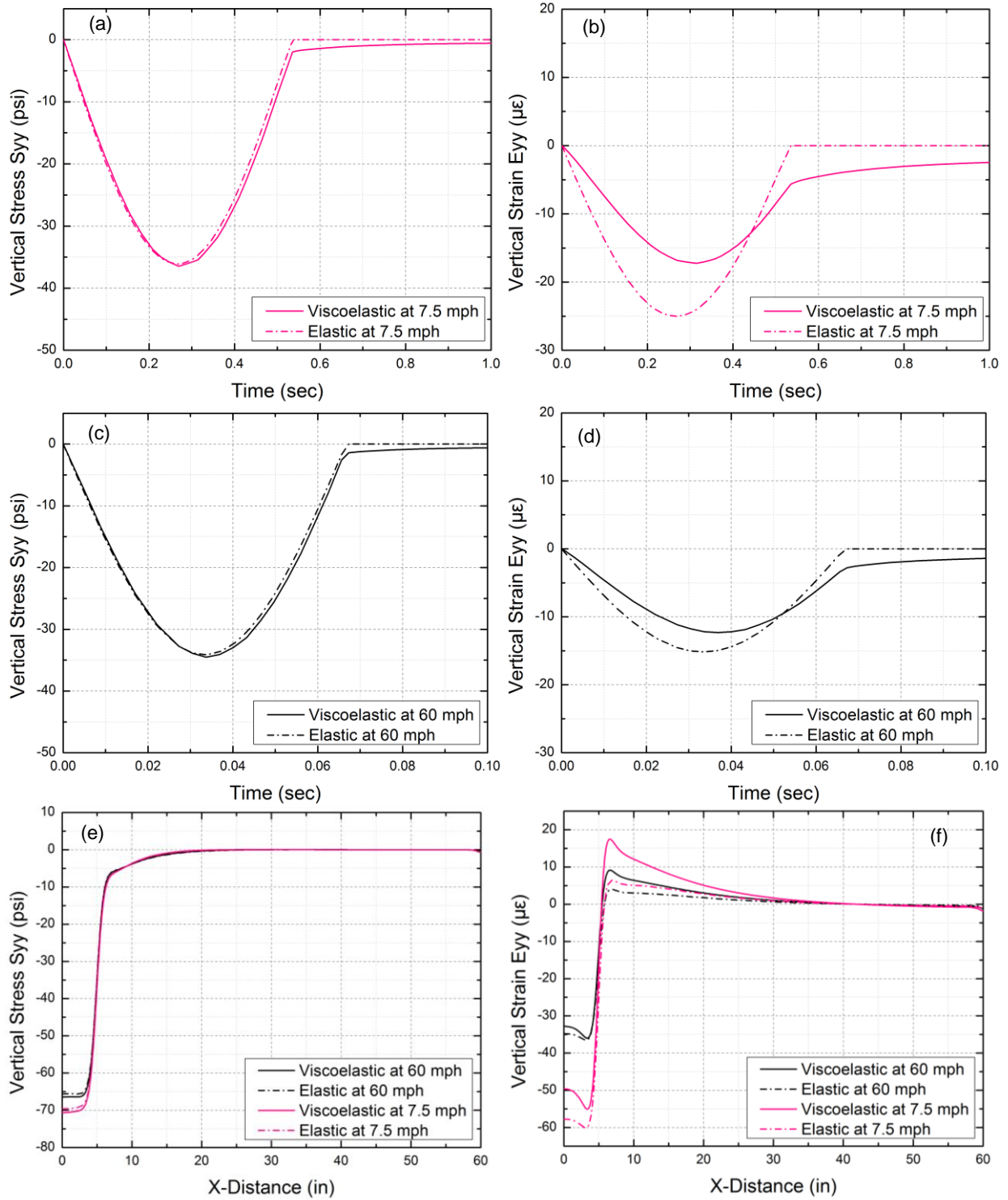


Figure 3-11 Axisymmetric vertical stress/strain evaluation: a-b. Vertical stress/strain at L1 (slow traffic); c-d. Vertical stress/strain at L1 (fast traffic); e-f. Vertical stress/strain distribution along AC mid-depth at peak loading time (slow/fast traffic).

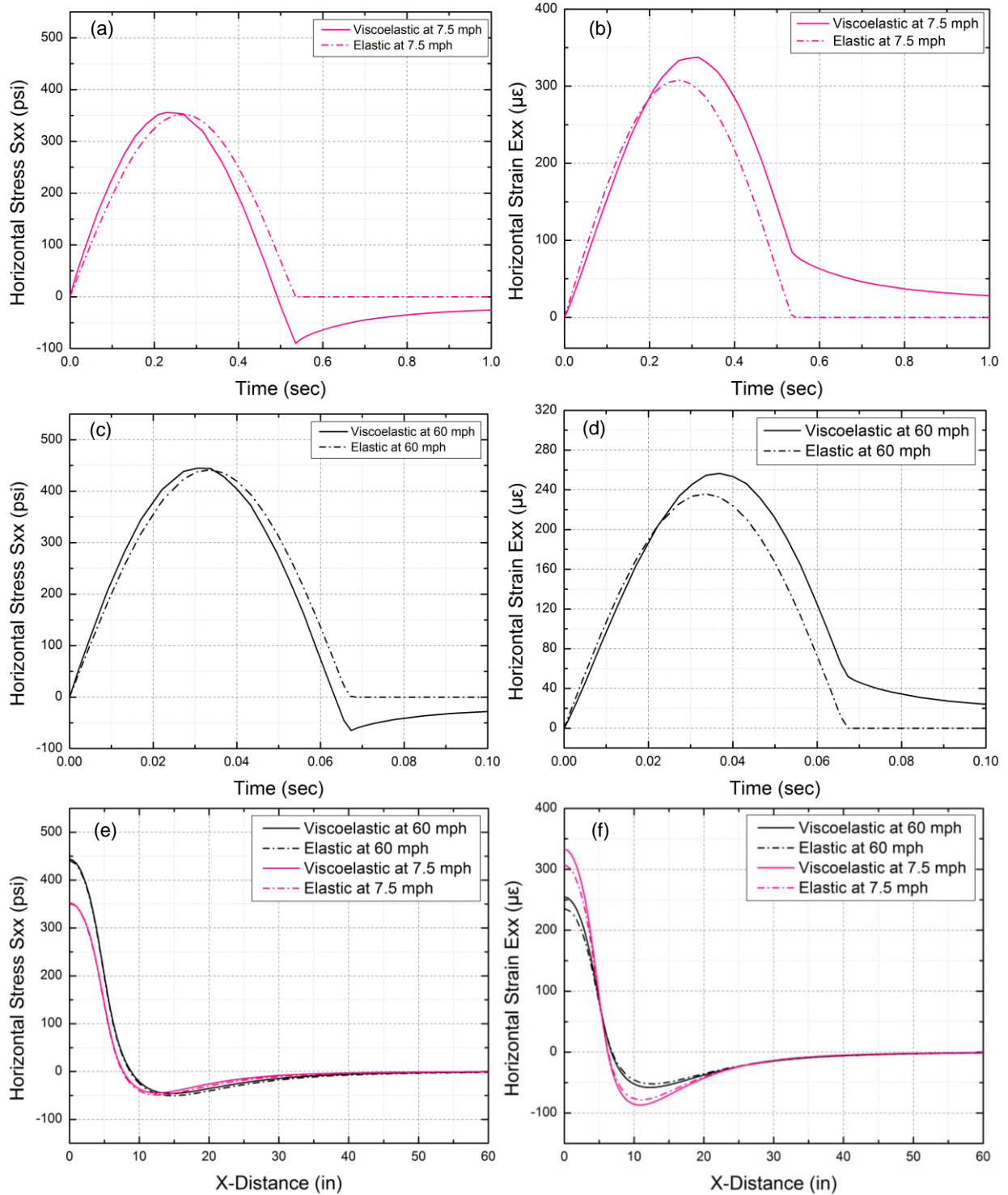


Figure 3-12 Time history of horizontal responses at L2: (a) horizontal stress (slow traffic); (b) horizontal strain (slow traffic); (c) horizontal stress (fast traffic); (d) horizontal strain (fast traffic); And, global distribution along the bottom of AC layer at the time of peak loading: (e) horizontal stress; (f) horizontal strain

Figures 3-10b and 3-10d show that the shear strain predicted by the viscoelastic model was significantly greater than that of the equivalent elastic model. Also, the viscoelastic response of the AC material caused a delay in peak strain and delayed strain recovery during unloading. The increase in vehicle speed resulted in lower shear strain and reduced difference between the viscoelastic and elastic solutions. As for the shear stress/strain distribution along the AC mid-depth at the loading peak time (Figures 3-10e and 3-10f), shear stress predicted by the viscoelastic model was slightly lower than that of the elastic model whereas shear strain was notably higher than that of the elastic model for both vehicle speeds. Note that the location of peak shear stress and strain remained the same (i.e., L1) regardless of AC material model and vehicle speed.

Vertical stress time history at L1 predicted by both viscoelastic and equivalent elastic models for slow and fast traffic is illustrated in Figures 3-11a and 3-11c, respectively. Overall, the viscoelastic and equivalent elastic predictions were almost identical during the entire loading and unloading cycle, except for a small delay in stress recovery due to AC viscoelasticity. Vehicle speed increase yielded slightly lower vertical stress. Figures 3-11b and 3-11d show the equivalent elastic vertical compressive strain was larger than the viscoelastic one for both speed values. A delay in viscoelastic strain peak and strain recovery was also found in the case of vertical strain. Also, the increase in vehicle speed resulted in significantly lower vertical strain and smaller difference between the viscoelastic and elastic solutions. At the time of peak loading, viscoelastic and equivalent elastic vertical stress along the AC mid-depth were identical (Figure 3-11e). However, vertical strain predicted by the viscoelastic model appeared to be smaller in the compressive zone but greater in the tensile zone than that of the elastic model for both vehicle speeds (Figure 3-11f).

Figures 3-12a and 3-12c plot horizontal stress time history at L2 predicted by both viscoelastic and equivalent elastic models for slow and fast traffic, respectively. Like shear stress response, AC viscoelasticity caused a reversal (change of sign) in horizontal stress during unloading. The viscoelastic predictions were slightly greater than the elastic ones during loading but became smaller than the elastic ones throughout the unloading portion. An increase in vehicle speed yielded higher horizontal stress and smaller difference between the viscoelastic and elastic

solutions. Of note, the equivalent elastic horizontal stress along the AC bottom at the peak loading time remarkably matched the viscoelastic prediction for both vehicle speeds (Figure 3-12e). Figures 3-12b and 3-12d show the viscoelastic horizontal strain tended to be greater than the elastic one. Again, viscoelasticity caused a delay in peak strain and strain recovery during unloading. Also, vehicle speed reduced horizontal strain as well as the difference between the viscoelastic and elastic solutions. Finally, viscoelastic horizontal strain along the AC bottom at peak loading time (Figure 3-12f) was greater than the equivalent elastic one in both tensile and compressive zones for both vehicle speeds.

It appeared that viscoelastic analysis of the axisymmetric representation of a pavement structure under a stationary half-sine load successfully captured the time-dependent response of the AC layer, including stress reversal (change in sign), delay in peak strain and delayed recovery during unloading. An increase in vehicle speed (or loading frequency) increased shear and horizontal stresses and reduced vertical stress and all three strain components, which is consistent with elastic analysis results using equivalent elastic moduli. Furthermore, the equivalent elastic analysis produced time records and global stress distributions (shear, horizontal and vertical) that were close to those of the viscoelastic model, although bigger discrepancy was observed in strain. Overall, both viscoelastic and equivalent elastic analyses identified a zone of high shear in combination with low vertical stress (confinement) where onset of debonding is likely. For axisymmetric models subjected to a stationary half-sine load, this zone can be pictured on a plan view as a ring-shaped area at the mid-depth of AC layer with a width of 1 to 2 in around the circular tire load.

3.2.3 Three-dimensional (viscoelastic vs. elastic) analysis under a moving load

In this section, the more sophisticated three-dimensional (3D) representation of a pavement structure shown in Figure 3-6 was subjected to a more realistic loading scenario in which a rectangular pressure load moved along a predefined path in the longitudinal direction (positive Z-axis). Based on the element size (1 in) along the moving path, the load (8 in long) was devised to move one inch per step. In total, 53 steps were required to complete one pass of the 60-in long moving distance. The total time and step time employed for one load pass of at the two selected vehicle speeds are summarized in Table 3-4.

In order to validate the 3D finite element model, stresses obtained with equivalent elastic moduli were first compared to predictions by the multilayer linear elastic program BISAR using the loading configuration depicted in Figure 3-13.

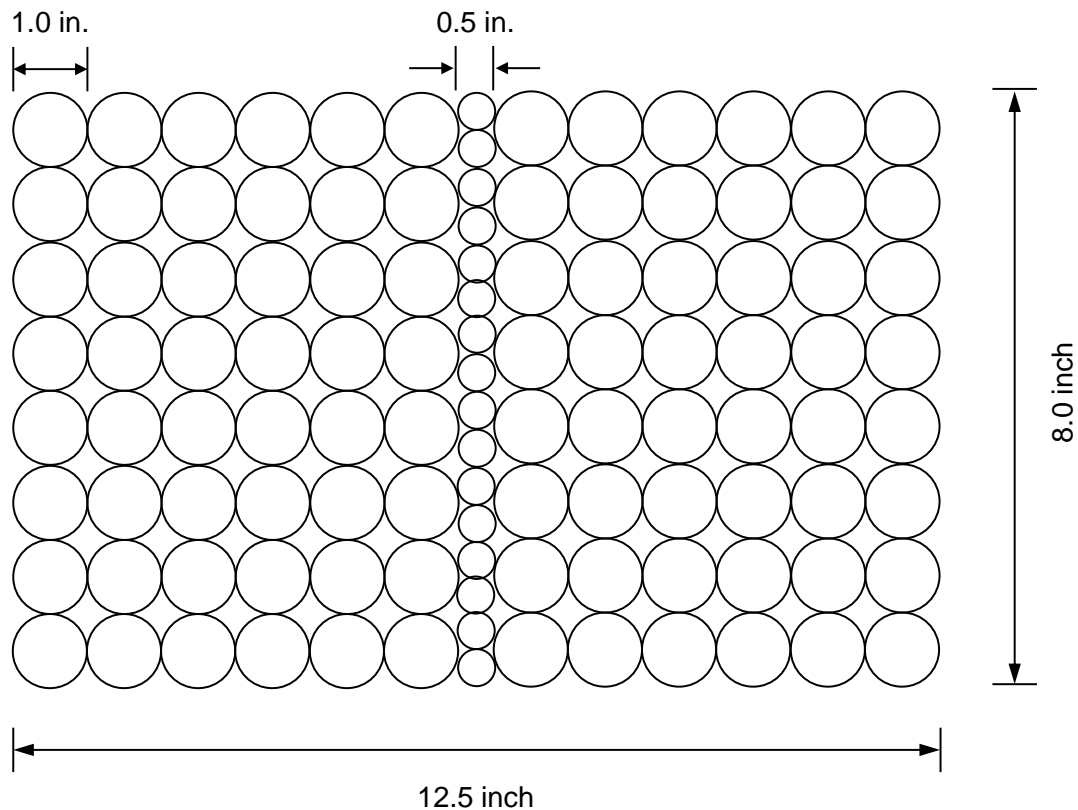


Figure 3-13 Representation of the rectangular loading area in BISAR

Figure 3-14 compares the stress distributions along the transverse and longitudinal cross-sections obtained from 3D FEA (continuous lines) with those produced by BISAR (scattered marks). FEA results including all three stress components (i.e., shear, horizontal and vertical components) in both transverse and longitudinal cross-sections matched BISAR results for both speeds, which demonstrated the accuracy of the developed 3D finite element model. As expected, a higher speed (a stiffer AC layer) led to higher shear stress and lower vertical compressive stress along the AC mid-depth and higher horizontal tensile stress at the AC bottom. However, stress peak locations remained the same. While peak shear and vertical stresses at the AC mid-depth were almost identical in both directions, peak tensile stress in the transverse cross-section was about 10% smaller than that in the longitudinal one (Figures 3-14e and 3-14f).

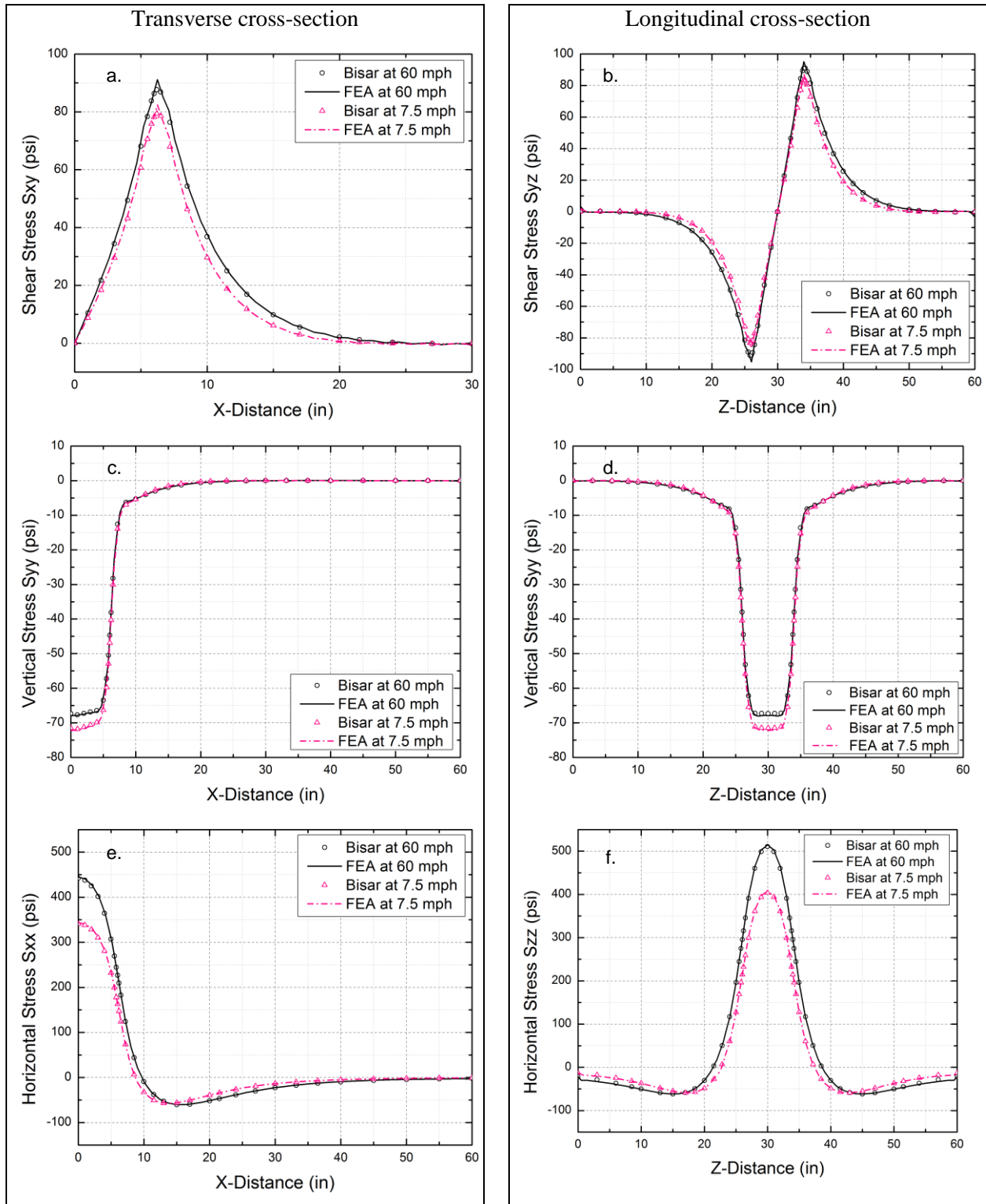


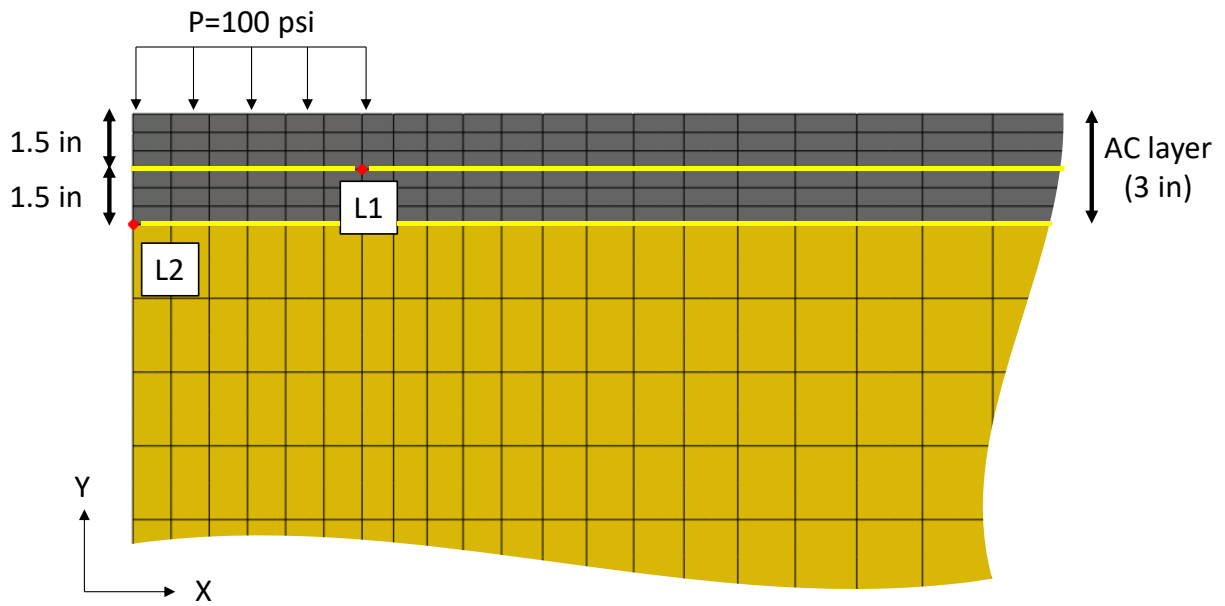
Figure 3-14 Validation results of 3D FE model along transverse and longitudinal cross-sections.

a-b. Shear stress at AC mid-depth; c-d. Vertical stress at AC mid-depth; e-f. Horizontal stress at AC bottom.

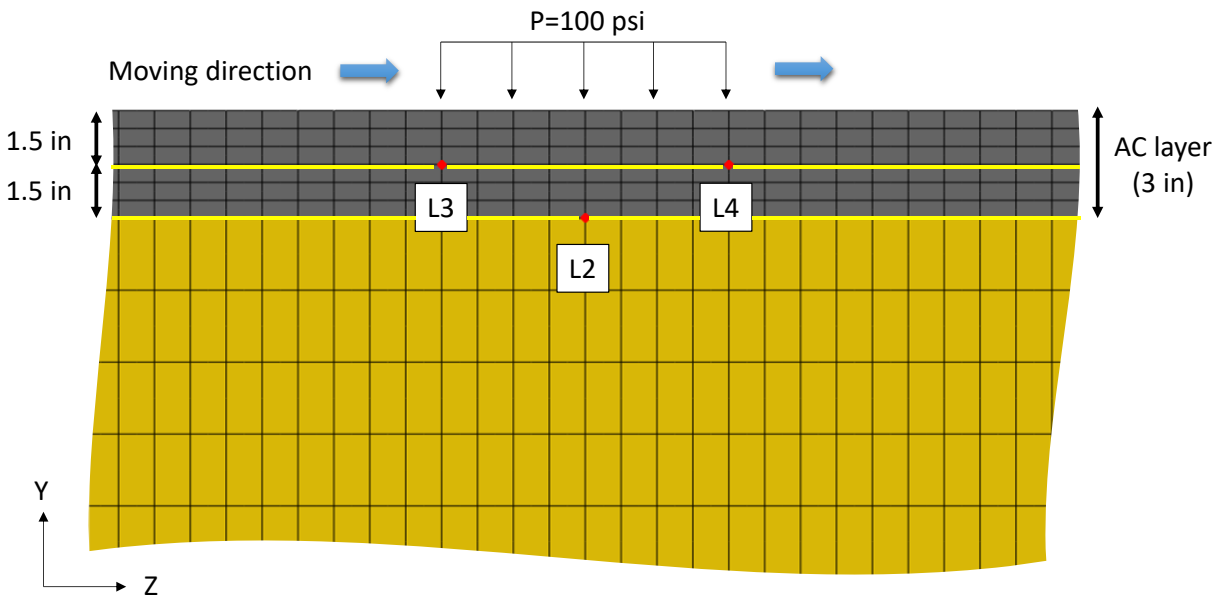
Results of 3D viscoelastic and equivalent elastic analysis at two different speeds are discussed in the following sub-sections. In addition to a moving load, results of the same pavement models subjected to a stationary half-sine load sitting in the middle of the moving path were also included to better understand the effect of loading condition on pavement response. The locations selected for analysis along the transverse and longitudinal cross-sections are illustrated in Figure 3-15. It is important to note that only stress responses were examined in determination of critical debonding locations (strain responses are included in Appendix A as supplemental information).

3.2.3.1 Transverse cross-section

Figure 3-16 compares viscoelastic and equivalent elastic shear stress responses along the transverse cross-section of a pavement structure subjected to a moving load and a stationary half-sine load. As can be seen in Figures 3-16a and 3-16c, equivalent elastic predictions at location L1 were similar to the viscoelastic ones during most of the moving period except as the load moved toward the end of the path (i.e., unloading period). The viscoelastic response of the AC material caused a reversal (change in sign) in shear stress during the unloading period. Also, shear stress increased when vehicle speed rose from 7.5 to 60 mph. The shear stress time history induced by a moving load exhibited an impulse shape with a notably shorter response time than the half-sine shape resulting from a stationary load (Figures 3-16b and 3-16d). Although it appeared that the shape of the shear stress time history due to a moving load could not be adequately simulated using a half-sine stationary load, the peak values were reasonably captured. The snapshot shown in Figure 3-16e when the moving load reached the center of the path shows that shear stress along the AC mid-depth predicted by the equivalent elastic model was identical to that of the viscoelastic model for both vehicle speeds. A similar shear stress distribution was observed when the pavement was subjected to a stationary half-sine load (Figure 3-16f). Furthermore, the location of peak shear stress (i.e., L1) remained independent of AC material model type and vehicle speed.



a.



b.

Figure 3-15 Locations selected for evaluation of 3D FE models: a. Transverse cross-section; b. Longitudinal cross-section.

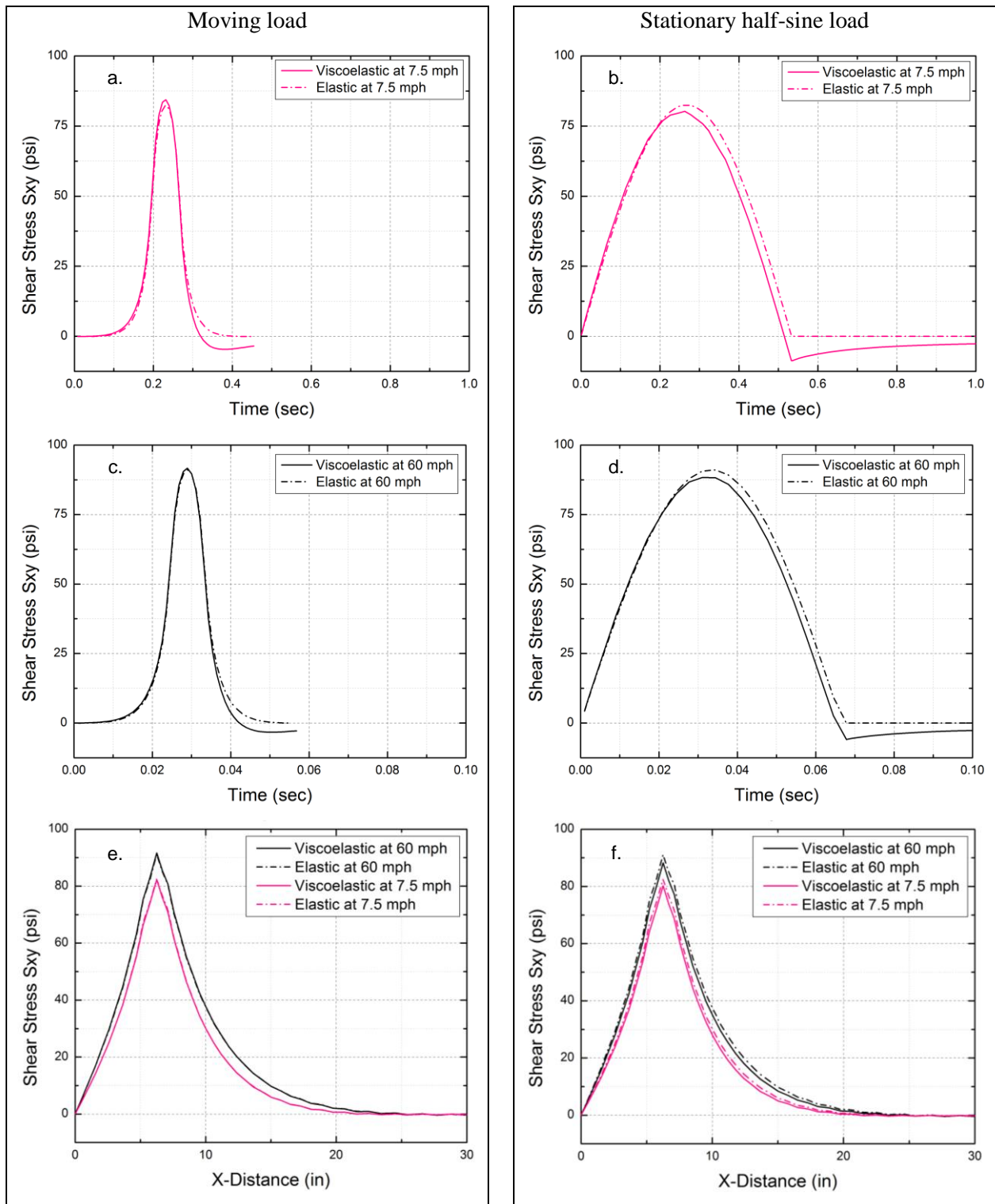


Figure 3-16 3D shear stress (transverse) evaluation for moving and stationary half-sine load: a-b.

Shear stress at L1 (slow traffic); c-d. Shear stress at L1 (fast traffic); e. Shear stress along AC mid-depth when moving load reached path center (slow/fast traffic); f.

Shear stress along AC mid-depth at peak loading time (slow/fast traffic).

Figures 3-17a and 3-17c show vertical stress time history at location L1 in the transverse cross-section predicted by both viscoelastic and equivalent elastic models for slow and fast moving load, respectively. Equivalent elastic predictions agreed very well with viscoelastic ones during the entire moving period, although AC viscoelasticity seemed to induce a slight reduction in peak stress value. An increase in vehicle speed reduced the magnitude of vertical stress. Again, the vertical stress time history induced by a moving load exhibited an impulse shape with a notably shorter response time than the half-sine shape resulting from a stationary load (Figures 3-17b and 3-17d). Thus, the shape of the vertical stress time history due to a moving load could not be adequately simulated using a half-sine stationary load; however, peak vertical stress value was effectively captured. Figures 3-17e and 3-17f show that vertical stress distribution along the AC mid-depth predicted by the equivalent elastic model matched that resulting from the viscoelastic model for both vehicle speeds and loading scenarios.

Horizontal stress time history at L2 in the transverse cross-section predicted by both viscoelastic and equivalent elastic models for slow and fast moving load are plotted in Figures 3-18a and 3-18c, respectively. Similar to the trend observed for shear stress, viscoelasticity caused reversal and delayed recovery in horizontal stress as the load moved toward the end of the path. The viscoelastic predictions were greater than the elastic ones during loading but became smaller during unloading. An increase in vehicle speed resulted in greater horizontal stress and smaller difference between the viscoelastic and elastic solutions. Furthermore, the impulse-shape horizontal stress time history when subjected to a moving load exhibited higher peak values (14% and 6% for slow and fast speed, respectively) than the half-sine shape time history of a stationary load (Figures 3-18b and 3-18d). In this case, it appeared that both shape and peak value of the horizontal stress time history due to a moving load could not be adequately simulated using a half-sine stationary load. Figure 3-18e shows the horizontal tensile stress along the AC bottom predicted by the viscoelastic model when the moving load reached the center of the path was greater than that of the elastic model (the difference between the viscoelastic and elastic solutions decreased with the increase in vehicle speed). However, equivalent elastic prediction of horizontal stress along the AC bottom matched that of the viscoelastic model when a stationary load was used (Figure 3-18f).

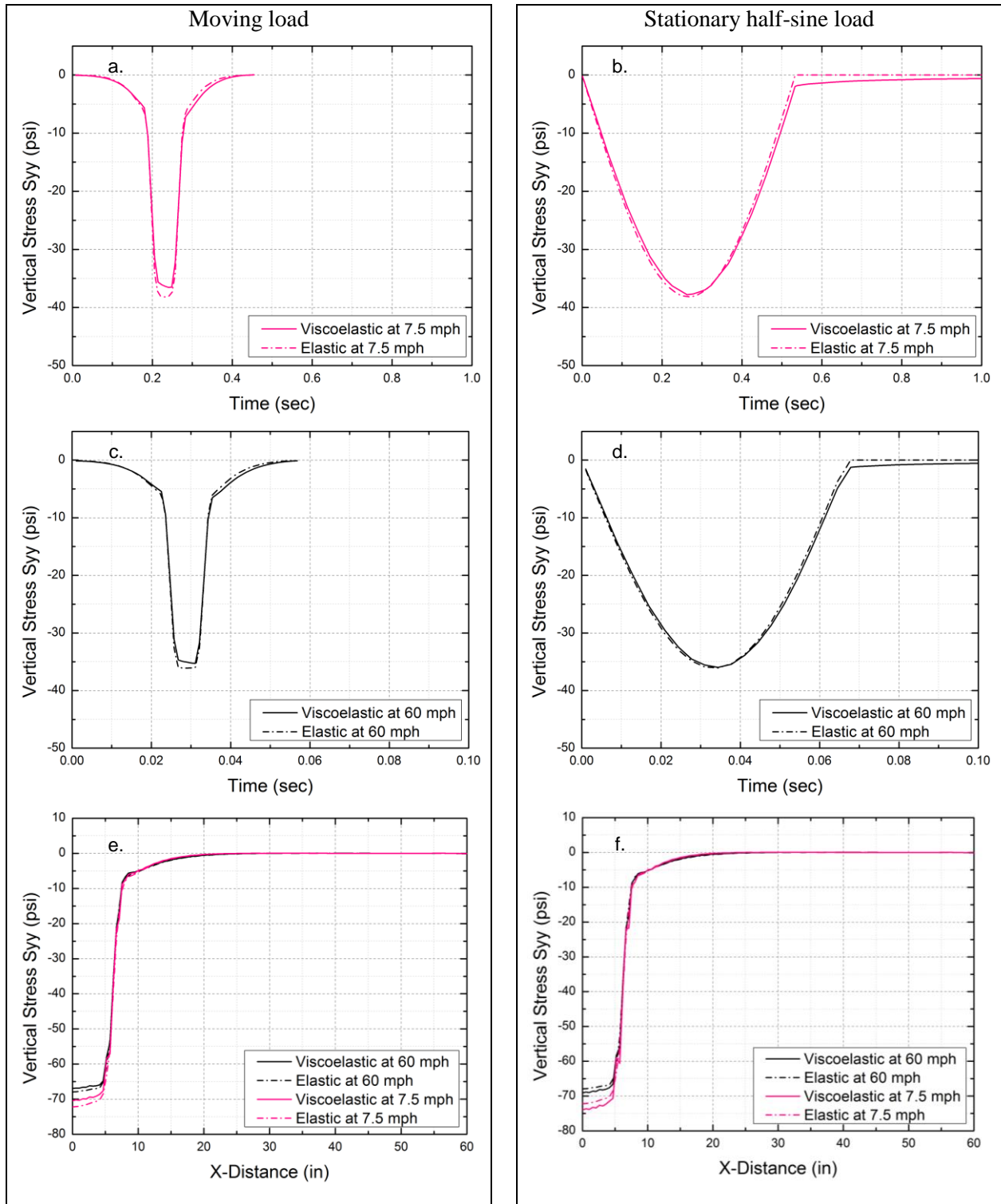


Figure 3-17 3D vertical stress (transverse) evaluation for moving and stationary half-sine load: a-

b. Vertical stress at L1 (slow traffic); c-d. Vertical stress at L1 (fast traffic); e.

Vertical stress along AC mid-depth when moving load reached path center (slow/fast

traffic); f. Vertical stress along AC mid-depth at peak loading time (slow/fast traffic).

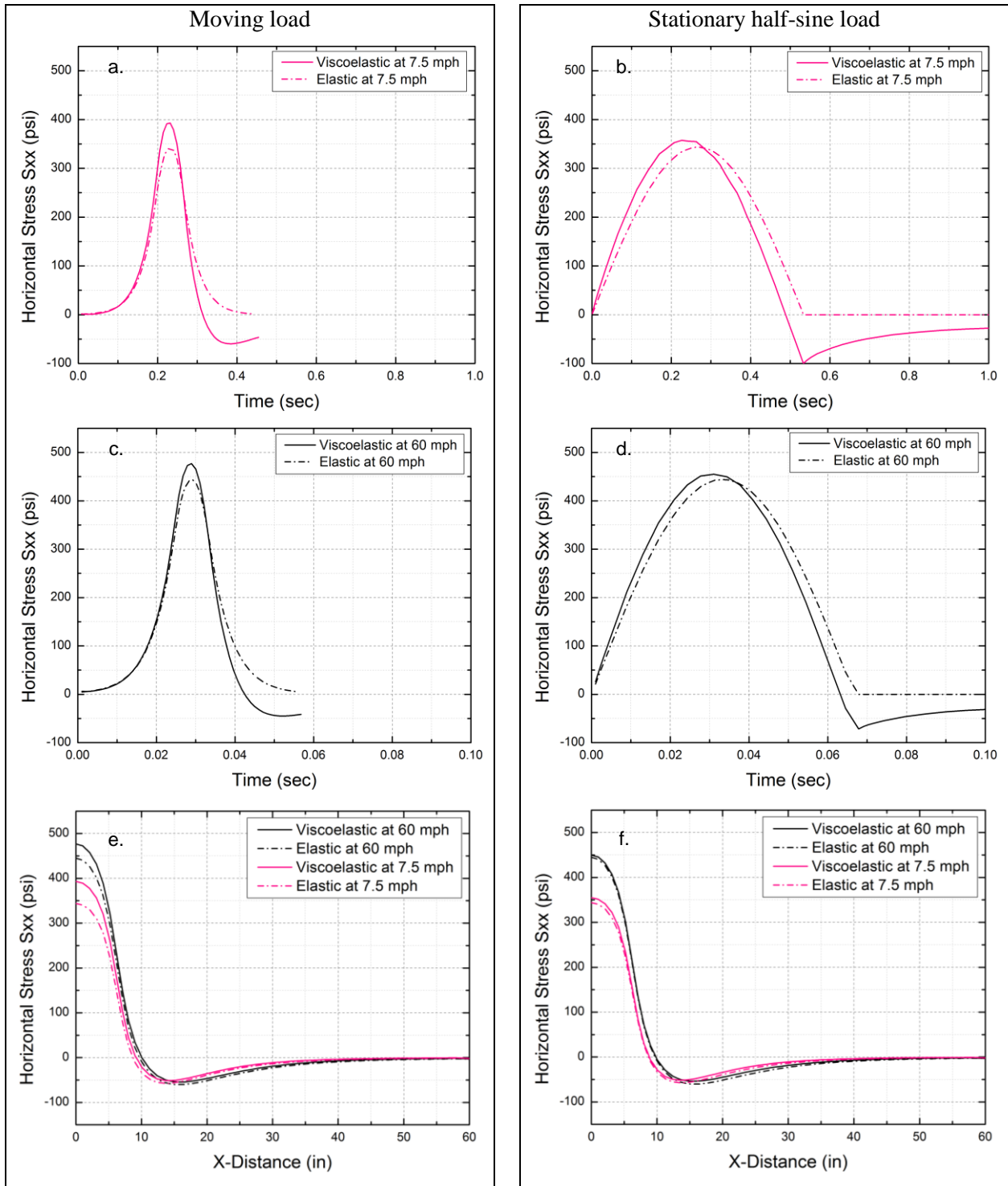


Figure 3-18 3D horizontal stress (transverse) evaluation for moving and stationary half-sine load:
 a-b. Horizontal stress at L2 (slow traffic); c-d. Horizontal stress at L2 (fast traffic); e.
 Horizontal stress along AC bottom when moving load reached path center (slow/fast
 traffic); f. Horizontal stress along AC bottom at peak loading time (slow/fast traffic).

3.2.3.2 Longitudinal cross-section

Figures 3-19a and 3-19c show horizontal stress time history at location L2 in the longitudinal cross-section predicted by both viscoelastic and equivalent elastic models for slow and fast moving load, respectively. In contrast to the trend observed at the same location in the transverse cross-section (only tension occurred during loading), L2 in the longitudinal cross-section experienced compression before being subjected to tension. Viscoelastic predictions tended to be slightly greater than the elastic ones in tension during loading and compression during unloading. AC viscoelasticity caused a delay in horizontal stress recovery as the load moved away from the center of the path (i.e., during unloading). Moreover, an increase in vehicle speed increased horizontal stress reduced the difference between the viscoelastic and elastic solutions. As previously found along the transverse cross-section, the impulse-shape horizontal stress time history due to a moving load differed from the half-sine shape resulting from a stationary load (Figures 3-19b and 3-19d). In addition, stress peak magnitude was 15% and 8% higher for the moving load case at slow and fast traffic speed, respectively. The horizontal stress distribution along the AC bottom when the moving load reached the center of the path (Figure 3-19e) shows greater values for the viscoelastic model than for the elastic one in both tension and compression. As expected, the horizontal stress distribution predicted by the equivalent elastic model was symmetric with respect to the loading center whereas the viscoelastic one was clearly not due to the loading history dependency exhibited by the viscoelastic AC layer. Furthermore, note that asymmetry was not found for the stationary loading scenario (Figure 3-19f).

Shear stress time history at L3 in the longitudinal cross-section predicted by both viscoelastic and equivalent elastic models for slow and fast moving load is depicted in Figures 3-20a and 3-20c, respectively. As opposed to the single stress impulse observed at L1 in the transverse cross-section (Figures 3-16a and 3-16c), shear stress at L3 exhibited two impulses in reversed directions during one load pass. Equivalent elastic predictions matched the viscoelastic ones before the second peak and became slightly smaller afterward. The viscoelastic response of the AC material caused a slightly higher stress peak in the second impulse, shear stress reversal and a delayed recovery as the load moved toward the end of the path. As expected, an increase in vehicle speed resulted in higher shear stress.

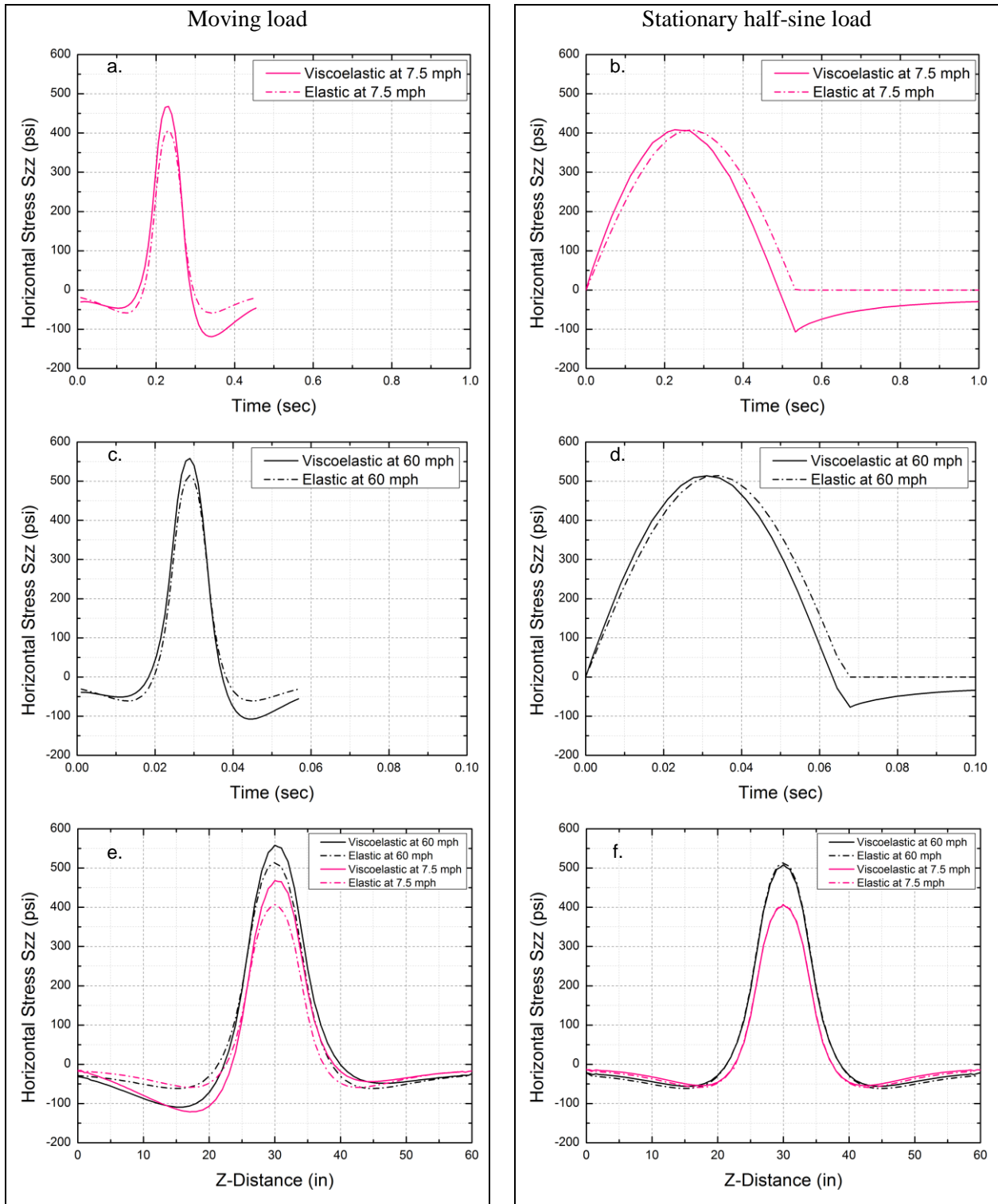


Figure 3-19 3D horizontal stress (longitudinal) evaluation for moving and stationary half-sine load: a-b. Horizontal stress at L2 (slow traffic); c-d. Horizontal stress at L2 (fast traffic); e. Horizontal stress along AC bottom when moving load reached path center (slow/fast); f. Horizontal stress along AC bottom at peak loading time (slow/fast).

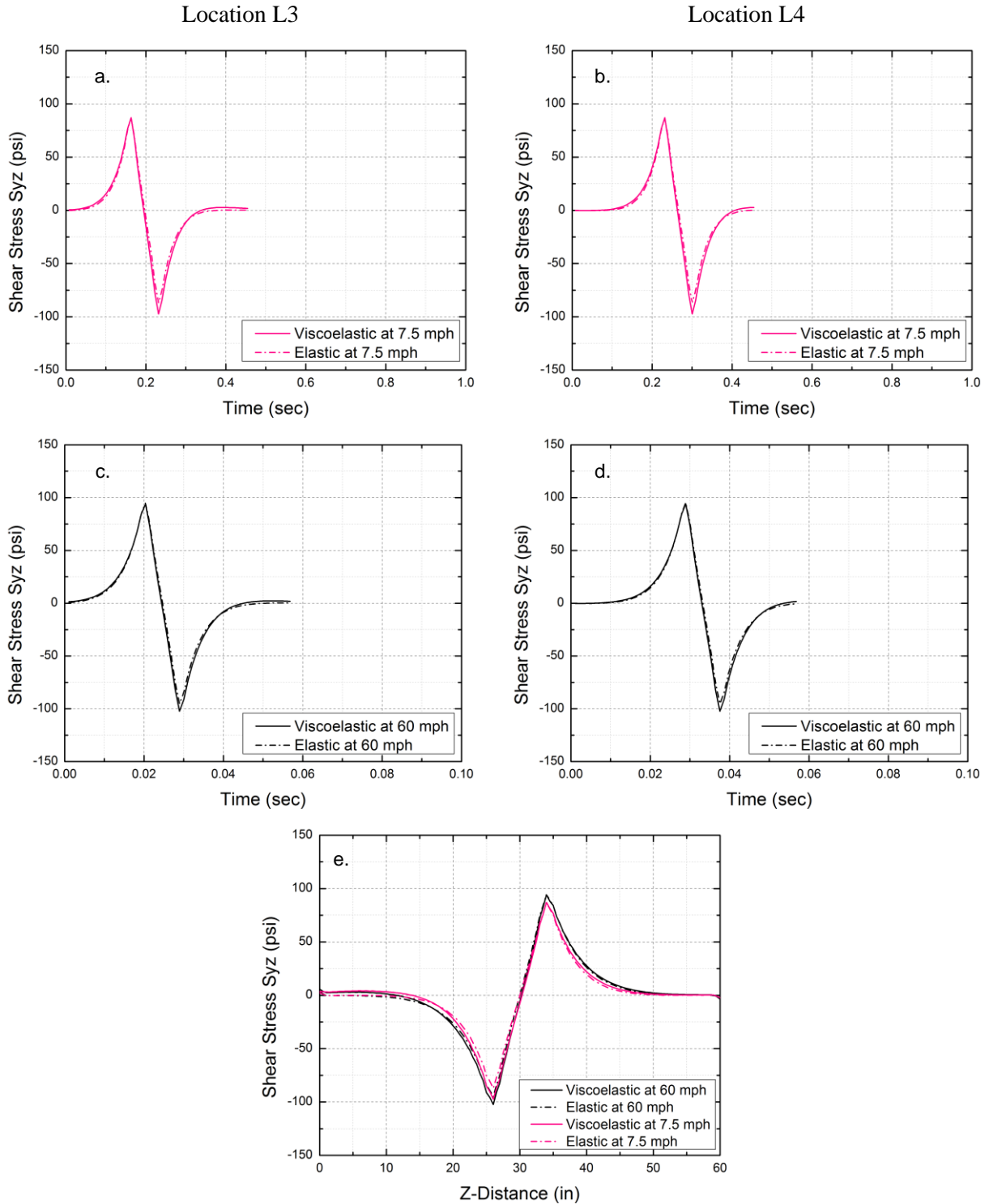


Figure 3-20 3D shear stress (longitudinal) evaluation for moving load: a. L3 (slow traffic); b. L4 (slow traffic); c. L3 (fast traffic); d. L4 (fast traffic); e. Shear stress along AC mid-depth when moving load reached path center (slow/fast traffic).

Shear stress time records at L4 for slow and fast moving load are shown in Figures 3-20b and 3-20d, respectively. As expected, L4 experienced two shear stress impulses occurring sequentially after those at L3. When the load reached the center of the path, both L3 and L4 were subjected to the peak value of two separate shear impulses in reverse directions (Figure 3-20e). In other words, the second impulse at L3 occurred at the same time as the first impulse at L4.

When shear stress time history induced by the moving load at L3 and L4 (Figure 3-20) was compared to that resulting from a stationary half-sine load (Figure 3-21), clear differences were found. Whereas the former exhibited a double impulse shape, the latter showed a half-sine shape. Also, shear stress impulses were induced sequentially due to the movement of the load, while the stress induced at L3 and L4 by the stationary load occurred simultaneously. Furthermore, the shear stress distribution along the AC mid-depth induced by the stationary load was symmetric (Figure 3-21e) whereas that of a moving load was not.

Figures 3-22a and 3-22c show vertical stress time history at L3 in the longitudinal cross-section predicted by both viscoelastic and equivalent elastic models for slow and fast moving load, respectively. While peak vertical stress did not reach 40 psi at L1 (transverse cross-section), peak vertical stress at L3 exceeded 70 psi. Overall, equivalent elastic and viscoelastic predictions were almost identical during the entire moving period. An increase in vehicle speed slightly reduced vertical stress. As shown in Figures 3-22b and 3-22d, L4 experienced one vertical stress impulse after that at L3. When the moving load reached the center of the path, both L3 and L4 were subjected to a vertical stress of about 70 psi (Figure 3-22e). Note that at that moment the vertical stress at L3 was decreasing after reaching the peak, while that at L4 was approaching the peak.

As compared to the vertical stress time history caused by a moving load, vertical stress resulting from a half-sine stationary load (Figure 3-23) exhibited lower peak value and longer response time. In addition, peak stress occurred simultaneously at L3 and L4 when the pavement was subjected to a stationary load whereas there was a small delay when a moving load was used. Finally, vertical stress distribution along the AC mid-depth was asymmetric in the case of a moving load and symmetric for a stationary load (Figure 3-23e).

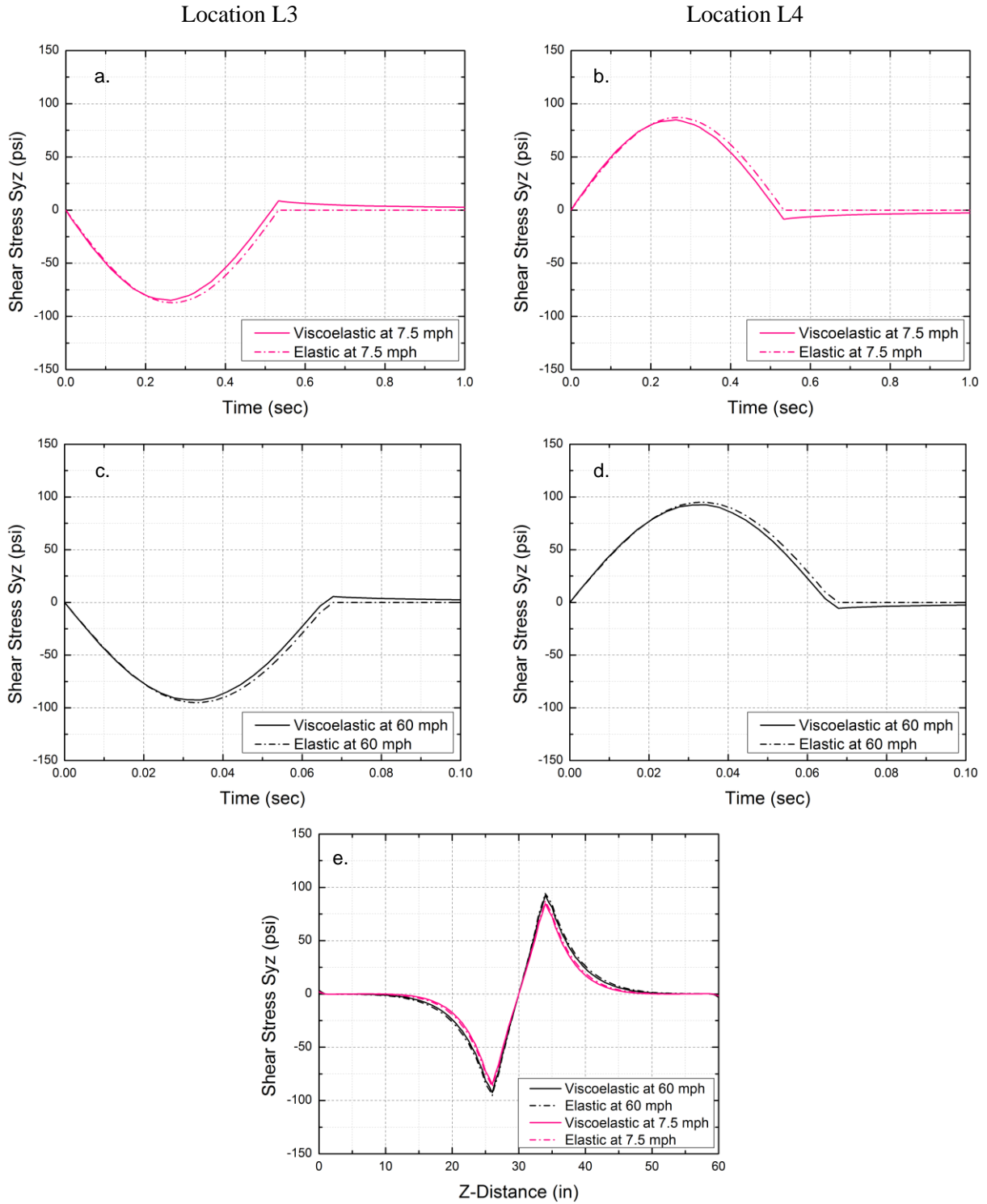


Figure 3-21 3D shear stress (longitudinal) evaluation for a stationary half-sine load: a. L3 (slow traffic); b. L4 (slow traffic); c. L3 (fast traffic); d. L4 (fast traffic); e. Shear stress along AC mid-depth at peak loading time (slow/fast traffic).

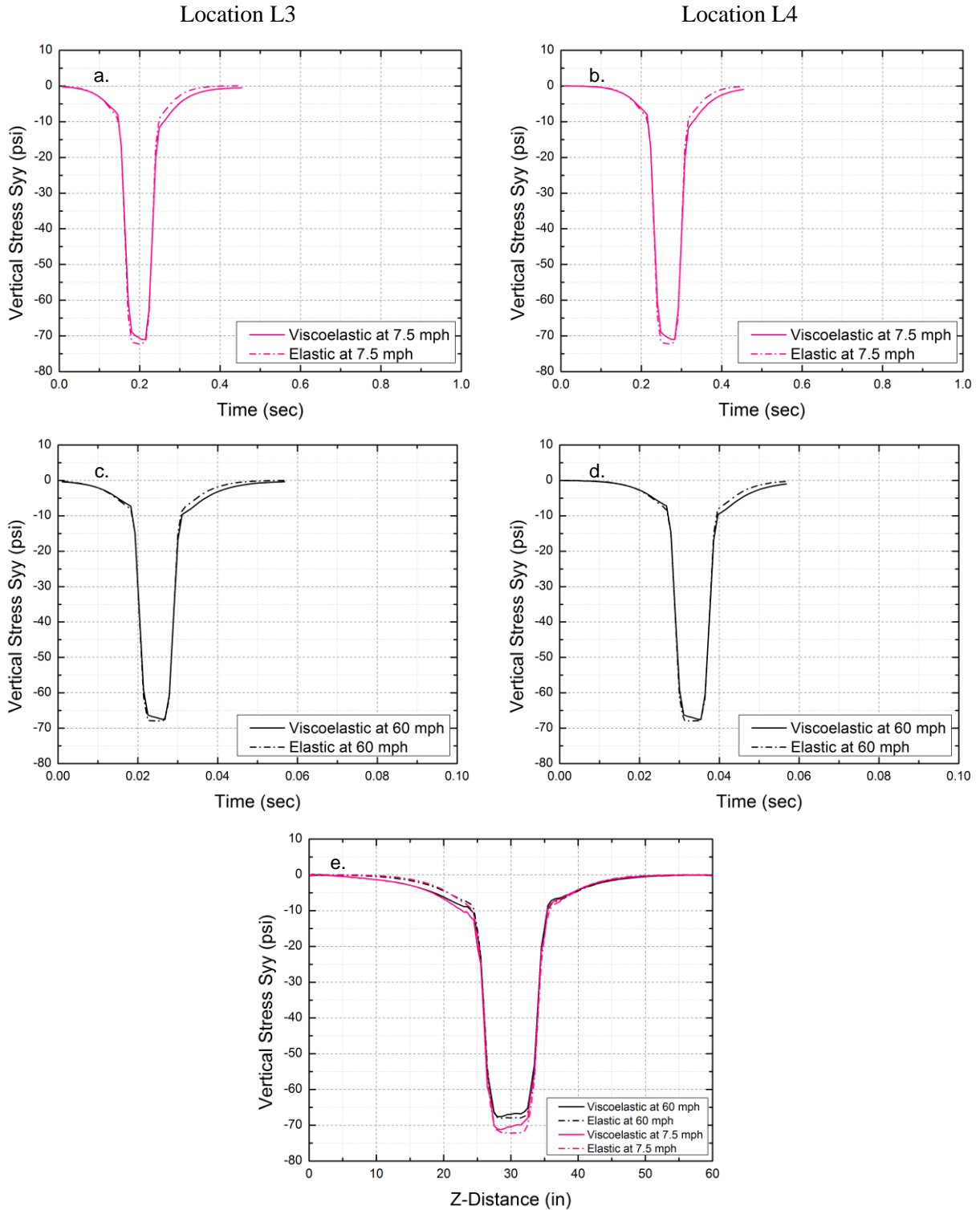


Figure 3-22 3D vertical stress (longitudinal) evaluation for a moving load: a. L3 (slow traffic); b. L4 (slow traffic); c. L3 (fast traffic); d. L4 (fast traffic); e. Vertical stress along AC mid-depth when moving load reached path center (slow/fast traffic).

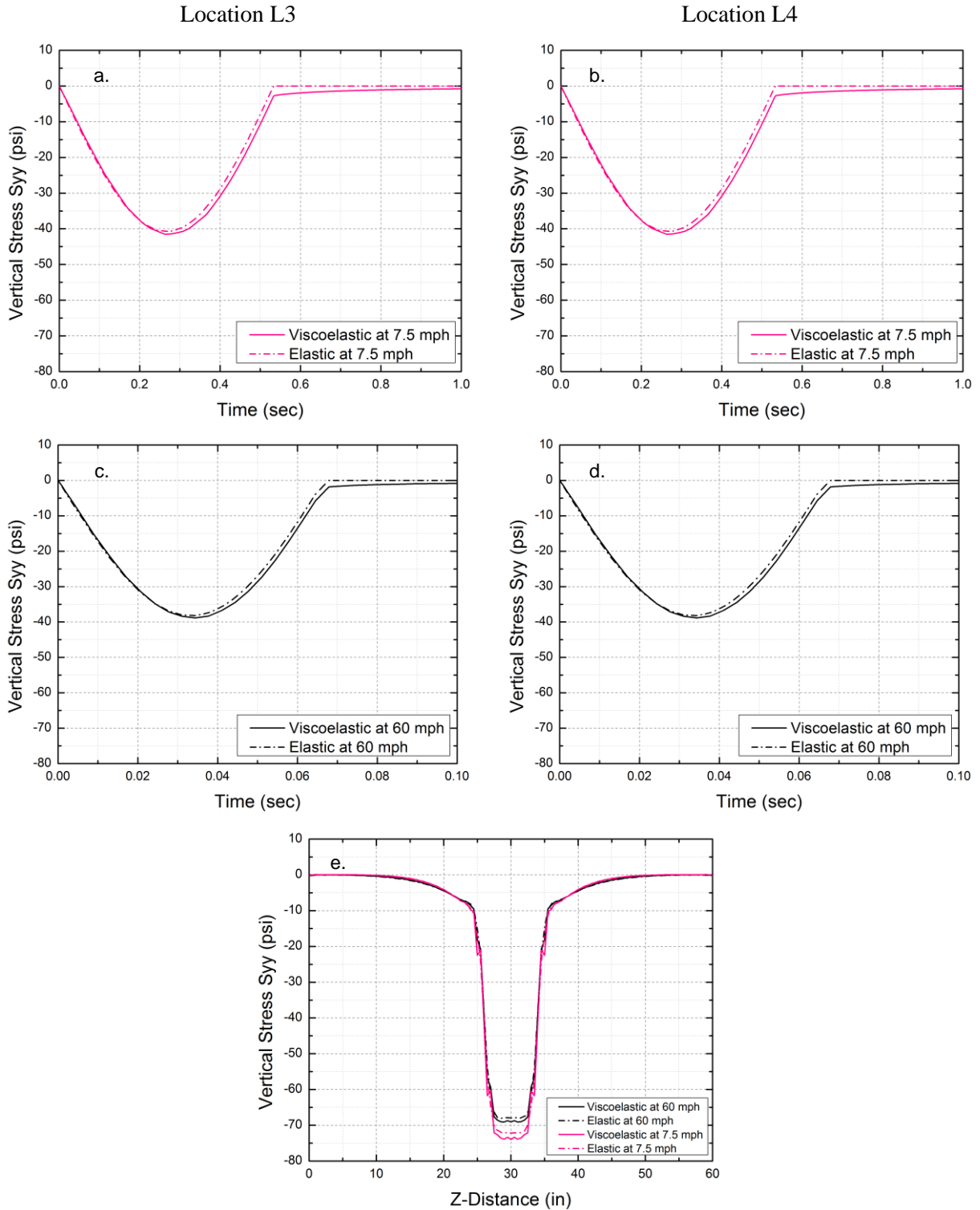


Figure 3-23 3D vertical stress (longitudinal) evaluation for a stationary half-sine load: a. L3 (slow traffic); b. L4 (slow traffic); c. L3 (fast traffic); d. L4 (fast traffic); e. Vertical stress along AC mid-depth at peak loading time (slow/fast traffic).

3.2.3.3 Preliminary analysis of critical stress states

A plan view of maximum shear stress and vertical compressive stress (confinement) contours at the AC mid-depth of a pavement structure subjected to a load moving at low speed is presented in Figure 3-24. Because of the presence of in-plane shear stresses along two perpendicular directions, maximum shear stress on a horizontal plane (XZ) was defined as follows:

$$S_{max} = \sqrt{S_{xy}^2 + S_{zy}^2} \quad (3.10)$$

where S_{xy} and S_{zy} are shear stresses in the transverse and longitudinal directions, respectively. Stress predictions obtained with a viscoelastic model (Figures 3-24b and 3-24d) show a 1-2 in wide U-shaped zone of high shear stress (70 to 100 psi) coupled with low confinement (20 to 40 psi) surrounding the rectangular tire loading area. A further examination of the stress distribution in the zone showed the stress state behind the tire was more critical than that in front of the wheel. Note that AC viscoelasticity resulted in an asymmetric stress distribution whereas the stress distribution obtained with an equivalent elastic model (Figures 3-24c and 3-24e) was symmetric. Similar results were obtained for the fast-moving load scenario.

Overall, results from viscoelastic and equivalent elastic analyses indicated the presence of a critical zone around the tire defined by high shear stress in combination with low confinement where onset of debonding is likely. Under the moving loading condition, this critical zone can potentially cause continuous debonding along the wheelpath (longitudinal direction).

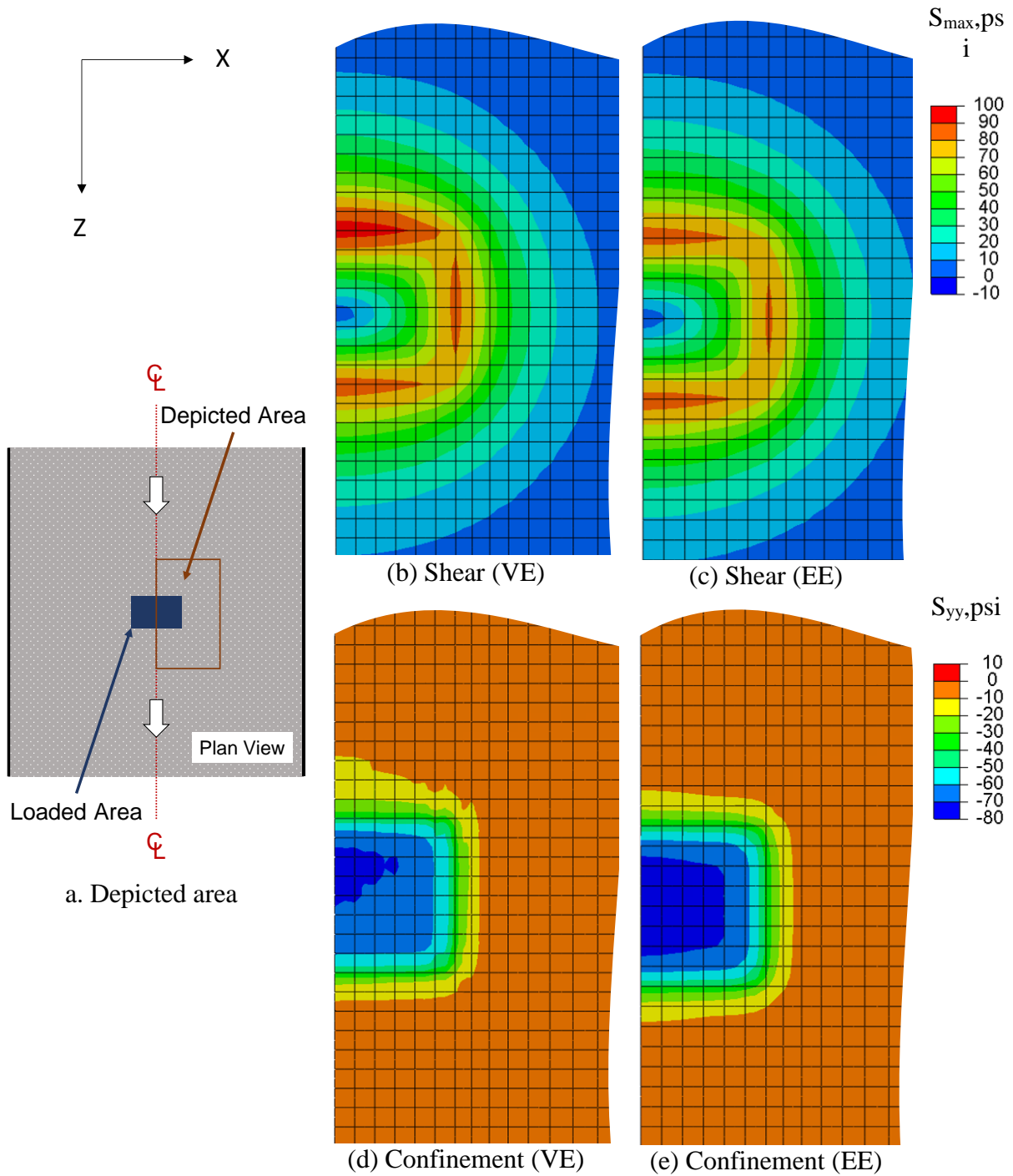


Figure 3-24 Stress contours at AC mid-depth for low moving speed (plan view): a. Plan view of depicted area; b. Maximum shear stress (viscoelastic); c. Maximum shear stress (equivalent elastic); d. Vertical compressive stress (viscoelastic); e. Vertical compressive stress (equivalent elastic).

3.3 Concluding remarks

Results from a comprehensive modeling effort of a pavement structure under varying modeling conditions (axisymmetric and three-dimensional; viscoelastic and equivalent elastic AC layer) and loading modes (stationary and moving) yielded the following findings:

- A stationary half-sine load yielded global distributions similar to those of a moving load in the transverse cross-section, but was unable to capture the impulse shape in time records of all stress components. The use of a stationary load with a different waveform (e.g., haversine) may help better simulate the response of a moving load in the transverse cross-section. However, the stationary load was not able to simulate stress time records of a moving load in the longitudinal cross-section, including double reversal in horizontal stress, double impulse in shear stress, high peak value in vertical stress, and sequential stress change between different points along the path. Also, the asymmetry in stress distribution exhibited by a moving load could not be achieved with a stationary load.
- Viscoelastic analysis of the 3D representation of a pavement structure subjected to a moving load successfully captured the time-dependent response of the AC layer, including stress reversal and delay in stress recovery for all stress components (shear, horizontal, vertical stresses) in both transverse and longitudinal cross-sections as well as asymmetric global distributions of all stress components in the longitudinal cross-section.
- An increase in vehicle speed (or loading frequency) resulted in an increase in shear and horizontal stresses and a reduction in vertical stress, which is consistent with the results from elastic analysis using equivalent elastic moduli.
- Shear and vertical stress time history in the transverse and longitudinal cross-sections predicted by the equivalent elastic model agreed with that of the viscoelastic model. However, peak values of bending stress were off by 8 to 15% depending on vehicle speed.
- Global distribution of all stress components predicted by the equivalent elastic model were symmetric with respect to the loading center. This trend was consistent with viscoelastic results in the transverse cross-section, but different from the asymmetric feature exhibited in the longitudinal cross-section.

- Results from 3D viscoelastic and equivalent elastic analyses indicated that interface debonding, which is associated with zones of high shear and low confinement, can potentially occur along the wheelpath.

Since interface debonding is associated with stress states of high shear combined with low confinement and shear and vertical stress peaks predicted by equivalent elastic analysis were consistent with those from viscoelastic models, it was concluded that equivalent elastic analysis seemed to be suitable to accurately determine the potential location and extent of localized debonding. Therefore, an elastic AC layer will be employed for the calculations required in the next chapters of this project. Furthermore, elastic materials are independent of loading history so a static loading condition is envisioned to be sufficient to examine the stress peak response of various pavement structures.

CHAPTER 4 POTENTIAL LOCATION AND EXTENT OF DEBONDING

4.1 Effect of pavement structure

This section examines the effect of pavement structure characteristics on the potential location and extent of debonding between asphalt layers. Factors considered included asphalt concrete (AC) layer thickness, AC stiffness and base stiffness. Two AC thicknesses were evaluated: 4 in, which represents a thin asphalt layer; and 8 in, which can be found on interstate pavements and major highways with a relatively long service life and rehabilitation history. Regarding AC stiffness, the previous chapter showed a viscoelastic analysis is not necessary and the use of an equivalent elastic approach is suitable for the objectives of this project. A broad range of AC elastic moduli was covered from 200,000 psi, which represents an asphalt layer on a hot summer day, to 800,000 psi, which is more illustrative of a late Fall/early Spring evening. It should be noted that these two extreme AC stiffness values can also be interpreted in terms of the response of an asphalt layer to a tire load moving at a low speed and intermediate speed, respectively. Finally, two stiffness values were considered for a 12-in granular base: 25,000 and 40,000 psi.

Figure 4-1 summarizes the various pavement structure characteristics evaluated in this section. Note that pavement sections were labeled according to their corresponding stiffness ratio (SR), i.e., the ratio of AC stiffness to base stiffness. Also, an additional section with a stiffness gradient through the depth of the AC layer was included to study the effect of field oxidative aging.

The multilayer linear elastic program BISAR was employed to conduct an axisymmetric analysis and obtain responses at selected locations. All materials were considered linear elastic and were defined by their elastic modulus and Poisson's ratio. Subgrade stiffness was fixed at 15,000 psi. Poisson's ratio values of 0.35, 0.40 and 0.45 were assumed for AC, base and subgrade layers, respectively. An 18-kip single axle load with a uniform tire pressure of 100 psi was selected, which resulted in a circular tire imprint with a radius of 5.35 in. The analysis focused on locating critical stress states, defined by high shear stress combined with low confinement levels, where the onset of debonding is likely. Thus, the AC layer was assumed fully bonded at this stage.

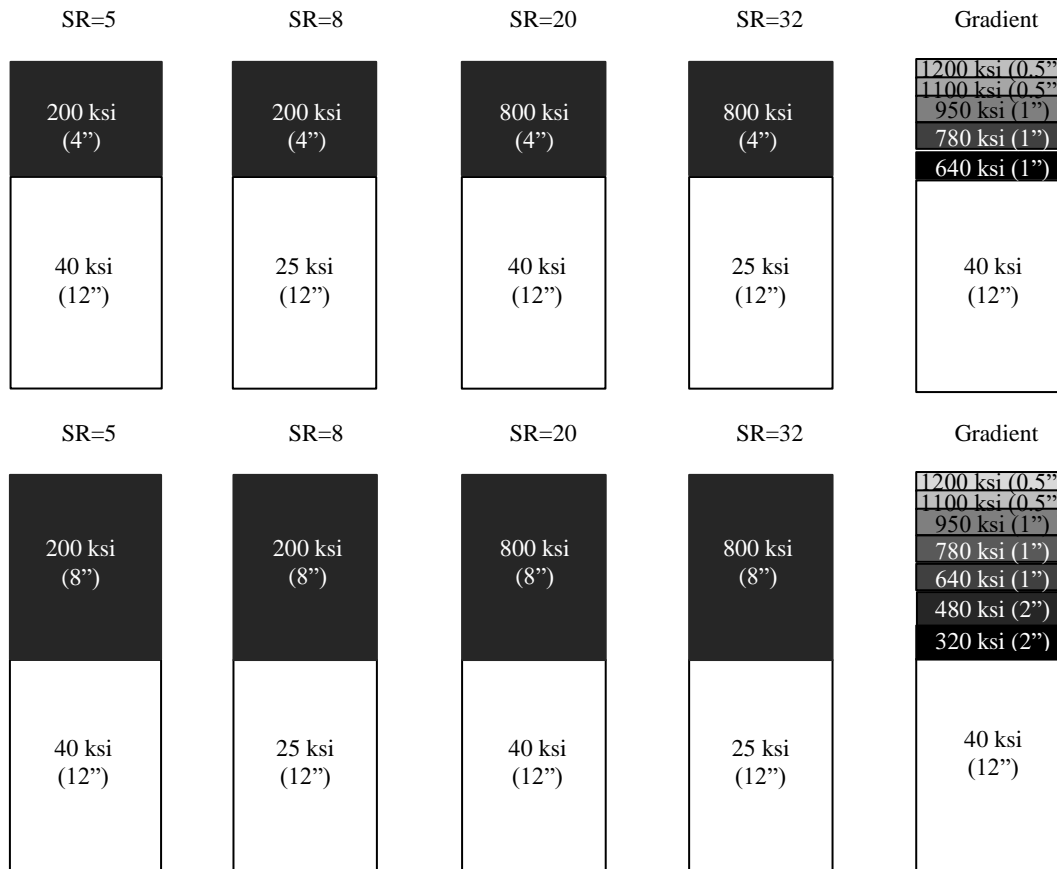
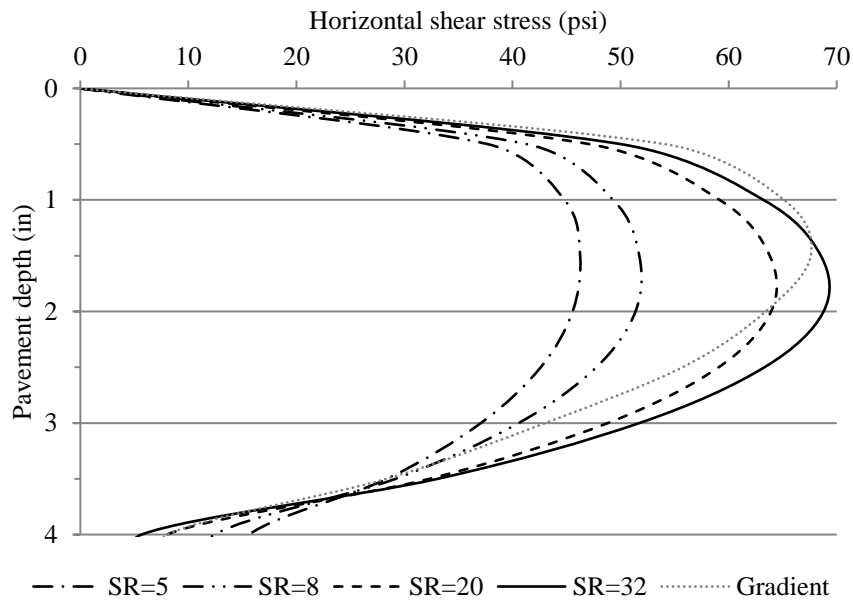
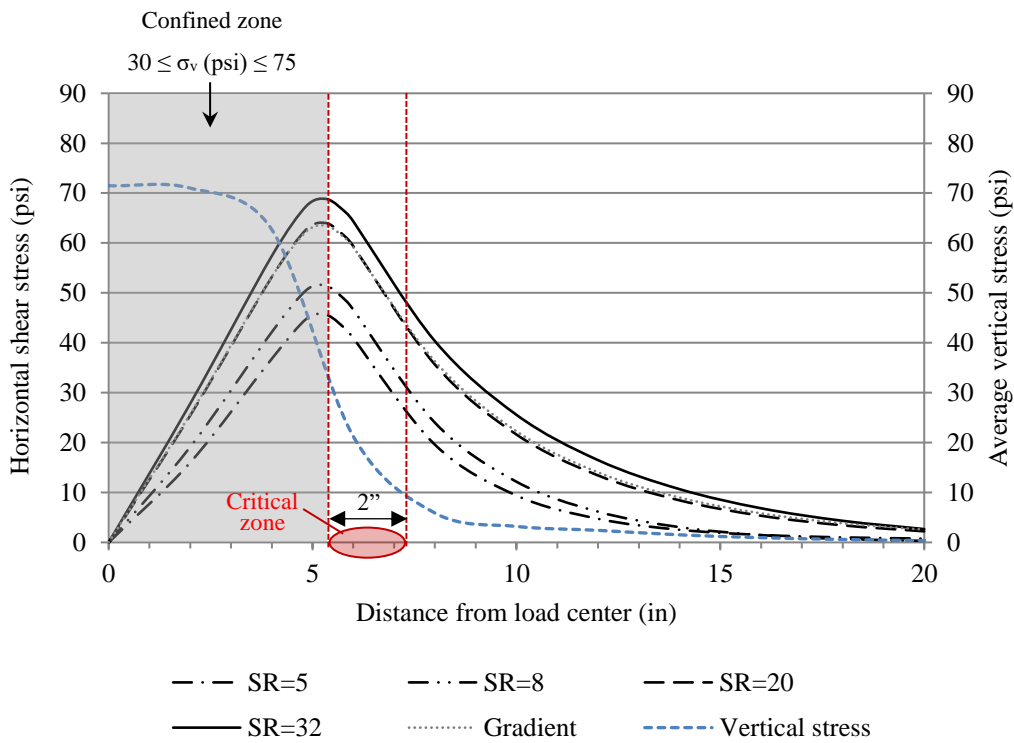


Figure 4-1 Pavement sections selected for evaluation of structural characteristics (layer thickness shown in brackets).

Stress distribution results for the pavement structures with a 4-in thick AC layer are shown in Figure 4-2. Figure 4-2a illustrates the horizontal shear stress through the depth of the AC layer under the edge of the tire (i.e., at a radial distance of 5.35 in). High shear stress was observed for a broad range of depths around the center of the layer (1 to 3 in), with a maximum at a depth slightly less than 2 in. This agreed with the depth at which debonding was observed in the field by Muench and Moomaw (2008) and Roque et al. (2011). Maximum shear stress occurred for SR=32. This was expected as shear stress is a function of bending, which increases with SR. Figure 4-2b shows the horizontal shear stress distribution along a horizontal plane located 2 in below the surface. The maximum shear stress was under the edge of the tire for all cases. Figure 4-2b also illustrates the existence of an area of high confinement under the tire (confined zone), but confinement drastically decreased below 30 psi outside the edge of the tire.

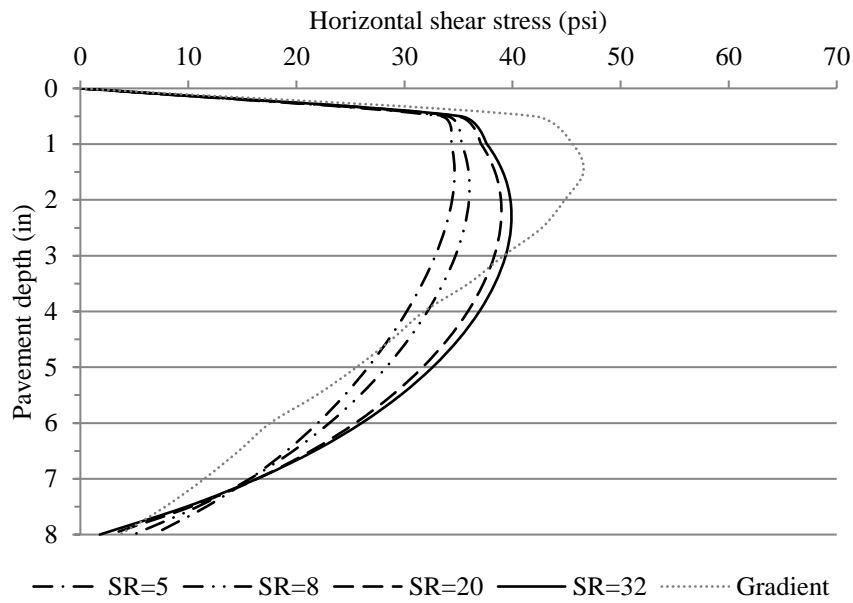


a. Horizontal shear stress through the depth of the asphalt layer under the tire edge

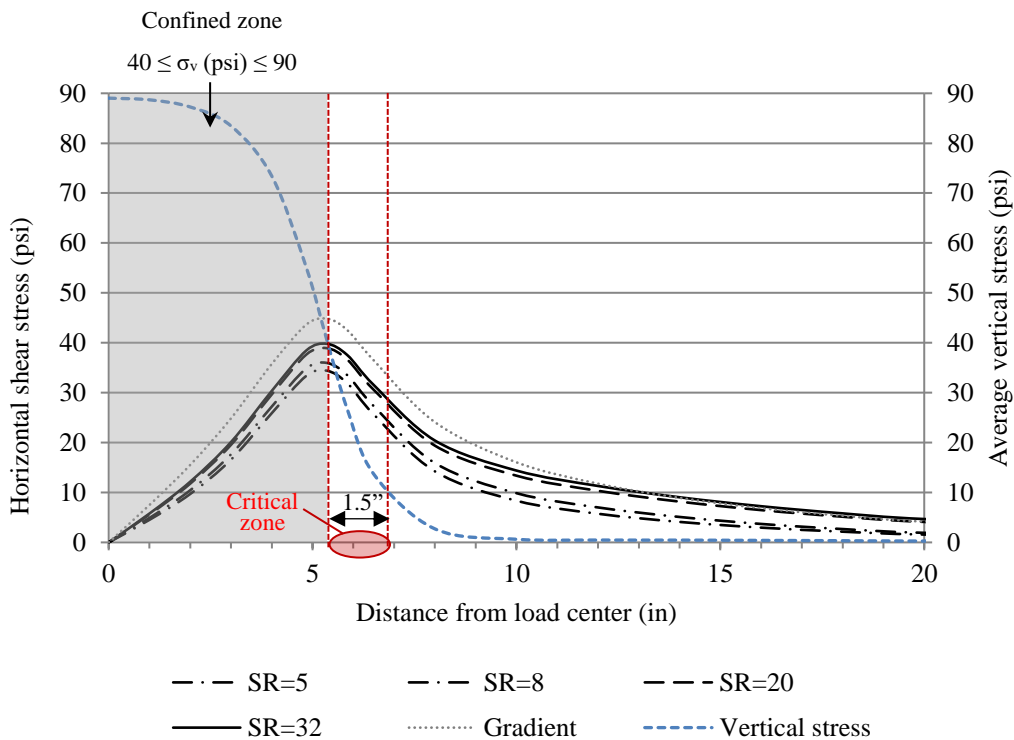


b. Horizontal shear stress and average vertical stress at a depth of 2 in

Figure 4-2 Shear stress distribution of pavement structures with a 4-in AC layer.



a. Horizontal shear stress through the depth of the asphalt layer under the tire edge



b. Horizontal shear stress and average vertical stress at a depth of 2 in

Figure 4-3 Shear stress distribution of pavement structures with an 8-in AC layer.

Figure 4-3 outlines the shear stress distribution for the pavement structures with an 8-in thick AC layer. Horizontal shear stress magnitude through the depth of the AC layer under the edge of the tire was lower than in the case of a 4-in AC layer. This was expected given the reduction in bending resulting from a thicker AC layer. Furthermore, Figure 4-3a shows the existence of an area of high shear stress between 1 and 3 in from the surface, with a maximum at a depth of about 2 in, which agreed with the results obtained for a 4-in AC layer. Thus, it seemed that horizontal shear stress tended to peak below the edge of the tire at a depth of 2 in regardless of AC thickness for the wide range of pavement structures analyzed. Figure 4-3b plots the horizontal shear stress distribution and average vertical stress along this critical depth of 2 in. Like the 4-in AC layer case, an area of high confinement was found under the tire (confined zone). However, confinement dropped outside the edge of the tire where high shear stresses still exist.

Results in Figures 4-2 and 4-3 identified the existence of a critical zone of high shear stress (>25 psi) coupled with low confinement at a depth of 2 in and extending to 2 in from the edge of the tire. It is believed that the repetition of these critical stress state conditions can cause localized debonding of an interface located about 2-in deep in the pavement structure.

4.2 Effect of interface conditions

The literature review presented in Chapter 2 showed that one of the most widely-used models to simulate interface bonding conditions between asphalt layers is that derived by Uzan (1976). In Uzan's model (Figure 4-4), a linear relationship between shear stress (τ) and the relative displacement between the two surfaces in contact at the interface (Δu) is defined by a parameter called interface reaction modulus (K). This model is used to simulate the entire interface as either bonded, debonded or partially bonded, i.e., to simulate smeared bonding conditions. The interface reaction modulus can account for different levels of interface compliance associated with the presence of a bonding agent between two asphalt layers. For example, harder bonding agents applied at a low rate will tend to be less compliant (higher K value) than softer bonding agents at a high application rate (lower K value).

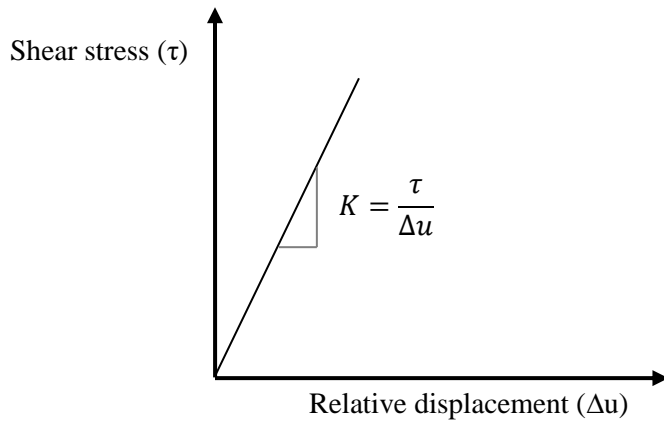


Figure 4-4 Interface model for evaluation of smeared bonding conditions proposed by Uzan (1976).

Field experiences discussed by Uzan et al. (1978) suggested the state of adhesion in real conditions is an intermediate one between full adhesion and zero adhesion, depending on material properties and construction quality. In other words, there is some inherent compliance associated with the interface. As a reference, Uzan et al. (1978) recommended a K value of 10 N/mm³ to model an interface in the upper part of an asphalt pavement subjected to a tire pressure of 75 to 100 psi at normal highway speed and 25 °C.

An axisymmetric analysis with the multilayer linear elastic program BISAR was performed to evaluate the effect of interface conditions following the model shown in Figure 4-4. Figure 4-5 plots the results obtained for the pavement structure with a 4-in AC layer and a stiffness ratio of 32 (this structure was selected for yielding the greatest shear stress found in Figures 4-2 and 4-3). Following findings from Figure 4-2, an interface with varying reaction modulus was introduced at the critical depth of 2 in. Note that trends shown in Figure 4-5 agreed with observations reported by Uzan (1976): K values above 100 N/mm³ yielded similar results to the fully bonded case, and K values below 1 N/mm³ tended to represent the fully debonded scenario. The horizontal shear stress distribution along the interface followed the same pattern regardless of K value: shear stress started at zero under the center of the load due to the symmetry conditions, peaked below the edge of the tire, and gradually reduced away from the tire. Also, interface conditions were found to have a minimal effect on vertical stress distribution: in all cases, high

vertical stress existed under the tire but dropped outside the edge of the tire. Therefore, it was concluded that even when smeared bonding interface conditions were considered by way of the interface reaction modulus model, an area of high shear stress coupled with low confinement where localized debonding can potentially develop was still present.

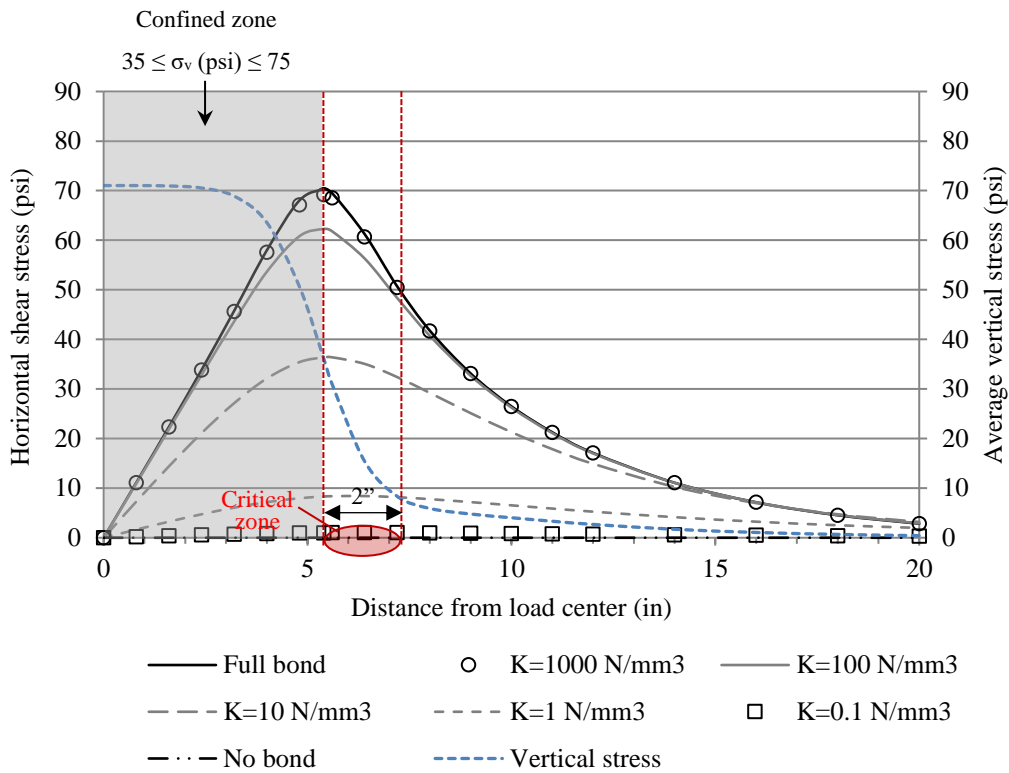
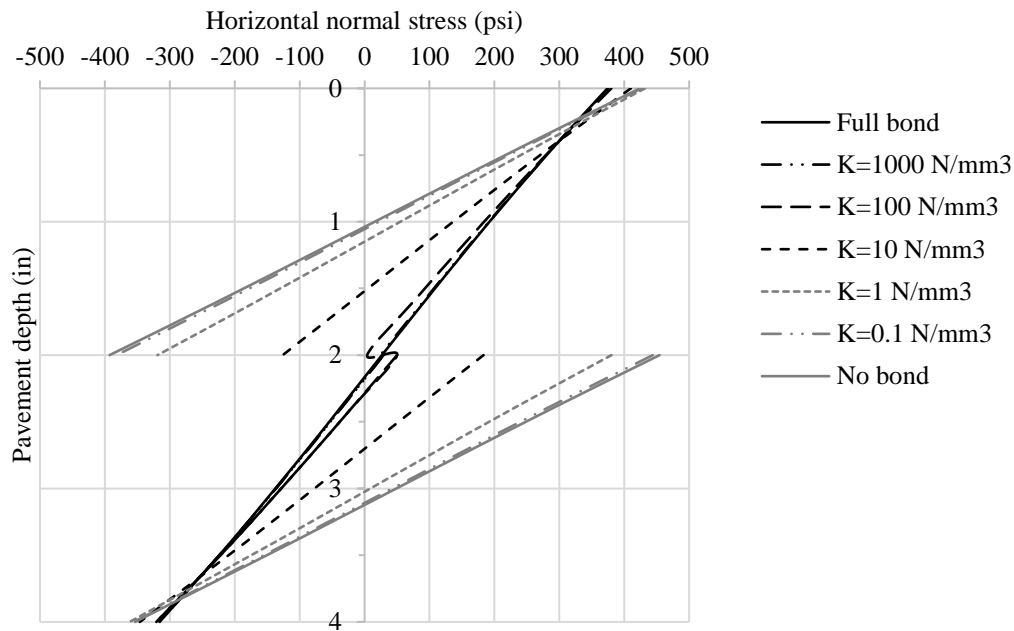


Figure 4-5 Horizontal shear stress and average vertical stress at a depth of 2 in for different interface reaction modulus (K) values (4-in AC layer pavement structure, stiffness ratio=32).

Note that in the case of excessively compliant interfaces, for example interfaces with K values below 1 N/mm³, the maximum horizontal shear stress in the unconfined portion of the interface would barely reach 10 psi. Under these conditions, development of localized interface debonding seems rather unlikely. However, as Figure 4-6 depicts, an excessively compliant interface or, in an extreme scenario, a fully debonded interface would result in high tension above the interface, which could theoretically lead to bottom-up cracking under the center of the tire. Nevertheless, it is important to keep in mind that the area under the tire is subjected to high vertical stress

(confined zone), which allows for development of horizontal frictional resistance along the interface. The development of horizontal frictional resistance reduces the tensile stress above the interface and, consequently, makes the presence of a debonded interface through the confined zone less critical.



Note: negative values denote tension.

Figure 4-6 Horizontal normal stress under the center of the tire through the depth of the AC layer for different interface reaction modulus (K) values (4-in AC layer pavement structure, stiffness ratio=32).

4.3 Effect of tire size and traffic wander

Section 4.1 identified the presence of a critical zone up to 2-in wide from the edge of the tire where interface debonding can potentially occur. This section is aimed at providing insight on the potential extent of localized debonding considering tire size and traffic wander.

Figure 4-7 depicts a plan view of a truck axle on a highway lane (circular tire imprints were considered for illustration purposes). As the truck travels down the highway, the critical zone of high shear and low confinement identified around the edge of the tire (represented as a red ring

in Fig. 4-7) moves longitudinally along both wheelpaths. Consequently, the presence of a critical stress-state zone around a tire can end up promoting a completely debonded strip along both wheelpaths. This mechanism, which to the authors' knowledge has not been reported in the literature, is consistent with the presence of localized debonding in the wheelpath found in field studies by Muench and Moomaw (2008).

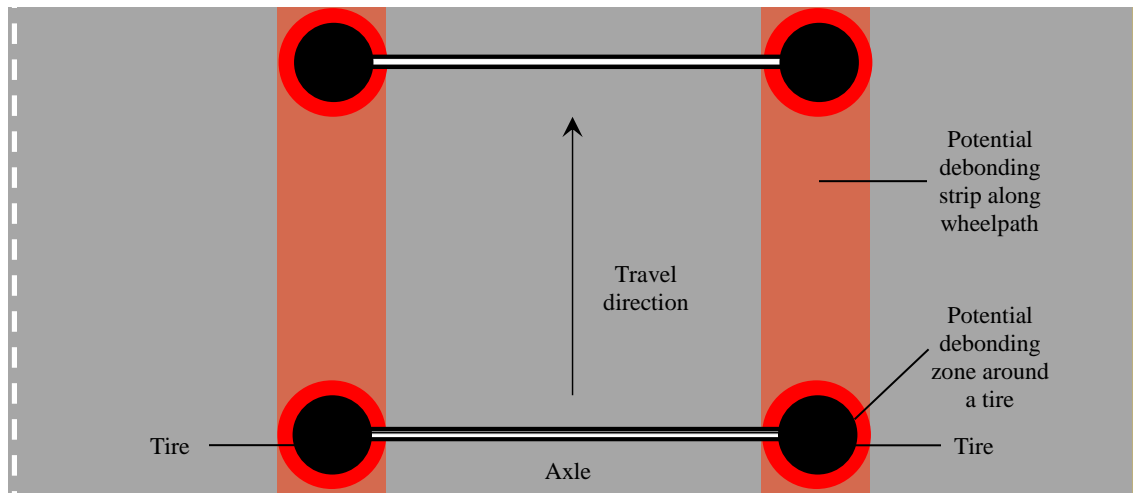
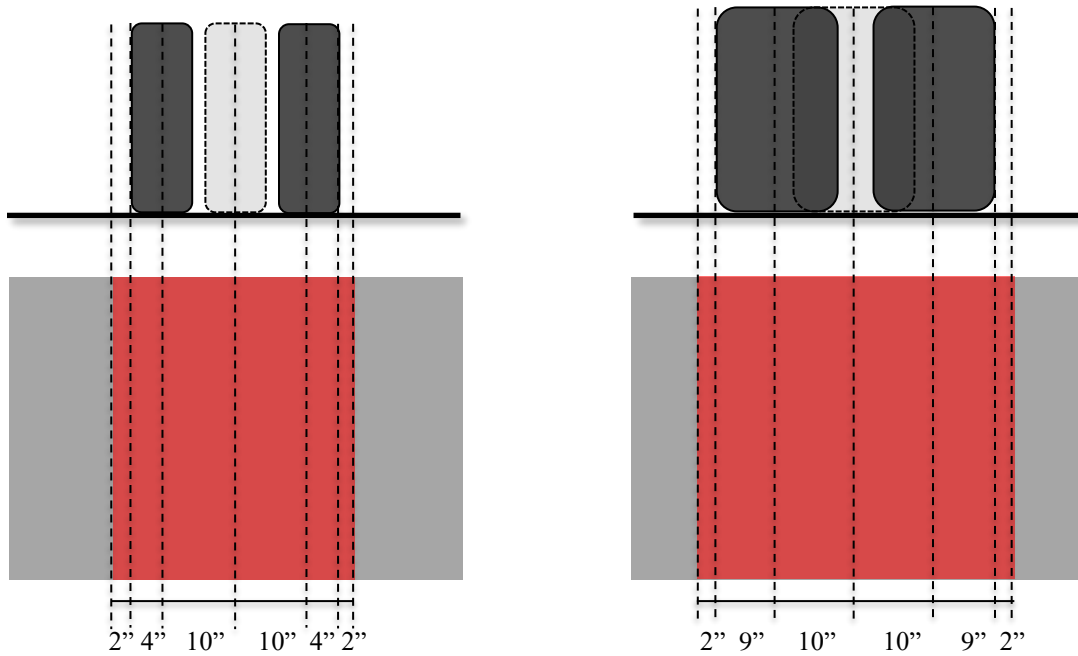


Figure 4-7 Schematic representation of development of a debonded strip along the lane wheelpath.

Within the last two decades, trucking companies have gradually introduced wide-base radial tires due to economic and environmental benefits such as improved fuel efficiency, reduced emissions and increased load capacity. Compared to a conventional radial tire with a typical contact width of 8 inches, wide-base tires range from 12 inches (first generation) up to 18 inches (new generation), as illustrated in Table 4-1. Thus, tire type has a significant effect on the extent of the potentially debonded strip along the wheelpath. Furthermore, debonding extent is also affected by the lateral movement of the tire within the lane, referred to as traffic wander. Field studies showed the lateral position of wheel loads within a lane follows a normal distribution with a standard deviation of about 10 in (Erlingsson et al., 2012; Timm and Priest, 2005). Since 68% of a normal distribution lies within one standard deviation of the mean, it is reasonable to believe the width of the potentially localized debonding strip along the wheelpath can extend up to 10 in to each side. Thus, debonding width could reach 42 in when new-generation wide-base tires are common (Figure 4-8).

Table 4-1 Approximate contact width of different radial tires (Myers et al., 1999; Wang and Roque, 2011; Greene et al., 2009).

Category	Tire denomination	Assembly	Contact width (in)
Conventional	275/80R22.5	Dual	8
First-generation wide-base (super-single)	385/65R22.5	Single	11.5
	425/65R22.5	Single	12.5
New-generation wide-base (NGWB)	445/50R22.5	Single	17.8
	455/55R22.5	Single	18



a. Conventional radial tire (8-in wide)

b. New-generation wide-base tire (18-in wide)

Figure 4-8 Potential extent of localized debonding strip along the wheelpath considering traffic wander and tire width.

4.4 Summary

The factorial simulation effort conducted in this chapter proved existence of a zone of high shear stress coupled with low confinement at a depth that ranges from 1 to 3 inches below the surface, with the more critical condition being about 2-in deep, regardless of pavement thickness and stiffness ratio. Presence of an interface through this critical location can potentially result in a debonded strip along the interface, even in the case of thick asphalt pavements or relatively compliant interfaces. The width of the debonded strip can range from 12 in for conventional tires with no wander to 42 in in the case of new-generation wide-base tires and a traffic wander standard deviation of 10 in.

CHAPTER 5
IMPACT OF LOCALIZED DEBONDING ON STRESS DISTRIBUTION AND CRACK
DEVELOPMENT

5.1 Introduction

This chapter describes a modeling effort to examine the effect of a localized debonded strip along the wheelpath identified in Chapter 4 on the stress distribution of different pavement structures and, ultimately, the potential for crack initiation and development. The presence of a debonded strip not only invalidates the use of an axisymmetric model but also results in different boundary conditions and stress distributions across the transverse and longitudinal lane cross-sections, respectively. As shown in Figure 5-1, the debonded strip is seen as a localized debonded zone under the tire along the transverse direction (Section AA'). High stress concentration is expected where the localized debonded zones meet the remaining bonded interface. Conversely, the interface is fully debonded along the longitudinal direction (Section BB') and no significant stress concentration will take place.

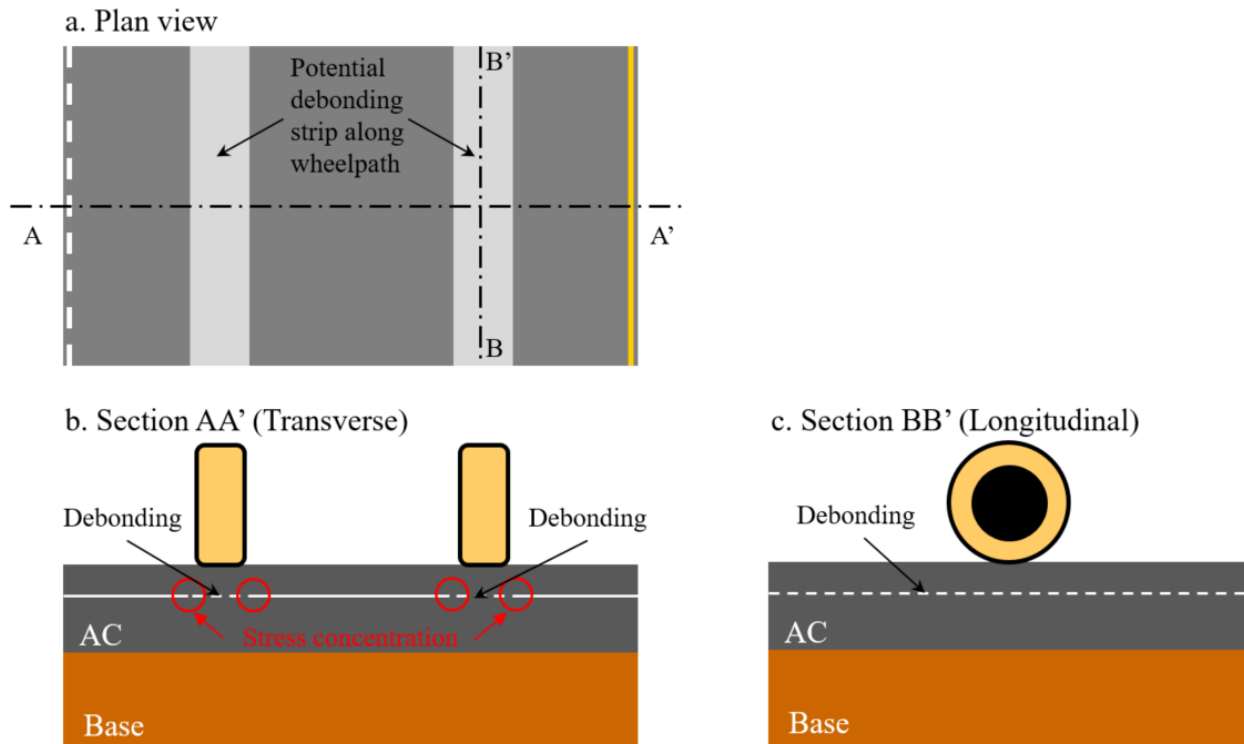


Figure 5-1 Geometry of a pavement with localized interface debonding along the wheelpath.

The most important consequence of this finding is that stresses induced by traffic loads in a system with localized debonding along the wheelpath will tend to be more critical on the transverse plane due to singularities (i.e., the tip of a debonded zone) in the geometry of the problem. In other words, stresses on the transverse plane are expected to be higher than those on the longitudinal cross-section. For example, if the maximum tensile stress is on a transverse plane, cracking will be longitudinal (i.e., perpendicular to the plane of maximum tension). This argument is consistent with the fact that near-surface cracking in the wheelpath is predominantly longitudinal. Given the geometry of the problem (i.e., longitudinal debonded strip along wheelpath) and the presence of maximum stress on a transverse cross-section, it seems reasonable to employ 2D plane-strain modeling instead of a more computationally expensive 3D model. It should be pointed out that the load in a 2D plane-strain model results in a different bending pattern than a wheel load in 3D analysis. Bending occurs along the transverse and longitudinal directions in a 3D model whereas bending exists only along the transverse direction in a 2D plane-strain model. However, previous work done by Myers (1998) showed that 2D plane-strain analysis can be related by way of pavement structural characteristics to the stresses predicted by 3D analysis. Therefore, the use of 2D plane-strain modeling appears suitable for assessing the effect of localized debonding on stress redistribution and the potential for crack development.

5.2 Model development

5.2.1 General description

The finite element (FE) computer program ABAQUS was employed to develop 2D plane-strain models of a pavement structure. Eight-node quadrilateral elements were selected to prevent overly stiff response (shear locking) sometimes found with four-node elements when used to model flexure. All nodes had two translational degrees of freedom. In terms of loading conditions, load width was determined by using an equivalent circular tire corresponding to an 18-kip single axle load with a uniform pressure of 100 psi. This resulted in a tire imprint width of 10.7 in. Since the interface of interest is relatively far from the surface (2-in deep), introduction of real tire contact stresses seemed unnecessary at this stage and the use of a static, uniform load was considered adequate. Only a half section was modeled because of symmetry. Lateral

boundaries were fixed in the horizontal direction and free in the vertical direction whereas the bottom of the pavement was fixed in both directions to simulate the presence of bedrock.

The pavement structure was composed of asphalt concrete (AC), granular base and subgrade. Each layer was considered homogeneous, isotropic and linear elastic. Table 5-1 summarizes layer thickness and material properties. The 4-in AC case was chosen for yielding a more critical condition in terms of stress magnitude. Moreover, a localized debonded strip was introduced in the AC layer, 2 in below the surface (Figure 5-2). This debonded zone extended from the center of the load up to 2 in from the outside edge of the tire (total debonded length of 7.35 in). The debonded strip was frictionless and no penetration was allowed between surfaces in the normal direction (i.e., the two debonded faces of the interface were in contact when a normal pressure was applied, but one could not penetrate the other). Other interfaces were assumed fully bonded.

Table 5-1 Layer thickness and material properties of pavement structure.

Pavement layer	Thickness (in)	Elastic modulus (psi)	Poisson's ratio
Asphalt concrete	4	800,000	0.40
Base	12	25,000	0.35
Subgrade	-	15,000	0.35

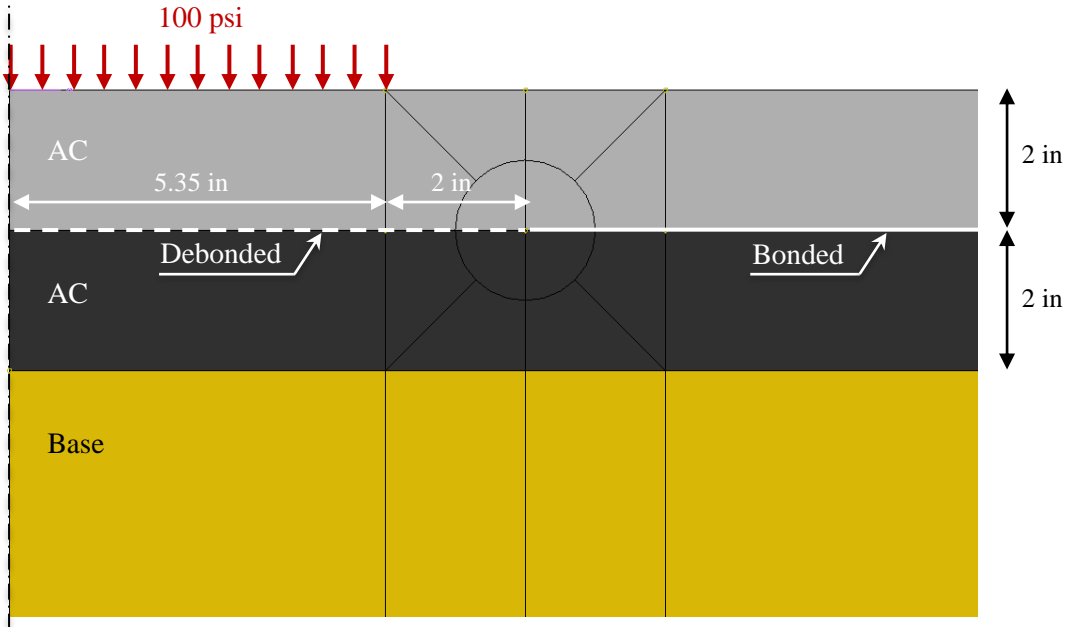
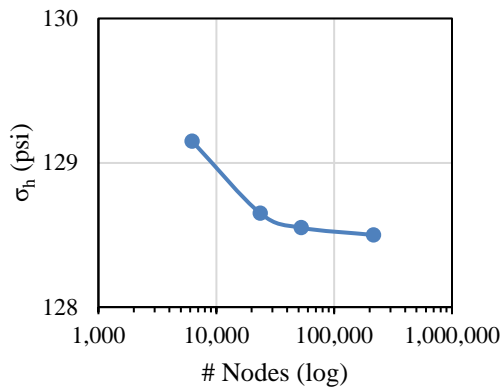


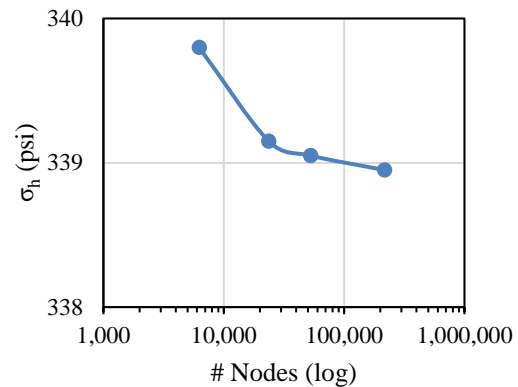
Figure 5-2 Presence of a debonded zone along the AC interface (2D plane-strain model).

5.2.2 Analysis of mesh quality

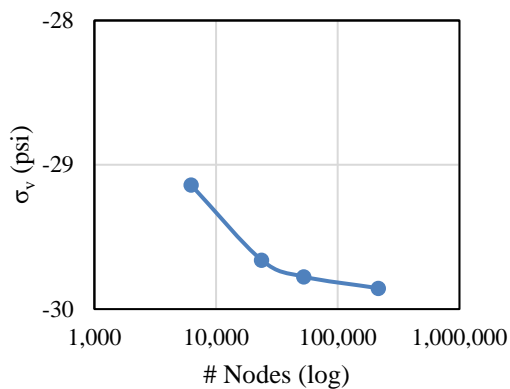
The general rule of thumb establishes that model dimensions should be about 12 times the width of the load to minimize the effect of model boundaries on stress distribution. For this reason, the model developed was 60-in wide and 64-in deep. The next step was to define the density of the mesh. Since no exact solution exists for the problem at hand, a convergence analysis was conducted to determine the variation in stress as a function of the number of nodes in the model. As shown in Figure 5-3, evaluated stresses started to flatten out around 20,000 nodes; however, a mesh density corresponding to 50,000 nodes was chosen to be conservative.



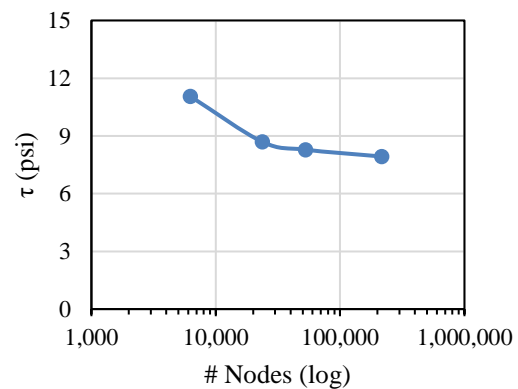
a. Horizontal normal stress above AC interface



b. Horizontal normal stress at AC bottom



c. Vertical normal stress at AC bottom



d. Maximum horizontal shear stress at AC bottom

Note: positive normal stress denotes tension.

Figure 5-3 Convergence analysis of different stresses for evaluation of mesh quality. Note: positive normal stress denotes tension.

5.2.3 Final model

The final 2D plane-strain FE model is depicted in Figure 5-4. This model consisted of 17,316 elements, 52,610 nodes and 104,860 degrees of freedom. Furthermore, Figure 5-5 shows a close-up view of the mesh around the tip of the debonded zone. A circular mesh was defined to better capture the stress field associated with the presence of a singularity in the geometry of the model.

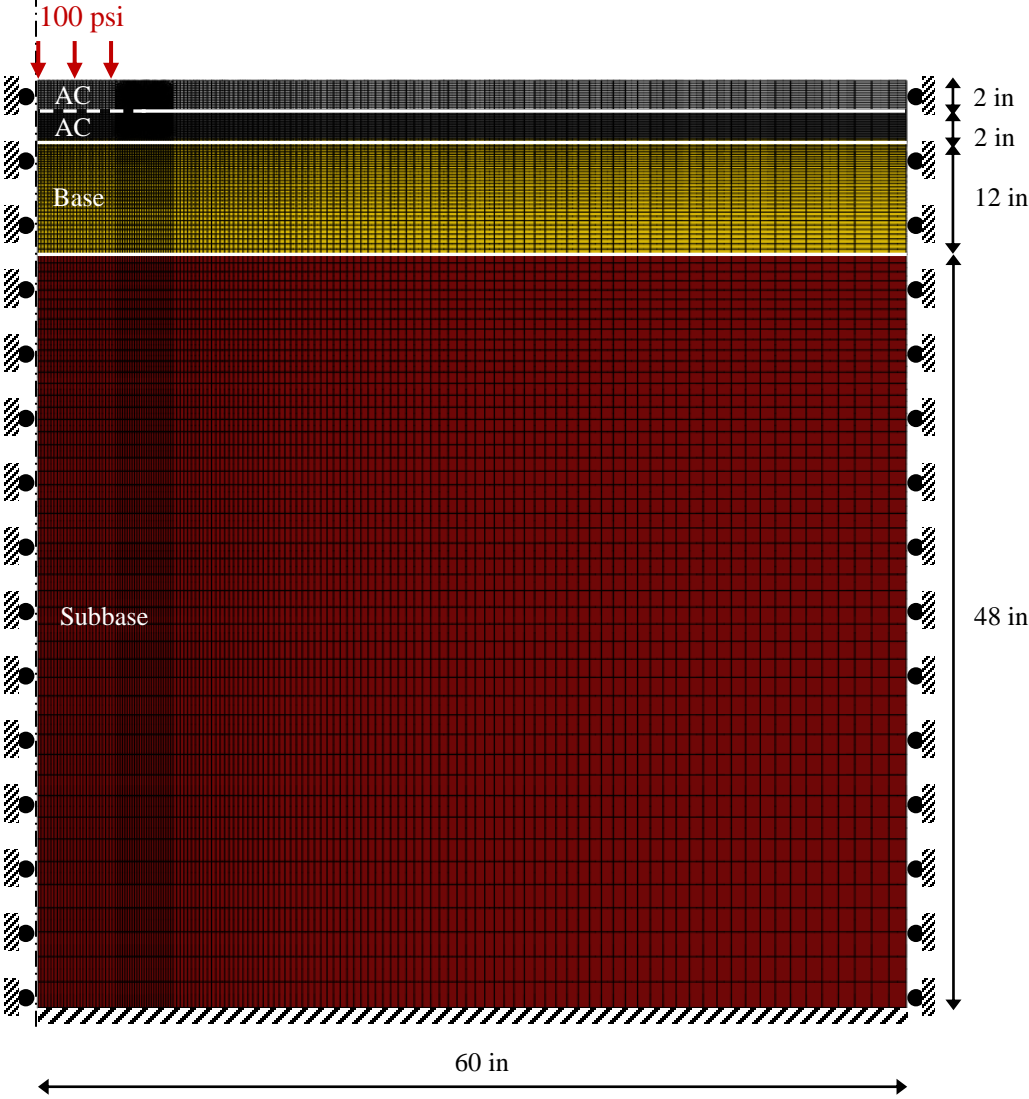


Figure 5-4 2D plane-strain FE model (half model due to symmetry).

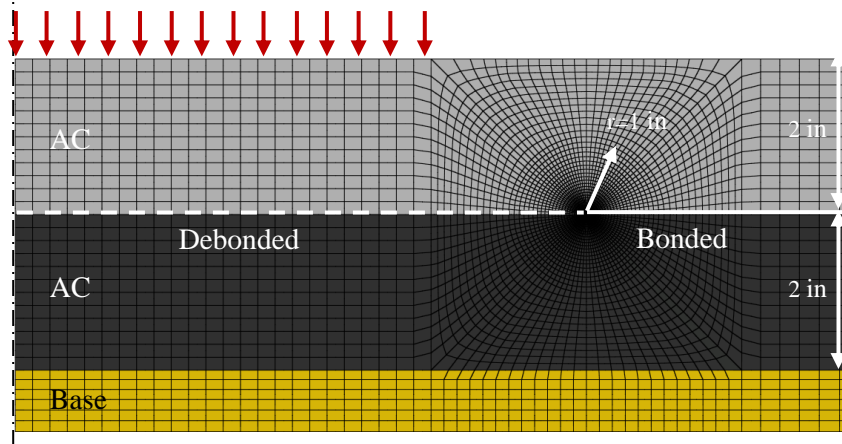


Figure 5-5 Close-up view of the mesh around the tip of the debonded zone (singularity).

5.2.4 Bending stress ratio (BSR)

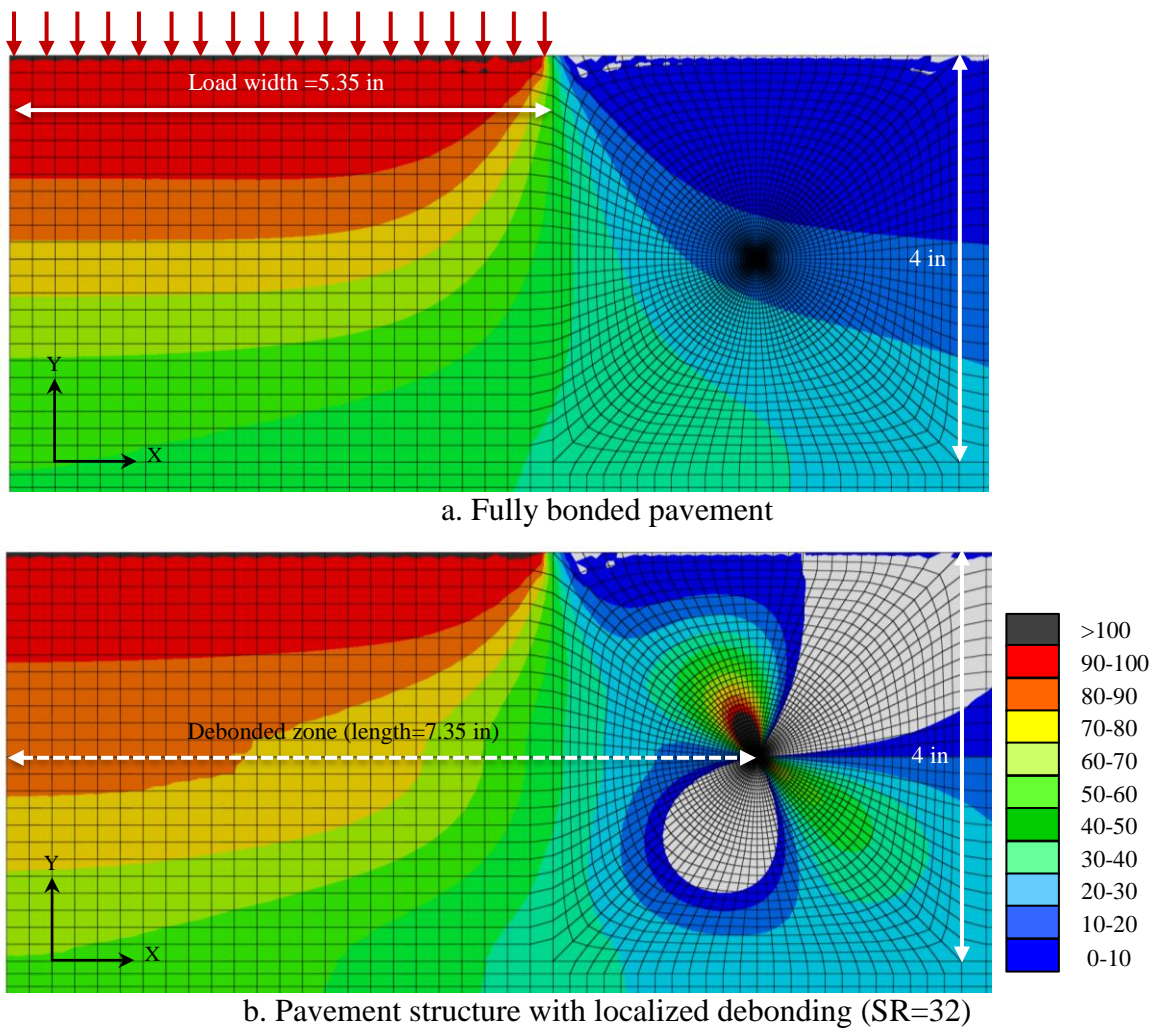
The load in the 2D plane-strain model shown in Figure 5-4 represents a strip load, which results in a different bending pattern than a wheel load in 3D analysis. In order to account for this difference, Myers (1998) developed an approach to obtain bending stress distributions using a 2D plane-strain model that reasonably estimated the stress predicted by a true 3D model. This approach consists of calculating a bending stress ratio (BSR) to act as a modifying factor for 2D results. BSR is defined as the ratio of 3D critical tensile stress to 2D critical tensile stress and is a function of the AC layer to base stiffness ratio (E_1/E_2) and thickness ratio (h_1/h_2):

$$\log BSR = -0.29655 \cdot \left(\frac{E_1}{E_2}\right)^{0.29531} \cdot \left(\frac{h_1}{h_2}\right)^{0.95659} \quad (5.1)$$

For example, a BSR value of 0.5 was obtained for the stiffness ratio ($E_1/E_2=32$) and thickness ratio ($h_1/h_2=1/3$) of the pavement structure described in Table 5-1. Therefore, bending stresses (horizontal normal stress and horizontal shear stress) obtained from 2D plane-strain were reduced by 50% to obtain more accurate stress predictions. Vertical stress distribution is relatively unaffected by 2D or 3D representation, particularly under the load and near surface, so stress magnitude was used as directly provided by 2D plane-strain models. Additional discussion on BSR can be found in Appendix B.

5.3 Overall stress distribution

This section describes the stress distribution (AC layer only) of the pavement structure with localized debonding shown in Figure 5-4 and compares the results with a fully bonded system. As shown in Figure 5-6, the vertical stress distribution was relatively similar under the load, but clear differences were observed outside the tire. The debonded system (Fig. 5-6b) exhibited small concentrations of compression around the tip of the debonded zone and, more importantly, areas of tension (shown in white) that were not present in the case of a fully bonded pavement.



Note: white areas denote tension.

Figure 5-6 Vertical compressive stress distribution (psi) for different bonding conditions.

The horizontal shear stress distribution is depicted in Figure 5-7. As expected, the maximum shear stress for the fully bonded system (Fig. 5-7a) was located under the edge of the tire around the mid-depth of the AC layer. The presence of a debonded interface in Figure 5-7b caused the two AC layers to respond independently so shear stress in the area directly beneath the tire peaked around the mid-depth of each layer. However, the maximum shear stress was located ahead of the tip of the debonded zone between the two AC layers.

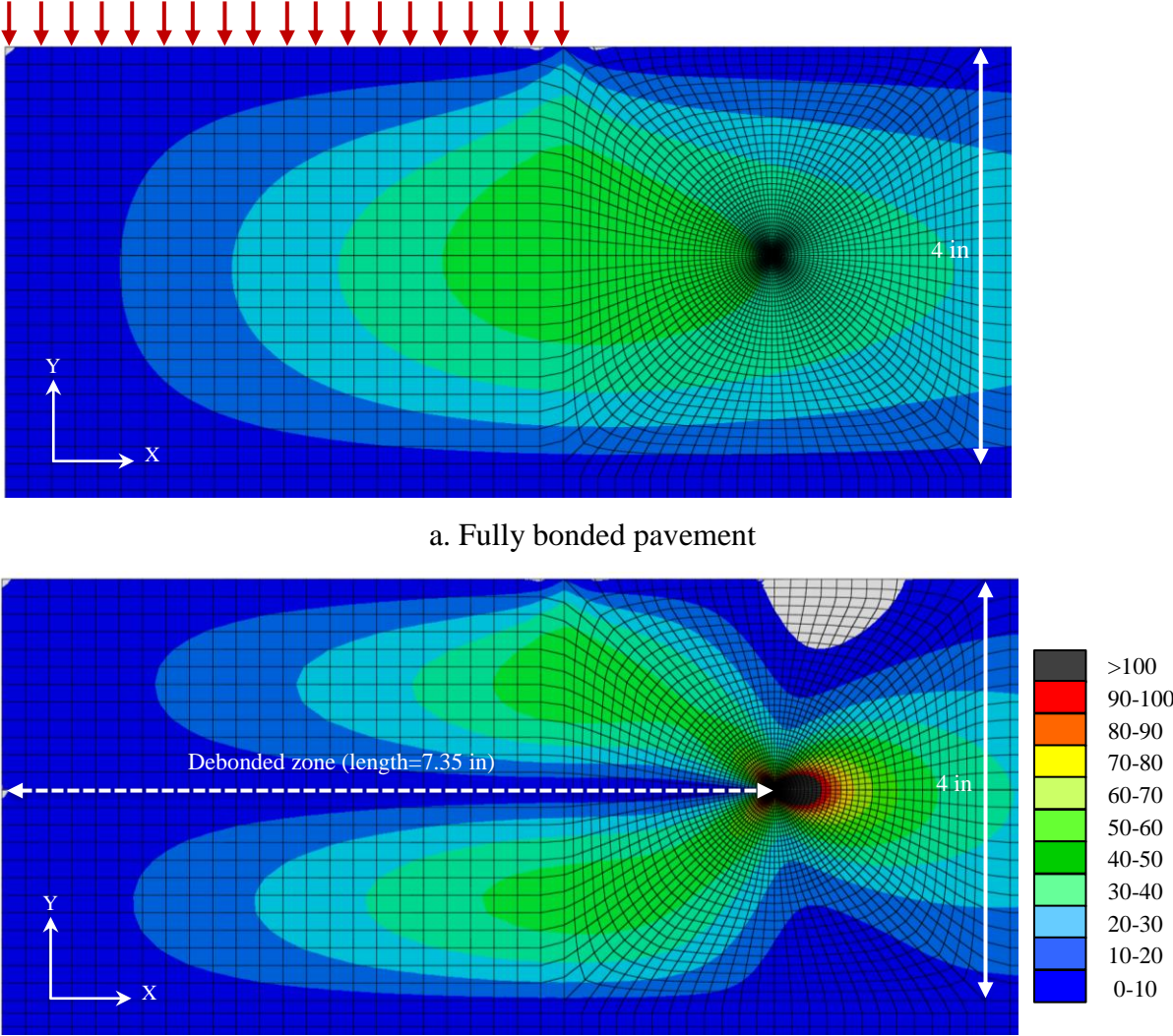


Figure 5-7 Horizontal shear stress distribution (psi) for different bonding conditions.

The horizontal shear stress along the interface between AC layers (2-in deep) is detailed in Figure 5-8. As shown, shear stress along the debonded interface was zero due to the frictionless

condition. Consequently, stresses redistributed and shear stress intensified ahead of the tip of the debonded zone. There is a zone about 1.2-in wide over which shear stress exceeded the maximum value found for a fully bonded system (50 psi).

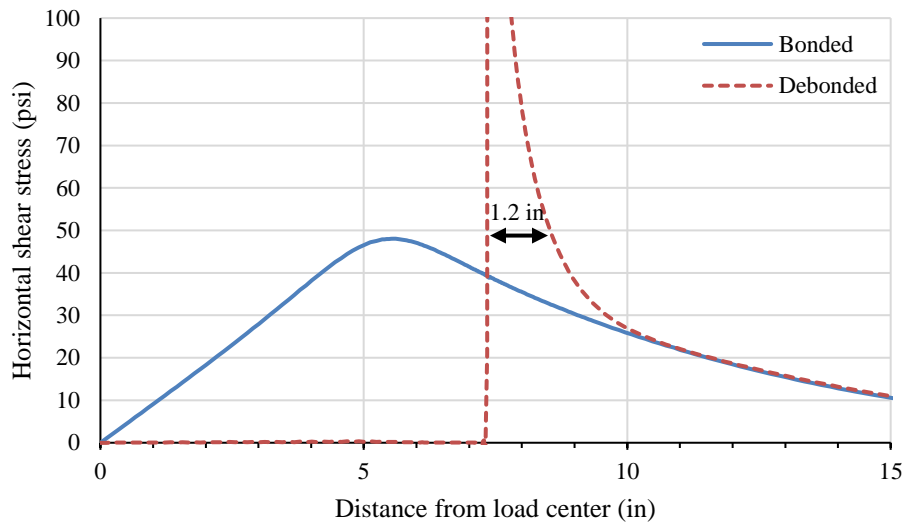
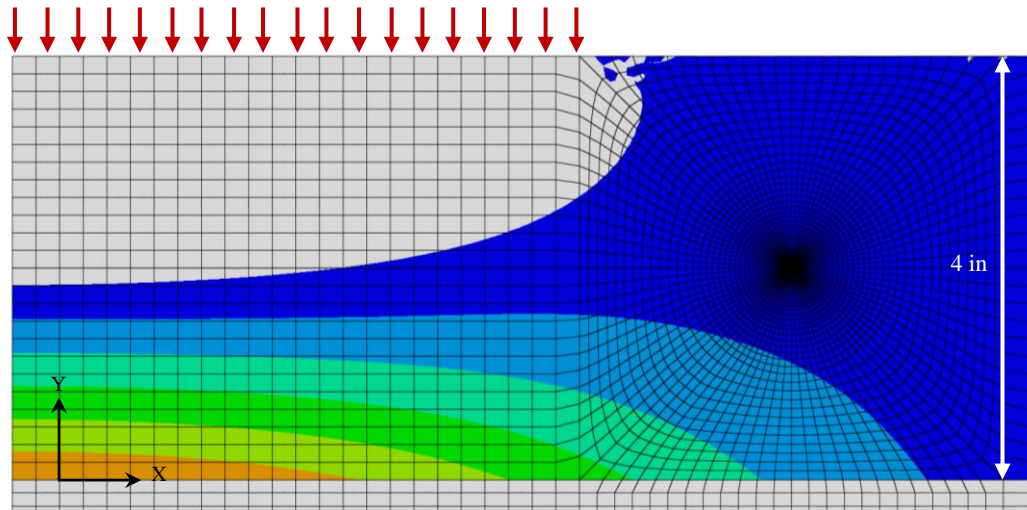
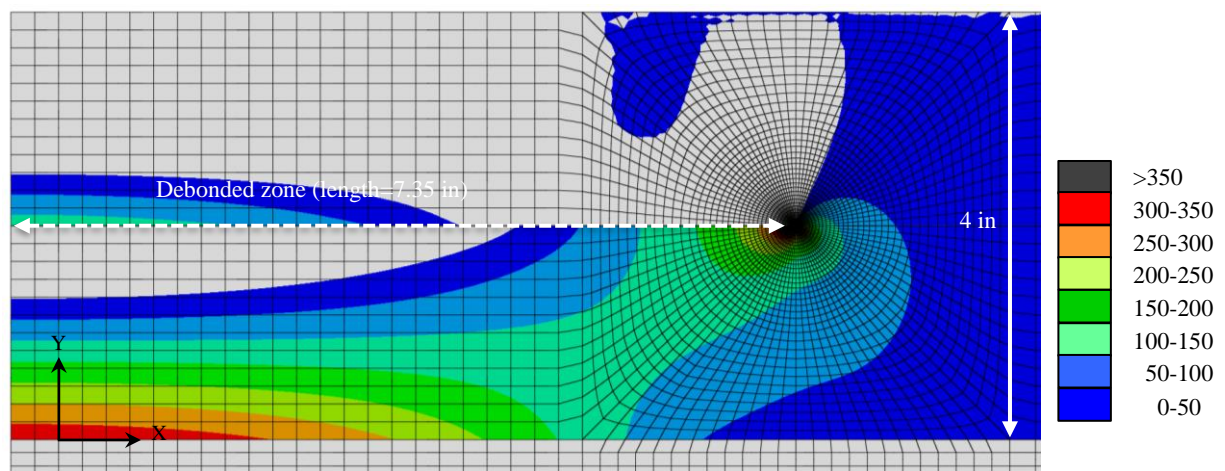


Figure 5-8 Horizontal shear stress along AC interface (psi) for different bonding conditions.

Although an intensification in shear stress could promote progressive debonding along the interface, field observations seemed to indicate debonding is localized in the wheelpath (as opposed to extended across the entire lane). Thus, it appears reasonable to assume that crack initiation becomes more dominant than progressive debonding. For this reason, maximum tensile stress was examined in Figure 5-9. Maximum tension in the fully bonded system was found under the center of the tire, at the bottom of the AC layer. The pavement structure with localized debonding also exhibited high tension at this location, but the maximum tensile stress was located behind the tip (i.e., to the left of the tip in these figures) of the debonded zone, below the interface. As illustrated in Figure 5-10, tensile stress intensified behind the tip of the debonded zone and there was a zone about 0.4-in wide where tensile stress exceeded the values found under the center of the tire at the AC bottom. Given the high magnitude of the tensile stress at this location, it is believed that a crack can initiate immediately below the interface at the tip of the debonded zone. Note that comparison to the fully bonded case showed no tension would exist along the interface unless localized debonding was introduced.



a. Fully bonded pavement

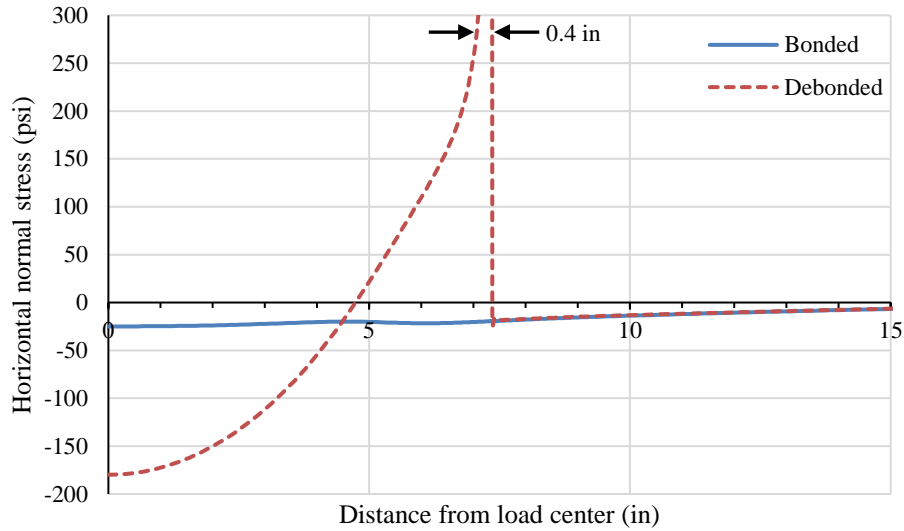


b. Pavement structure with localized debonding (SR=32)

Note: white areas denote compression.

Figure 5-9 Maximum tensile stress distribution (psi) for different bonding conditions.

It should be mentioned the high tensile stress found at the bottom of the AC layer was caused by the high stiffness ratio (SR) between AC layer and base (SR=32). Lower stresses are expected for pavement structures with a lower SR. However, stress intensification behind the tip of the debonded zone will still be present due to the singularity in geometry. Thus, although traditional bottom-up cracking may occur in a debonded pavement, initiation of a crack below the interface at the tip of the debonded zone may be a more likely mechanism.



Note: positive values denote tension.

Figure 5-10 Horizontal normal stress below AC interface (psi) for different bonding conditions.

The direction of principal stresses was investigated in order to determine the potential direction of crack initiation. As shown in Figure 5-11, principal tensile stress below the interface near the tip of the debonded zone was horizontal. This was expected given the absence of shear stress along the interface (frictionless condition). Therefore, if a crack develops, it would do so in the vertical direction (i.e., perpendicular to the direction of maximum tensile stress).

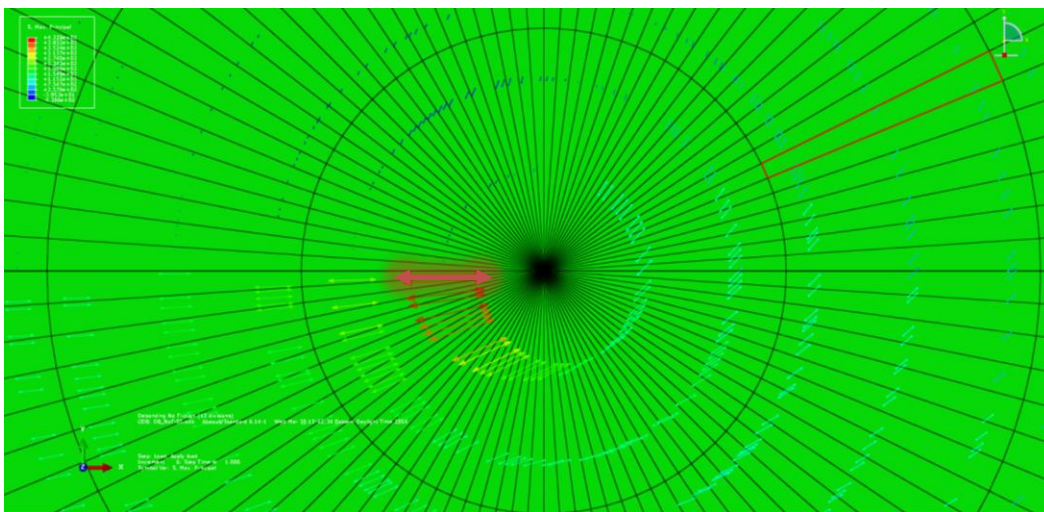


Figure 5-11 Direction of principal tensile stress around the tip of the debonded zone.

5.4 Investigation based on tensile stress

5.4.1 Parametric study

5.4.1.1 Bending stress ratio

The bending stress ratio (BSR) approach was utilized to predict 3D bending stress distributions from 2D plane-strain models of additional pavement structures. Table 5-2 summarizes the BSR values for the structures under evaluation. For the section with a stiffness gradient, an equivalent AC modulus was first calculated through the following equation from Huang (2004):

$$E_{eq} = \left[\frac{\sum_{i=1}^n h_i \cdot (E_i)^{1/3}}{\sum_{i=1}^n h_i} \right]^3 \quad (5.2)$$

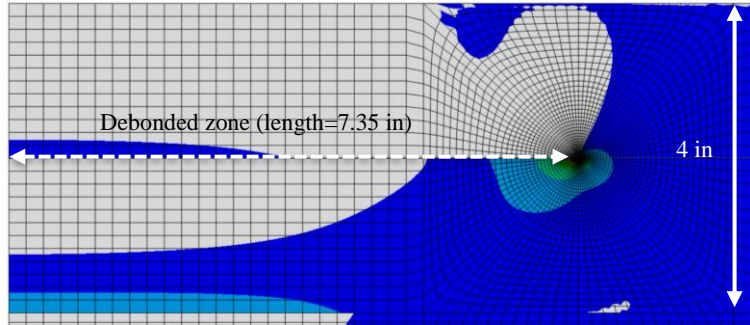
where h_i and E_i are the thickness and modulus of the different sub-layers within the AC layer.

Table 5-2 Bending stress ratio (BSR) values for pavement sections under evaluation

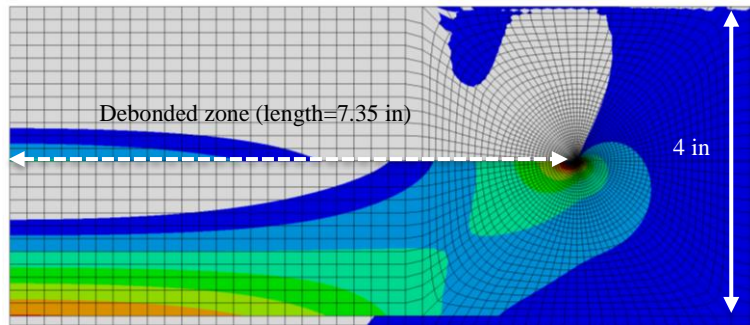
Section	AC modulus (psi)	Base modulus (psi)	AC thickness (in)	Base thickness (in)	BSR
SR=5	200,000	40,000	4	12	0.681
SR=8	200,000	25,000	4	12	0.643
SR=20	800,000	40,000	4	12	0.561
SR=32	800,000	25,000	4	12	0.500
Gradient	866,000	40,000	4	12	0.553

5.4.1.2 Effect of stiffness ratio

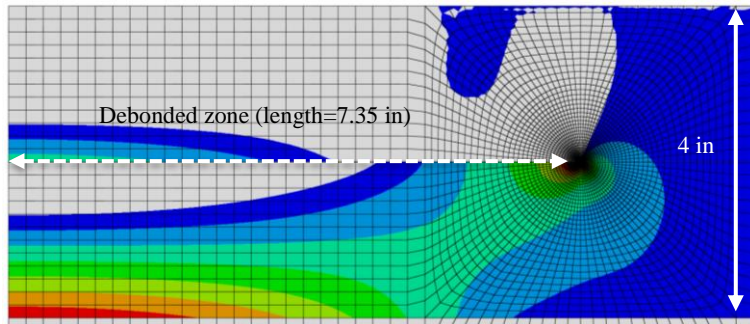
This section studied the effect of AC-to-base stiffness ratio (SR) on tensile stress distribution for the 4-in AC pavement model with a debonded strip shown in Figure 5-4. The debonded strip was modeled as two frictionless surfaces in contact, whereas the remaining portion of the interface was defined as fully bonded (no slip allowed). Figure 5-12 shows the maximum tensile stress distribution throughout the AC layer for a pavement section with four different stiffness ratios (5, 20, 32 and a gradient). As SR increased, the maximum tension at the bottom of the AC layer went up due to the increase in bending stress. The stress magnitude at this location for the section with a stiffness gradient was lower than that of the sections with SR of 32 and 20.



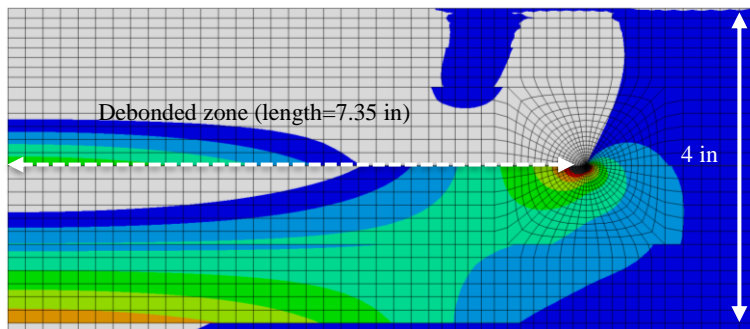
a. SR=5



b. SR=20



c. SR=32



d. Gradient

Note: white areas denote compression.

Figure 5-12 Maximum tensile stress distribution (psi) throughout the AC layer of a 4-in AC pavement section with varying stiffness ratio (SR).

However, when tension near the tip of the debonded zone was examined (location of greatest tension), the section with the stiffness gradient slightly exceeded the values found for SR=32 (Figure 5-13). Although all sections exhibited high tensile stress below the tip of the debonded zone, sections with a stiffness gradient (which simulated field aging conditions) or high stiffness ratio posed a more critical condition from the standpoint of cracking initiation.

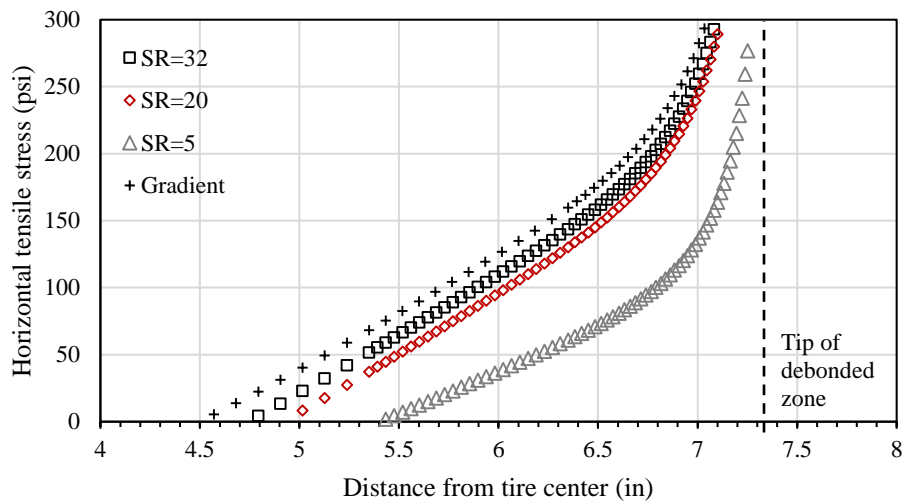


Figure 5-13 Horizontal tensile stress below 2-in deep interface for a 4-in AC pavement section with varying stiffness ratio (SR).

5.4.1.3 Effect of interface friction

The previous section considered the two surfaces in contact along the debonded strip to be frictionless. However, some remaining resistance is expected given the frictional nature of the two asphalt surfaces in contact, particularly under the tire where high vertical stresses act on the normal direction. According to the Coulomb friction model, no relative motion occurs if the equivalent frictional (shear) stress is less than the critical stress, which is proportional to the contact pressure (Figure 5-14). In other words, two contacting surfaces can carry shear stress up to a critical magnitude across their interface before they start sliding relative to another.

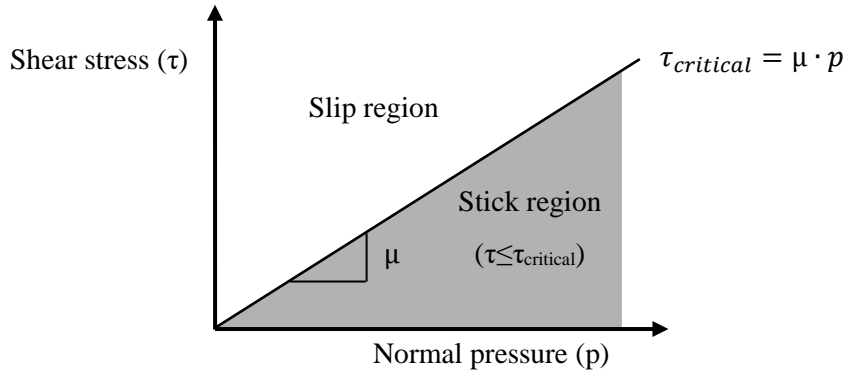
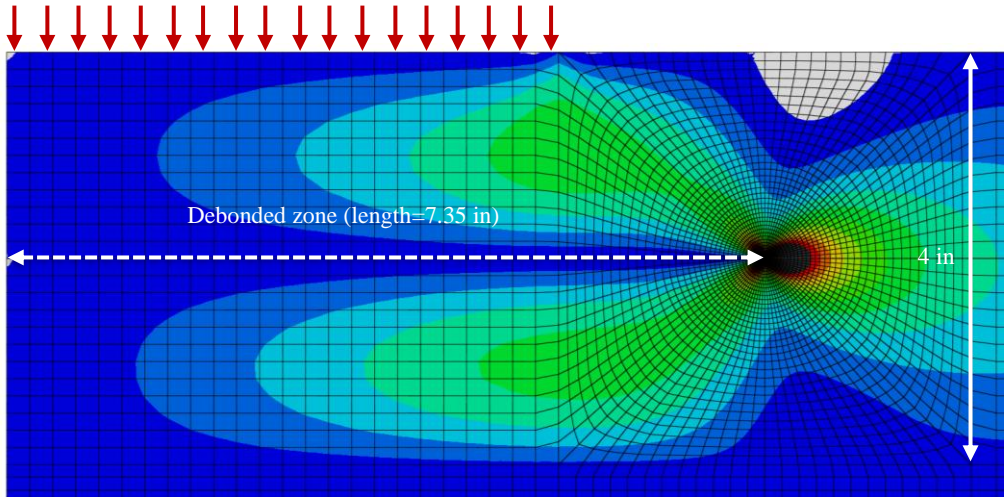


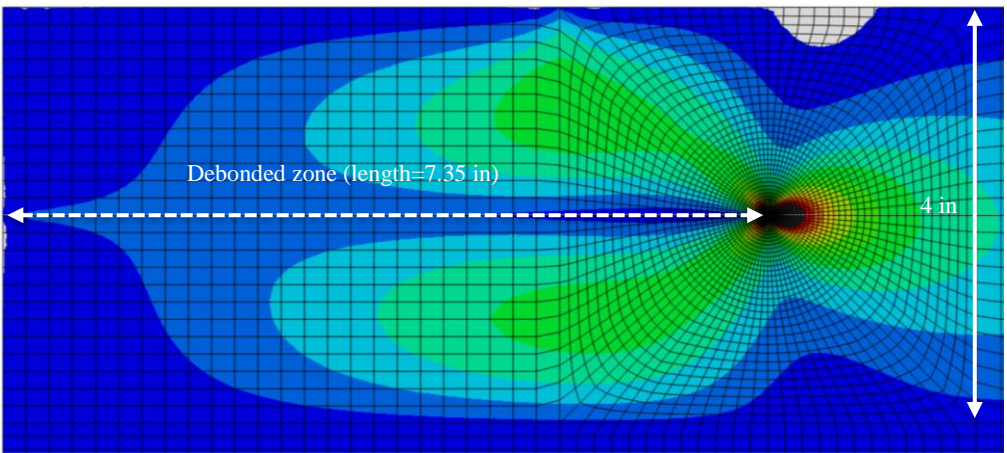
Figure 5-14 Relationship between critical shear stress and normal pressure for a frictional interface according to Coulomb frictional model.

This section evaluated the response of the 4-in AC model shown in Figure 5-4 with two extreme stiffness ratios (SR=5 and SR=32) and three different static friction coefficients. A maximum static friction coefficient (μ , mu) of 0.65 was selected following shear test results reported by Romanoschi and Metcalf (2001a); additionally, an intermediate coefficient of 0.3 (similar to that of a soil with a friction angle of 20°) and a null value (frictionless condition) were chosen for comparison. The remaining portion of the interface was considered fully bonded.

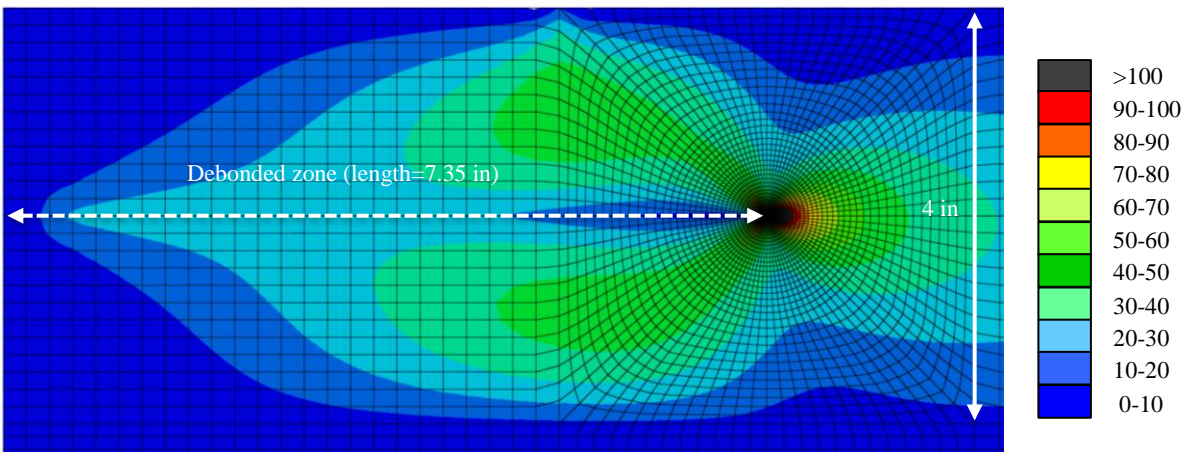
Figure 5-15 shows the shear stress distribution throughout the AC layer of the 4-in AC section with a stiffness ratio of 32. As expected, the higher the friction coefficient, the more shear stress was transferred across the interface, which was observed as an increase in the magnitude of shear stress around the interface. Furthermore, introduction of the interface frictional response improved the structural efficiency of the section, as illustrated by the maximum tensile stress distributions provided in Figure 5-16. There was a moderate decrease (less than 13%) in tensile stress at the AC bottom as the friction coefficient increased. However, the most significant impact of the interface frictional response was the reduction of tension above the interface below the center of the tire from 129 psi in Fig. 5-16a to zero in Fig. 5-16c. This observation supports the hypothesis that initiation of bottom-up cracking at this location is rather unlikely, even in the case of a debonded interface. The high tensile stress traditionally predicted under the center of the tire in a debonded pavement is the result of an excessively simplified model in which the frictional resistance resulting from the high vertical stress under the tire is not captured.



a. Frictionless interface

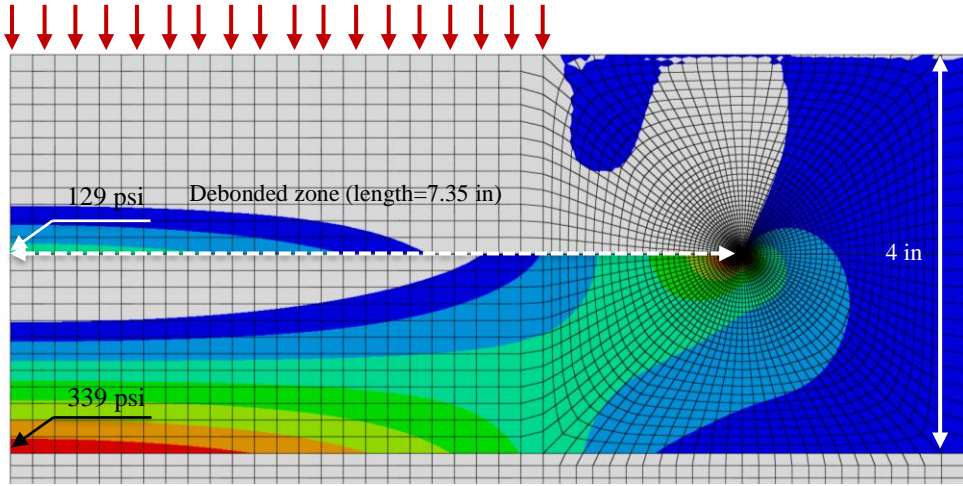


b. Coefficient of friction=0.3

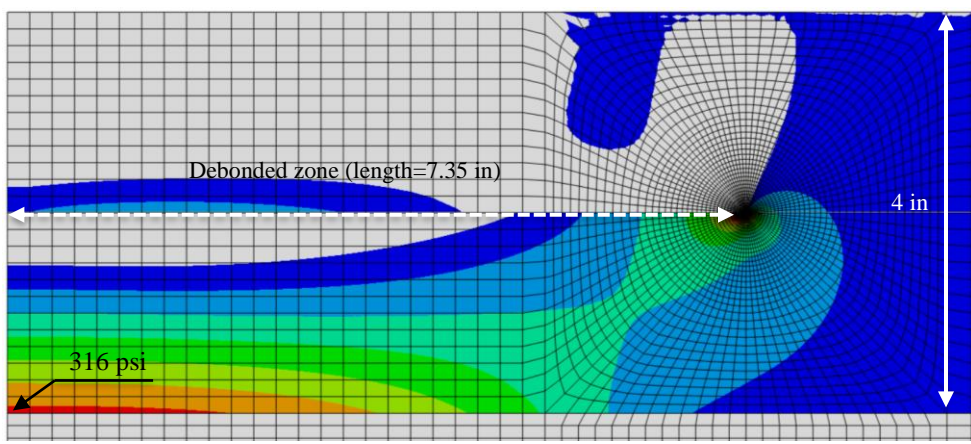


c. Coefficient of friction=0.65

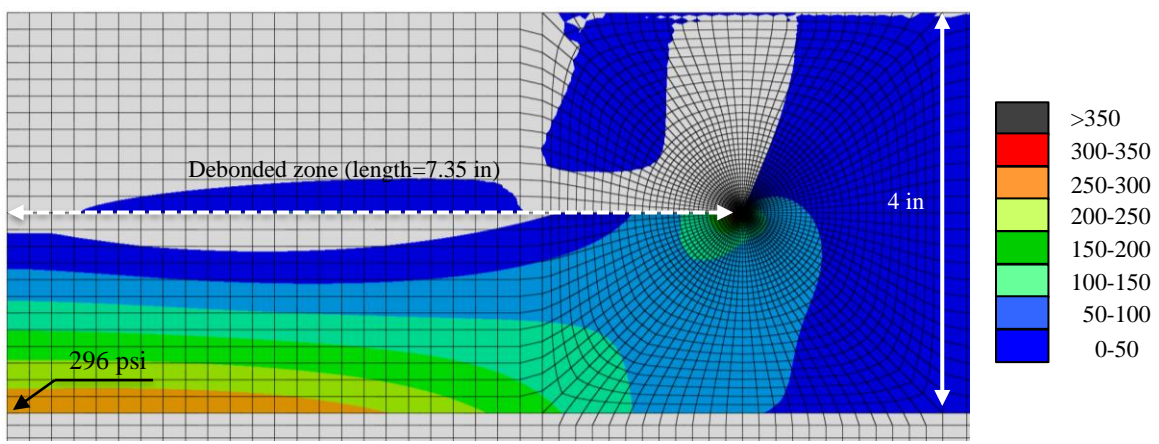
Figure 5-15 Horizontal shear stress distribution (psi) throughout the AC layer of a 4-in AC section with SR=32 for different interface friction coefficients.



a. Frictionless interface



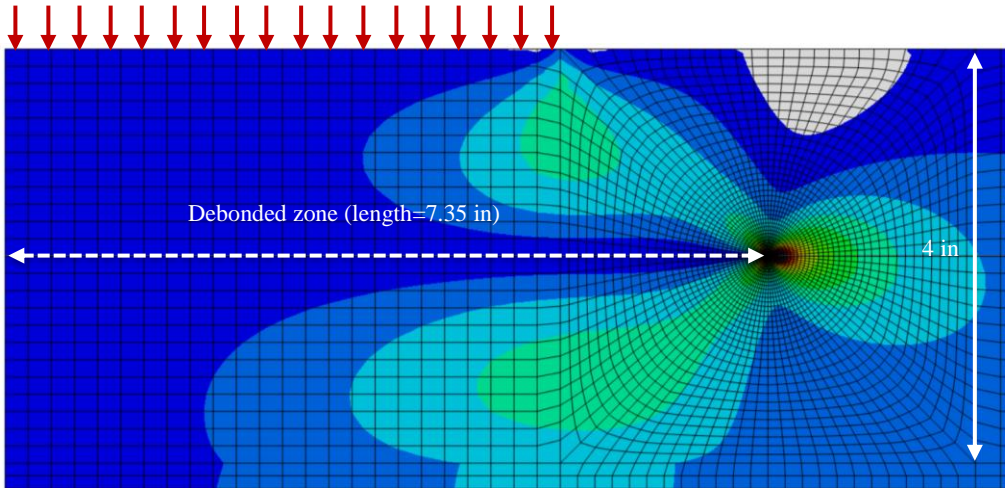
b. Coefficient of friction=0.3



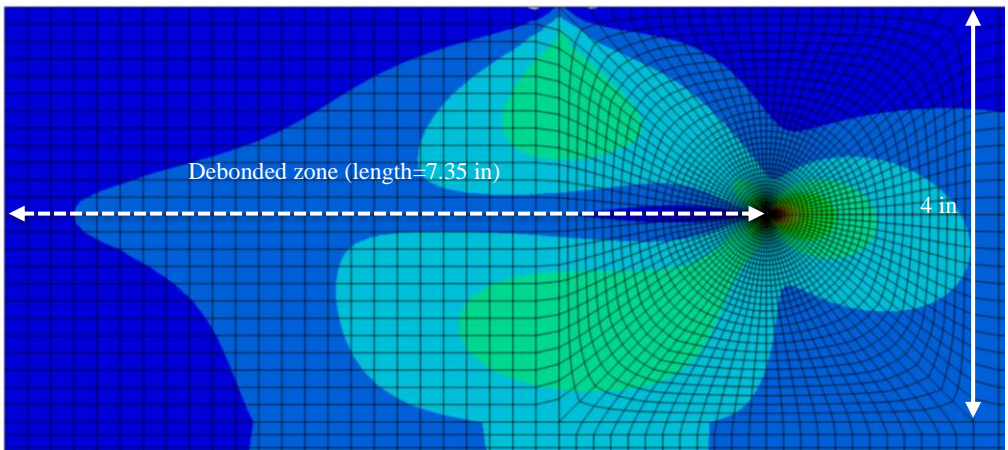
c. Coefficient of friction=0.65

Note: white areas denote compression

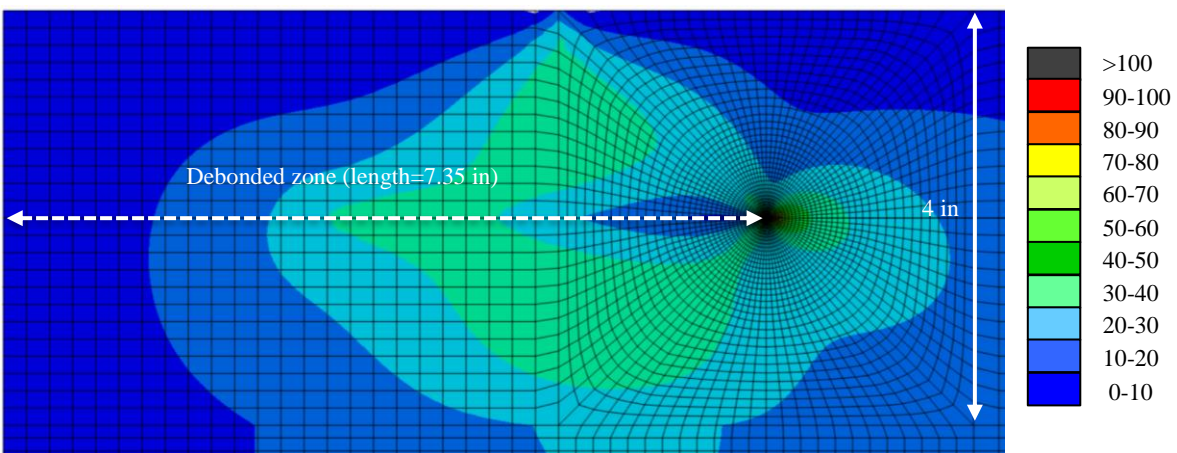
Figure 5-16 Maximum tensile stress distribution (psi) throughout the AC layer of a 4-in AC section with SR=32 for different interface friction coefficients.



a. Frictionless interface

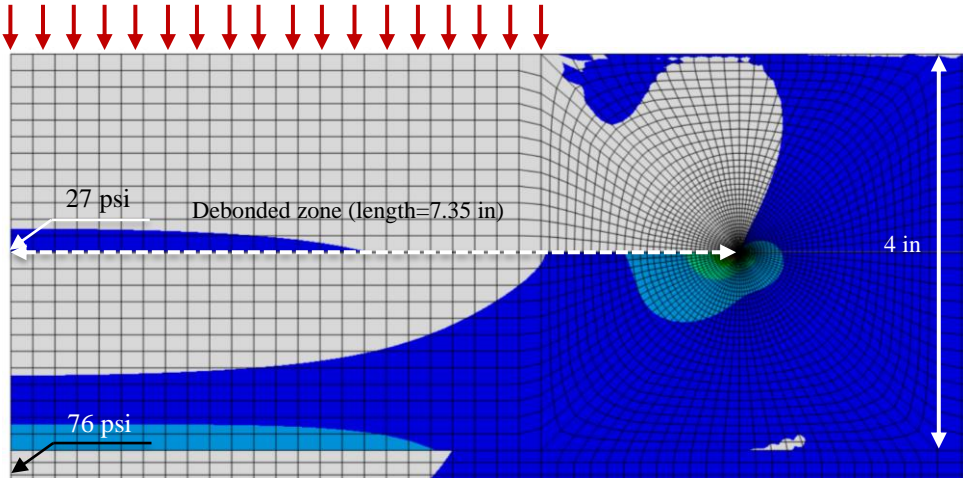


b. Coefficient of friction=0.3

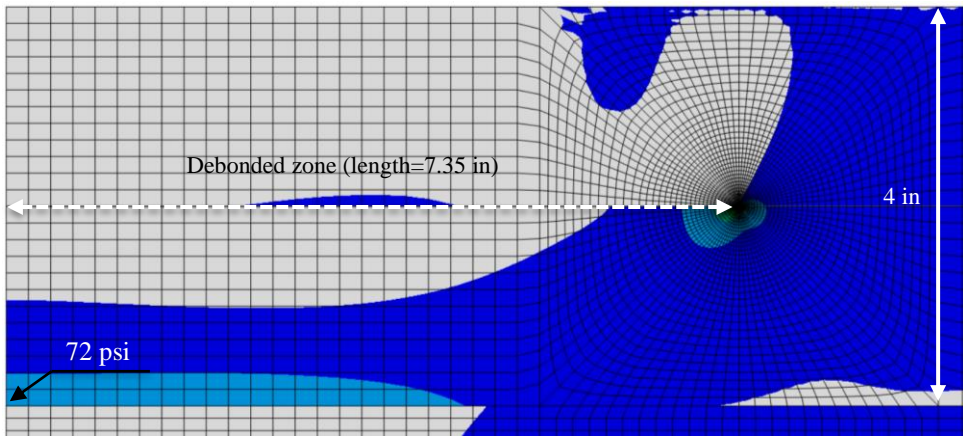


c. Coefficient of friction=0.65

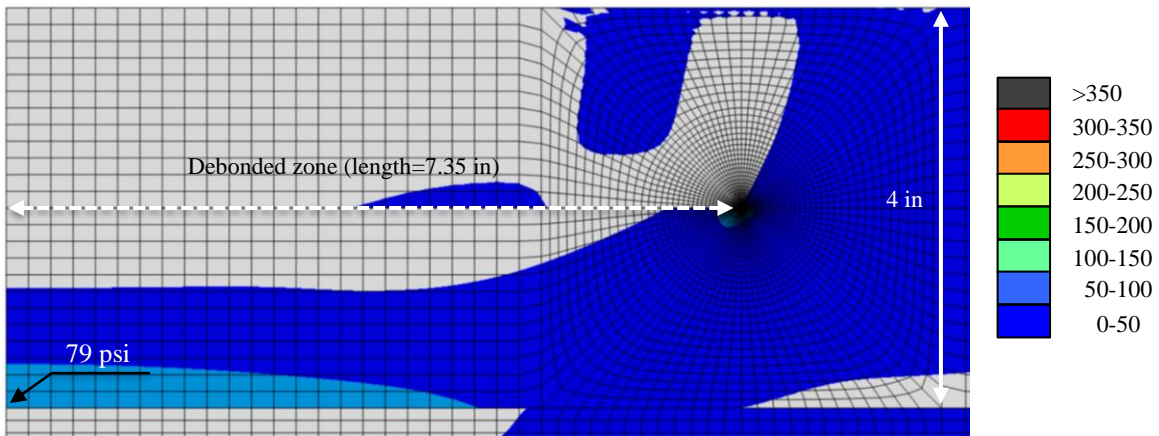
Figure 5-17 Horizontal shear stress distribution (psi) throughout the AC layer of a 4-in AC section with SR=5 for different interface friction coefficients.



a. Frictionless interface



b. Coefficient of friction=0.3



c. Coefficient of friction=0.65

Note: white areas denote compression

Figure 5-18 Maximum tensile stress distribution (psi) throughout the AC layer of a 4-in AC section with SR=5 for different interface friction coefficients.

An increase in shear stress around the interface was also observed when a friction coefficient was assigned to the section with SR=5 (Figure 5-17). Although the tensile stress at the AC bottom barely changed for this section (Figure 5-18), the absence of tension above the interface resulting from its frictional response was even more evident than in the case of SR=32.

Finally, the effect of interface frictional response on the tensile stress below the tip of the debonded zone is plotted in Figure 5-19. For both stiffness ratios, the introduction of frictional resistance along the localized debonded zone reduced the magnitude of tensile stress.

Nonetheless, an intensification zone immediately behind the debonded tip, where cracking can initiate, was found in all cases.

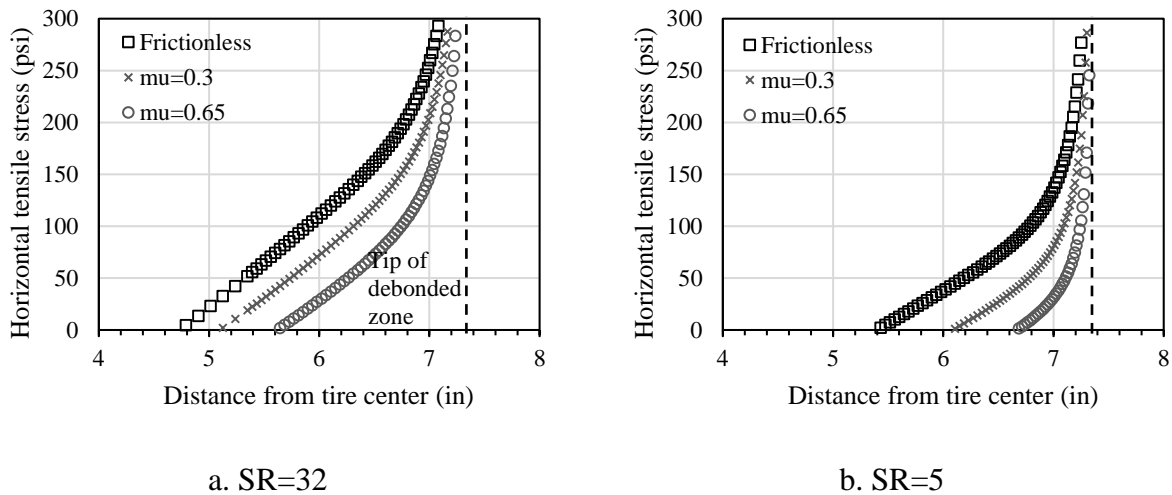


Figure 5-19 Horizontal tensile stress below 2-in deep interface (psi) for a 4-in AC pavement section with varying friction coefficients.

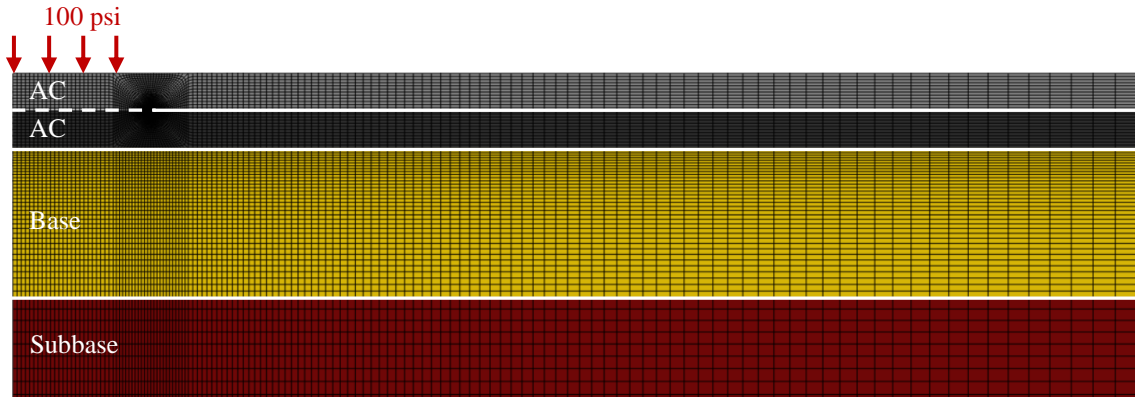
These results show the frictional response of the debonded portion of the interface reduced the likelihood of bottom-up cracking under the tire while the potential remained for cracking to initiate below the tip of the debonded zone. Although a frictional response is more realistic, it is computationally very expensive and sometimes prevents convergence of the solution. For this reason, a frictionless condition will be used for the remaining analyses in favor of faster computational time and a better ability to evaluate more factors. Furthermore, the focus will be placed on the area surrounding the tip of the debonded strip (as opposed to under the tire) since

the analysis showed that this location yielded the maximum tension and, thus, the greatest likelihood of crack development.

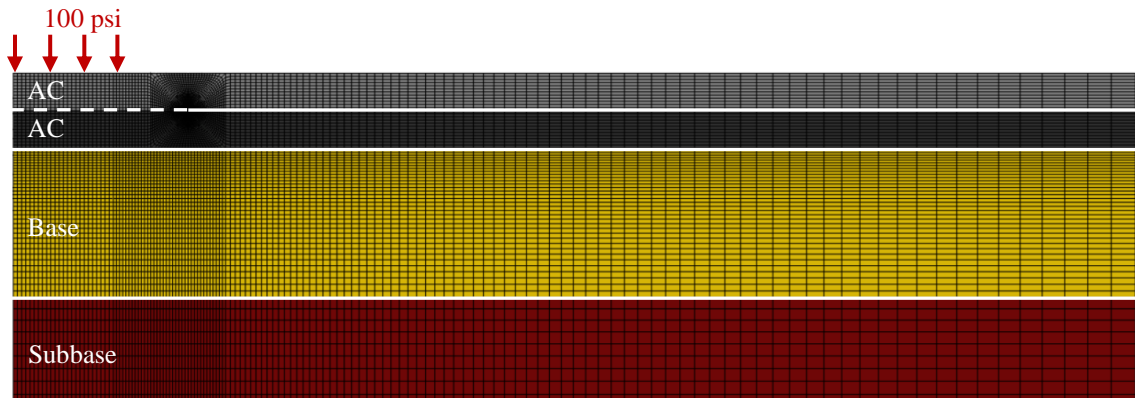
5.4.1.4 Effect of debonding extent

Section 4.3 showed the lateral movement of traffic loads within the lane can increase the extent of the debonded strip up to 10 inches from each edge of the tire when a typical standard deviation is considered for traffic wander. This section investigated the effect of debonding extent on the stress distribution of a 4-in AC pavement section with SR=32. As illustrated in Figure 5-20, the evaluated debonded extent, measured from the center of the tire to the tip of debonded zone, was 7.35 in (2 in from tire edge), 9.35 (4 in from tire edge) and 15.35 (10 in from tire edge).

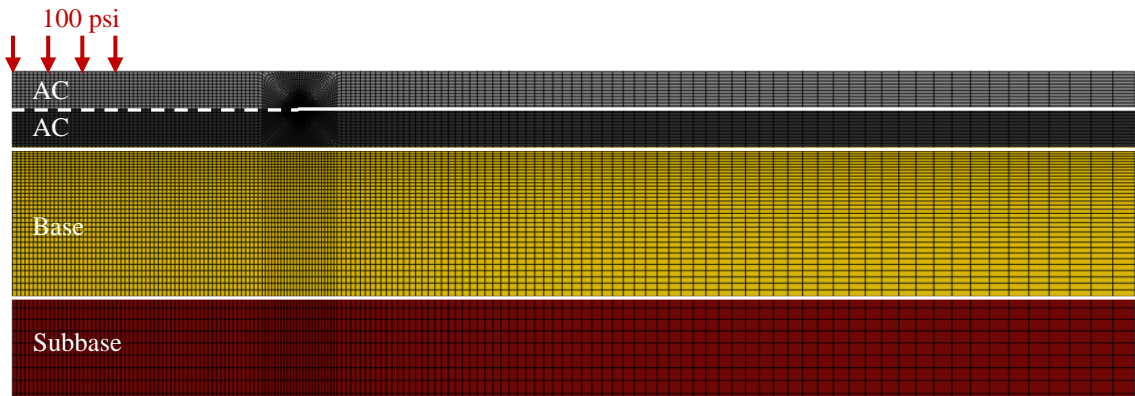
Figure 5-21 plots the horizontal tensile stress distribution below the interface for three different debonding extent values. For a fair comparison, the horizontal axis refers to the distance from the tip of the debonded zone as opposed to the distance from the tire center used above. Negative values of the horizontal axis indicate the zone of analysis is behind the tip of the debonded zone. As shown in Figure 5-21, the average tensile stress behind the tip increased with the extent of the debonded zone, regardless of the fact the distance between the edge of the tire and the tip of the debonded zone increases. This may be explained by the loss in the structural efficiency of the section resulting from a larger debonded zone. Note that this effect diminished as the distance to the tip reduced, i.e., the tensile stress distribution for the three extents tended to collapse together. Overall, the average tensile stress behind the tip was greater for debonding extend values of 9.35 in and above.



a. Debonding extent = 7.35 in (2 in from tire edge)



b. Debonding extent = 9.35 in (4 in from tire edge)



c. Debonding extent = 15.35 in (10 in from tire edge)

Figure 5-20 Finite element models for evaluation of extent of debonded zone (half model due to symmetry).

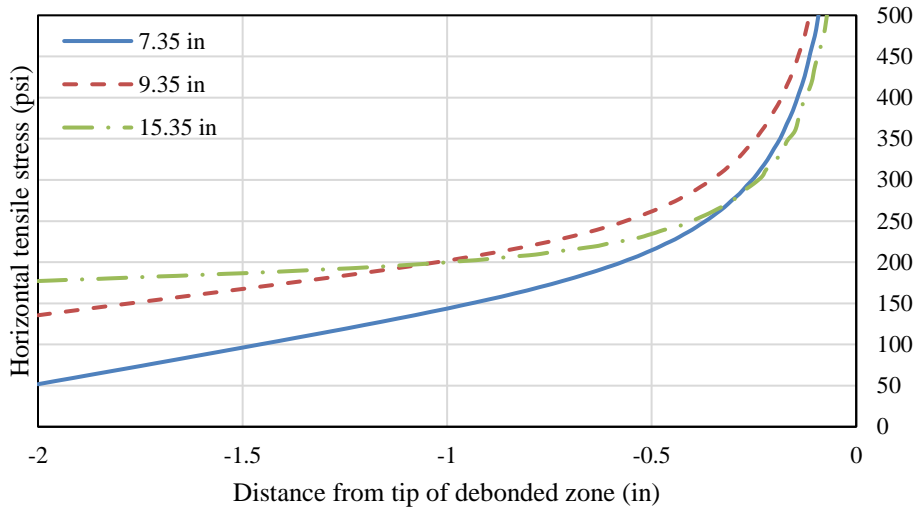


Figure 5-21 Horizontal tensile stress below 2-in deep interface for a 4-in AC pavement section with SR=32 and varying debonding extent.

5.4.1.5 Effect of traffic wander

Traffic wander was examined by laterally moving a tire load relative to a 24-in wide debonded strip in the wheelpath (debonding extent comprised a 10-in wide tire load, 2 in of debonding from each tire edge and 10 in of wander). Since the model is no longer symmetric when wander is introduced, the original FE model had to be modified, resulting in the 2D plane-strain model shown in Figure 5-22. The load was moved only in one direction (left) and a maximum lateral displacement of 22 in from the center of the wheelpath to the center of the tire was considered.

Maximum tensile stress distributions for a 4-in AC pavement section with SR=32 and different tire load locations are detailed in Figure 5-23. When the load was located at the center of the wheelpath, tensile stresses concentrated below both tips of the debonded strip as noted by the red areas in Fig. 5-23a. However, as the load moved toward the outside of the wheelpath, tension at the nearest tip started to decrease (Fig. 5-23b) until the center of the load aligned with the tip of the debonded strip and tension peaked above the interface (Fig. 5-23c). Moreover, tension above the interface was also found when the inner edge of the tire aligned with the tip of the debonded strip (Fig. 5-23d). The same pattern was found for a pavement section with SR=5, as shown in Figure 5-24.

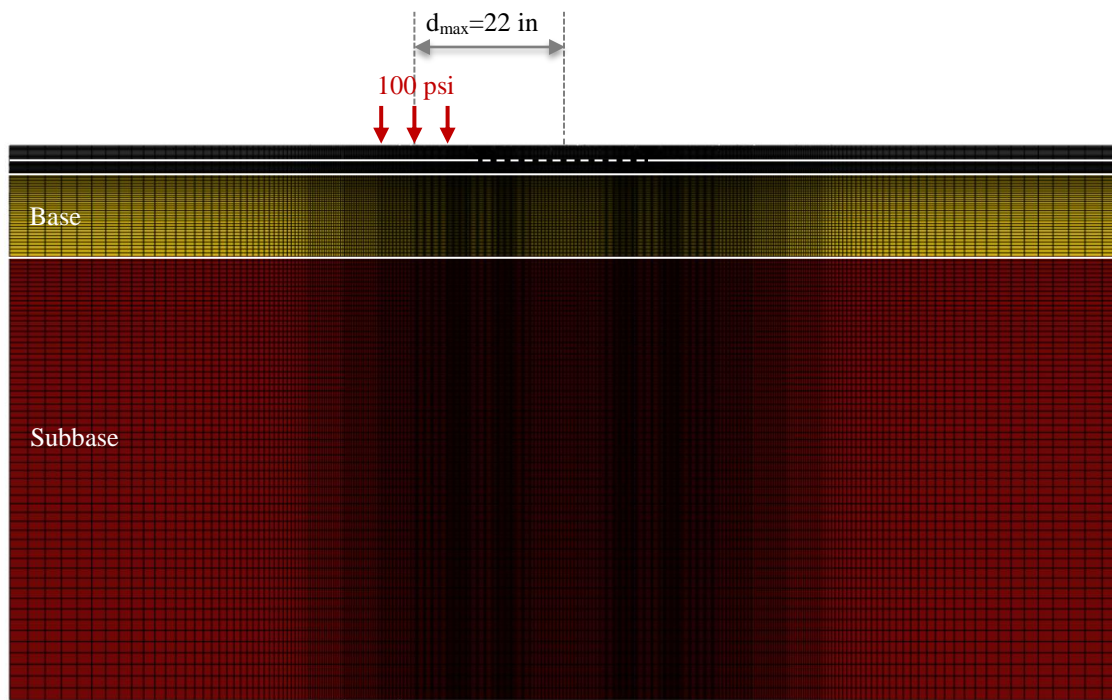
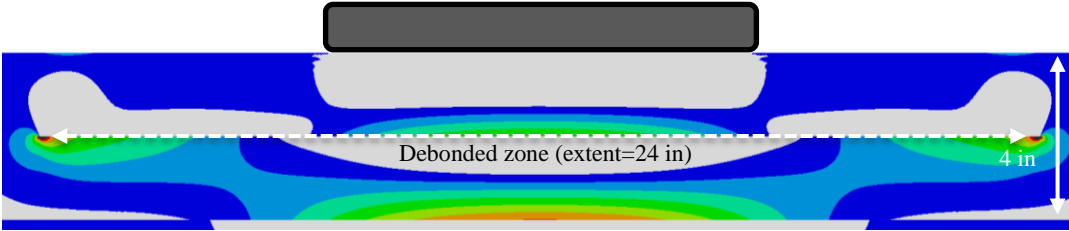


Figure 5-22 2D plane-strain FE model for evaluation of traffic wander effects (entire wheelpath).

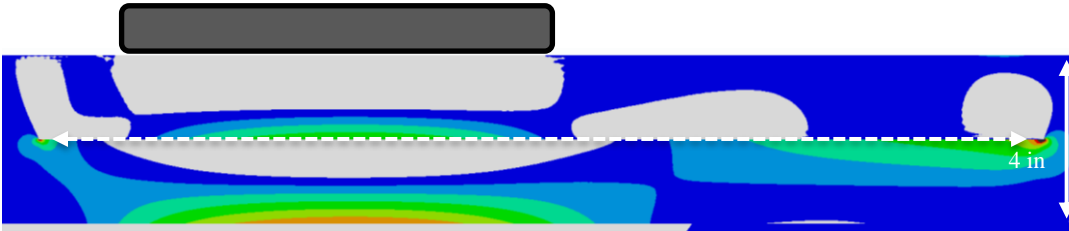
Results in Figures 5-23 and 5-24 show that, in addition to the tensile zone identified below the tip of the debonded zone, traffic wander may also promote crack initiation above the interface.

5.4.2 Potential failure mechanisms

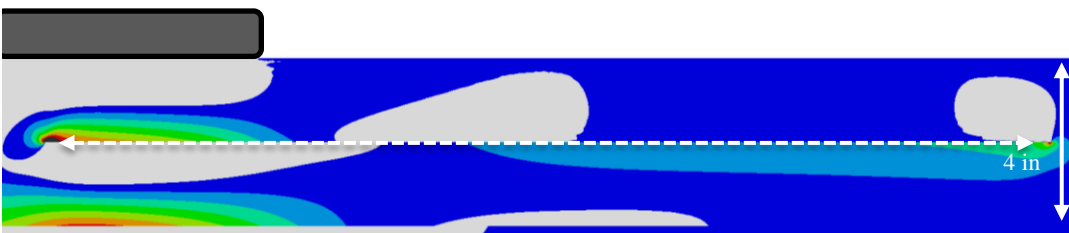
The evaluation of maximum tensile stress (i.e., maximum tensile stress failure criterion) identified two potential locations for crack initiation in a pavement with a debonded strip located 2 in below the wheelpath. The first location was below the tip of the debonded strip due to bending of the pavement structure when a load was applied at the center of the wheelpath. The second location was above the tip of the debonded strip when the load was moved laterally in the wheelpath to simulate traffic wander. The objective of this section was to study the potential propagation of a crack initiated at these two locations.



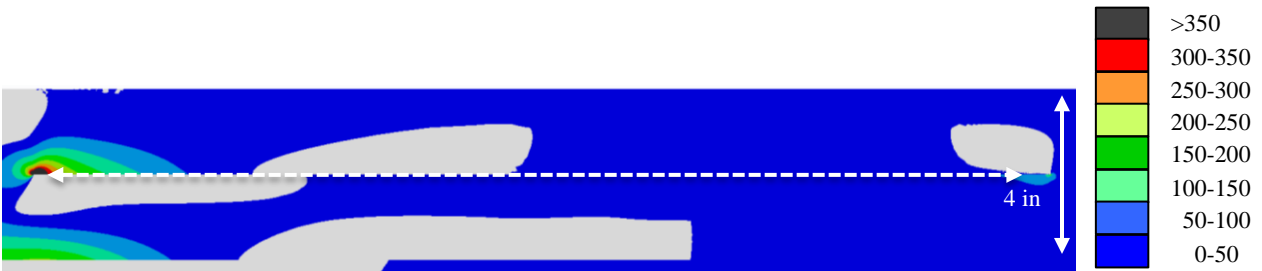
a. Load centered on wheelpath



b. Load center moved 5 in from wheelpath center



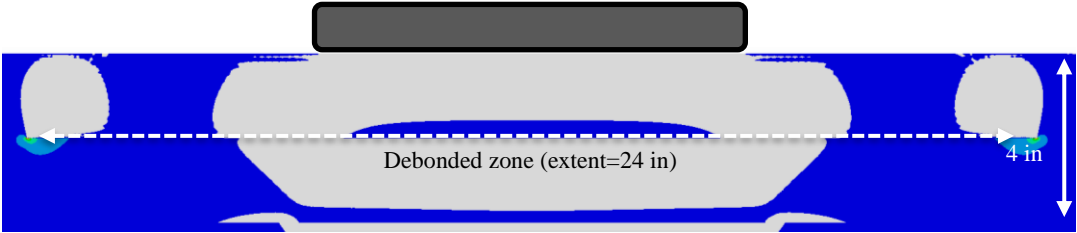
c. Load center moved 12 in from wheelpath center



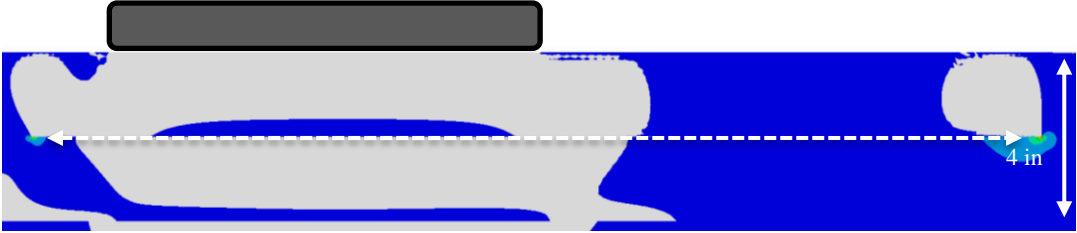
d. Load center moved 17 in from wheelpath center

Note: white areas denote compression.

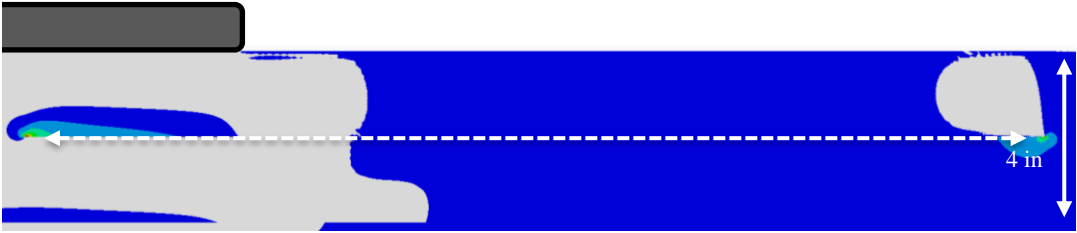
Figure 5-23 Maximum tensile stress distribution (psi) throughout the AC layer of a 4-in AC section with SR=32 for different tire load locations.



a. Load centered on wheelpath



b. Load center moved 5 in from wheelpath center



c. Load center moved 12 in from wheelpath center



d. Load center moved 17 in from wheelpath center

Note: white areas denote compression.

Figure 5-24 Maximum tensile stress distribution (psi) throughout the AC layer of a 4-in AC section with SR=5 for different tire load locations.

5.4.2.1 Crack initiated below tip of debonded strip

A debonded strip along the wheelpath led to high tensile stress below the tip of the debonded zone, particularly in the case of a high surface-to-base stiffness ratio or a stiffness gradient in the AC layer. Moreover, analysis of the principal stresses revealed the most likely direction for crack initiation was vertical since tensile stress was maximum along a horizontal plane. This section describes the results of analyses performed on a 4-in AC pavement structure in which a vertical crack was introduced below the tip of the debonded strip. Prior research at the University of Florida (Zhang et al., 2001) showed crack propagation in asphalt mixtures is a step-wise process where cracks tend to propagate in increments of about 0.2 in (approximately the average mixture particle size). For this reason, initial crack length was set at 0.2 in. Introduction of a crack required to redefine the model geometry to properly capture the stress field around the crack tip (Figure 5-25). The crack was modeled by means of two frictionless surfaces with no penetration allowed in the normal direction.

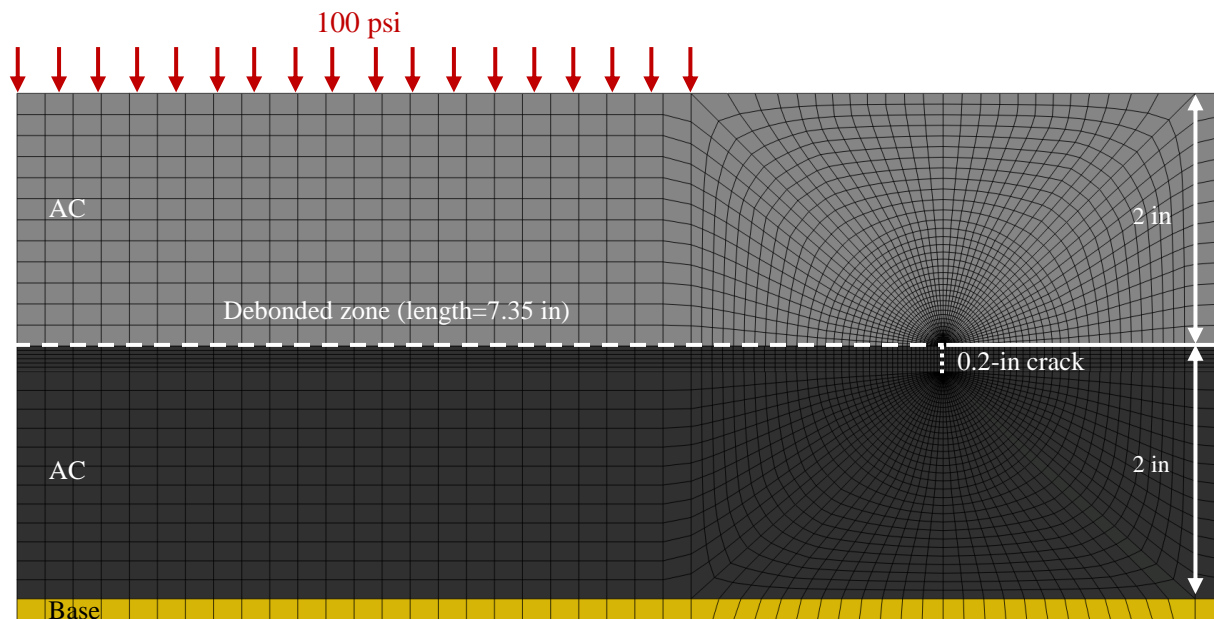


Figure 5-25 2D plane-strain FE model with a 0.2-in crack below tip of debonded strip (half model due to symmetry).

Figure 5-26 shows the maximum tensile stress distribution for two different stiffness ratios (SR) in a 4-in AC pavement structure with a 0.2-in crack below the tip of the debonded strip. An area of stress intensification below the lower tip of the crack was found in both cases (note the

potential direction of crack propagation was initially unknown). No tension was found above the tip of the debonded strip. Hence, this finding indicated cracking could potentially propagate downward.

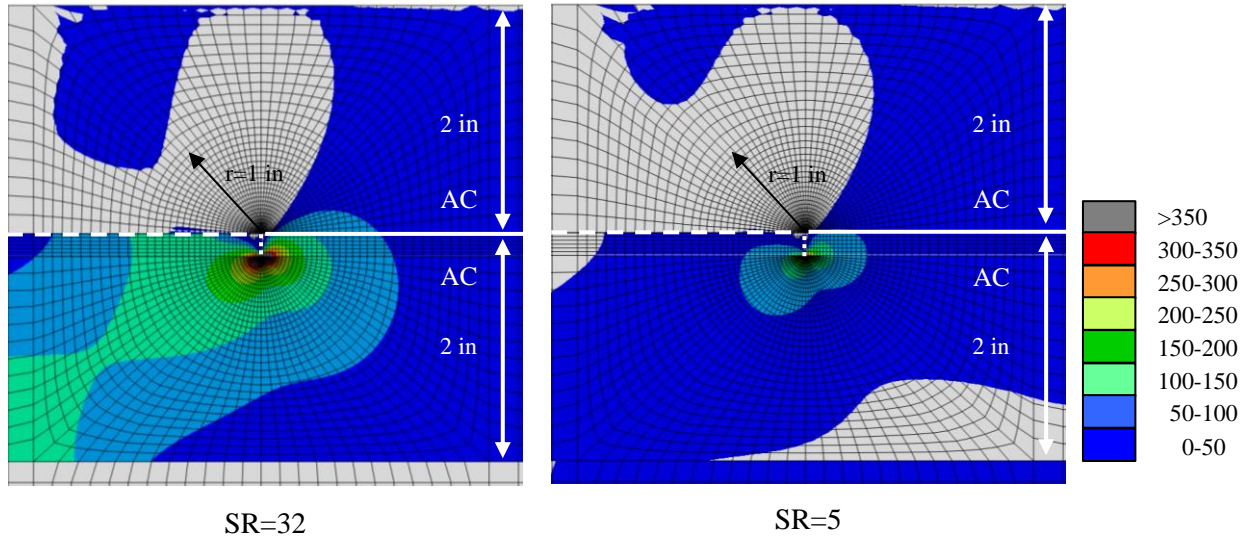


Figure 5-26 Maximum tensile stress distribution of a 4-in AC pavement structure with a 0.2-in crack below tip of debonded strip and varying stiffness ratio (SR).

Although these results seemed to indicate a debonded strip below the wheelpath may lead to progressive downward crack propagation, field studies show longitudinal cracks in the wheelpath rarely, if ever, reach the bottom of the AC layer without reaching or reflecting to the surface of the pavement (Figure 5-27). Therefore, it appears that factors other than bending due to wheel load represented by the FEM analysis are involved in propagation to the surface of a crack initiated at the interface. Additional factors may include thermal cycles, differential aging and wheel load wander. For example, these factors are known to promote the reflection of longitudinal joints in composite pavements in the form of longitudinal cracks on the surface. Similarly, a crack initially developed below the tip of the debonded strip may potentially result in reflective longitudinal cracking (as detailed in Figure 5-28), which is more consistent with field observations than progressive downward propagation.

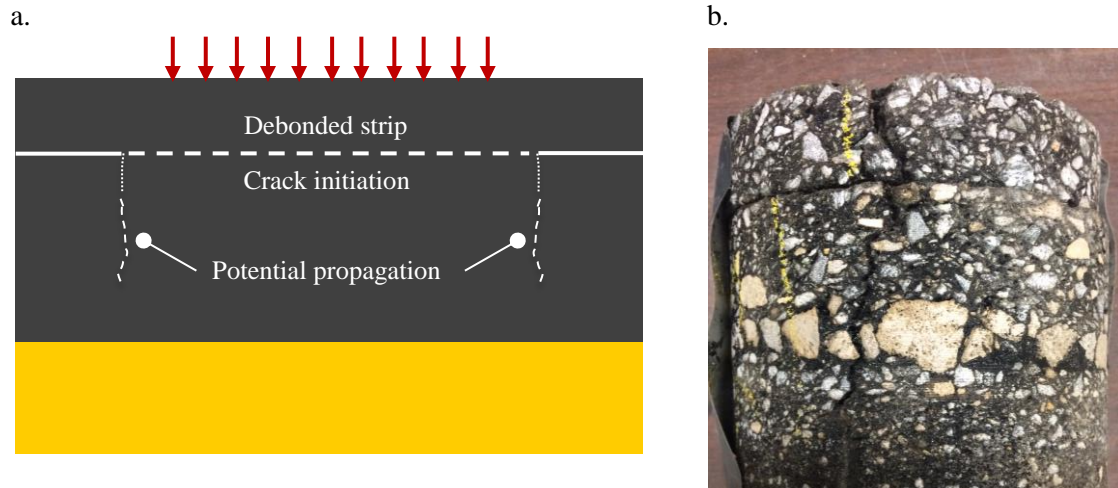


Figure 5-27 Propagation of a crack initiated below tip of debonded strip: a. Prediction from FE model (downward propagation); b. Field observation (crack through the entire AC layer).

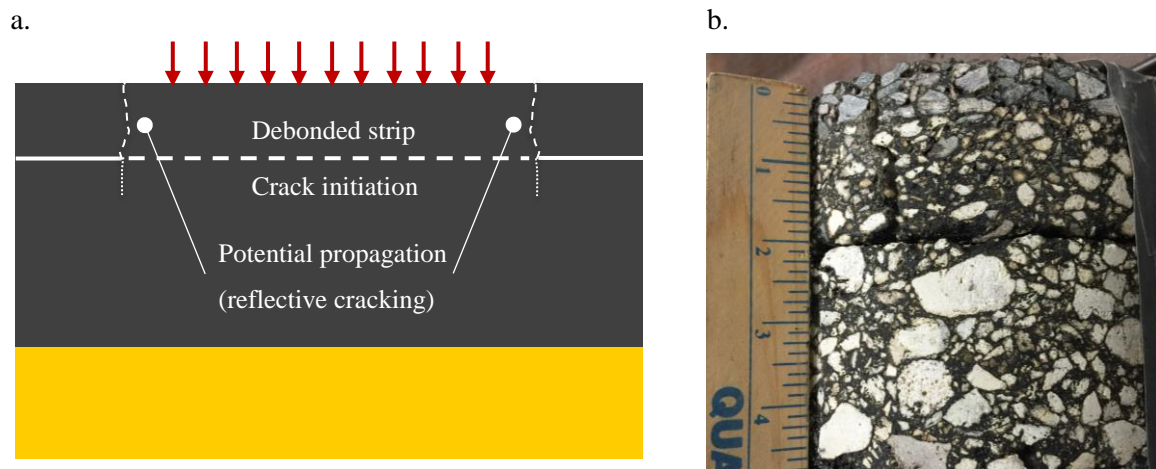


Figure 5-28 Propagation of a crack initiated below tip of debonded strip: a. Interpretation of FE results (reflective cracking); b. Field observation (crack above the interface).

5.4.2.2 Crack initiated above tip of debonded strip

This section examines the potential propagation of a crack initiated above the tip of a debonded strip as a result of traffic wander. Since the load was moved laterally to simulate traffic wander, symmetry no longer applied and a model of the entire wheelpath had to be developed. As shown in Figure 5-29, a debonded strip was located 2 in below the wheelpath and the center of a load

was aligned with one of the tips of the debonded strip to simulate the lateral displacement of a tire within the lane. Debonding extent was set to 24 in, which comprised a 10-in wide tire load, 2 in of debonding from each tire edge and 10 in of wander. As detailed in Figure 5-30, a 0.2-in crack was introduced above the edges of the debonded strip in order to study the potential direction of propagation.

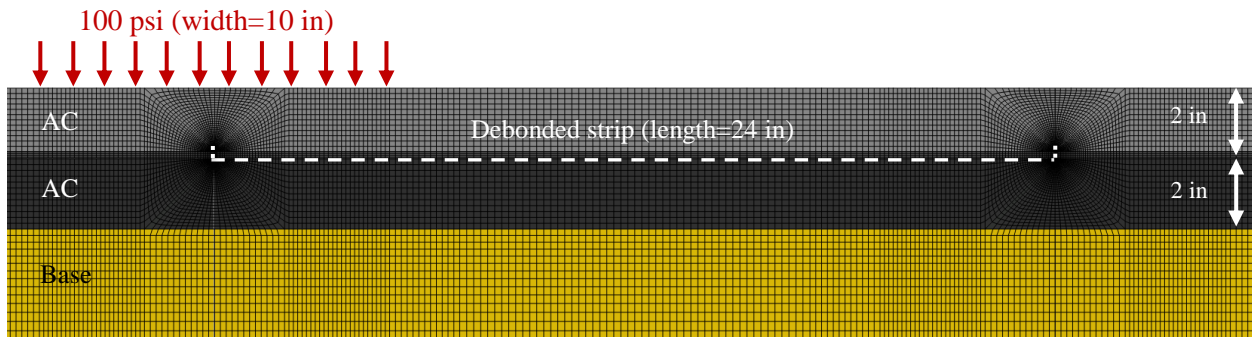


Figure 5-29 2D plane-strain FE model with a 0.2-in crack above tip of debonded strip (entire wheelpath).

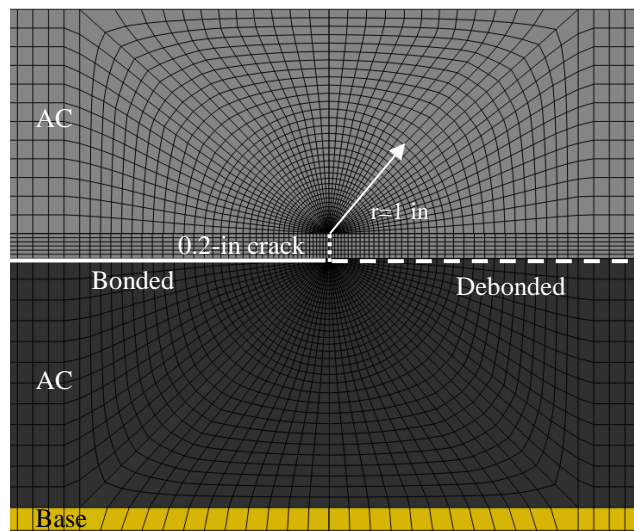


Figure 5-30 Detail of FE model with a 0.2-in crack above tip of debonded strip (left tip shown).

Maximum tensile stress distribution for two different stiffness ratios (SR) in a 4-in AC pavement structure with a 0.2-in crack above the tip of the debonded strip is shown in Figure 5-31. A large area of intensified tensile stress was found above the upper tip of the crack for both SR values. Therefore, upward propagation of a crack initiated at the interface seemed to be a likely cracking

mechanism when traffic loads reached the tip of the debonded strip. This mechanism could explain the presence of near-surface longitudinal cracking in the wheelpath observed in the field.

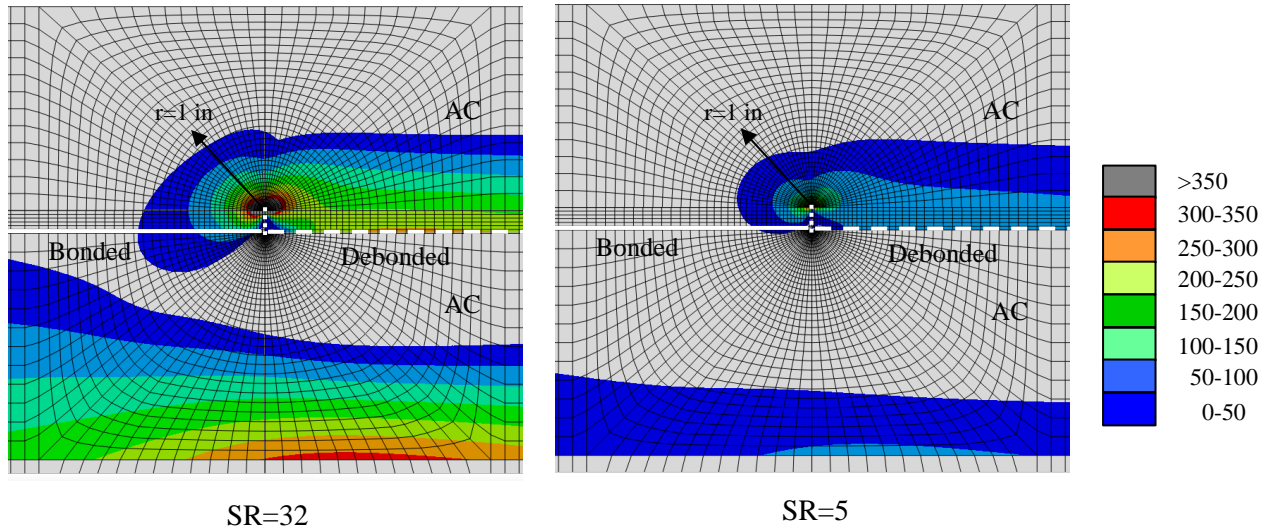


Figure 5-31 Maximum tensile stress distribution of a 4-in AC pavement structure with a 0.2-in crack above tip of debonded strip and varying stiffness ratio (SR).

5.5 Investigation based on energy of distortion

5.5.1 Distortion concept

Section 5.4 evaluated potential mechanisms of cracking based on a maximum tensile stress failure criterion alone. However, stress distributions presented in Figure 5-7 revealed existence of high shear stress, particularly around the tip of the debonded zone, which can result in large material distortion. Different criteria have been reported in the literature to study failure when large distortion is involved. One of these criteria involves the octahedral shear stress, which represents the maximum shear distortion at a point. Several authors have used this approach to study rutting potential of asphalt mixture in the intermediate-high temperature range (Wang and Al-Qadi, 2009, Ozer et al., 2012). Another criterion more commonly used for the study of cracking is the maximum distortion strain energy (energy associated with changes in material shape), also known as Von Mises failure theory. Von Mises stress is calculated as follows:

$$\sigma_{VM} = \sqrt{\frac{(\sigma_1 - \sigma_2)^2 + (\sigma_2 - \sigma_3)^2 + (\sigma_3 - \sigma_1)^2}{2}} \quad (5.3)$$

where σ_1 , σ_2 , and σ_3 are the three principal stresses at a point.

The distortion strain energy at a point (Eq. 5.2) is related to the square of Von Mises stress and two material properties: elastic modulus (E) and Poisson's ratio (ν). Thus, the greater the Von Mises stress at a point, the greater the distortion experienced by the material.

$$U_{distortion} = \frac{1 + \nu}{3E} \cdot \sigma_{VM}^2 \quad (5.4)$$

Distortion has been extensively studied in granular materials. Figure 5-32 depicts a planar array of rigid spheres that represent the different particles of a granular material. When a densely-packed array is loaded, the particles override each other in order to accommodate the deformation imposed by the load (Fig. 5-32b). This motion must be accompanied by an increase in the volume of the array, which is known as dilation. Thus, when a densely-packed array of granular particles is loaded, volume increases (space is created) prior to failure.

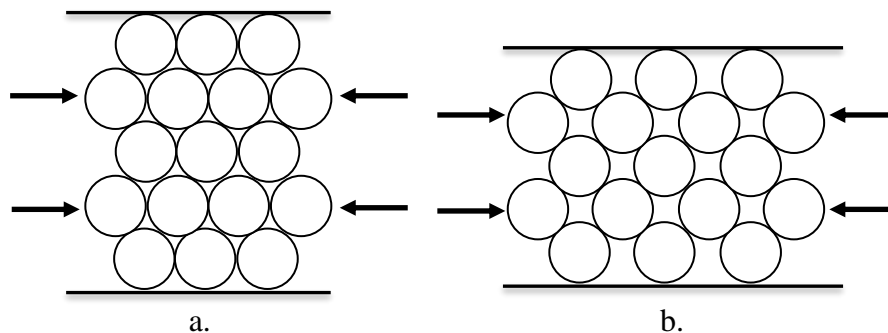


Figure 5-32 Effect of loading in a granular material. a. Initially dense array of particles; b. Increase in volume (dilation) before failure (Lambe and Whitman, 1969).

This phenomenon, clearly known in granular materials, is believed to occur also in asphalt mixtures (Figure 5-33). However, the difference is that mixtures contain asphalt binder filling most of the voids within the densely-packed granular particles (aggregates). Therefore, when a

mixture is loaded, the increase in volume is partially restrained by the asphalt binder (Fig. 5-33b), which will internally experience tension (Fig. 5-33c). This tension can lead to failure, either by detachment of the binder from the surface of the aggregate (adhesive failure) or by initiation of a crack within the binder (cohesive failure).

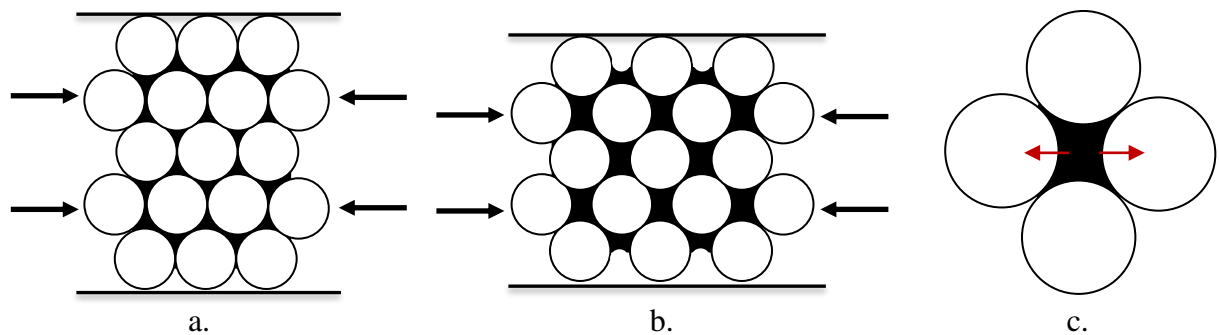


Figure 5-33 Effect of loading in an asphalt mixture. a. Initially dense array of particles; b. Increase in volume (dilation) before failure; c. Internal tension induced in the binder.

The development of internal tensile stresses resulting from large distortion that can lead to failure in asphalt mixtures was verified through micromechanical analysis by Wang et al. (2003). Therefore, the study of Von Mises stress as a surrogate for the strain energy of distortion is key to identifying potential mechanisms of cracking since it reflects the presence of internal stresses not directly predicted by conventional stress analyses of layered systems. This section examined the Von Mises stress for a range of pavement sections with the purpose of identifying potential locations of failure as well as assessing the relative effect of multiple factors (stiffness ratio, interface friction and traffic wander) on the stress distribution of a pavement with a debonded strip along an interface located 2 in below the wheelpath. Results were obtained from finite element analyses with the computer program ABAQUS on 2D plane-strain models of linear elastic pavement structures subjected to a uniform, static load.

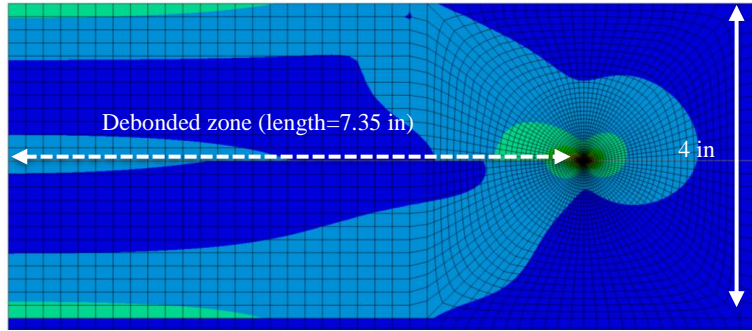
5.5.2 Parametric study

5.5.2.1 Effect of stiffness ratio

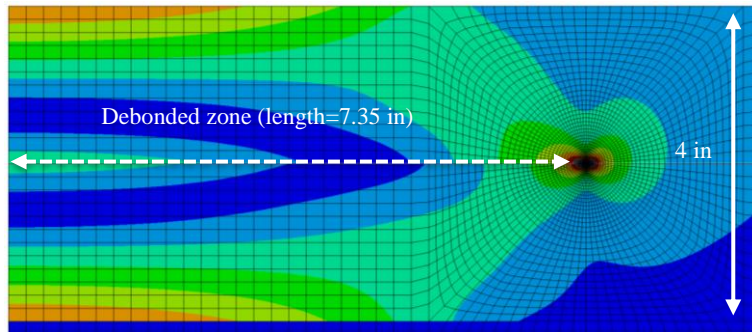
This section employed the 4-in AC pavement section modeled in Figure 5-4 with a debonded strip located 2 in below the wheelpath. The debonded strip was modeled as two frictionless surfaces in contact, whereas the remaining portion of the interface was defined as fully bonded (no slip allowed).

Figure 5-34 shows Von Mises stress distribution throughout the AC layer for a pavement section with four different stiffness ratios (5, 20, 32 and a gradient). The four cases evaluated showed that Von Mises stress intensified (red areas) around the tip of the debonded zone. For the case of a stiffness gradient in the AC layer (Figure 5-34d), which simulates the fact that oxidative aging is greatest at the surface and decreases with depth, a large area of high stress was found under the tire. However, maximum stress still occurred at the tip of the debonded zone. This suggests the tip of the debonded zone is the most likely location of failure in a pavement with localized interface debonding. Sections with higher AC-to-base stiffness ratio or a stiffness gradient posed a more critical condition given a larger area of high Von Mises stress.

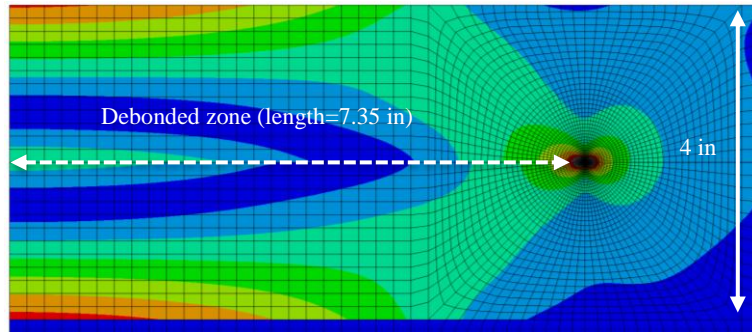
One significant difference between the maximum tensile stress criterion and Von Mises stress criterion is that the former identified a potential zone of failure only under the tip of the debonded strip whereas the latter yielded an entire failure zone surrounding the tip. Thus, when maximum strain energy of distortion is set as failure criterion, cracking can potentially initiate in any direction. Therefore, additional understanding of the conditions near the interface is needed to better define a direction of crack initiation. Studies by Coleri et al. (2012) showed both asphalt layers above and below the interface tend to show high air void content near the interface because of cooler boundaries during compaction. Air voids weaken the mixture and act as stress concentrators, which increase the likelihood for failure around the tip of the debonded zone. In other words, it is likely that air voids in one of the layers that meet at the interface define a plane of weakness along which a crack initiates. Furthermore, the layer above the interface is subjected to greater aging, which makes this layer stiffer, more brittle, less tough and generally more susceptible to failure. These factors suggest a greater chance for a crack to initiate in the layer above the interface.



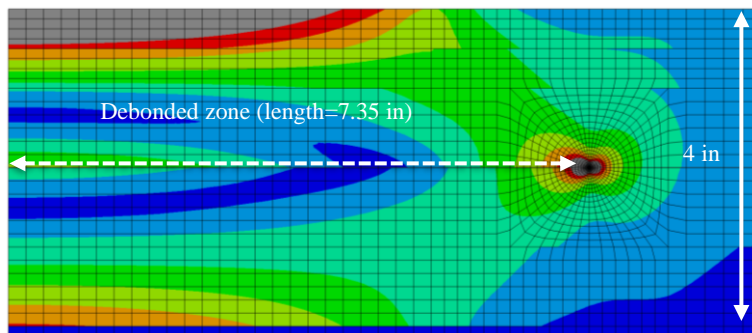
a. SR=5



b. SR=20



c. SR=32



d. Gradient

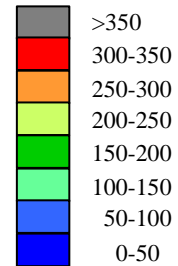


Figure 5-34 Von Mises stress distribution (psi) throughout the AC layer of a 4-in AC pavement section with varying stiffness ratio (SR).

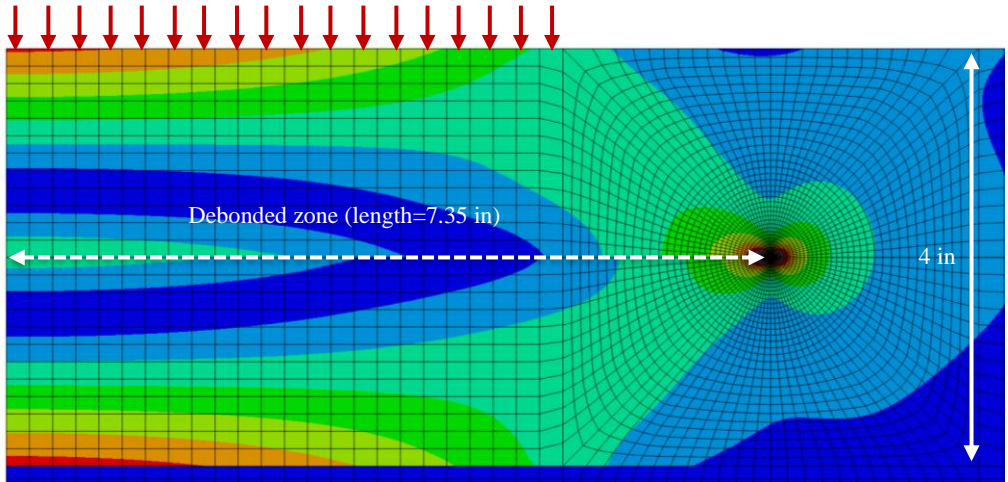
5.5.2.2 Effect of interface friction

Results in the previous section assumed the two surfaces in contact along the debonded strip were frictionless. This section evaluated the response of a 4-in AC pavement with two extreme stiffness ratios (SR=5 and SR=32) and three different static friction coefficients (0, 0.3 and 0.65). Friction coefficients were introduced to simulate a more realistic response of the debonded strip along the interface. The remaining portion of the interface was kept fully bonded.

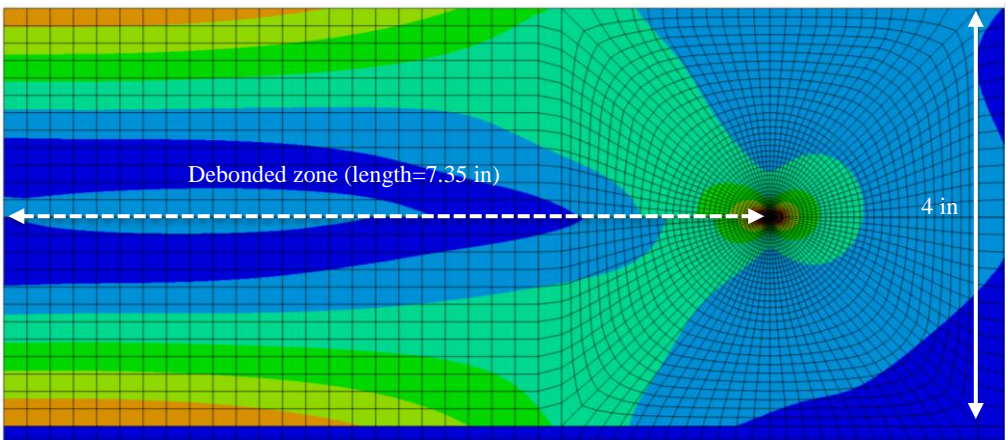
Figure 5-35 illustrates Von Mises stress distribution throughout the AC layer of a 4-in AC section with a stiffness ratio of 32. As the friction coefficient increased, stresses reduced due to the improved structural efficiency of the section, particularly near the interface and at the bottom of the AC layer. Note that the area of intensified stress around the tip of the debonded strip did not significantly reduce as the friction coefficient increased. Maximum stress was found at the tip of the debonded strip regardless of friction coefficient, indicating this was the location most likely for failure. The same observation was made when the stiffness ratio was reduced to 5 (Figure 5-36). Figures 5-35 and 5-36 support the existence of a potential zone of failure all around the tip of the debonded zone. Nevertheless, as described in the previous section, cracking is more likely to initiate above the tip of the debonded zone given the more aged conditions of the layer above the interface.

5.5.2.3 Effect of debonding extent

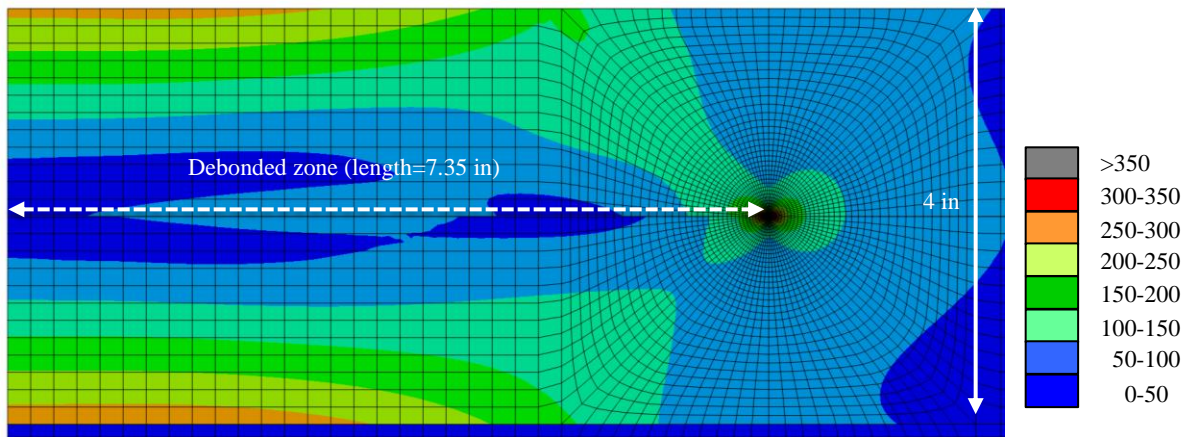
Debonding extent was examined by using the models depicted in Figure 5-20. Figure 5-37 shows Von Mises stress distribution around the tip of the debonded strip for three debonded extent values (measured from the center of the tire to the tip of debonded zone): 7.35 in (2 in from tire edge), 9.35 (4 in from tire edge) and 15.35 (10 in from tire edge). The three cases exhibited areas of high stress around the tip where failure is likely to occur. However, it is unclear whether an increase in debonding extent resulted in a more critical condition (maximum tensile stress analysis suggested failure was more likely as debonding extended increased). In fact, Figure 5-37b shows debonding extending up to 4 in from the tire edge yielded a larger area of intensified stress (gray area), which could indicate the existence of a critical debonding extent.



a. Frictionless interface

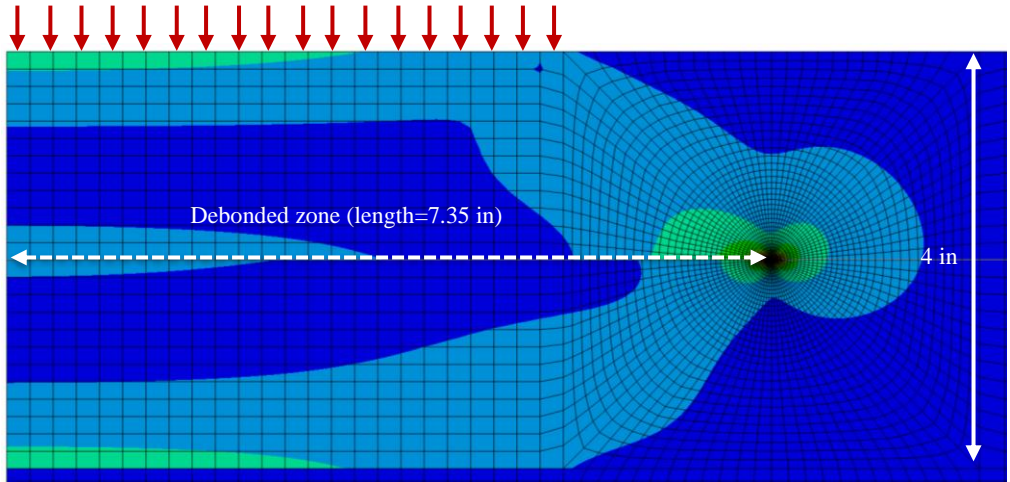


b. Coefficient of friction=0.3

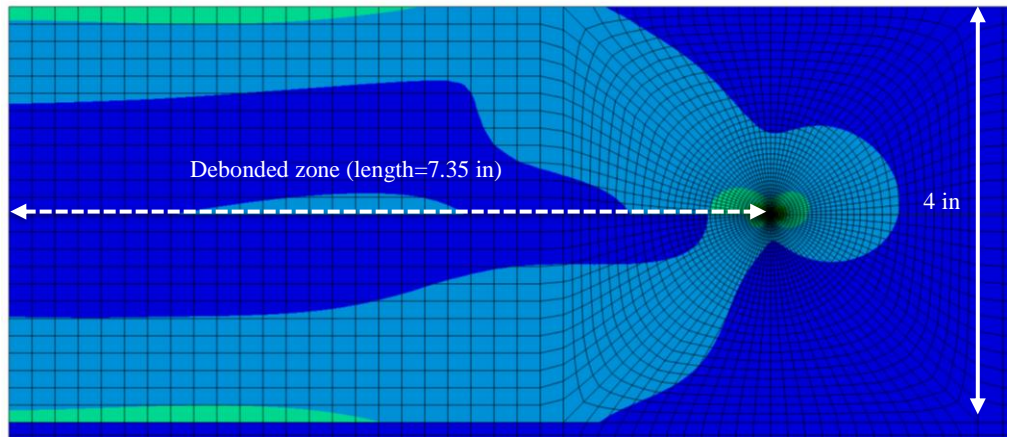


c. Coefficient of friction=0.65

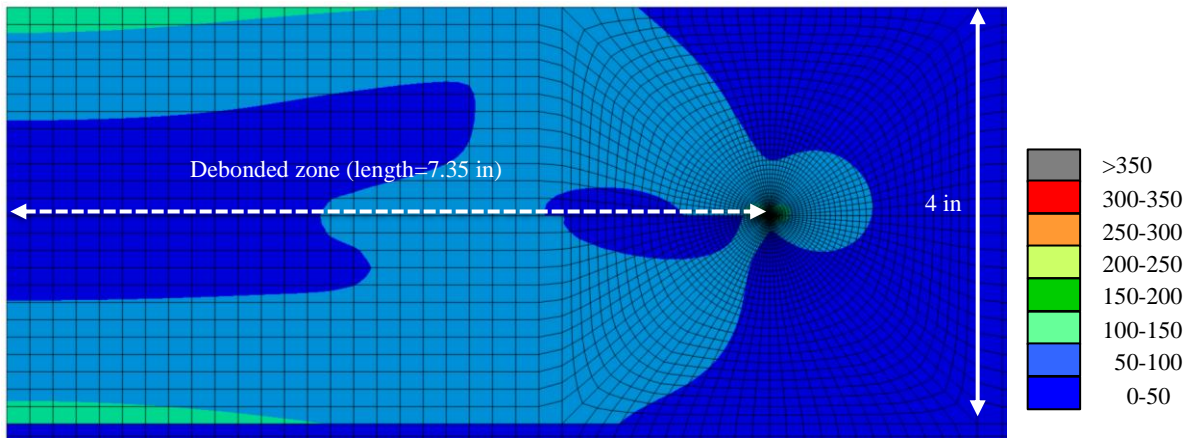
Figure 5-35 Von Mises stress distribution (psi) throughout the AC layer of a 4-in AC section with SR=32 for different interface friction coefficients.



a. Frictionless interface

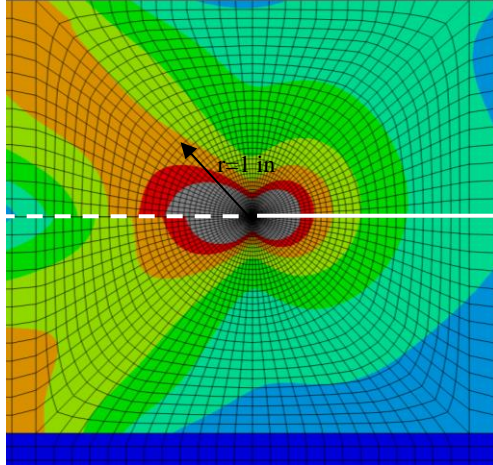


b. Coefficient of friction=0.3

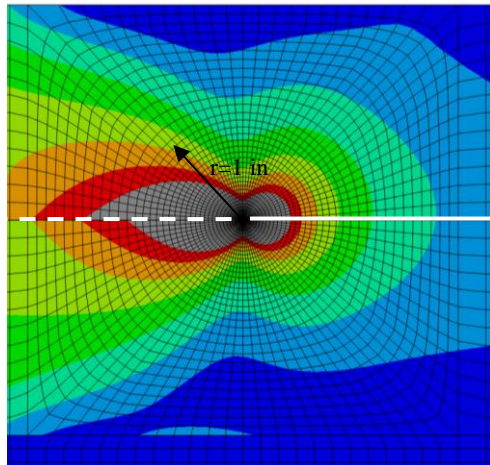


c. Coefficient of friction=0.65

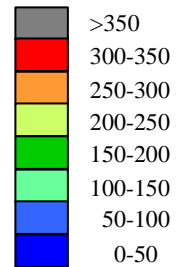
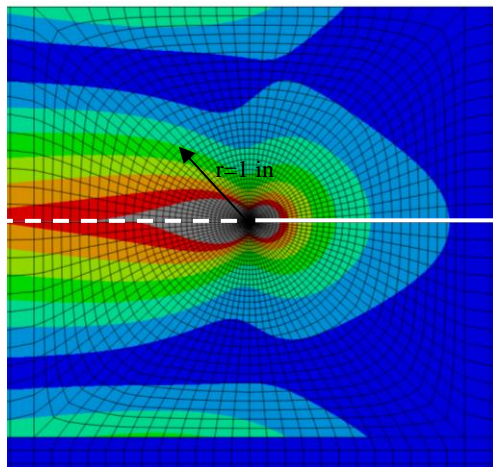
Figure 5-36 Von Mises stress distribution (psi) throughout the AC layer of a 4-in AC section with SR=5 for different interface friction coefficients.



a. Debonding extent = 7.35 in (2 in from tire edge)



b. Debonding extent = 9.35 in (4 in from tire edge)



c. Debonding extent = 15.35 in (10 in from tire edge)

Figure 5-37 Von Mises stress distribution (psi) around the tip of the debonded strip of a 4-in AC section with SR=32 and varying debonding extent.

5.5.2.4 Effect of traffic wander

The effect of traffic wander on Von Mises stress distribution was examined by laterally moving a tire load relative to a 24-in wide debonded strip in the wheelpath (debonding extent comprised a 10-in wide tire load, 2 in of debonding from each tire edge and 10 in of wander). The 2D plane-strain model of a complete wheelpath shown in Figure 5-22 was utilized for the analysis. Due to symmetry, the load was moved only in one direction (left) and the left tip of the debonded zone was chosen for analysis.

Results in Figure 5-39 show high concentration of stress around the tip of the debonded zone when the tire was applied at the center of the wheelpath (Figure 5-38a). When the tire moved toward the outside of the wheelpath, stress at the analyzed tip reduced (Fig. 5-38b and c) until the load center was aligned with the tip of the debonded strip (Fig. 5-38d), which was the condition where Von Mises stress was maximum and the probability of crack initiation was the greatest. Additional lateral movement (Fig. 5-38e and f) resulted in lower stress. These results showed traffic wander can promote initiation of cracking, particularly in the event of a tire load reaching the tip of the debonded zone. Again, a complete zone of potential failure was found around the tip when distortion was set as failure criterion.

5.5.3 Potential failure mechanisms

Section 5.4 revealed existence of a potential zone of failure around the tip of the debonded strip, where a crack can potentially develop. Since the asphalt layer above the interface is subjected to higher levels of aging, its tolerance to fracture is diminished and crack initiation is more likely through this upper layer. This section evaluated the case of a 4-in AC pavement structure with two different SR values (5 and 32) in which a 0.2-in crack was introduced above the tip of the debonded strip. When the load was located in the middle of the wheelpath (Figure 5-39), both cases exhibited an intensification in Von Mises stress around the crack, which indicated propagation is likely to happen. Again, it is believed the presence of a stiffer, more brittle and less fracture tolerant asphalt mixture near the pavement surface may promote upward crack propagation.

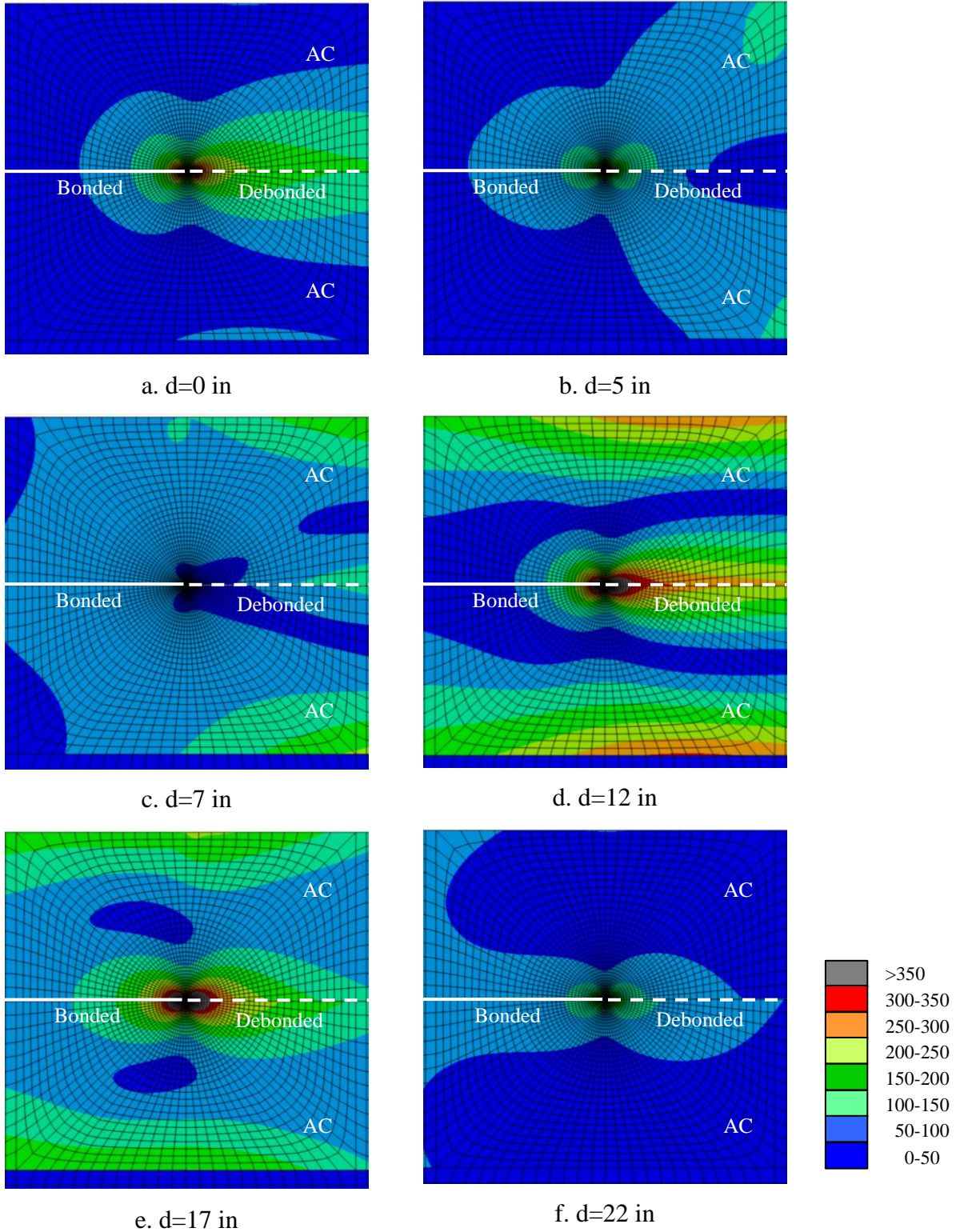


Figure 5-38 Von Mises stress distribution (psi) throughout the AC layer of a 4-in AC section with $SR=32$ for different tire load locations (d =distance from the center of the wheelpath to the load center).

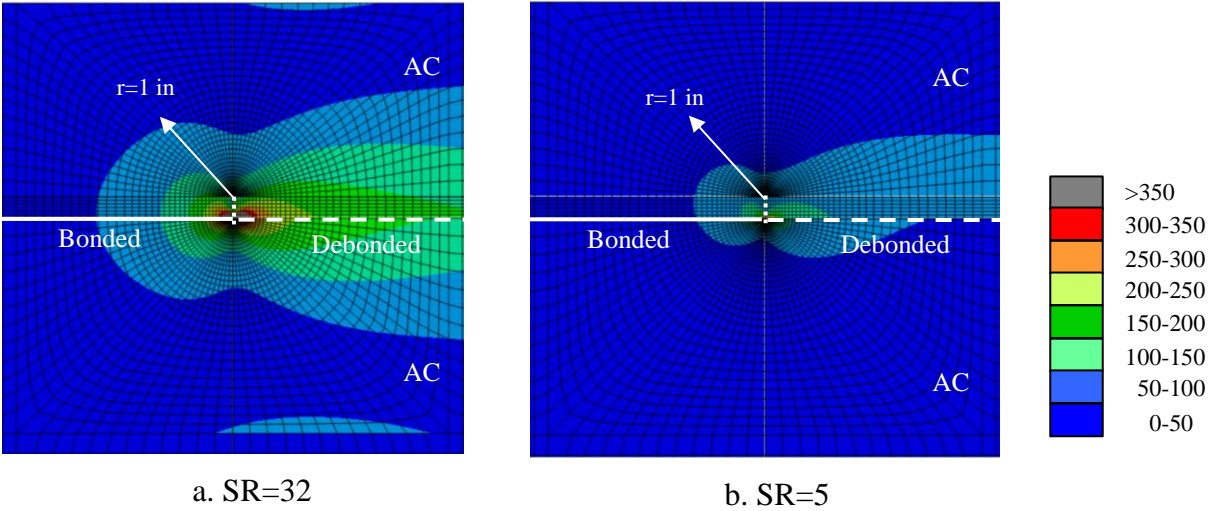


Figure 5-39 Von Mises stress distribution (psi) throughout the AC layer of a 4-in AC section with a 0.2-in crack above the interface (load centered in wheelpath).

Figure 5-40 depicts Von Mises stress was notably greater (larger distortion level) when a load was laterally moved to the edge of the debonded strip to simulate traffic wander. Comparison of stress distributions in Figures 5-39 and 5-40 revealed a crack initiated above the tip of the debonded zone was more likely to propagate when the center of the load aligned with the tip of the debonded strip, in other words, traffic wander can potentially accentuate crack propagation. Of note, a greater stiffness ratio posed a more critical condition at both loading locations.

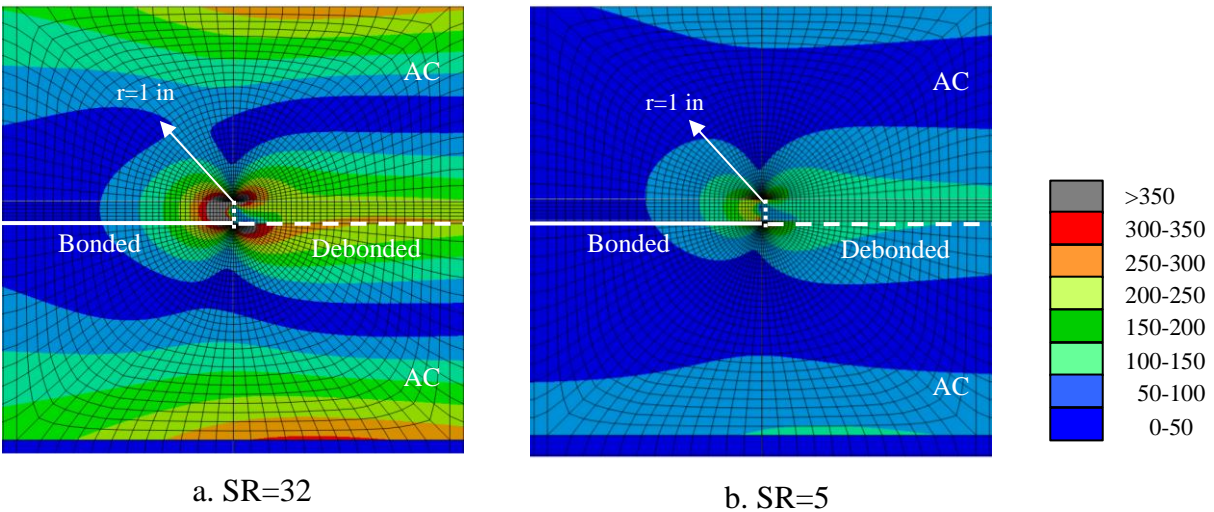


Figure 5-40 Von Mises stress distribution (psi) throughout the AC layer of a 4-in AC section with a 0.2-in crack above the interface (load aligned with tip of debonded strip).

CHAPTER 6

FINDINGS AND CONCLUSIONS

6.1 Summary of findings

This report described a comprehensive modeling effort aimed at examining the potential impact of localized interface debonding on near-surface longitudinal cracking in the wheelpath of asphalt pavements. The following findings were made:

- Analyses of a pavement structure under varying modeling conditions and loading modes showed the use of an equivalent elastic analysis with a static load was suitable for the study of critical stress states potentially conducive to interface debonding.
- A critical zone defined by stress states of high shear stress (>25 psi) coupled with low confinement was found for a broad range of depths (between 1 and 3 in) with a maximum at about 2 in and extending to 2 in from the edge of the tire regardless of AC thickness. Structures with a high AC-to-base stiffness ratio or a stiffness gradient in AC layer resulting from field oxidative aging were more critical. This indicated localized interface debonding can potentially occur as a result of the repetition of these critical stress states when an interface between asphalt layers is present at an approximate depth of 2 in.
- Existence of a critical stress-state zone around the edge of a tire can promote a debonded strip along the wheelpath as truck traffic travels down the highway. The width of the debonded strip can range from 12 in for conventional tires with no wander to 42 in in the case of new-generation wide-base tires and a traffic wander standard deviation of 10 in.
- Singularities associated with a longitudinal debonded strip along the wheelpath result in more critical stresses on the transverse cross-section of a lane. Given the geometry of the problem, the use of 2D plane-strain modeling with a static load and equivalent elastic analysis appeared to be a suitable and computationally efficient way to examine the stress distribution resulting from a longitudinal debonded strip.
- The introduction of a debonded strip along the interface caused a stress redistribution that intensified shear stress ahead of the tip of the debonded zone and tensile stress immediately behind the tip. Tension at this location exceeded that under the tire, indicating near-surface longitudinal cracking is more likely at the wheelpath edges, which is consistent with field observations.

- A parametric study of maximum tensile stress on a pavement structure with a debonded strip under the wheelpath showed that sections with high AC-to-base stiffness ratio or a gradient in stiffness (field oxidative aging effect) were more susceptible to crack development. Also, crack initiation appeared to be more likely as debonding extent increased. Furthermore, introduction of frictional resistance along the debonded strip reduced the likelihood of bottom-up cracking below the center of the tire while the potential remained for cracking to initiate below the tip of the debonded zone. However, traffic wander was found to promote crack development above the tip of the debonded strip.
- A parallel parametric study of Von Mises stress, which is associated with the strain energy of distortion, revealed that the entire area surrounding the tip of the debonded strip was subjected to large distortion that can lead to internal tension and failure. High AC-to-base stiffness ratio and gradient in AC stiffness caused by oxidative aging increased the susceptibility to failure. Frictional resistance along the debonded strip did not significantly reduce stress intensification at the tip. Moreover, while the maximum tension criterion showed the likelihood of crack development increased as debonding extent increased, Von Mises stress indicated the existence of a critical debonding extent at which initiation of a crack was more likely. Regarding crack development, initiation of a crack above the tip of the debonded strip followed by upward propagation seemed dominant given the presence of an asphalt layer above the interface subjected to higher levels of aging with diminished tolerance to fracture.

6.2 Conclusions

This study identified the presence of critical stress states that can potentially lead to a debonded strip along an interface located about 2 inches below the wheelpath. Investigation of the stress redistribution resulting from the introduction of a debonded strip found three potential mechanisms for development of near-surface longitudinal cracking in asphalt pavements:

1. Bending caused by repeated traffic loads applied at the center of the wheelpath can initiate a crack below the tip of the debonded strip that can reflect to the surface due to traffic wander and thermal cycles, especially given near-surface differential aging in the asphalt mixture.

2. Traffic wander can initiate a vertical crack above the edge of the debonded strip and promote further upward propagation.
3. Internal tension due to partially restrained dilation in areas of large distortion around the edge of the debonded strip can induce failure. Since the asphalt layer above the interface is subjected to higher levels of aging, its tolerance to fracture is diminished, thereby making upward crack propagation more likely.

CHAPTER 7

RECOMMENDATIONS

The parametric analysis conducted in this study concluded that near-surface longitudinal cracking can likely develop in a pavement with a debonded strip along an interface below the wheelpath. Therefore, future efforts towards mitigating near-surface longitudinal cracking should focus on preventing debonding in the first place. A better understanding of the mechanism of interface bond breakdown under repeated shear stress induced by bending of the pavement structure (i.e., bending-induced shear) is warranted to prevent debonding. The current practice does not consider repeated shear when evaluating interfaces, but rather involves the use of strength tests to compare the potential performance of different bonding conditions. While this approach may be helpful in the case of slippage (failure of the uppermost interface due to large braking-induced shear), it remains to be seen whether strength is a meaningful property in terms of the resistance of a bonding agent to breakdown under repeated bending-induced shear stress. Identification of bonding agents and interface surface characteristics more resistant to interface bond breakdown can help prevent and, in turn, mitigate the occurrence of near-surface longitudinal cracking.

LIST OF REFERENCES

Asphalt Institute. (2001). *Construction of Hot Mix Asphalt Pavements*, Manual Series No. 22 (MS-22), Second edition. The Asphalt Institute, Lexington, KY.

Asphalt Institute. (2008). *Basic Asphalt Emulsion Manual*, Manual Series No. 19 (MS-19), Fourth edition. The Asphalt Institute, Lexington, KY.

Bonaquist, R. (2008). *Refining the Simple Performance Tester for Use in Routine Practice* (NCHRP Report 614). National Cooperative Highway Research Program, Transportation Research Board, Washington, D.C.

Canestrari, F., Santagata, E. (2005). “Temperature Effects on the Shear Behavior of Tack Coat Emulsions Used in Flexible Pavements”. *International Journal of Pavement Engineering*, Vol. 6 (1), pp. 39–46.

Cho, S., Karshenas, A., Tayebali, A. A., Guddati, M. N., Kim, Y. R. (2016). “A Mechanistic Approach to Evaluate the Potential of the Debonding Distress in Asphalt Pavements”. *International Journal of Pavement Engineering*, In Press.

Chun, S., Kim, K., Greene, J., Choubane, B. (2015). “Evaluation of Interlayer Bonding Condition on Structural Response Characteristics of Asphalt Pavement using Finite Element Analysis and Full-scale Field Tests”. *Construction and Building Materials*, Vol. 96, pp. 307-318.

Coleri, E., Harvey, J. T., Yang, K., Boone, J. M. (2012). “A Micromechanical Approach to Investigate Asphalt Concrete Rutting Mechanisms”. *Construction and Building Materials*, Vol. 30, pp. 36-49.

COST-Transport. (1997). *Long Term Performance of Road Pavements* (COST Action 324, Final Report). Office for Official Publications of the European Communities, Brussels/Luxembourg.

COST-Transport. (1999). *Development of New Bituminous Pavement Design Guide* (COST Action 333, Final Report). Office for Official Publications of the European Communities, Brussels/Luxembourg.

Diakhaté, M., Millien, A., Petit, C., Phelipot-Mardelé, A., Pouteau, B. (2011). “Experimental Investigation of Tack Coat Fatigue Performance: Towards an Improved Lifetime Assessment of Pavement Structure Interfaces”. *Construction and Building Materials*, Vol. 25, pp. 1123–1133.

Erlingsson, S., Said, S., McGarvey, T. (2012). “Influence of Heavy Traffic Lateral Wander on Pavement Deterioration”. *4th European Pavement and Asset Management Conference*, Malmö, Sweden, September 5-7.

Greene, J., Toros, U., Kim, S., Byron, T., Choubane, B. (2009). *Impact of Wide-Base Single Tires on Pavement Damage* (Research Report 09-528). Florida Department of Transportation (FDOT), State Materials Office, Gainesville, FL.

Huang, Y. H. (2004). *Pavement Analysis and Design* (2nd Edition). Pearson Education, Inc., Upper Saddle River, NJ.

Kim, J., Byron, T., Sholar, G. A., Kim, S. (2008). “Comparison of a Three-Dimensional Viscoelastic Pavement Model with Full-Scale Field Tests”. *87th Annual Meeting of the Transportation Research Board*, Washington, D.C.

Kruntcheva, M. R., Collop, A. C., Thom, N. H. (2006). “Properties of Asphalt Concrete Layer Interfaces”. *ASCE Journal of Materials in Civil Engineering*, Vol. 18 (3), pp. 467–471.

Lambe, T. W., Whitman, R. V. (1969). *Soil Mechanics*. John Wiley & Sons, New York, NY.

Maina, J. W., De Beer, M., Matsui, K. (2007). “Effects of Layer Interface Slip on the Response and Performance of Elastic Multi-layered Flexible Airport Pavement Systems”. *Proceedings of*

the 5th International Conference on Maintenance and Rehabilitation of Pavements and Technological Control, Utah, USA, August 8-10, pp. 145–150.

Mohammad, L. N., Elseifi, M. A., Bae, A., Patel, N., Button, J., Scherocman, J. A. (2012). *Optimization of Tack Coat for HMA Placement* (NCHRP Report 712). National Cooperative Highway Research Program, Transportation Research Board, Washington, D.C.

Mohammad, L. N., Raqib, M. A., Huang, B. (2002). “Influence of Asphalt Tack Coat Materials on Interface Shear Strength”. *Transportation Research Record: Journal of the Transportation Research Board*, No. 1789, pp. 56–65.

Muench, S. T., Moomaw, T. (2008). *De-Bonding of Hot Mix Asphalt Pavements in Washington State: An Initial Investigation* (Report No. WA-RD 712.1). Washington State Department of Transportation, Olympia, WA.

Myers, L. A. (1998). *Development and Propagation of Surface-Initiated Longitudinal Wheel Path Cracks in Flexible Highway Pavements*. Ph.D. Dissertation, University of Florida, Gainesville, FL.

Myers, L. A., Roque, R., Ruth, B., Drakos, C. (1999). “Measurement of Contact Stresses for Different Truck Tire Types to Evaluate Their Influence on Near-Surface Cracking and Rutting”. *Transportation Research Record: Journal of the Transportation Research Board*, No. 1655, pp. 175-184.

Ozer, H., Al-Qadi, I. L., Leng, Z. (2008). “Fracture-Based Friction Model for Pavement Interface Characterization”. *Transportation Research Record: Journal of the Transportation Research Board*, No. 2057, pp. 54–63.

Ozer, H., Al-Qadi, I. L., Wang, H., Leng, Z. (2012). “Characterisation of Interface Bonding between Hot-Mix Asphalt Overlay and Concrete Pavements: Modelling and In-situ Response to

Accelerated Loading”. *International Journal of Pavement Engineering*, Vol. 13 (2), pp. 181–196.

Raab, C., Partl, M. N. (2004). “Effect of Tack Coats on Interlayer Shear Bond of Pavements”. *Proceedings of the 8th Conference on Asphalt Pavements for Southern Africa*, Sun City, South Africa, 12-16 September.

Romanoschi, S. A., Metcalf, J. B. (2001a). “Characterization of Asphalt Concrete Layer Interfaces”. *Transportation Research Record: Journal of the Transportation Research Board*, No. 1778, pp. 132–139.

Romanoschi, S. A., Metcalf, J. B. (2001b). “Effects of Interface Conditions and Horizontal Wheel Loads on the Life of Flexible Pavement Structures”. *Transportation Research Record: Journal of the Transportation Research Board*, No. 1778, pp. 123–131.

Roque, R., Chun, S., Zou, J., Lopp, G., Villiers, C. (2011). *Continuation on Superpave Projects Monitoring* (FDOT Final Report BDK-75-977-06). University of Florida, Gainesville, FL.

Roque, R., Guarin, A., Wang, G., Zou, J., Mork, H. (2007). *Develop Methodologies/Protocols to Assess Cracking Potential of Asphalt Mixtures using Accelerated Pavement Testing* (FDOT Final Report BD545-49). University of Florida, Gainesville, FL.

Sholar, G. A., Page, G. C., Musselman, J. A., Upshaw, P. B., Moseley, H. L. (2004). “Preliminary Investigation of a Test Method to Evaluate Bond Strength of Bituminous Tack Coats”. *Journal of the Annual Meeting of the Association of Asphalt Paving Technologists*, Vol. 73, pp. 771–806.

Smitha, G., Ramachandramurthy, A., Nagesh, R. I., Shahulhameed, E. K. (2014). “Constitutive Modeling and Numerical Simulation of FRP Confined Concrete Specimens”. *Slovak Journal of Engineering*, Vol. 22 (3), pp. 31–36.

Sutanto, M. H. (2009). *Assessment of Bond between Asphalt Layers*. Ph.D. Dissertation, University of Nottingham, Nottingham, UK.

Tashman, L., Nam, K., Papagiannakis, T., Willoughby, K., Pierce, L., Baker, T. (2008). “Evaluation of Construction Practices that Influence the Bond Strength at the Interface between Pavement Layers”. *Journal of Performance of Constructed Facilities*, Vol. 22 (3), pp. 154–161.

Timm, D., Priest, A. (2005). *Wheel Wander at the NCAT Test Track* (Report 05-02). National Center for Asphalt Technology, Auburn, AL.

Uzan, J. (1976). “Influence of the Interface Condition on Stress Distribution in a Layered System”. *Transportation Research Record: Journal of the Transportation Research Board*, No. 616, pp. 71–73.

Uzan, J., Livneh, M., Eshed, Y. (1978). “Investigation of Adhesion Properties between Asphaltic Concrete Layers”. *Journal of the Annual Meeting of the Association of Asphalt Paving Technologists*, Vol. 47, pp. 495–521.

Wang, H. (2011). *Analysis of Tire-Pavement Interaction and Pavement Responses Using a Decoupled Modeling Approach*. Ph.D. Dissertation, University of Illinois at Urbana-Champaign, Urbana, IL.

Wang, G., Roque, R. (2011). “Impact of Wide-Based Tires on the Near-Surface Pavement Stress States Based on Three-Dimensional Tire-Pavement Interaction Model”. *Road Materials and Pavement Design*, Vol. 12 (3), pp. 639-662.

Wang, H., Al-Qadi, I. L. (2009). “Combined Effect of Moving Wheel Loading and Three-Dimensional Contact Stresses on Perpetual Pavement Responses”. *Transportation Research Record: Journal of the Transportation Research Board*, No. 2095, pp. 53-61.

Wang, L. B., Myers, L. A., Mohammad, L. N., Fu, Y. R. (2003). “Micromechanics Study on Top-Down Cracking”. *Transportation Research Record: Journal of the Transportation Research Board*, No. 1853, pp. 121-133.

West, R., Zhang, J., Moore, J. (2005). *Evaluation of Bond Strength between Pavement Layers* (NCAT Report No. 05-08). National Center for Asphalt Technology, Auburn, AL.

Willis, J. R., Timm, D. H. (2007). “Forensic Investigation of Debonding in Rich Bottom Pavement”. *Transportation Research Record: Journal of the Transportation Research Board*, No. 2040, pp. 107-114.

Zhang, Z., Roque, R., Birgisson, B., Sangpetngam, B. (2001). “Identification and Verification of a Suitable Crack Growth Law for Asphalt Mixtures”. *Journal of the Annual Meeting of the Association of Asphalt Paving Technologists*, Vol. 70, pp. 206-241.

APPENDIX A
 STRAIN RESPONSES OF THREE-DIMENSIONAL FINITE ELEMENT ANALYSIS

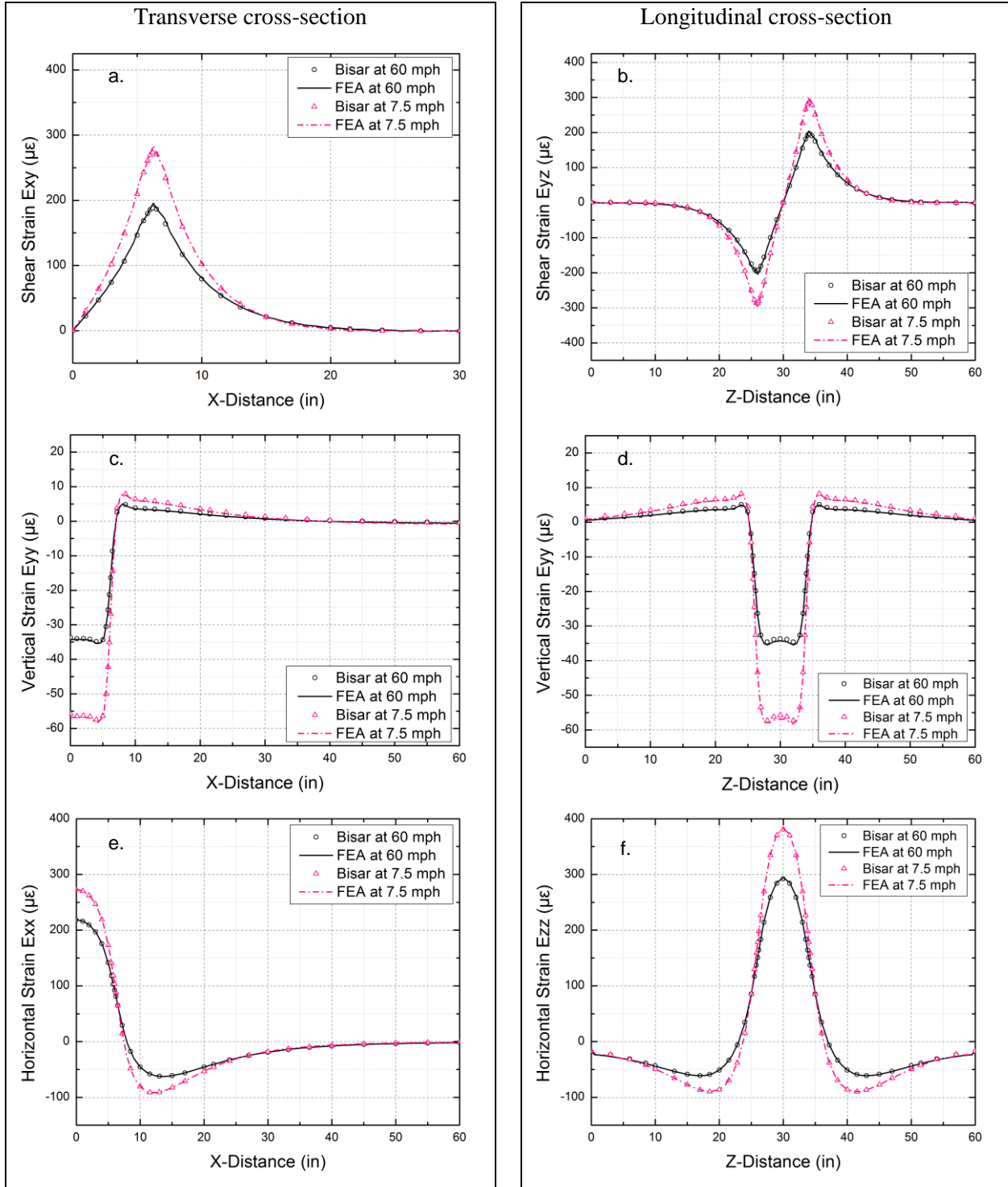


Figure A-1 Validation results of 3D FE model along transverse and longitudinal cross-sections.

a-b. Shear strain at AC mid-depth; c-d. Vertical strain at AC mid-depth; e-f. Horizontal strain at AC bottom.

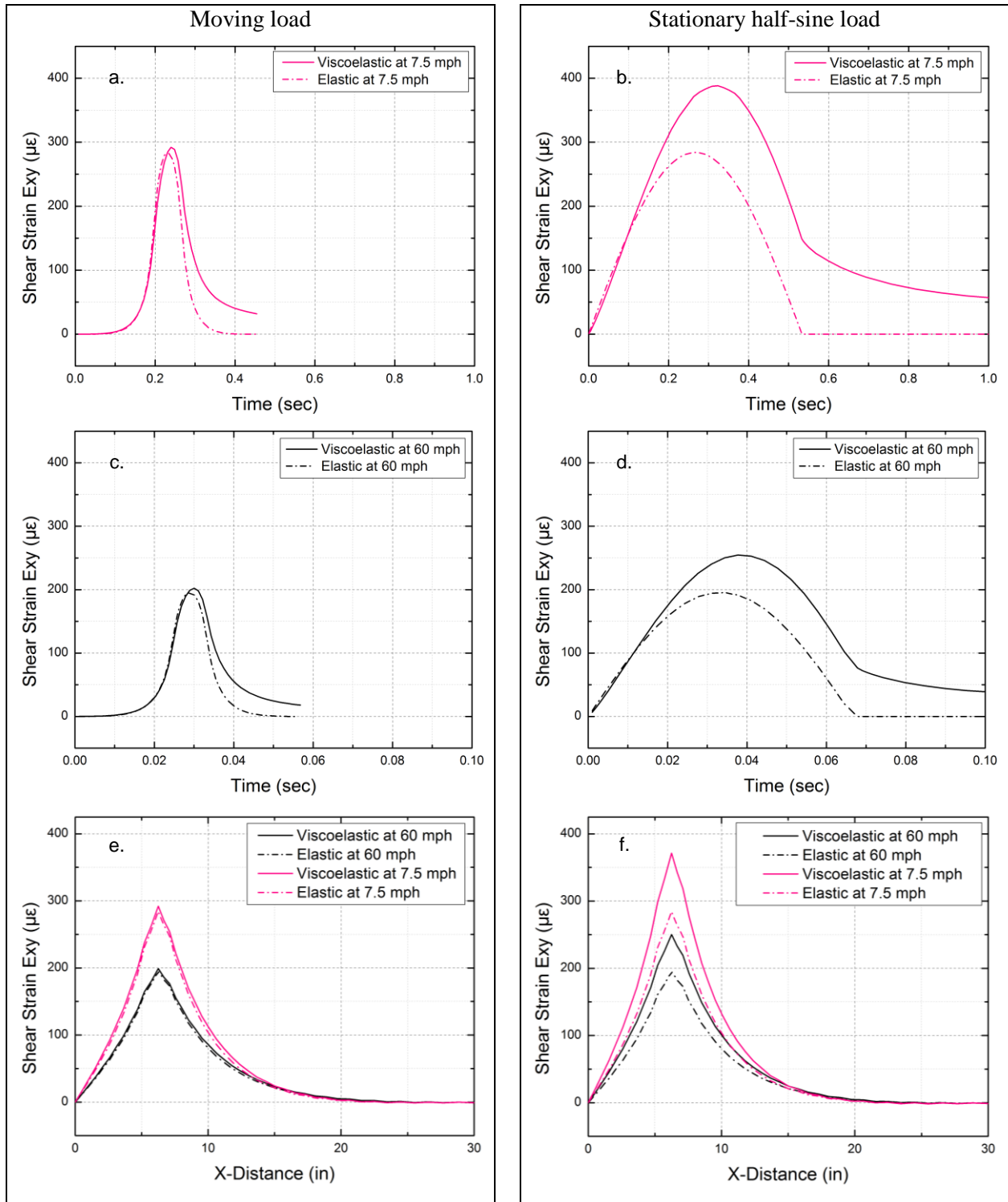


Figure A-2 3D shear strain (transverse) evaluation for moving and stationary half-sine load: a-b. Shear strain at L1 (slow traffic); c-d. Shear strain at L1 (fast traffic); e. Shear strain along AC mid-depth when moving load reached path center (slow/fast traffic); f. Shear strain along AC mid-depth at peak loading time (slow/fast traffic).

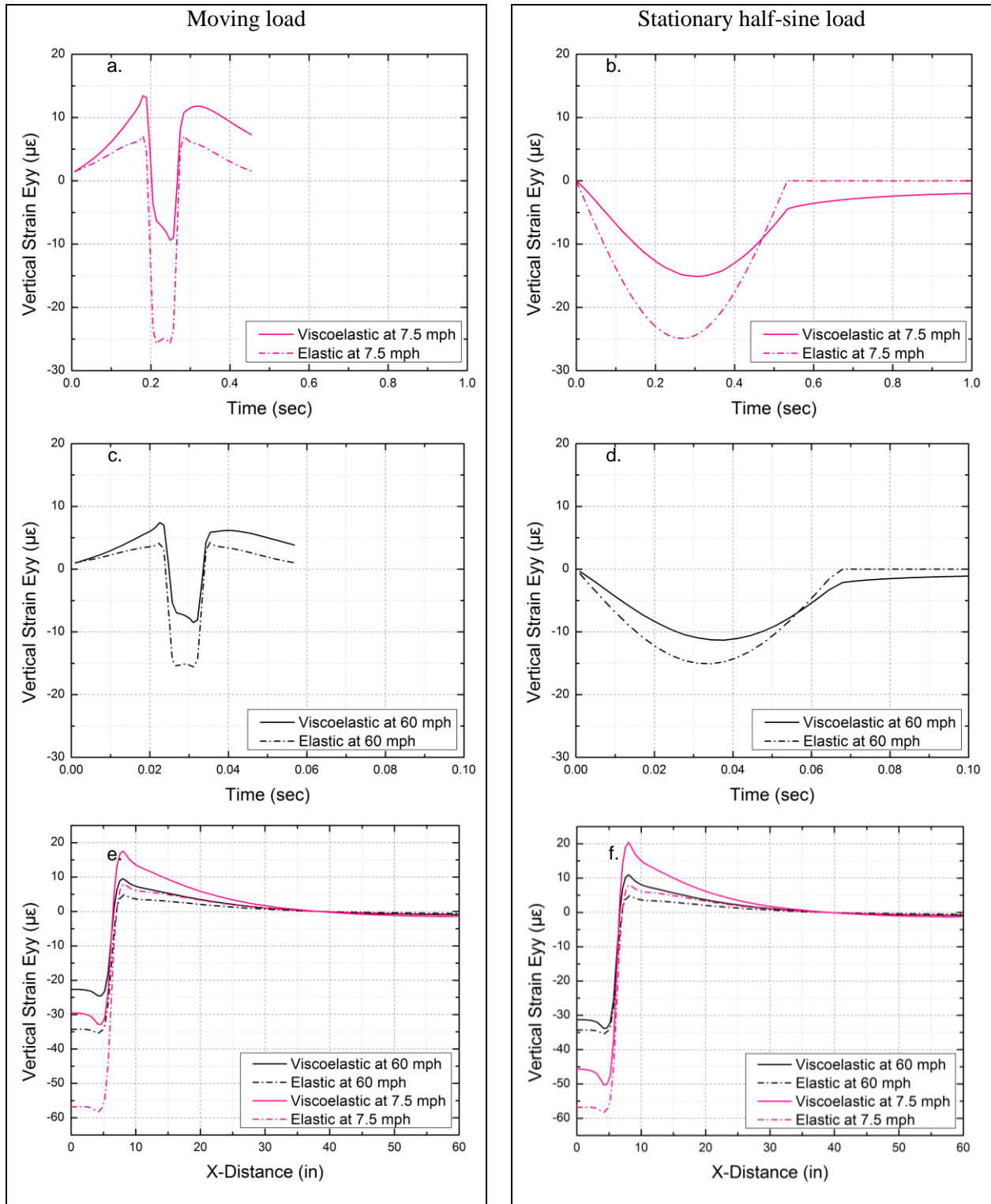


Figure A-3 3D vertical strain (transverse) evaluation for moving and stationary half-sine load: a- b. Vertical strain at L1 (slow traffic); c-d. Vertical strain at L1 (fast traffic); e. Vertical strain along AC mid-depth when moving load reached path center (slow/fast traffic); f. Vertical strain along AC mid-depth at peak loading time (slow/fast traffic).

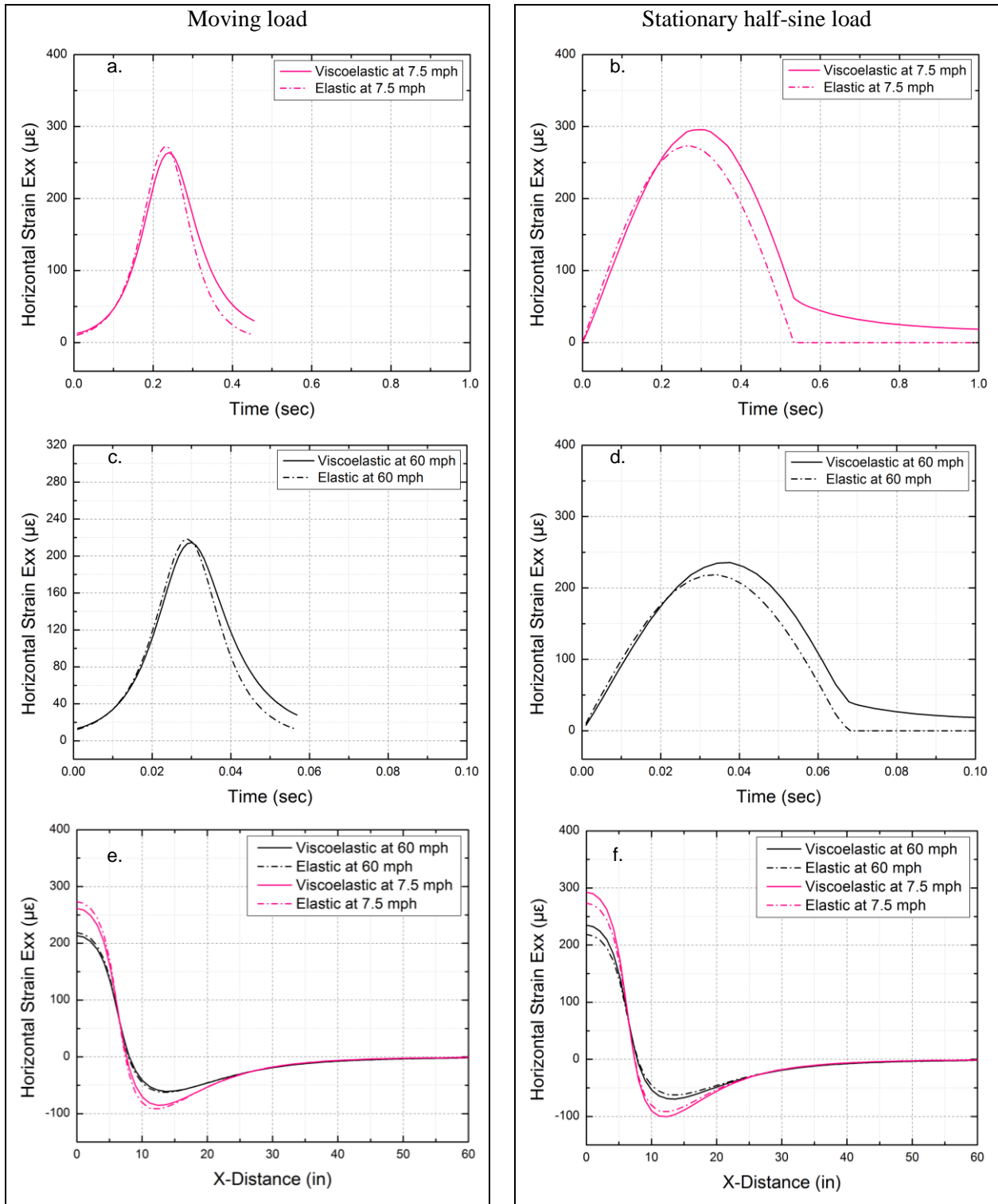


Figure A-4 3D horizontal strain (transverse) evaluation for moving and stationary half-sine load: a-b. Horizontal strain at L2 (slow traffic); c-d. Horizontal strain at L2 (fast traffic); e. Horizontal strain along AC bottom when moving load reached path center (slow/fast traffic); f. Horizontal strain along AC bottom at peak loading time (slow/fast traffic).

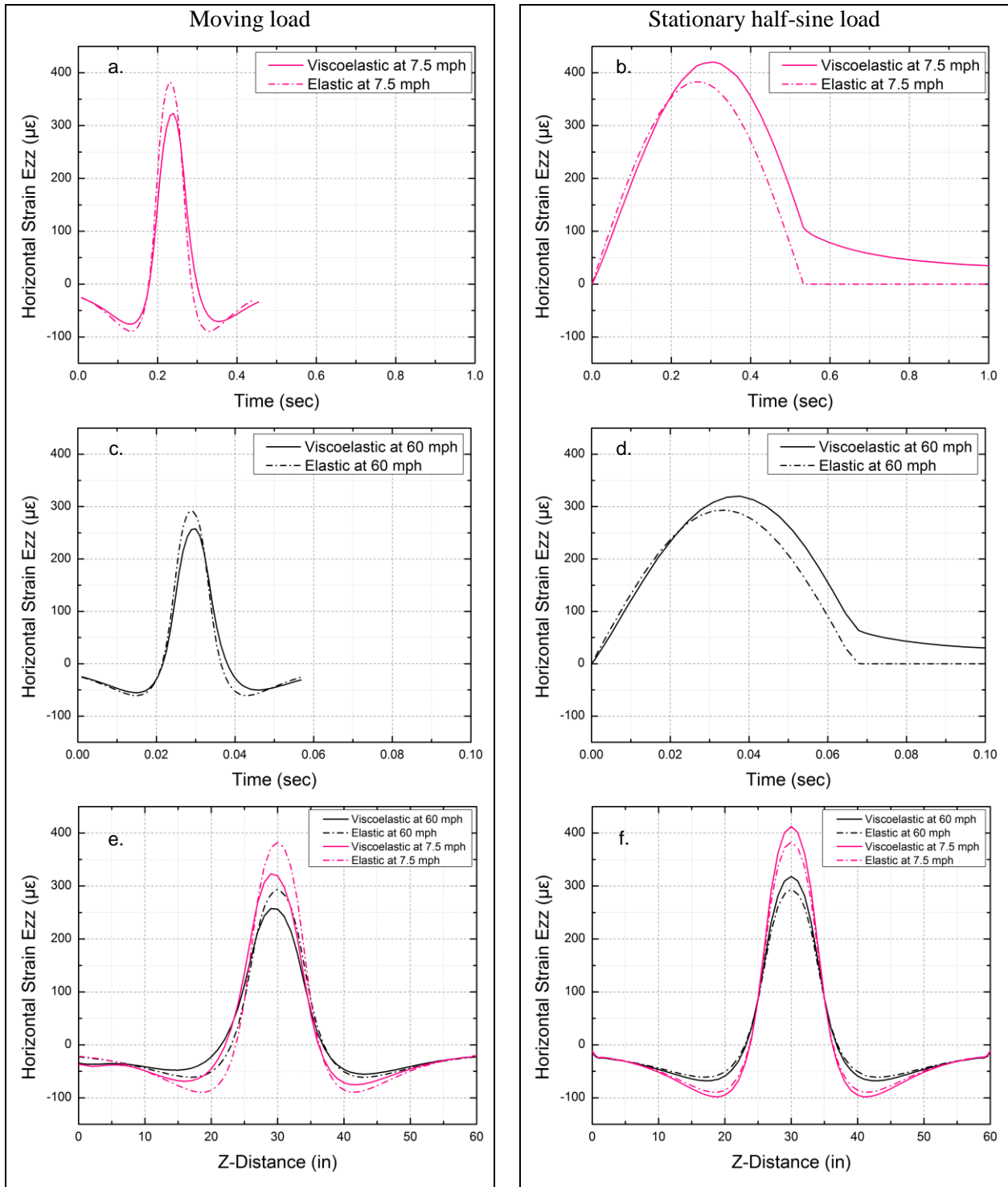


Figure A-5 3D horizontal strain (longitudinal) evaluation for moving and stationary half-sine load: a-b. Horizontal strain at L2 (slow traffic); c-d. Horizontal strain at L2 (fast traffic); e. Horizontal strain along AC bottom when moving load reached path center (slow/fast); f. Horizontal strain along AC bottom at peak loading time (slow/fast).

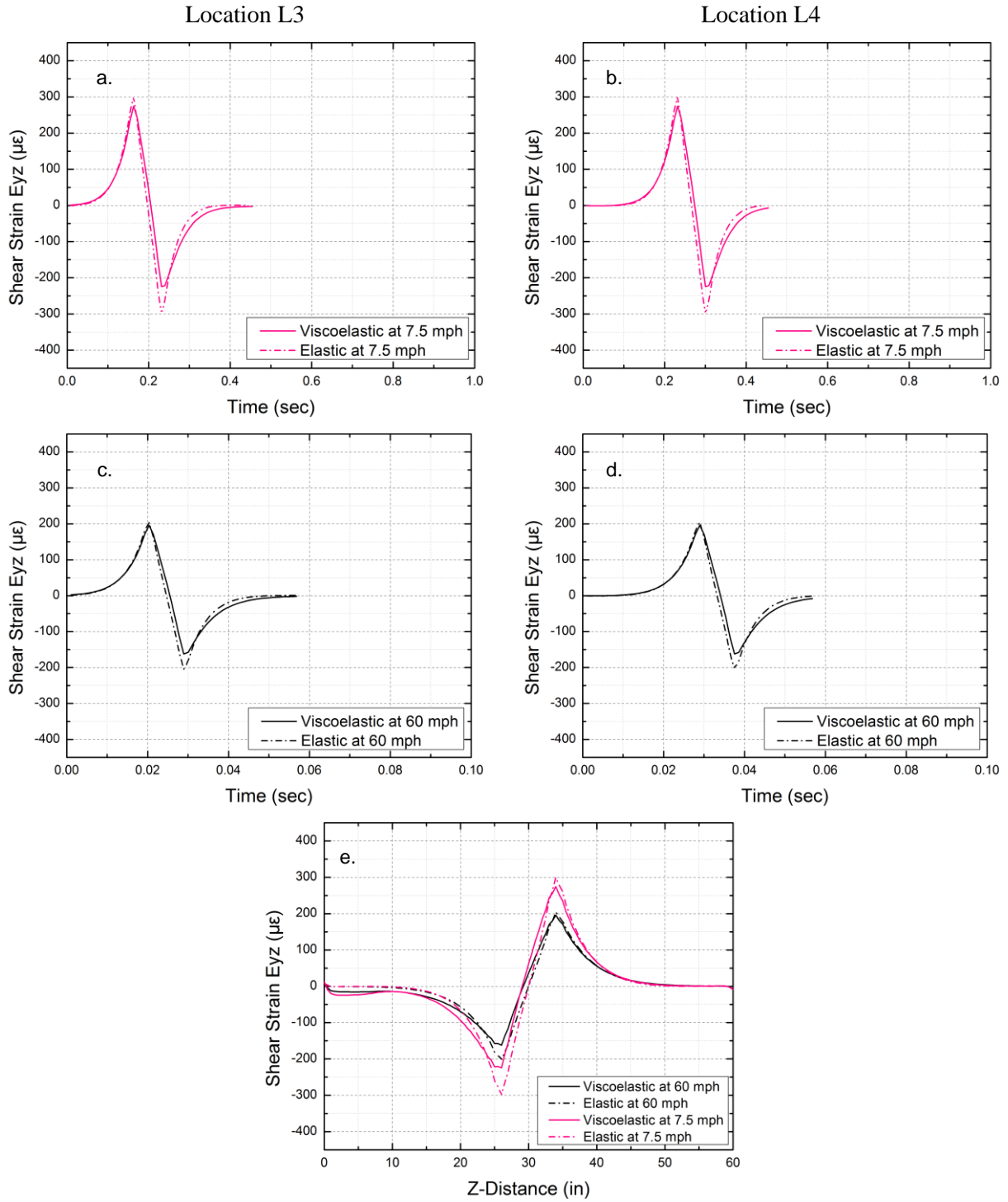


Figure A-6 3D shear strain (longitudinal) evaluation for moving load: a. L3 (slow traffic); b. L4 (slow traffic); c. L3 (fast traffic); d. L4 (fast traffic); e. Shear strain along AC mid-depth when moving load reached path center (slow/fast traffic).

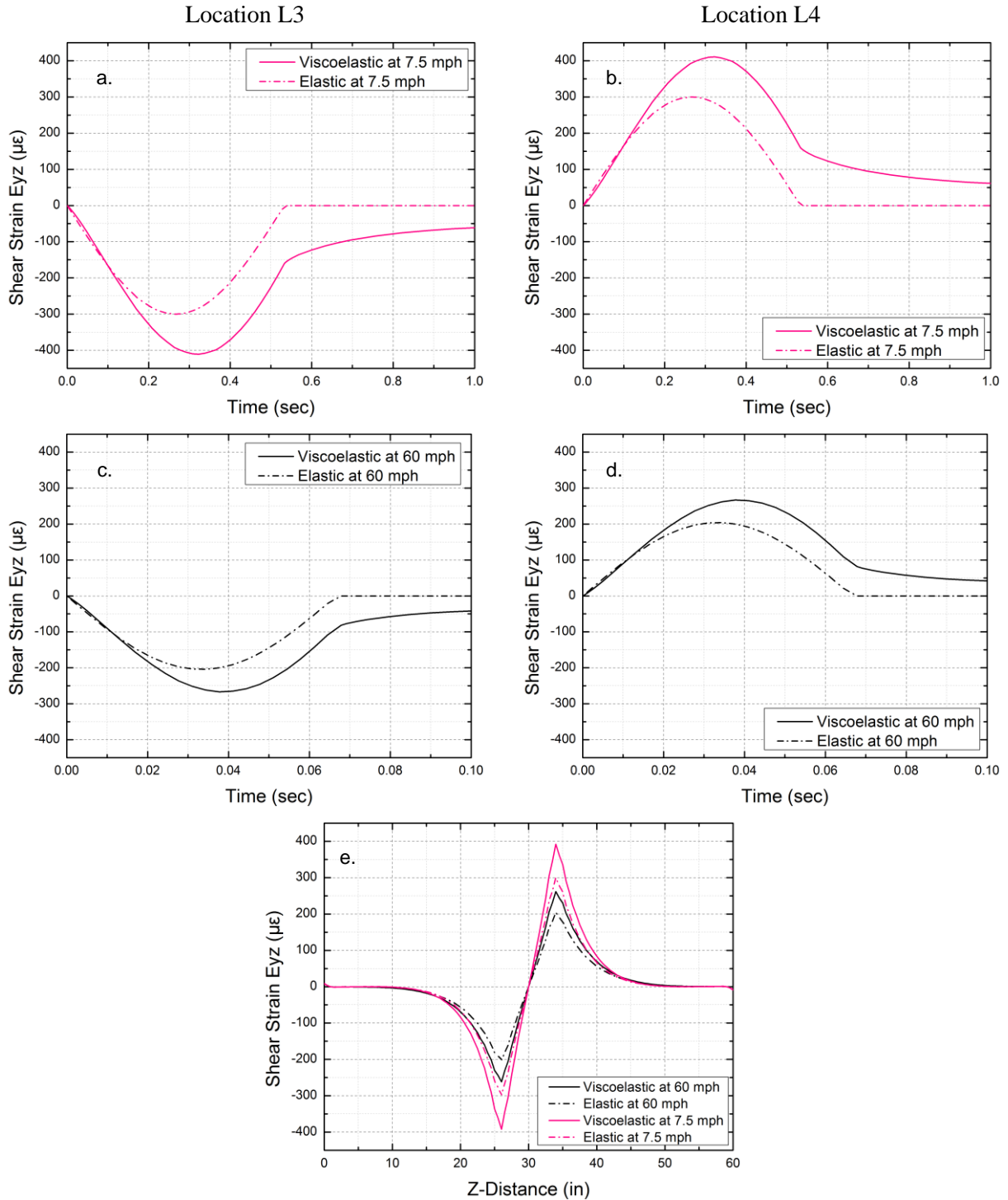


Figure A-7 3D shear strain (longitudinal) evaluation for a stationary half-sine load: a. L3 (slow traffic); b. L4 (slow traffic); c. L3 (fast traffic); d. L4 (fast traffic); e. Shear strain along AC mid-depth at peak loading time (slow/fast traffic).

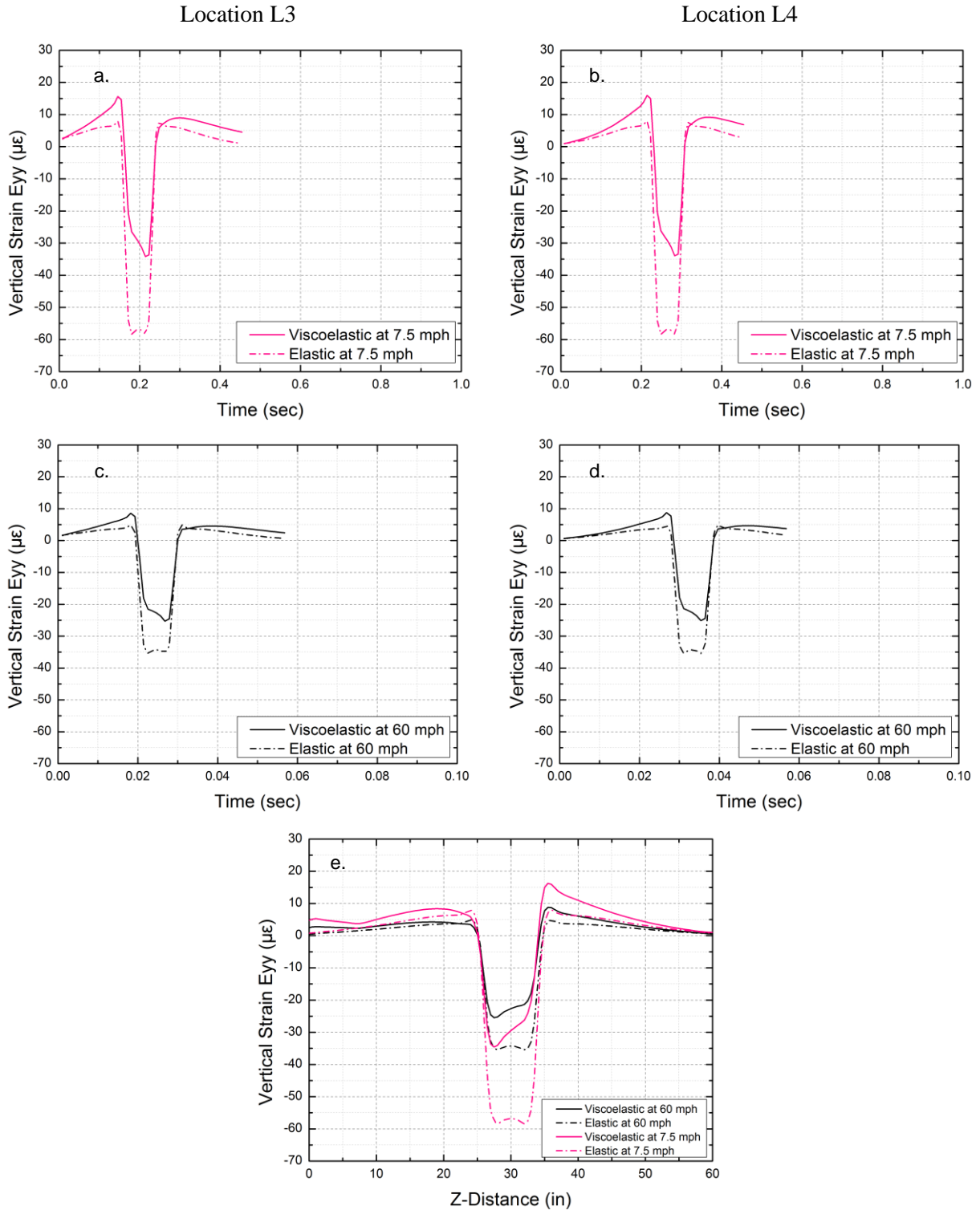


Figure A-8 3D vertical strain (longitudinal) evaluation for a moving load: a. L3 (slow traffic); b. L4 (slow traffic); c. L3 (fast traffic); d. L4 (fast traffic); e. Vertical strain along AC mid-depth when moving load reached path center (slow/fast traffic).

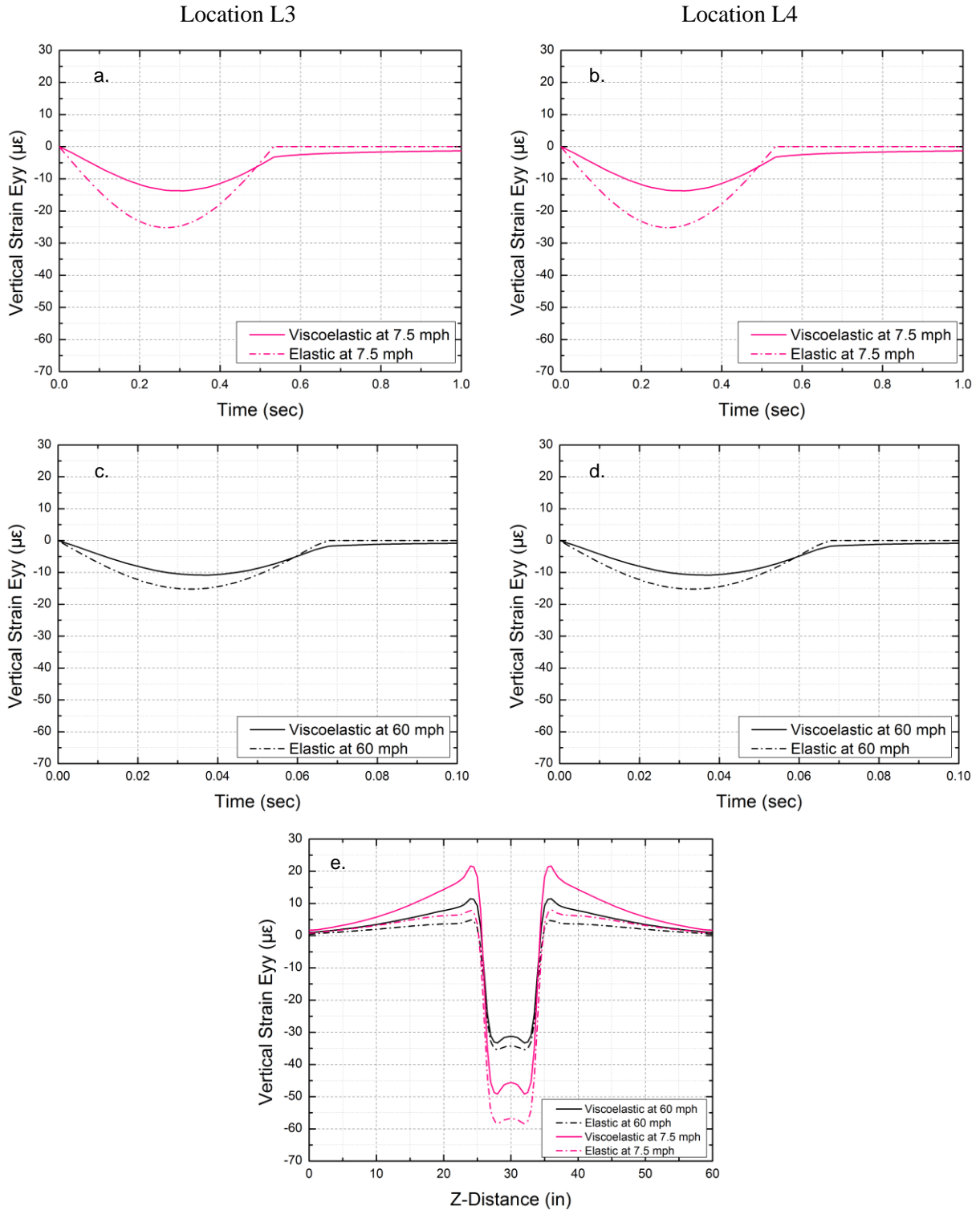
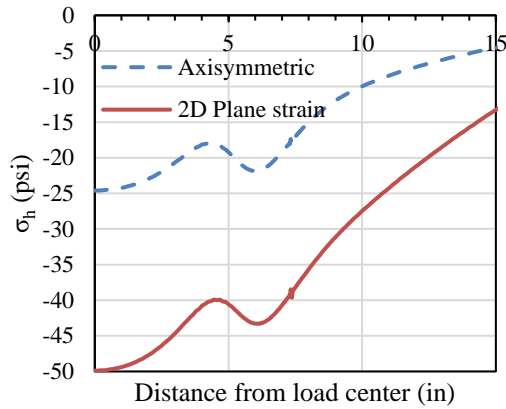


Figure A-9 3D vertical strain (longitudinal) evaluation for a stationary half-sine load: a. L3 (slow traffic); b. L4 (slow traffic); c. L3 (fast traffic); d. L4 (fast traffic); e. Vertical strain along AC mid-depth at peak loading time (slow/fast traffic).

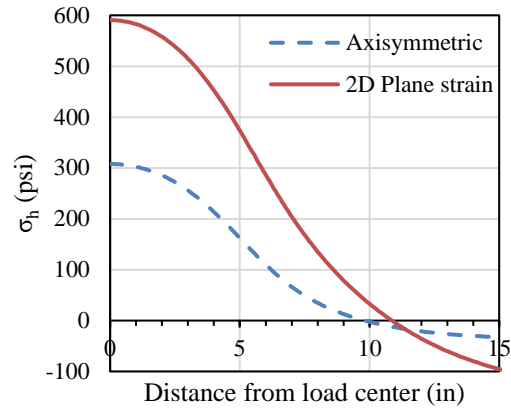
APPENDIX B VERIFICATION OF BENDING STRESS RATIO (BSR)

The bending stress ratio (BSR) was initially developed based on the maximum horizontal tensile stress at the AC bottom (under the center of the tire). However, the focus of this project is on stress distribution around the mid-depth of the AC layer. Thus, further verification of the BSR was warranted. This section discusses the results obtained with an axisymmetric and a 2D plane-strain model at two locations (AC interface and AC bottom) for two different conditions: fully bonded system and a pavement with a localized debonded zone. The pavement structure used was that showed in Table 5-1 ($E_1/E_2=32$, $h_1/h_2=1/3$, $BSR=0.5$).

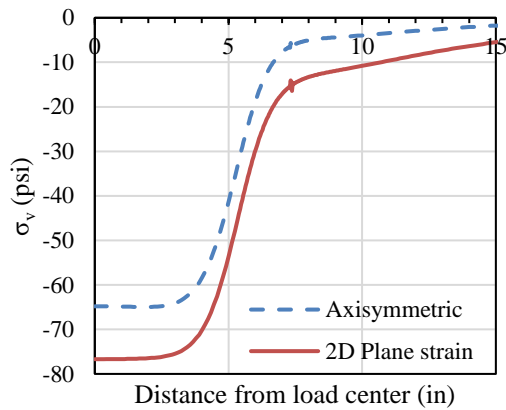
Stress distributions for the fully bonded condition are plotted in Figure A-1. As expected, the 2D plane-strain model predicted higher stresses than the axisymmetric one, but both models exhibited rather similar stress pattern (i.e., distribution was captured, magnitude was not). The ratio of stress from the axisymmetric model to that from 2D plane-strain is illustrated in Figure A-2. As shown in Figure A-2a, a value of 0.5 predicted by the BSR approach agreed fairly well with the stress ratio obtained for the horizontal normal stress and horizontal shear stress in the area of interest (around the tip of the debonded zone) along the AC interface. With respect to vertical normal stress, the ratio under the tire was close to 0.85, which is significantly higher than the prediction. This result confirmed confinement near the tire is primarily controlled by the magnitude of the load (100 psi in both cases) and not much by 2D or 3D representation. Figure A-2b shows BSR prediction was very accurate along the AC bottom for the three stresses evaluated. The spike observed for the ratio in horizontal normal stress at approximately 11 in from the load center was due to an offset in the point at which the axisymmetric and 2D plane-strain models reversed the curvature (i.e., stress changed from tension to compression). However, the stress magnitude at this location was relatively small (Figure A-1d) and this effect can be ignored.



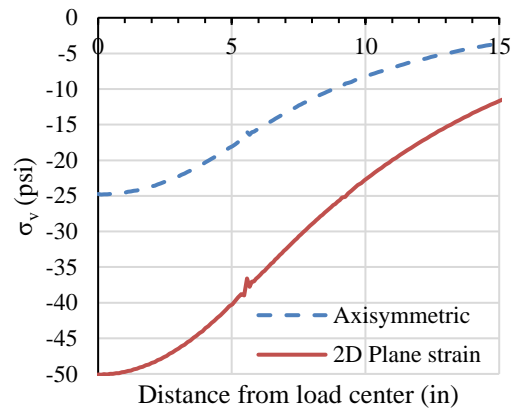
a. Horizontal normal stress along AC interface



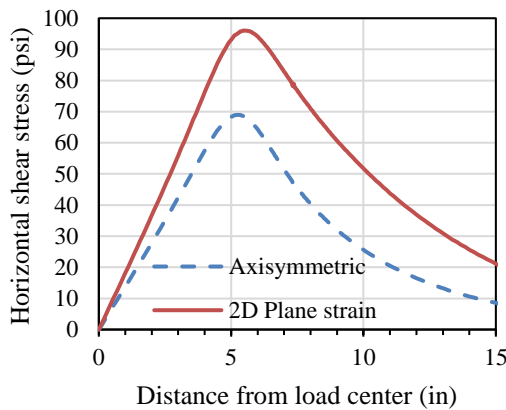
d. Horizontal normal stress along AC bottom



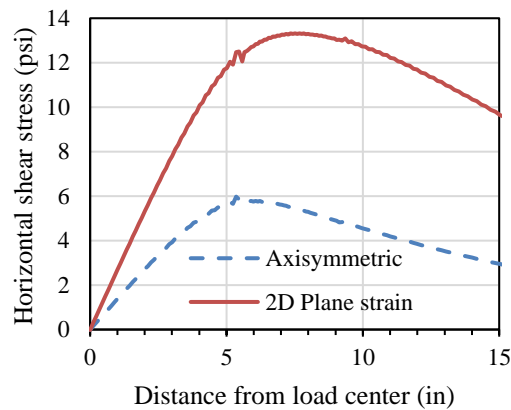
b. Vertical normal stress along AC interface



e. Vertical normal stress along AC bottom



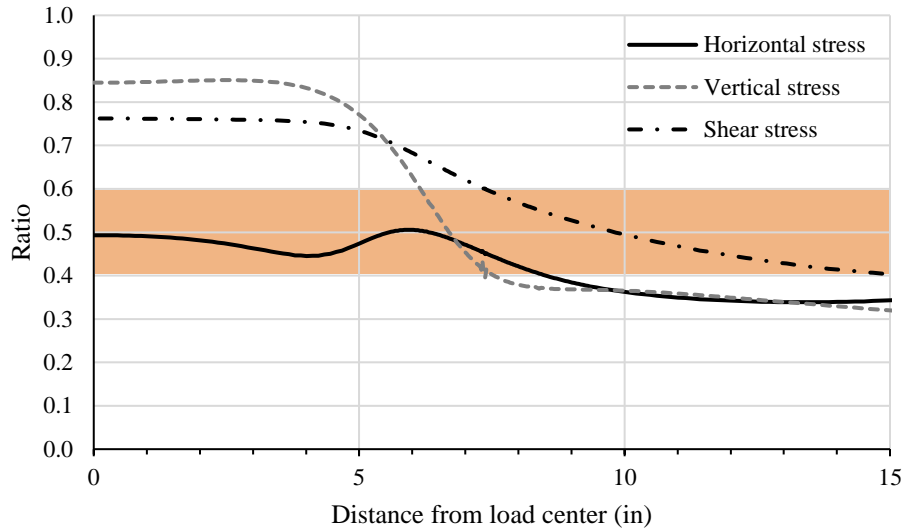
c. Horizontal shear stress along AC interface



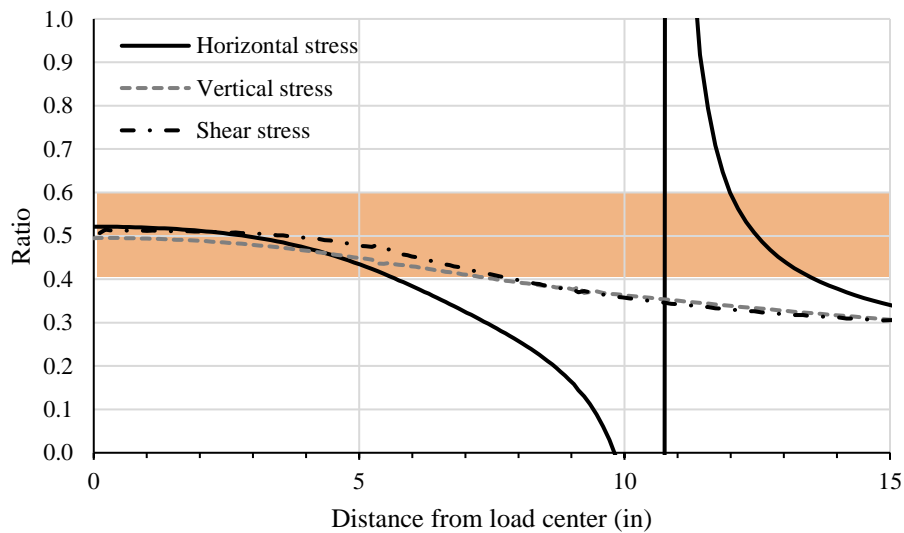
f. Horizontal shear stress along AC bottom

Figure B-1 Stress distribution along AC interface and AC bottom for a fully bonded pavement.

Note: positive normal stress denotes tension.



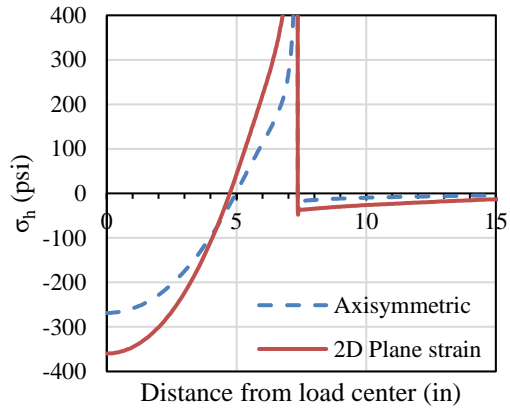
a. AC interface



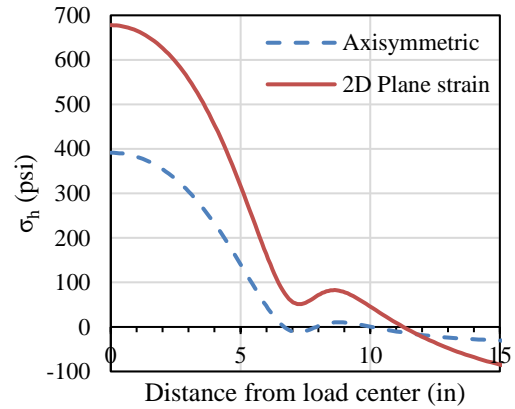
b. AC bottom

Figure B-2 Ratio between stresses from an axisymmetric model and a 2D plane-strain model.

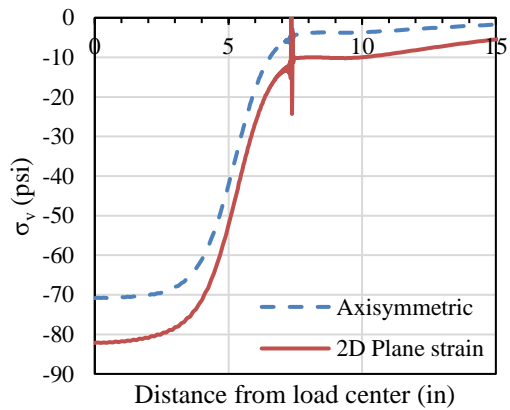
Figure A-3 plots the stress distribution for a localized debonding condition (a 7.35-in zone debonded from the load center along the AC interface). For the debonded zone along the AC interface, stresses were chosen immediately below the interface. Again, the 2D plane-strain model captured the general pattern of the stress distribution, but not the magnitude. Then, the ratio of stress predicted by the axisymmetric model to that predicted by the 2D plane-strain model was calculated and summarized in Figure A-4.



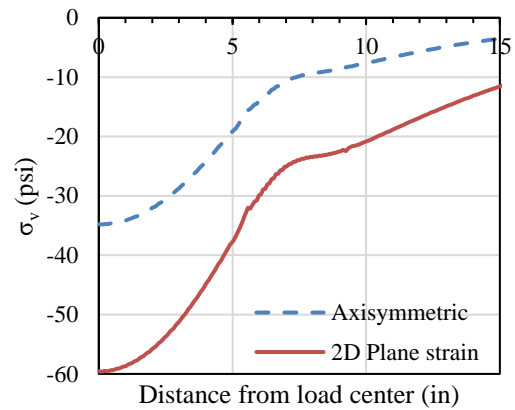
a. Horizontal normal stress below AC interface



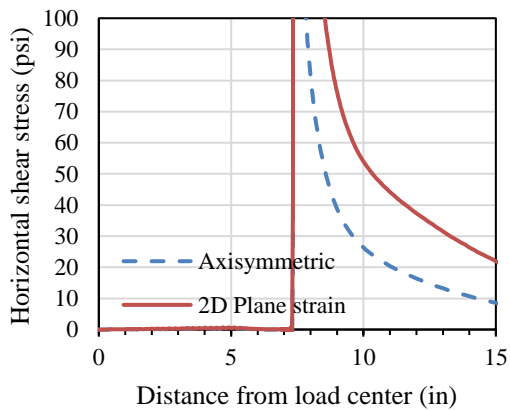
d. Horizontal normal stress along AC bottom



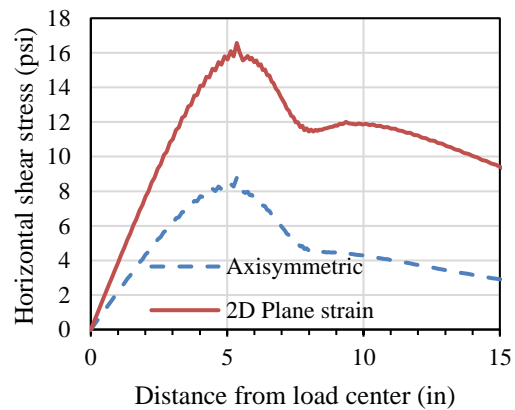
b. Vertical normal stress below AC interface



e. Vertical normal stress along AC bottom

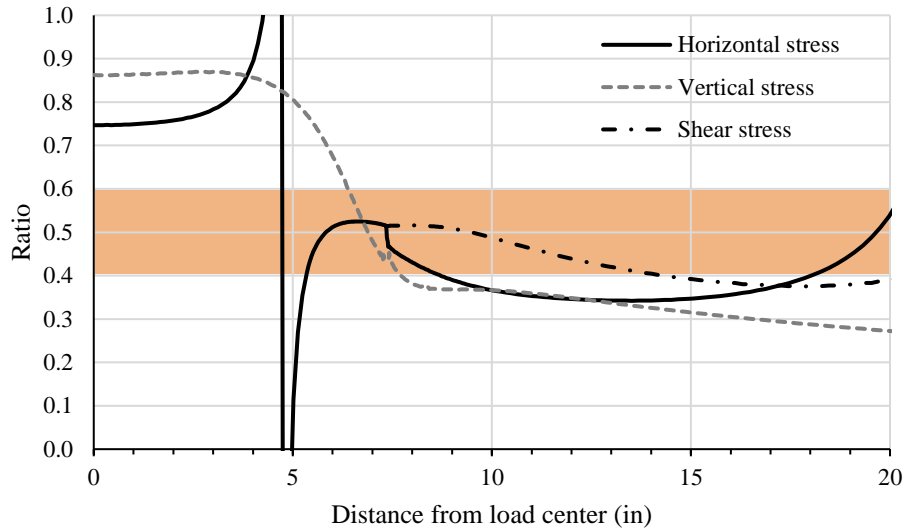


c. Horizontal shear stress below AC interface

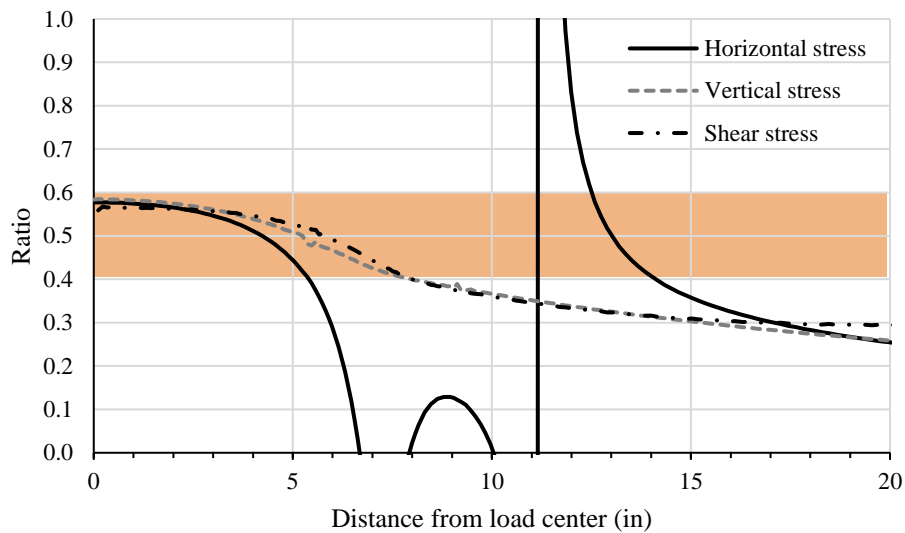


f. Horizontal shear stress along AC bottom

Figure B-3 Stress distribution immediately below AC interface and along AC bottom for a pavement with localized debonding. Note: positive normal stress denotes tension.



a. Below AC interface



b. AC bottom

Figure B-4 Ratio between stresses from an axisymmetric model and a 2D plane-strain model.

Figure A-4 shows the stress ratio around the tip of the debonded zone (i.e., 7.35 in from the load center) agreed with the value of 0.5 predicted by the BSR approach. As mentioned above, spikes on horizontal normal stress were caused by an offset in the point at which the axisymmetric and 2D plane-strain models changed from tension to compression or vice versa. Of note, a ratio of 0.75 was found for the horizontal normal stress under the center of the tire immediately below the AC interface (Figure A-4a). This value, which was not observed for the fully bonded system,

means the tensile stress at this location was higher than initially expected. A possible explanation is that the high bending stress at this location is caused by the localized debonded zone introduced near the surface rather than by the overall structure. In other words, localized discontinuities may increase bending stress under the tire (particularly near surface), but global bending is still governed by the pavement structure.

In conclusion, the results presented in this section showed the BSR approach can be employed to reasonably predict 3D bending stresses (horizontal normal stress and shear stress) near the mid-depth of the AC layer from a 2D plane-strain model with localized debonding along the interface. Regarding normal vertical stress, BSR seemed to underpredict stress magnitude under the tire, particularly near surface, so it is recommended that stress magnitude be used as directly provided by 2D plane-strain models.